De relatie tussen wandschuifspanningsparameters en atherosclerose: een experimentele en computationele studie bij muizen

Wall Shear Stress Metrics and Their Relation to Atherosclerosis: an Experimental and Computational Study in Mice

David De Wilde

Promotoren: prof. dr. ir. P. Segers, prof. dr. G. De Meyer, dr. ir. B. Trachet
Proefschrift ingediend tot het behalen van de graad van
Doctor in de Ingenieurswetenschappen: Biomedische Ingenieurstechnieken

Vakgroep Elektronica en Informatiesystemen
Voorzitter: prof. dr. ir. R. Van de Walle
Faculteit Ingenieurswetenschappen en Architectuur
Academiejaar 2015 - 2016

UNIVERSITEIT GENT

ISBN 978-90-8578-875-1
NUR 954
Wettelijk depot: D/2016/10.500/7

Supervisors:

Prof. dr. ir. Patrick Segers
Prof. dr. Guido De Meyer
Dr. ir. Bram Trachet

Research lab:

Institute Biomedical Technology
Biofluid, Tissue and Solid Mechanics for Medical Applications (bioMMeda)
Ghent University
De Pintelaan 185 - Blok B
B–9000 Gent
Belgium

Members of the exam committee:

Chairman:	
Prof. dr. ir. Luc Taerwe	Faculty of Engineering and Architecture, UGent
Secretary:	
Prof. dr. ir. Abigail Swillens	Faculty of Engineering and Architecture, UGent
Reading committee:	
Prof. dr. ir. Peter Weinberg	Imperial College London, United Kingdom
Prof. dr. ir. Frank Gijsen	Erasmus MC, Rotterdam, The Netherlands
Prof. dr. ir. Jan Vierendeels	Faculty of Engineering and Architecture, UGent
Other members:	
Prof. dr. Christian Vanhove	Faculty of Engineering and Architecture, UGent
Dr. Paul Fransen	Division of Physiopharmacology, University of Antwerp

This research was funded by a research grant of the Agency for Innovation by Science and Technology in Flanders (IWT/111618).

The only way to keep your health is to eat what

you don't want, drink what you don't like, and do

what you'd rather not.

Mark Twain

Preface

It is already quite some time ago that I started my PhD research. As my colleagues know, the start of a PhD is challenging, exciting but most of all abrupt. First, all the people in the lab are introduced and you get assigned your very own desk. That desk will start to feel a little bit like home over the years (especially since I had the luck to be assigned a spot in office awesome). The second announcement goes like: *"Hey, you should write a grant proposal for the IWT within 2 weeks! Could you write down what you plan to do in the next 4 years?'*. It's only then that the PhD journey officially starts and it starts with the realization: *"I will never be able to do this on my own"*.

This is especially the case since my work is mainly an aggregating study, combining the methods and hard work of my predecessors. As such, I consider the major part of my PhD thesis as a big puzzle, bringing together all those fruits of labour. Because the help and support of specialists in all these different domains was vital, I puzzled together a long list of people that provided me with help and guidance.

Right from the start, the four corner pieces were already defined: Patrick, Bram, Guido and Carole. It was really astonishing how the roadmap of a whole 4 year IWT project was defined in the 2 week time frame with their help. First of all, I'd like to thank Patrick for helping me every step of the way. Next to the help with setting up the direction of the research, his help consisted of convincing me of the importance of my own results, proofreading a lot of text and sometimes warning me that I was making everything too complicated. He reminded me countless times that the story is the most important part, which led directly to the coherent story in this PhD thesis.

Bram introduced me to the basics of almost all important tools and methodologies, for which I am very grateful. Furthermore, Bram tremendously improved the literal style of basically everything I have written, thanks to the very thorough corrections that he provided time and time again.

The Antwerp corner pieces consisted of Guido and Carole, with both of them being essential for the successful outcome of this project. Thanks to them, the whole (difficult) breeding process of the laboratory mice, was

reduced to the simple question: *"Can I have some mice please?"*. Moreover, their experience with histology was crucial to validate important parts of this work. For the interpretation of the results, their different background and point of view was highly valuable. Also thanks to Mandy for proofreading the first two chapters of this thesis.

The *in vivo* imaging of the mice was another important piece of the puzzle. For this part, I mainly want to thank the people from INFINITY (Benedicte, Christian and Scharon) together with Bert and Francisco. I would not have been able to do any FSI simulations without the help of Liesbeth, Joris, Joris, Alessandra, Abigail and Jan. I also want to thank Mathias, Francesco and Nic for the help with the solid mechanics.

I thank the past and present members of my office (Gianluca, Koen, Liesbeth, Alessandra, Darya, Margo, Wouter, Danilo, Giussepe, Daniela, Giorgia, Hicham) for the "homemade" birthday cakes, the coffee breaks, the colour advice, brightening up the day with some Italian flair, the helping hands and the listening ears. Of course I also want to thank all the other members of bioMMeda. Special thanks go to Annette for volunteering to help me with the most boring part of my research. I would like to thank Saskia for all the administrative support. My gratitude goes to Jurgen for the technical assistance and for the nice times when we were trying to piece together a website.

I also want to thank Ruoyu, Kim and Frank of the Erasmus MC Rotterdam for the fruitful discussions, helpful remarks and warm welcome at the yearly shear stress symposium. I hope the future brings more collaborations between both research groups.

Uiteraard wil ik ook nog mijn vrienden en familie bedanken. Maarten en Karel voor de (verplichte) interesse en het geduld wanneer PhD besognes luchtigere cafépraat in de weg stonden. Mijn zussen, ouders, grootouders en familie wil ik bedanken om in mij te geloven, me te steunen, de hulp en voor de ludieke insteek die altijd beschikbaar was.

Maar vooral wil ik ook Sofie nog bedanken. Ze vormt de laatste jaren het belangrijkste puzzelstuk in mijn leven. Bedankt om er altijd te zijn voor mij, geduld te hebben als het nodig was, me bij te staan met raad en daad en om samen met mij stap voor stap aan een toekomst te bouwen.

Finally, thanks to you, my dear reader. By now you have already read two pages of my thesis. Thank You… (You're almost there.)

David De Wilde
Gent, January 2016

Samenvatting

Inleiding

Hart- en vaatziekten zijn wereldwijd de belangrijkste doodsoorzaak. Atherosclerose of slagaderverkalking wordt gekenmerkt door de ontwikkeling van plaque in de middelgrote tot grote slagaders. Gedurende het langdurende ontwikkelingsproces zijn vele verschillende biologische processen betrokken die uiteindelijk leiden tot de opstapeling van vetten in de slagaderwand en de inflammatie (ontsteking) van diezelfde slagaderwand.

De meeste risicofactoren zijn systemisch van aard, zoals roken, leeftijd, hoge bloeddruk en hoge concentraties van vetten in het bloed. Ze "bevoordelen" dus geen specifieke locaties. In tegenstelling tot voorgaande risicofactoren ontwikkelen atherosclerotische plaques zich echter voornamelijk aan de binnenbocht en in vertakkingen van de bloedvaten. Het wordt algemeen aanvaard dat de bloedstroom (hemodynamica) een (mede-)oorzaak van dit lokale karakter van plaque ontwikkeling is. De bloedstroom beïnvloedt de ontwikkeling van atherosclerose via de wandschuifspanning (WSS, de wrijfkracht gedeeld door de oppervlakte) die ze uitoefent op de endotheelcellen aan de binnenkant van de bloedvatwand. Een lage en/of oscillerende WSS activeert en/of faciliteert de biologische processen die leiden tot plaque ontwikkeling.

Eén van de moeilijkheden in het onderzoek naar de rol van de hemodynamica bij plaquevorming, is dat de oorspronkelijke wandschuifspanning, voordat enige atherosclerose was ontwikkeld, gelinkt moet worden met de plaatsen waar de atherosclerose ontwikkelt op een later tijdstip. Om dit mogelijk te maken, vergelijken de meeste beschikbare studies WSS in een eerste groep gezonde proefpersonen/dieren (zonder plaque ontwikkeling) met de plaque locaties, gemeten in een tweede groep proefpersonen/dieren (deze onderzoeken vergelijken dus twee verschillende groepen in plaats van een langdurige opvolging van de dieren). Hiertoe vergelijkt men de gemiddelde waardes gevonden voor de metingen in beide groepen. Het gevaar van uitmiddeling is echter dat de finale correlatie tussen WSS en atherosclerosevorming wordt overschat. In deze PhD thesis is het dus ons doel om te onderzoeken

of er een link bestaat tussen WSS en atherosclerose, en dit op een individuele basis in een studie die individuele dieren opvolgt doorheen de tijd. Deze aanpak maakt het overbodig om de meetwaardes uit te middelen. De centrale onderzoeksvraag is dan ook:

Bestaat er een individuele en kwantitatieve link tussen de wandschuifspanning in een gezonde referentietoestand en de daaropvolgende plaqueontwikkeling in muismodellen van atherosclerose?

In dit werk maken we gebruik van muismodellen van atherosclerose omdat deze ons toelaten om de proefdieren op te volgen gedurende de gehele tijdspanne van atherscleroseontwikkeling. Om de onderzoeksvraag te kunnen beantwoorden, dienen er verschillende tussenliggende technische doelen gehaald te worden. Ten eerste moet er een *in vivo* methode ontwikkeld worden om de locaties van atherscleroseontwikkeling in muizen te kunnen bepalen. Ten tweede is het nodig dat er verscheidene (bestaande) computermodellen en technieken aangepast en gecombineerd worden om de bloedstroom en bloedvaten van muizen te simuleren. Ten slotte dient het correcte statistisch model toegepast te worden om de link tussen WSS en atherosclerose te kwantificeren.

Deel I: Het bestuderen van atherosclerose in muizen

Hoofdstuk 1: Atherosclerose

Dit eerste hoofdstuk bevat algemene achtergrondinformatie bij de anatomie en de fysiologie van het humane cardiovasculaire systeem dat bestaat uit het hart en de bloedvaten. Een overzicht wordt gegeven van de belangrijkste slagaders in het menselijke lichaam. Daarnaast wordt ingezoomd op de anatomische beschrijving van de bloedvaten in de hals en het hoofd. De halsslagader (common carotid artery - CCA) vertakt in de binnenste (internal carotid artery - ICA) en de buitenste (external carotid artery - ECA) halsslagaders. Deze drie slagaders vormen het onderwerp van deze thesis. In een tweede deel wordt er dieper ingegaan op atherosclerose of slagaderverkalking. Deze ziekte wordt gekenmerkt door de vorming van plaques in de slagaderwand. De belangrijkste processen die hier een rol in spelen zijn de infiltratie van vetten in de vaatwand en inflammatie (ontsteking) van de vaatwand. Vervolgens worden de ernstige klinische complicaties van atherosclerose kort besproken. Atherosclerotische plaques kunnen scheuren

en zo kunnen er bloedklonters ontstaan wat kan leiden tot een hartaanval of een beroerte, wat de belangrijkste doodsoorzaken zijn wereldwijd. Verder worden twee verschillende classificatiesystemen overlopen om de plaques in te delen op basis van de histologische kenmerken enerzijds en op basis van het risico tot complicaties anderzijds. Verschillende risicofactoren voor het ontwikkelen van hart- en vaatziekten zijn algemeen bekend. Meer specifiek voor atherosclerose zijn deze risicofactoren: geslacht, leeftijd, genetische factoren, een hoge bloeddruk, obesitas, roken en overmatig alcohol verbruik. In tegenstelling tot wat men zou kunnen verwachten op basis van deze systemische risicofactoren, ontwikkelt atherosclerose zich op specifieke plaatsen in het cardiovasculair systeem. De lokale hemodynamica is een mechanisme dat deze specificiteit qua locaties kan verklaren. In het laatste deel van dit hoofdstuk wordt beschreven hoe de bloedstroming het ontstaan van plaques kan beïnvloeden. De endotheelcellen, die de grens vormen tussen het bloed en de bloedvatwand, spelen hier een belangrijke rol in door het "voelen" van de wandschuifspanning (WSS) die de bloedstroom uitoefent.

Hoofdstuk 2: Muismodellen van atherosclerose

Het trage tijdsverloop van de ontwikkeling van atherosclerose bij de mens bemoeilijkt het onderzoek naar atherosclerose. Daarom zijn verschillende diermodellen ontwikkeld die humane atherosclerose nabootsen. Dit tweede hoofdstuk geeft een overzicht van enkele diermodellen die dikwijls gebruikt worden bij atherosclerose onderzoek, zoals konijnen, varkens en apen. Vervolgens wordt het muismodel in meer detail beschreven vanwege de specifieke voordelen: ze zijn goedkoop, er is snelle ontwikkeling van atherosclerose, er is gemakkelijke genetische manipulatie mogelijk en de atherosclerotische plaques vertonen grote gelijkenissen met humane plaques. Daarnaast is het bij muizen ook mogelijk om studies op te zetten met een gro(o)t(er) aantal dieren, wat noodzakelijk kan zijn om de resultaten statistisch te onderbouwen. Daarnaast is het ethisch meer algemeen aanvaard om muizen te gebruiken voor preklinisch onderzoek in vergelijking met andere diermodellen. Eén strategie om de invloed van de hemodynamica op atherosclerosevorming te bestuderen, is om de bloedstroom te manipuleren met een chirurgische ingreep. Het grootste nadeel van muizen is echter dat de normale wildtype muis behoorlijk resistent is tegen de ontwikkeling van atherosclerose. Er zijn echter verschillende rassen gekweekt die gevoelig zijn aan atherosclerose wanneer ze een vetrijk dieet voorgeschoteld krijgen. De normale, zwarte labo muis (C57BL/6J) is het meest gebruikte ras. Om de concentratie van lipoproteïnes in het bloedplasma nog verder te verhogen, zijn het lage-dichtheid-lipoproteïne-receptor knockout ($LDLR^{-/-}$) ras en het ras dat apolipoproteïne E ($ApoE^{-/-}$) mist, ontwikkeld. In het $ApoE^{-/-}$ muismodel ontwikkelen zich de meest vergevorderde plaques en dus wordt dit muismodel regelmatig gebruikt. Aan de universiteit van Antwerpen werd vervolgens een muismodel

ontwikkeld dat naast de apolipoproteïne E deficiëntie ook een heterogene mutatie in het fibrilline 1 gen heeft (ApoE$^{-/-}$ Fbn1$^{C1039G+/-}$). Bij dit muismodel treedt spontane ruptuur op van de atherosclerotische plaques, wat grotendeels afwezig is bij de andere muismodellen. In dit werk werden zowel ApoE$^{-/-}$ als ApoE$^{-/-}$ Fbn1$^{C1039G+/-}$ muizen gebruikt om een diepgaande studie te doen naar de invloed van hemodynamica op de vorming van deze complexe plaques.

Hoofdstuk 3: Beeldvorming van atherosclerose bij muizen

Ultrageluid (ultrasound - US) en micro-computertomografie (μCT) zijn de twee *in vivo* beeldvormingstechnieken die voornamelijk worden gebruikt in dit onderzoek. Ultrageluid is gebaseerd op ultrasone akoestische golven boven de hoorbare frequentie. Met behulp van deze techniek kunnen verschillende soorten beelden bekomen worden, afhankelijk van de precieze beeldverwerking van de signalen. Een weergave van de anatomische structuren in 2D wordt bekomen met B-mode beeldvorming. Bij M-mode beeldvorming wordt de variatie over de tijd van metingen langsheen 1 enkele scanlijn weergegeven. Dit kan gebruikt worden om bijvoorbeeld de pulsatiliteit van een bloedvat op te meten. Pulsed Doppler is nog een andere techniek, die de snelheid van de bloedstroom opmeet. Meer specifiek voor muizen, vormen de hogere hartslag en de kleinere grootte van de bloedvaten een uitdagende omgeving, vergeleken met mensen. Daarom werd een specifieke scanner, de Vevo2100, gebruikt voor dit onderzoek.

Micro-computertomografie (μCT) is gebaseerd op ioniserende röntgenstraling. Een μCT scanner bestaat uit 3 delen: de röntgenbron, het object en de detector. De röntgenbron genereert een kegelvormige bundel van röntgenstraling die doorheen het te beeldvormen object (een muis) gaat. Nadien wordt deze straling opgevangen en geregistreerd door een detector. Een deel van de straling wordt geattenueerd door de weefsels waardoorheen de straling penetreert. De hoeveelheid attenuatie is afhankelijk van de lokale attenuatie-coëfficiënten. Voor een μCT meting worden verschillende projecties onder verschillende hoeken opgemeten. Om dit te doen, wordt zowel de röntgenbron als de detector rond de muis geroteerd. Voor de beeldvorming van de bloedvaten is het behalen van voldoende contrast de grootste uitdaging. Recent werden er echter verscheidene contrastmiddelen ontwikkeld in verband met deze toepassing. In het huidige onderzoek werd gebruikgemaakt van het goud-nanopartikel contrastmiddel Aurovist.

Deel II: Computationele technieken voor de studie van de arteriële hemodynamica

Hoofdstuk 4: Numerieke simulaties van de arteriële hemodynamica

Om een voldoende gedetailleerde weergave van het stromingsveld in de arteriën te bekomen, maakt men dikwijls gebruik van computationele vloeistofdynamica (computational fluid dynamics (CFD)). In dit hoofdstuk worden de algemene principes van de numerieke technieken uitgelegd van de methodes toegepast in hoofdstukken 8 en 9. Eerst worden de vergelijkingen opgelijst die de stroming van onsamendrukbare vloeistoffen beschrijven. Nadien volgen de algemene principes van CFD, dat wordt gebruikt om deze vergelijkingen op te lossen. Het bufferende effect van de halsslagaders wordt in rekening gebracht door de beweging van de bloedvatwand, onder impuls van de bloedstroom en de bloeddruk, in beschouwing te nemen. In het tweede deel van dit hoofdstuk worden de vergelijkingen van de vastestofmechanica overlopen en de oplossingsmethode van deze differentiaalvergelijkingen (computationele vastestofmechanica - computational solid mechanics (CSM)). Als laatste is het nog nodig om beide deelproblemen (de vloeistofmechanica en de vastestofmechanica) aan elkaar te koppelen om tot een vloeistof-structuur interactiemodel te komen. In het laatste stuk van het huidige hoofdstuk wordt deze koppelingstechniek Tango kort uiteengezet.

Hoofdstuk 5: Hemodynamische wandschuifspanningsparameters

In deze PhD thesis zijn we eerder geïnteresseerd in de invloed die het bloed heeft op de endotheelcellen dan op het snelheidsveld van de bloedstroom zelf. De endotheelcellen vormen de grens tussen de bloedstroom en de bloedvatwand en vormen dus het gedeelte van de bloedvatwand dat de bloedstroming waarneemt en waar processen die leiden tot atherosclerose vorming worden geactiveerd. Meer specifiek ondervinden de endotheelcellen de wandschuifspanning (WSS) die de bloedstroom uitoefent. Verschillende parameters werden reeds ontwikkeld om het atherogene effect van verschillende stroompatronen zo optimaal mogelijk te kwantificeren. De belangrijkste van deze parameters worden geïllustreerd in hoofdstuk 5. In het eerste deel worden de op de magnitude gebaseerde hemodynamische wandschuifspanningsparameters opgelijst: de tijdsgemiddelde wandschuifspanning (time averaged wall shear stress (TAWSS)), de oscillatie index (oscillatory shear index (OSI)), de relatieve verblijftijd (relative residence time (RRT)) en de zijdelingse wandschuifspanning (transverse wall shear stress (transWSS)). Al deze parameters beschrijven (een combinatie van) de volgende fenomenen: de grootte van de wandschuifspanning, het oscillerende karakter van de wandschuifspanning en de multi-directionaliteit. Een tweede groep van hemodynamische wandschuifspanningsparameters is gebaseerd op het harmonisch karakter en

de frequentie inhoud van de wandschuifspanning. Tot deze groep behoren de harmonische index (harmonic index (HI)) en de dominante frequentie (dominant harmonic (DH)).

Deel III: Pathofysiologie van atherosclerose in muismodellen: beeldvormingsresultaten

Hoofdstuk 6: Beeldvorming van de anatomie en (patho)fysiologie met ultrageluid

Dit hoofdstuk geeft een overzicht van de ultrageluid meetresultaten. In beide muizenrassen, het ApoE$^{-/-}$ en het ApoE$^{-/-}$ Fbn1$^{C1039G+/-}$ ras, werd het ultrageluid onderzoek 5 wekelijks uitgevoerd. We onderzochten de halsslagader (CCA), de interne halsslagader (ICA) en de externe halsslagader (ECA) aan zowel de linker- als de rechterzijde. Eerst werd de bloedsnelheid opgemeten met Pulsed Doppler ultrageluid. De belangrijkste trends waren: (i) een stijging van de snelheid in de ECA en ICA met het verloop van tijd, (ii) een kleine daling in de pieksnelheid van de CCA na verloop van tijd, (iii) geen statistisch verschil tussen linker en rechter halsslagaders en (iv) de meeste snelheidswaarden verschilden tussen de ApoE$^{-/-}$ en de ApoE$^{-/-}$ Fbn1$^{C1039G+/-}$ muizen. Gebaseerd op deze snelheden werden een resistieve index (RI) en een pulsatiele index (PI) berekend. Met uitzondering van RI in de ECA (hoger voor het ApoE$^{-/-}$ Fbn1$^{C1039G+/-}$ ras), had het ras geen statistische invloed op beide parameters. Vervolgens werden de diameters van dezelfde bloedvaten opgemeten met M-mode ultrageluid. Deze diameters vertoonden geen statistisch significante trends, behalve dat tijd een significante factor was voor de ECA diameter, waarbij de diameter gemiddeld genomen afneemt naarmate het experiment vordert. De distensibiliteit van de CCA was hoger dan van andere twee takken.

Hoofdstuk 7: Goud partikel contrast μCT: detectie van kwetsbare plaques

De infiltratie van macrofagen in atherosclerotische plaque is één van de tekenen die wijzen op een kwetsbare plaque die mogelijks aanleiding geeft tot klinische complicaties. Dit hoofdstuk beschrijft een nieuwe techniek om de infiltratie van macrofagen in de plaque te meten aan de hand van goudnanopartikels contrast μCT. Op deze manier is een functionele component toegevoegd aan μCT dat anders beperkt blijft tot anatomische beeldvorming.

In deze studie werden zowel ApoE$^{-/-}$ als ApoE$^{-/-}$ Fbn1$^{C1039G+/-}$ muizen opgevolgd gedurende een vetrijk dieet van 20 weken. Op weken 10, 15 en 20 werd er een μCT scan protocol uitgevoerd. Dit protocol bestond uit een pre- en een post-contrastinjectie beeld. Een interessante observatie was dat op

de pre-contrastinjectie beelden van weken 15 en 20 er nog contrast zichtbaar was in de bloedvatwand van vorige meetpunten. Histologisch onderzoek bevestigde dat deze contrastpartikels zich op dezelfde plaats bevinden als de macrofagen.

Nadat er een angiografisch beeld gecreëerd was, werden de halsslagaders gesegmenteerd met het publiek beschikbare softwareplatform VMTK. De aanwezigheid van contrast in de vaatwand werd op het lumen oppervlakte geprojecteerd door een speciaal ontwikkeld algoritme. Daardoor werd een grafische weergave (aan de hand van een kleurcodering) bekomen van de macrofaaginfiltratie op de lumen oppervlakte.

Voor de drie takken van de bifurcatie (CCA, ECA en ICA) werd de oppervlakte berekend van de vaatwand waar macrofaaginfiltratie kon worden gedetecteerd (contrast-enhanced area fraction (CAF)). Deze numerieke waarde vertoonde een duidelijke stijging van week 15 naar week 20. Bovendien toonde dit ook aan dat er een hogere mate van macrofaaginfiltratie merkbaar was bij de ApoE$^{-/-}$ Fbn1$^{C1039G+/-}$ muizen in vergelijking met de ApoE$^{-/-}$ muizen. De sterkste mate van macrofaaginfiltratie werd gemeten in de ECA en de zwakste in de ICA.

Nadat de globale aanwezigheid van macrofaaginfiltratie was bestudeerd aan de hand van de CAF waarden, werden de precieze locaties langsheen de bloedvaten waar dit optrad, onderzocht. Dit toonde dat de macrofaaginfiltratie in de CCA beperkt bleef tot de regio net proximaal van de bifurcatie. Voor beide takken van de bifurcatie (ECA en ICA) vertoonde de macrofaaginfiltratie echter meer uitgesmeerde patronen.

Als slot van dit hoofdstuk is nog een extra sectie toegevoegd waar de mogelijkheid wordt onderzocht om een angiografisch beeld van de bloedvaten in de muizenhersenen te maken. Om dit angiografisch beeld te bekomen, wordt het pre-contrast injectie beeld (met daarop de schedel zichtbaar) van het post-contrastinjectie beeld (met daarop zowel de bloedvaten als de schedel zichtbaar) afgetrokken. Dit resulteert in een 3D-beeld waar enkel de vasculatuur nog in overblijft.

Deel IV: De rol van wandschuifspanning in de pathofysiologie van atherosclerose in muismodellen

Hoofdstuk 8: Bestuderen van de wandschuifspanningsparameters met behulp van muisspecifieke vloeistof-structuur interactie simulaties

Dit hoofdstuk beschrijft een methodologie die gebruikt kan worden om de wandschuifspanning en afgeleide grootheden te berekenen ter hoogte van de vertakking van de halsslagader in muizen. Dit algoritme is gebaseerd op

vloeistof-structuur interactie (fluid-structure interaction (FSI)) simulaties van 8 verschillende halsslagaders (4 linkse en 4 rechtse) voor 4 verschillende $ApoE^{-/-}$ muizen. De metingen waarop deze modellen zijn gebaseerd, zijn uitgevoerd wanneer de muizen 10 weken op het vetrijke dieet waren. Op dat tijdstip was er nog geen vernauwing van het bloedvat merkbaar.

Voor het opstellen van het model is er gebruik gemaakt van *in vivo* beeldvorming om de fysiologische realiteit zo dicht mogelijk te benaderen. De snelheidsmetingen van de bloedstroom in de CCA, ECA en ICA werden herschaald naar een massadebiet. Door beperkingen qua meetnauwkeurigheid, was de tijdsgemiddelde massa-instroom niet gelijk aan de gemiddelde massa-uitstroom. Daarom werden de massadebieten van de ECA en de ICA herschaald om te voldoen aan de massabalans, uitgemiddeld over 1 cyclus. Nadien werd het massadebiet van zowel de CCA en de ECA aan de randen van het model opgelegd. Voor de ICA werd de opgemeten diameter lineair herschaald naar een drukcurve met literatuur gebaseerde diastole en systole waarden. Samen met het massadebiet laat dit ons toe om een 3-elementen windketelmodel aan te passen aan de metingen. Dit windketelmodel linkt het massadebiet aan de druk aan deze rand van het model.

De geometrie was bekomen door de segmentatie van de μCT metingen. Vervolgens werd de geometrie gekrompen naar de diastole diameter, gemeten met M-mode ultrageluid.

De *in vivo* spanningstoestand onder een axiale voorspanning en een inwendige druk werd berekend op basis van twee opeenvolgende "backwards incremental method (BI)" stappen. De BI methode is een iteratief proces waarbij de inwendige spanningen worden berekend onder een bepaalde belasting, gegeven de vervormde geometrie. Deze interne spanningstoestand werd opgelegd als een initiële spanningstoestand bij de numerieke simulaties. Daarnaast werd het externe weefsel dat het bloedvat omgeeft gemodelleerd met veer-elementen. Zowel de voorspanning als het externe weefsel werden toegevoegd om de beweging en dus ook de bufferende werking van het bloedvat zo realistisch mogelijk te benaderen. Daarnaast hebben beide modellen een stabiliserende invloed op de berekeningen.

Met behulp van Tango werden de structuurmechanica en de vloeistofdynamica gekoppeld. Na het bepalen van de oplossing werden dan de wandschuifspanning en afgeleide grootheden bepaald.

Op basis van deze FSI resultaten kon dan de buitenkant van de sinus van de ECA geïdentificeerd worden als regio met het meeste kans op ontwikkeling van atherosclerose, uitgaande van de veronderstelling dat de zones onderworpen aan lage en oscillerende wandschuifspanning het meest vatbaar zijn voor de ontwikkeling van slagaderverkalking. Voor al de verschillende

berekende bifurcaties had deze zone de meest kritische waarde van de drie berekende grootheden: TAWSS, OSI en RRT. Bovendien toonden we ook aan dat de bufferende capaciteit van de bloedvatwand onontbeerlijk is om de randvoorwaarden correct te kunnen opleggen.

Hoofdstuk 9: Vergelijken van verschillende numerieke methodologieën om wandschuifspanning te berekenen

Het vloeistof-structuur interactiemodel dat beschreven is in hoofdstuk 8, is één van de meer geavanceerde mogelijkheden om de WSS te berekenen. Eenvoudigere methodes zijn reeds meermaals gebruikt. De meest eenvoudige zijn de CFD-simulaties waar de tijdsafhankelijkheid wordt verwaarloosd en een constante bloedstroom wordt verondersteld (=tijdonafhankelijke CFD). Bij deze techniek kan ofwel de gemiddelde snelheid ofwel de maximale snelheid worden opgelegd als randvoorwaarden. Transiënte CFD berekeningen zijn een andere mogelijkheid. Deze modellen zijn gelijkaardig aan de FSI-modellen in het vloeistofdomein, maar ze houden geen rekening met de beweging en dus ook bufferende werking van het bloedvat.

Voor de verschillende simulatietechnieken bekwamen we vervolgens verschillende (tijdsgemiddelde) waardes voor de WSS van 3.25, 7.54, 3.42 en 2.85Pa voor respectievelijk de gemiddelde snelheid tijdonafhankelijke CFD, de maximale snelheid tijdonafhankelijke CFD, de transiënte CFD en de transiënte FSI simulaties. Wanneer de bekomen resultaten echter werden genormaliseerd (door te delen door de gemiddelde waarde), waren de bekomen patronen zeer gelijkaardig. Het oscillerend karakter van de WSS kon niet bestudeerd worden met de tijdonafhankelijke berekeningen. De transiënte FSI berekeningen vertoonden stromingspatronen met een hoger oscillerende karakter in vergelijking met de transiënte CFD-berekeningen.

In het tweede deel van hoofdstuk 9 wordt onderzocht of de fysieke activiteit van de muis een invloed heeft op de bekomen resultaten. Een muis onder verdoving zal immers een lagere hartslag, een lagere debiet van de bloedstroom en een lagere bloeddruk hebben ten opzichte van een muis die bij bewustzijn is. In de literatuur werd reeds de hypothese geopperd dat dit een invloed kan hebben op de waargenomen WSS patronen*. Wanneer de muis fysiek actief is, zullen de fysiologische parameters nog meer toenemen en dus nog verder weg afdrijven van de waardes opgemeten onder anesthesie. Daarom wordt onderzocht of anesthesie en de graad van fysieke activiteit een invloed hebben op de numerieke resultaten.

*Z. Mohri, E. M. Rowland, L. A. Clarke, A. De Luca, V. Peiffer, R. Krams, S. J. Sherwin en P. D. Weinberg, „Elevated Uptake of Plasma Macromolecules by Regions of Arterial Wall Predisposed to Plaque Instability in a Mouse Model", *PLoS ONE*, deel 9, nr. 12, e115728, 2014

Van *Anesthesie* naar *Rust* en vervolgens *Actief* nam de TAWSS telkens toe. De genormaliseerde TAWSS patronen vertoonden echter amper verschillen. Voor alle OSI berekeningen was dezelfde locatie blootgesteld aan de hogere waardes. Voor de case *Actief* was deze zone wel meer uitgebreid. Voor de hogere niveaus van activiteit werden zones waargenomen waar de WSS van richting omkeerde. Dit gebeurde hoofdzakelijk aan de buitenkant van de ECA, wat waarschijnlijk de grotere zone met een verhoogde OSI verklaart.

Hoofdstuk 10: De correlatie tussen atherosclerose en op wandschuifspanning gebaseerde grootheden

In hoofdstuk 7 werd de macrofaaginfiltratieverdeling overheen het lumen oppervlak berekend op weken 15 en 20 na de start van het vetrijke dieet. Daarnaast werd in hoofdstuk 8 de WSS-verdeling berekend voor 8 bifurcaties van 4 ApoE$^{-/-}$ muizen. Deze berekeningen waren gebaseerd op metingen gedaan 10 weken na de start van het vetrijke dieet, voordat vernauwing van de bloedvaten zichtbaar was. Daardoor hebben we de unieke mogelijkheid om beide datasets te linken aan elkaar op een individuele muis basis. In tegenstelling tot wat de meeste studies beschrijven in de wetenschappelijke literatuur, hebben wij immers de WSS grootheden distributie en de macrofaag distributie voor dezelfde proefdieren, wat ons toelaat om een gepaarde statistische test uit te voeren.

Deze vergelijking werd uitgevoerd op 3 verschillende niveaus: (i) het individuele bloedvatniveau, (ii) het individuele bifurcatieniveau en (iii) de totale populatie (= 7 bifurcaties). Al deze vergelijkingen werden uitgevoerd voor de macrofaaginfiltratie datasets van weken 15 en 20. De vergelijking gebeurde aan de hand van de Spearman correlatiecoëfficiënt ρ_s. Deze correlatiecoëfficiënt veronderstelt niet dat het verband lineair is zoals de Pearson correlatiecoëfficiënt wel doet. Bij ρ_s wordt er enkel een monotoon verband verondersteld tussen beide grootheden. Om een vergelijking mogelijk te maken werden de datasets van de 3 verschillende tijdstippen (week 10 - FSI, weken 15/20 - macrofaaginfiltratie) op eenzelfde rechthoekige grid geprojecteerd per bloedvat met behulp van VMTK.

Op het individuele bloedvatniveau werd de surrogaat sample data analyse (SSDA) herhaaldelijk uitgevoerd voor de individuele bloedvaten van de individuele muizen. De SSDA is een eenzijdige statistische test om spatiële correlaties tussen 2 distributies te bestuderen. Deze methode wordt in meer detail beschreven in Appendix B. Als resultaat van deze test bekomen we de waarde voor ρ_s, zijn betrouwbaarheidsgrens (enkelzijdig equivalent van het betrouwbaarheidsinterval) en de p-waarde. Voor de dataset op week 15 werden geen significante correlaties gevonden. Een statistisch significante positieve correlatie werd gevonden tussen de macrofaaginfiltratie op week

20 en de RRT waarde op week 10 voor 4 van de 7 geteste CCA. De TAWSS was statistisch significant negatief gecorreleerd met de macrofaag infiltratie in 4 van de 7 CCA. Voor zowel de transWSS en de OSI werden voor 2 van de 7 CCA een significante positieve correlatie gevonden. Voor zowel de ECA als de ICA werden geen significante correlaties gevonden.

Voor het individuele bifurcatieniveau werd dezelfde testmethode toegepast, hoewel hier de drie takken (CCA, ECA en ICA) per bifurcatie nu in 1 enkele test werden samengevoegd. Dit resulteerde in respectievelijk 4, 2, 4, 2, 1 en 0 significante correlaties voor de TAWSS, OSI, RRT, transWSS, HI en de DH. Op het individuele bifurcatieniveau is de correlatie dus meer uitgesproken aanwezig dan op het individuele bloedvatniveau. Tevens was de ruimtelijke correlatie met de macrofaaginfiltratie het hoogst voor de RRT.

Voor de statistische testen, uitgevoerd op het populatieniveau, werd een verschillende methodologie gevolgd. Voor de verschillende bifurcaties werd ρ_s reeds bepaald als resultaat van de testen, op het individuele bifurcatieniveau (vorige paragraaf). Een Fisher r naar z transformatie werd uitgevoerd op deze ρ_s waardes. Vervolgens kon dan een gepaarde t-test uitgevoerd worden om zowel de populatie gemiddelde ρ_s, de betrouwbaarheidsgrens en de p-waarde te berekenen. De populatie gemiddelde ρ_s waardes waren -0.144, 0.118, 0.148, 0.121, 0.057 en 0.016 voor respectievelijk de TAWSS, OSI, RRT, transWSS, HI en de DH. Voor de TAWSS, OSI, RRT en transWSS was de gevonden correlatie statistisch significant. Op het populatieniveau is de correlatie dus hoger dan op het individuele bifurcatieniveau. Ter vergelijking werd ook een SSDA uitgevoerd over de uitgemiddelde waarde, zoals algemeen wordt uitgevoerd in de literatuur. Dit resulteerde in een overschatting van de gevonden correlaties.

Tot slot werd dezelfde methodologie (Fisher r naar z transformatie gevolgd door een gepaarde t-test) toegepast om de verschillende WSS parameters met elkaar te vergelijken op het populatieniveau. De DH werd hierbij niet meegenomen in de vergelijking, omdat deze waarde constant was over de hele bifurcatie, met uitzondering van een kleine zone ter hoogte van het stagnatie punt van de bloedstroom. De correlatie tussen de transWSS en de andere WSS parameters was laag, wat een indicatie is dat de transWSS een andere fysisch proces beschrijft dan de overige WSS parameters. Voor de andere WSS parameters werd een uiterst significante, negatieve correlatie gevonden met de TAWSS. De overblijvende WSS parameters waren uiterst significant, positief met elkaar gecorreleerd. We kunnen dus besluiten dat de verschillende WSS parameters niet onafhankelijk zijn van elkaar.

Deel V: Conclusies

De 3 intermediaire doelen van dit onderzoek werden gerealiseerd. Ten eerste werd een *in vivo* beeldvormingstechniek ontwikkeld om macrofaaginfiltratie

te kwantificeren in atherosclerotische plaques in muizen. Deze techniek is gebaseerd op goud-nanopartikel contrast μCT. Ten tweede stelden we een op vloeistof-structuur interactie gebaseerde methodologie voor om de hemodynamica in de halsslagaders van muizen zo realistisch mogelijk te simuleren. Ten derde kwantificeerden we de ruimtelijke correlatie tussen verschillende wandschuifspanningsparameters enerzijds en de aanwezigheid van plaque in de bifurcatie van de halsslagader in de muis anderzijds. De sterkste correlaties met de macrofaag infiltratie werden gevonden voor een (lage) TAWSS en een (hoge) RRT.

Het is echter belangrijk om niet uit het oog te verliezen dat de hemodynamica slechts 1 aspect is van het complexe proces van atherosclerosevorming. Bovendien vertalen deze resultaten zich niet rechtstreeks naar de mens. De hemodynamische omgeving in de muis zijn behoorlijk verschillend van de menselijke hemodynamische omgeving, met veel lagere Reynolds (~25 keer lager[†]) en Womersley (~9 keer lager[†]) getallen die aanleiding geven tot laminaire en gestructureerde stroompatronen, met minder secundaire stroom en recirculatie in de zone van de bifurcatie. Een volgende stap richting humane applicaties kan dan ook zijn om een gelijkaardige methodologie toe te passen op een proefdier waarvan de hemodynamische omgeving deze van de mens beter benadert zoals het varken.

Plaqueruptuur, een belangrijk biomechanisch onderzoeksdomein, werd niet nader onderzocht in dit werk. De FSI-methodologie bevatte reeds een simpel mechanisch model van de bloedvatwand, maar een complexer model van zowel de bloedvatwand als de atherosclerotische plaque zijn nodig om ook plaque ruptuur te bestuderen. Hiervoor is echter hoge resolutie data nodig van zowel de morfologie als de samenstelling van de bloedvatwand en de plaque. Recente vooruitgang in hoge resolutie en hoog contrast *ex vivo* beeldvorming maken het mogelijk om onderzoek te doen in dit domein.

Dit werk integreert verschillende onderzoeksdomeinen. Significante verbeteringen / vooruitgang in één of meerdere van deze domeinen zullen nieuwe mogelijkheden creëren in de toekomst. Meer specifiek, vooruitgang met betrekking tot beeldsegmentatie en meshingtechnieken zullen de hoeveelheid manueel en dus tijdsintensief werk dat noodzakelijk is om kwalitatieve modellen te bekomen, beperken. Dit zal het mogelijk maken om de opgestelde methodologie uit te voeren op een grotere groep proefdieren om statistisch robuustere resultaten te bekomen.

[†]J. Suo, D. E. Ferrara, D. Sorescu, R. E. Guldberg, W. R. Taylor en D. P. Giddens, „Hemodynamic shear stresses in mouse aortas: implications for atherogenesis." *Arteriosclerosis, thrombosis, and vascular biology*, deel 27, nr. 2, p. 346–51, 2007

Summary

Introduction

Cardiovascular diseases are the main cause of death world-wide. Atherosclerosis is a cardiovascular disease characterised by the formation of plaque in large- to middle-sized arteries. Atherosclerosis is a slowly progressing disease, a complicated biological process that includes many different signalling pathways. The two main processes that occur are the accumulation of lipids in the arterial wall and the inflammation of the arterial wall.

Most of the known risk factors are systemic phenomena such as smoking, high blood pressure, age and high lipid levels. In contrast, atherosclerotic plaque develops preferentially at the inner bend of arteries and at bifurcations. It is generally accepted that local haemodynamics is a factor that can (partially) explain this focal character of atherosclerosis. The haemodynamics trigger the onset of atherosclerosis through the shear force (wall shear stress (WSS)) that the flow exerts on the endothelial cells lining the arterial wall. A low and/or oscillatory behaviour of this shear force results in the activation of atheroprone signalling pathways.

One of the factors complicating fundamental research on the role of haemodynamics is the fact that baseline shear stress patterns, prior to any disease development, need to be linked with the occurrence of atherosclerosis at a later stage. Therefore, most of the available studies compare WSS patterns, measured in a first group of subjects, with lesion maps measured in a second group of subjects (cross-sectional analysis rather than longitudinal). To do this, averaged datasets (=aggregating) are calculated for both groups. The risk of aggregating datasets is that the final correlation between the WSS and atherosclerosis development can be overestimated. In this PhD thesis, it is our goal to study the a link between WSS and atherosclerosis development on a within-subject basis in a longitudinal study design, eliminating the need for the aggregation step. This leads to the central research question of this thesis:

Is there an individual and quantitative link between baseline wall shear stress and subsequent plaque development in mouse models of atherosclerosis?

In the current work make use of mouse models of atherosclerosis, because these allow for a longitudinal follow up. More specifically, we target the carotid bifurcation of these mice as this is one of the locations prone to atherosclerosis development. To be able to answer the research question several intermediate goals need to be reached. An *in vivo* technique to measure the plaque locations in the murine vasculature has to be developed. Next, (existing) numerical methods need to be combined to simulate the murine vasculature. Finally, appropriate statistical testing is needed to quantify the link between WSS and atherosclerosis.

Part I: Studying atherosclerosis in mice

Chapter 1: Atherosclerosis

This first chapter provides a background on the anatomy and physiology of the human cardiovascular system that consists of the heart and the vasculature. A broad overview of the main arteries in the human body is given. A more in depth anatomical description of the arteries supplying the head and the brain is provided. The common carotid artery (CCA), external carotid artery (ECA) and internal carotid artery (ICA) are the region of interest in the current dissertation. The second section of this chapter explains the pathology of atherosclerosis, which is a disease characterised by the formation of plaques in the arterial wall. The two main processes are the infiltration of lipids in the arterial wall and inflammation. After the description of its pathogenesis, severe clinical complications of atherosclerosis are illustrated. Rupture of plaques can lead to thrombus formation resulting in myocardial infarction or stroke, the main causes of death worldwide. Afterwards two classification systems of atherosclerotic plaques are given. Several risk factors for cardiovascular diseases are generally known. For atherosclerosis these risk factors are: gender, age, genetic factors, hypertension, obesity, smoking and alcohol consumption. These risk factors are systemic risk factors, yet plaques tend to develop at specific locations. Haemodynamics are one mechanism explaining the focal atherogenicity. The last section of this first chapter, describes how the blood flow is responsible for activation of atherogenic pathways through the WSS sensed by the endothelial cells (ECs).

Chapter 2: Mouse models of atherosclerosis

The slow time course of atherosclerosis development in humans is a major drawback for studies on atherosclerosis. Therefore several animal models mimicking human atherosclerosis have been developed. This second chapter starts with an overview of rabbits, pigs and non-human primates as animal models for atherosclerosis. Afterwards, the mouse model is described in more detail because it has some very specific advantages: cheap, short generation time, easy genetic manipulation and complex lesions are present in specific strains. Next to this, the use of larger numbers of animals is feasible, allowing for statistically robust results. In addition, rodent models are ethically more accepted for pre-clinical research. One strategy to study the impact of haemodynamics on atherosclerosis development is to make use of surgical techniques to manipulate the blood flow. The main disadvantage of mouse models, however, is that the normal wild type mouse is rather resistant to atherosclerosis development. Some of the inbred strains, however, are susceptible to diet-induced atherosclerosis showing complex lesions with the C57BL/6J strain the most commonly used. To elevate the plasma levels of lipoproteins even further, the low density lipoprotein receptor knockout ($LDLR^{-/-}$) and apolipoprotein E knockout ($ApoE^{-/-}$) mice were introduced. The $ApoE^{-/-}$ mouse is commonly used because complex plaques are found in this mouse model. Recently, the apolipoprotein E deficient and fbn1 heterogeneous ($ApoE^{-/-}$ $Fbn1^{C1039G+/-}$) mouse model was developed at the University of Antwerp. This mouse model shows signs of spontaneous plaque rupture, which is rare in the other mouse models. In the current work, both $ApoE^{-/-}$ and $ApoE^{-/-}$ $Fbn1^{C1039G+/-}$ mice were studied, enabling in-depth investigation of complex atherosclerotic lesions.

Chapter 3: Imaging atherosclerosis in mice

Ultrasound (US) and micro-computed tomography (μCT), the two main *in vivo* imaging techniques that were used in this thesis, are introduced. US uses ultrasonic acoustic waves beyond the audible range. Several different images can be obtained depending on the processing technique. B-mode images provide a 2D view of the anatomical structures. M-mode show the variation of a single scan line over time and can be applied to assess the pulsatility of an artery. Pulsed Doppler imaging can be used to measure the velocity of the blood. The small animal US measurements are challenging due to the higher heart and smaller size of mice compared to humans. For this purpose a special scanner, the Vevo2100, was used for this dissertation.

Computed tomography (CT) is based on ionising radiation. A CT scanner consists of three parts: the X-ray tube (source), the object and the detector. The X-ray tube generates a cone beam of X-rays. These X-rays penetrate the

object, in the current work a mouse, before they are registered on a detector. When the X-rays travel through tissue, they get partially attenuated depending on the attenuation coefficients of the tissues it travels through. During a CT measurement, several projections for different angles are measured. In small animal μCT, both the X-ray tube and the detector rotate around the mouse to measure projections at different angles. After a reconstruction process, a 3D dataset with attenuation coefficients is obtained, describing the anatomy of the mouse. The main challenge for vascular small animal μCT, is obtaining enough contrast. Several contrast agents have been developed for this purpose. In the current research, a gold-nanoparticle contrastagent (Aurovist 15nm) has been used.

Part II: Computational techniques to study arterial haemodynamics

Chapter 4: Numerical simulations of arterial haemodynamics

To know the flow field at a great level of detail, it is generally calculated using computational fluid dynamics (CFD) simulations. In chapter 4, some background is given on the numerical techniques that are applied in chapters 8 and 9. First, the equations governing the flow of an incompressible fluid are described. These equations can be solved using computational fluid dynamics. The motion of the of the carotid arteries induced by the blood pressure and blood flow is included in the simulation methodology to incorporate their buffering capacity in the model. The second part of chapter 4 describes the equations governing the solid mechanics (arterial wall) and the solution method of these differential equations (computational solid mechanics (CSM)). Finally, the fluid mechanics and the solid mechanics models need to be coupled to solve the fluid-structure interaction (FSI) problem. A general overview of the partitioned, strongly coupling technique Tango is given in the last part of chapter 4.

Chapter 5: Haemodynamic wall parameters

In this PhD thesis, we are more interested in the biomechanical influence that the blood flow has on the ECs, rather than in the blood velocity field itself. The ECs form the barrier between the blood flow and the arterial wall and are thus a crucial component in the mechanosensing, that sets off the atheroprone pathways. More specifically, the ECs sense the shear force (WSS) that the blood flow exerts on the arterial wall. Over the years a vast amount of metrics (haemodynamic wall parameters (HWPs)) have been developed all aiming to quantify that component of WSS that optimally quantifies its atheroprone effect. Chapter 5 lists the most commonly calculated HWPs and illustrates them on the basis of an example. The first section lists the HWPs

that are based on the magnitude of the WSS: time averaged wall shear stress (TAWSS), oscillatory shear index (OSI), relative residence time (RRT) and transverse wall shear stress (transWSS). These parameters give a description of (a combination of) the magnitude, the oscillatory behaviour and the multi-directionallity of the WSS. A second group of HWPs are the harmonic based HWPs. These describe the atheroprone effect of WSS in function of the harmonic content in the frequency domain of the WSS. Both the harmonic index (HI) and the dominant harmonic (DH) metrics belong to this group and are described in this chapter.

Part III: Pathophysiology of atherosclerosis in mouse models: imaging results

Chapter 6: Assessment of carotid anatomy and (patho)physiology using US

This chapter gives an overview of the ultrasound measurement results. In both strains of mice that were followed up, the ApoE$^{-/-}$ and ApoE$^{-/-}$ Fbn1$^{C1039G+/-}$ strains, the US imaging protocol was performed 5-weekly, during the time when they were on a western-type diet. We investigated the common (CCA), external (ECA) and the internal (ICA) carotid artery, and this on both the left and the right side. First, the blood velocity was assessed using pulsed wave Doppler ultrasound (PW Doppler US). The main trends that were present are: (i) an increase in velocity for the ECA and the ICA with time, (ii) a small decrease in peak velocity for the CCA, (iii) no statistical difference between left and right side and (iv) most velocity based metrics were different for both strains of mice. From the measured velocities, the resistivity index (RI) and pulsatility index (PI) were calculated. With exception of the RI of the ECA, there was no significant influence of mouse strain for those parameters. Using M-mode imaging the luminal diameter of the arteries was measured 5-weekly at the same three locations. This showed no statistically significant trends except time was a significant grouping factor for the ECA diameter. For the distensibility the most important trend was that the distensibility of the CCA is higher compared to the other 2 branches.

Chapter 7: Gold particle–enhanced μCT: vulnerable plaque detection

Macrophage infiltration in atherosclerotic plaques is one of the determinants of the vulnerability to clinical complications of the plaque. Therefore, it is a main target for studies targeting molecular small animal imaging strategies. This chapter describes a novel methodology to measure macrophage infiltration into the murine atherosclerotic plaques using gold-nanoparticle-enhanced μCT. In this manner functional information is added to the otherwise purely anatomical μCT imaging technique.

In this study ApoE$^{-/-}$ and ApoE$^{-/-}$ Fbn1$^{C1039G+/-}$ mice were followed up during the time they were put on a western-type diet. At weeks 10, 15 and 20 after the start of the diet, a pre- and post-contrast injection μCT scan was taken. At the pre-contrast scan of weeks 15 and 20, contrast present in the arterial wall from the previous injections was still visible. Histology confirmed that this contrast was co-localised with macrophages.

After construction of an angiographic image, the carotid arteries were segmented using the Vascular Modeling Toolkit (VMTK). Using a dedicated methodology, the presence of contrast agent around the lumen (inside the arterial wall), was mapped on the luminal surface. As a result the presence of macrophage infiltration could be graphically represented on the luminal surface.

For the three branches of the carotid bifurcation (CCA, ECA and ICA), the area subject to macrophage infiltration could be calculated (contrast-enhanced area fraction (CAF)). This metric showed a clear increase from week 15 to week 20. Moreover, the ApoE$^{-/-}$ Fbn1$^{C1039G+/-}$ mice showed more macrophage infiltration than the ApoE$^{-/-}$ mice. Macrophage infiltrations was most extend in the ECA, and the least in the CCA.

Once the global presence of plaque was calculated using the CAF value, the precise locations of macrophage infiltration along the length of the separate branches were plotted. This showed that macrophage infiltration in the CCA was very well localised in the region immediately proximal to the carotid bifurcation. For the ECA and the ICA, the macrophage infiltration showed more spread out patterns.

In an extra section of this chapter, the angiographic imaging of the brain vasculature is explored, as this part of the mouse was also present in the measured μCT volume. For this goal, the pre-contrast injection μCT scan (with the skull visible) needs to be subtracted from the post-contrast injection scan (with both skull and vasculature visible). As such a 3D volume in which only the vasculature is highlighted is obtained.

Part IV: Role of wall shear stress in the pathophysiology of atherosclerosis in mouse models

Chapter 8: Assessment of WSS metrics using mouse-specific FSI simulations

This chapter presents a methodological framework to calculate the WSS and the HWPs in the murine carotid bifurcation. It is based on FSI simulations of the carotid bifurcation and is applied to 8 carotid bifurcations (4 left and 4 right) for 4 ApoE$^{-/-}$ mice. The measurements on which the simulations are

based, were performed at week 10 after the start of the diet. At that time point, no narrowing of the carotid arteries could be detected, and we consider these data as representative for the baseline, pre-disease state of the animal.

The model is based on *in vivo* measurements to as close as possible represent the physiological reality. The velocity measurements at the CCA, ECA and ICA were rescaled to mass flows. Due to measurement limitations, the cycle-averaged outflow was not equal to the cycle-averaged inflow, and thus a rescaling of the ECA and ICA flow was applied to assure a time-averaged balance of mass. Afterwards, the mass flow of the CCA and ECA were imposed as boundary conditions (BCs). For the ICA, the diameter waveform was used as a surrogate for the pressure waveform, and linearly scaled using literature values for the diastolic and systolic pressure. Together with the ICA mass flow this enabled us to fit a 3-element windkessel model that mimics the behaviour of the vasculature downstream of the ICA. This 3-element windkessel model was applied at the ICA boundary to link the pressure with the flow.

The μCT measurements were used to segment the geometry of the carotid bifurcation lumen. This geometry was geometrically shrunk to diastolic dimensions based on the diastolic diameters measured with ultrasound.

The *in vivo* stress state under an axial prestress and diastolic pressure was calculated using two sequential backwards incremental method (BI) steps. The BI method is an iterative approach to calculate the internal stresses when the load and the deformed geometry are given. These internal stresses were applied as an initial condition to the numeric simulations. Furthermore, the external tissue surrounding the arteries was modelled using spring elements. The prestress and the external tissue were added to optimally simulate the movement and buffering of the arterial wall and to stabilise the calculations.

Using Tango the solid and fluid models could be coupled and the FSI problem was solved. Finally,the WSS and the HWPs were calculated.

The results of the FSI simulations of those 8 carotid bifurcations identified the outer sinus of the ECA as the most atheroprone region based on the low and oscillatory WSS hypothesis. This zone had the most critical values for all three HWPs (TAWSS, OSI and RRT). Next to this, we demonstrated that the incorporation of the buffering capacity of the carotid arteries is indispensable for a correct application of the BCs.

Chapter 9: Comparison of numerical methodologies to assess WSS

The FSI model described in chapter 8, is one of the more sophisticated methodologies to calculate the WSS related parameters. Simpler methods have been applied abundantly. The most simple ones are based on steady state

CFD models, that ignore the pulsatility of the blood flow. In these models the blood flow is modelled as a steady flow with either the time-averaged or the maximum value of the measurements. As a BC either the average measured mass flow (or velocity) or the peak mass flow (or velocity) can be applied. Transient CFD simulations are another possibility. These models are similar to the FSI simulations for the fluid domain, but they do not take into account the buffering of the arteries.

The different simulation techniques led to a different (time averaged) wall shear stress value of 3.25, 7.54, 3.42 and 2.85Pa for respectively the average steady CFD, the peak steady CFD, transient CFD and transient FSI simulations. When, however, the values were normalised (by dividing them by the average value), the patterns were very similar. The oscillatory behaviour of the WSS could not be assessed with the steady CFD simulations. The FSI simulation showed a much higher value of OSI compared to the transient CFD simulation.

A second part of chapter 9 investigated the influence of the physical state of the mouse on the results. When a mouse is under anaesthesia several physiological parameters change: the animal has a lower heart rate (HR), lower blood flow and a lower blood pressure. It has been hypothesised in literature that this can have a considerable influence on the calculated WSS and flow patterns[‡]. When the mouse is highly active, these parameters drift even further away from the values under anaesthesia. Therefore, the influence of anaesthesia and activity level of the animal on the numerical results has been studied.

From *Anaesthesia*, *Rest* towards *Active*, the TAWSS increased. The normalised TAWSS patterns, however, (by dividing through the average value) showed very similar results. For the OSI, all regimens identified the same focal location (outer sinus of the ECA), as atheroprone. For the cases with a higher activity level, this zone was spread out further. Finally, at higher activity levels, the WSS vector reversed direction in the early deceleration phase. This phenomenon occurred at the outer sinus of the ECA, which explains the more spread out zone with high OSI.

Chapter 10: Correlation between atherosclerosis and shear stress metrics

In chapter 7 the macrophage infiltration maps were calculated at weeks 15 and 20 after the start of the diet when atherosclerosis was present. On the

[‡]Z. Mohri, E. M. Rowland, L. A. Clarke, A. De Luca, V. Peiffer, R. Krams, S. J. Sherwin and P. D. Weinberg, 'Elevated Uptake of Plasma Macromolecules by Regions of Arterial Wall Predisposed to Plaque Instability in a Mouse Model', *PLoS ONE*, vol. 9, no. 12, e115728, 2014

other hand, in chapter 8, the WSS distribution was calculated for 8 carotid bifurcations of 4 ApoE$^{-/-}$ mice at 10 weeks after the start of the diet (before any stenosis was present). This provides us with the unique opportunity to link both datasets on a within-subject level. In contrast to most studies described in literature, we have the HWP map and the lesion map (=macrophage infiltration) in the same subjects, allowing us to performed a paired statistical testing approach.

The spatial WSS patterns and the macrophage infiltration patters were compared at three different levels: (i) the individual branch level, (ii) the individual bifurcation level and (iii) the population level. All these comparisons were made for the week 15 and week 20 macrophage infiltration datasets. The maps were compared by calculating the Spearman's correlation coefficient ρ_s. This correlation coefficient does not assume linearity such as the Pearson's correlation coefficient, but only assumes a monotonic correlation between both parameters. Before the comparisons were made, the datasets of the three different time points (week10-FSI, weeks15/20-macrophage infiltration) were mapped per branch to the same rectangular grid using VMTK.

At the individual branch level, the surrogate sample data analysis (SSDA) was repeatedly applied to individual branches for individual mice. The SSDA is a 1-tailed statistical method to study spatial correlations between two maps and is described in more detail in Appendix B. As a result ρ_s, its confidence bound (CB) (1-tailed equivalent of the confidence interval) and the p-value are obtained. At week 15 no significant correlations were found. At week 20, for 4 out of 7 bifurcations a significant, positive correlation was found between the RRT and the macrophage infiltration in the CCA. The TAWSS was significantly, negatively correlated with macrophage infiltration for 4 CCA branches. For both the transWSS and the OSI, a significant positive correlation was found for 2 out of 7 CCA branches. For the ECA and ICA no significant correlations were present on the individual branch level.

The testing method applied to the individual bifurcation level was similar, although the three branches (= the whole bifurcation) were now included into the same test. This resulted in respectively 4, 2, 4, 2 ,1 and 0 bifurcations with a significant correlation for the TAWSS, OSI, RRT, transWSS, HI and DH. Therefore, we can conclude that the link between the HWP and the macrophage infiltration is more clearly present when assessed at the bifurcation level. The TAWSS and the RRT provided the highest spatial correlations with macrophage infiltration.

For the statistical testing at the population level, a different approach was followed. For the different bifurcations the ρ_s was already calculated in the previous section. A Fisher r to z transformation was performed on these ρ_s

values. Afterwards, a paired t-test provided the average ρ_s, its CB and the p-value. The population average correlations were -0.144, 0.118, 0.148, 0.121, 0.057 and 0.016 for respectively the TAWSS, OSI, RRT, transWSS, HI and DH. The correlations between the macrophage infiltration and TAWSS, OSI, RRT and transWSS were statistically significant. We can thus conclude that the association between WSS and macrophage infiltration is higher at the population level compared to the individual bifurcation level. As a comparison, an statistical test (SSDA) on the aggregated datasets was performed, as aggregating is commonly performed in literature. This overestimated the correlation between the HWPs and the macrophage infiltration for all the HWP.

Finally, a similar statistical testing approach (Fisher r to z transform followed by a paired t-test) was applied to correlate the different HWPs at the population level. The DH was not included in this analysis because it was constant in almost the complete bifurcation (for all bifurcations) except for a very small zone at the stagnation point. The statistical analysis showed that the ρ_s between the transWSS and the other HWPs is low, indicating that the transWSS describes a different process compared to the other HWPs. For the other HWPs highly significant, negative correlations were found with the TAWSS. Between all the remaining HWP-pairs a highly significant, positive correlation was found. We can thus conclude that the different HWPs are no independent measures.

Part V: Conclusions

Three major intermediate research goals have been achieved. First, an *in vivo* imaging technique of the macrophage infiltration in atherosclerotic plaques provided a quantitative marker for plaque development in mice. This technique is based on a novel application of gold-nanoparticle-enhanced μCT. Secondly, we provided a fluid-structure interaction based methodology to simulate the haemodynamics in the murine carotid bifurcation as realistic as possible. Thirdly, we quantified the association and spatial correlation between several shear stress metrics and presence of plaque in the mouse carotid bifurcation, with (low) TAWSS and (high) RRT providing the strongest correlation

It is, however, important to keep in mind that haemodynamics are only one aspect involved in this complex process, and that caution is warranted when extrapolating our findings to the human setting. Mouse haemodynamics are quite different from human haemodynamics, with the much lower

Reynolds (~25 times lower[§]) and Womersley (~9 times lower[§]) numbers giving rise to much more laminar and highly organised flow, with less secondary flow and recirculation in the bifurcation region. A next step to human applications could be the application of a similar framework to a laboratory animal better mimicking the human vasculature such as for example the pig.

An important biomechanical problem in atherosclerosis research, plaque rupture, was left untouched in the current work. The FSI methodology already incorporates a basic model of the arterial wall, but more refined finite element models of both the arterial wall and the atherosclerotic plaques are needed to expand the topic to plaque rupture. Furthermore, this will require high resolution data on the exact morphology and composition of the arterial wall and plaque. Recent advances in high resolution and high contrast *ex vivo* imaging, however, opened the doors for this field of research.

Because the current work integrates several different several research fields, advances in all these different fields will provide opportunities for future work. In particular, advances in image segmentation and meshing techniques may limit the manual and time consuming work needed to obtain high quality models. This would allow to apply the developed methodologies on larger animal groups to get more statistically robust results.

[§]J. Suo, D. E. Ferrara, D. Sorescu, R. E. Guldberg, W. R. Taylor and D. P. Giddens, 'Hemodynamic shear stresses in mouse aortas: implications for atherogenesis.' *Arteriosclerosis, thrombosis, and vascular biology*, vol. 27, no. 2, pp. 346–51, 2007

Table of contents

Abbreviations and Symbols

Abbreviations

μCT	micro-computed tomography.
AHA	American Heart Association.
ALE	arbitrary Lagrangian-Eulerian.
ANOVA	analysis of variance.
$ApoE^{-/-}$	apolipoprotein E knockout.
$ApoE^{-/-}$ $Fbn1^{C1039G+/-}$	apolipoprotein E deficient and fbn1 heterogeneous.
BC	boundary condition.
BI	backwards incremental method.
BP	blood pressure.
C57BL/6J	inbred strain of laboratory mouse.
CA	carotid artery.
CAF	contrast-enhanced area fraction.
CB	confidence bound.
CCA	common carotid artery.
CFD	computational fluid dynamics.
CI	confidence interval.
CLF	contrast-enhanced length fraction.
CSM	computational solid mechanics.
CT	computed tomography.
DH	dominant harmonic.
DH-axial	axial dominant harmonic.
DOSI	directional oscillatory shear index.
EC	endothelial cell.
ECA	external carotid artery.
ECG	electrocardiography.
ECM	extracellular matrix.
Fbn1	fibrillin-1.
FDG	fluorodeoxyglucose.
FEM	finite element method.
FFT	fast Fourier transformation.

FSI	fluid-structure interaction.
FVM	finite volume method.
GLM	general linear model.
HDL	high density lipoprotein.
HI	harmonic index.
HI-axial	axial harmonic index.
HR	heart rate.
HWP	haemodynamic wall parameter.
ICA	internal carotid artery.
IMPACT	Iterative Maximum-likelihood Polychromatic Algorithm for CT.
IQN-ILS	interface- quasi-Newton with inverse Jacobian from a least-squares model.
LCB	lower confidence bound.
LDL	low density lipoprotein.
$LDLR^{-/-}$	low density lipoprotein receptor knockout.
LIC	line integral convolution.
LMM	linear mixed model.
M-mode US	motion mode ultrasound.
MAP	mean arterial pressure.
MMP	matrix metalloproteinases.
MRI	magnetic resonance imaging.
NO	nitric oxide.
OSI	oscillatory shear index.
OSS	oscillatory shear stress.
oxLDL	oxidized low density lipoprotein.
PAD	peripheral artery disease.
PDE	partial differential equation.
PET	positron emission tomography.
PI	pulsatility index.
PP	pulse pressure.
PRF	pulse repetition frequency.
PW Doppler US	pulsed wave Doppler ultrasound.
RF	radio frequency.
RI	resistivity index.
RRT	relative residence time.
SA	stapedial artery.
SSDA	surrogate sample data analysis.
TAWSS	time averaged wall shear stress.
TIA	transient ischemic attack.
transWSS	transverse wall shear stress.

UCB	upper confidence bound.
US	ultrasound.
VCAM-1	vascular cell adhesion molecule-1.
VLDL	very low density lipoprotein.
VMTK	Vascular Modeling Toolkit.
VOI	volume of interest.
VSMC	vascular smooth muscle cell.
VTK	Visualization Toolkit.
WSS	wall shear stress.
WSSAG	wall shear stress angle gradient.
WSSG	wall shear stress spatial gradient.
WSST	wall shear stress temporal gradient.
XTM	Extended TreeMesh method.

Symbols

%	Percentage.
λ_m	lock stretch (Arruda-Boyce material).
$\vec{\tau}$	wall shear stress vector.
$\dot{\mathrm{m}}$	mass flow.
$\bar{S}_s$	2$^{\mathrm{nd}}$ Piola-Kirchhoff stress tensor.
$\bar{\sigma}$	stress tensor.
$\bar{\tau}$	shear stress tensor.
$\bar{\varepsilon}$	strain tensor.
μ	dynamic viscosity.
μ	shear modulus.
ρ_s	Spearman's rank correlation coefficient.
ρ	density.
σ	stress.
$\vec{f}$	body forces.
$\vec{u}$	displacement.
$\vec{v}$	velocity.
A	area.
c	body-mass exponent.
d	diameter.
i	iteration number.
$\mathrm{k_s}$	spring constant.
$\mathrm{l_{dec}}$	spatial de-correlation length.
$\mathrm{M_b}$	body mass.
n	total number of.
$\mathrm{n_{smp}}$	number of samples.

n_{sur}	number of surrogates.
P	pressure.
Q	flow.
r	Spearman's correlation coefficient.
s_{map}	size of the map (grid).
s_{smp}	sample size.
T	period.
t	time.
U	velocity.
V	velocity.
W	strain energy density function.
X	geometry.

Units

μA	micro Ampère.
μl	microlitre.
μm	micrometer.
$^{\circ}$	degrees.
$^{\circ}$C	degrees Celcius.
$\%_{area}$	percentage of the branch area.
$\%_{length}$	percentage of the centreline length.
bpm	beats per minute.
dl	decilitre.
g	grams.
GPa	Gigapascal.
Gy	Gray.
h	hour.
HU	Hounsfield units.
kg	kilograms.
kHz	kilohertz.
kVp	peak kiloVolt.
m	meter.
mg	milligrams.
MHz	Megahertz.
min	minute.
ml	millilitre.
mm	millimetre.
mmHg	millimeter of mercury.
MPa	Megapascal.
Pa	Pascal.
pH	pH.
s	seconds.

Subscripts

f	fuid.
s	solid.
avg	average.
ax	axial.
b	boundary.
cyl	cylinder.
dia	diastole.
ed	end diastole.
load axial	axial prestress load.
max	maximum.
mean	mean.
min	minimum.
smp	sample.
sur	surrogate.
sys	systole.

Introduction

Clinical Rationale

Cardiovascular diseases are the leading cause of death world-wide. They encompass all diseases affecting the cardiovascular system, that consists of the heart and the vasculature. The area of interest of this thesis is atherosclerosis, which is characterised by the formation of plaque in the arterial wall. It is a slowly progressing disease that sets off as soon as the first decade of life and is known as a "silent killer", as the disease can develop without any symptoms until it has reached an advanced or lethal state.

The typical atherosclerotic plaque consists of a soft core (*athēra*) filled with lipids and debris from dead cells. Over this core a hard fibrous cap (*sclerosis*) can develop. The formation of the atherosclerotic plaque is a complicated biological process that includes many different cascades. The two hall marks of the pathology are the accumulation of lipids within the arterial wall and inflammation of the arterial wall. Over time, atherosclerosis grows and develops different characteristics. When at a later stage the fibrous cap ruptures, the blood inside the artery comes into contact with the thrombogenic content of the plaque and a blood cloth (=thrombus) can form. When this blood cloth gets stuck in the circulation, possibly downstream from the spot of origination, this can obstruct the blood flow, depriving specific tissues from the blood flow. Atherosclerosis frequently occurs in the coronary arteries, which supply the heart muscle with nutrients and oxygen. When a concurrent thrombus clots the blood flow here, this damages the heart muscle and leads to myocardial infarction (heart attack). Next to this, atherosclerosis also frequently occurs in the carotid arteries that supply blood to the head and brain. In this case rupture of a plaque or thrombus formation can lead to stroke (brain attack).

Atherosclerosis is a broad and multidisciplinary research field including among others physicians, biologists and (biomedical) engineers. The biomedical engineering community has particularly focused on two specific research questions:

1. Why does atherosclerosis develop at very specific preferential locations?
2. What are the determinants of plaque rupture and which plaques are at risk of rupture?

plaque development and haemodynamics

The current PhD thesis focuses on the first question. Atherosclerotic plaques tend to develop at very specific locations; preferentially at the inner bends of curved arteries and at bifurcations, which are both regions where the blood flow is disturbed. In contrast most of the risk factors are systemic such as smoking, obesity, age, …

Blood flow exerts a shear force (wall shear stress (WSS)) on the arterial wall, that leads to the activation of atheroprone molecular pathways at very specific locations where this shear force is low and/or has an oscillatory behaviour. This association between WSS and atherosclerosis development has been studied in several experimental and computational models, as well as *in vivo*. However, quantitatively and unequivocally link WSS with the location and progression of plaque in living subjects remains challenging for several reasons

First, it is important for these studies to start from a non-diseased reference condition to be able to start from a clean baseline state from which point on the disease can develop. Second, the WSS is commonly calculated using computational fluid dynamics (CFD) models. Trustworthy CFD models are based on measurements providing information about both the geometry and the blood flow. As a result, *in vivo* measurements of the baseline state are necessary to determine the pre-disease WSS. Next to this, the plaque location should be measured at a stage when a reasonable and measurable amount of atherosclerosis is present. This is only possible after the time it took for the atherosclerosis to develop.

In humans, the early onset of atherosclerosis (already from the first decade in life) and its slow progression make it virtually impossible to acquire both measurements, the baseline state of the arteries and the post-disease development plaque locations, within the same person. Therefore, most of the studies investigating the relation between WSS and plaque development measure both variables in two separate groups of test subjects, a healthy one and a group with diseased subjects. Afterwards, the group averaged (=aggregated) datasets can be compared. The risk associated with this methodology is that it might overestimate the correlation between WSS and the plaque development. It is not because there is a correlation present on the averaged data sets, that this is also the case in the individual subjects.

Research question

Overall, there is still relatively scarce strong quantitative evidence relating WSS patterns in a non-diseased baseline condition with plaque development at a later stage on an individual subject basis.

Mice are widely used in atherosclerosis research, mainly because of the availability of mouse models with a rapid development and progression of atherosclerosis and with lesions that share many of the characteristics of atherosclerosis in humans. In this dissertation, we will make use of such mouse models of atherosclerosis, to answer the following overall research question of this work:

Is there an individual and quantitative link between baseline wall shear stress and subsequent plaque development in mouse models of atherosclerosis?

As the carotid bifurcation is one of the locations where atherosclerosis preferentially develops, we will focus on this location. To be able to answer the main research question several intermediate goals need to be reached:

1. Development of an *in vivo* measurement technique to localise atherosclerotic plaques in mice
2. Setup of a measurements-based computational model to calculate the WSS without sacrificing the animal
3. Applying a statistical model to quantify the link between the haemodynamic metrics and plaque location

Structure

The dissertation is divided into 3 different parts. Part I provides a background of the (patho-)physiology of atherosclerosis in chapter 1, a background on the use of mice in atherosclerosis research in chapter 2 and a background on small animal imaging in chapter 3. The second part (Part II), gives an overview of the different numerical techniques that were used in this thesis. The models needed to simulate the haemodynamics of the mouse carotid bifurcation are explained in chapter 4. From these simulations, we calculated different metrics that describe the influence of the WSS on the arterial wall as described

in chapter 5. This is necessary to get to results with physiological relevance. In part III, the main measurement results of the current work are described. In chapter 6, the results of the ultrasound (US) are listed. In the consequent chapter a new application of gold-nanoparticle-enhanced micro-computed tomography (μCT) to visualise the macrophage infiltration in plaques *in vivo* is introduced. Part IV lists the numerical results of this thesis. Chapter 8 describes the full fluid-structure interaction model and the derivation of the WSS with the help of computational modelling is explained. The results of this complex model are compared with simpler models and different activity levels of the mouse in chapter 9. Finally, the correlation between baseline haemodynamics and atherosclerosis development is discussed in chapter 10. Some conclusions are drawn in chapter 11.

List of publications

First author peer-reviewed papers

- D. De Wilde, B. Trachet, C. Van der Donckt, B. Vandeghinste, B. Descamps, C. Vanhove, G. R. Y. De Meyer and P. Segers, 'Vulnerable plaque detection and quantification with gold particle-enhanced computed tomography in atherosclerotic mouse models.' *Molecular imaging*, vol. 14, pp. 9–19, 2015
- D. De Wilde, B. Trachet, N. Debusschere, F. Iannaccone, A. Swillens, J. Degroote, J. Vierendees, G. R. Y. De Meyer and P. Segers, 'Assessment of Shear Stress Related Parameters in the Carotid Bifurcation using Mouse-Specific FSI Simulations', *Journal of Biomechanics*, In press
- D. De Wilde, B. Trachet, G. R. Y. De Meyer and P. Segers, 'Shear stress metrics and their relation to atherosclerosis: an in vivo follow-up study in atherosclerotic mice', *Annals of Biomedical Engineering*, In press

Coauthor peer-reviewed papers

- C. Debbaut *, D. De Wilde *, C. Casteleyn, P. Cornillie, D. Van Loo, L. Van Hoorebeke, D. Monbaliu, Y. Fan and P. Segers, 'Modeling the Impact of Partial Hepatectomy on the Hepatic Hemodynamics Using a Rat Model.' *IEEE transactions on bio-medical engineering*, vol. 59, no. 12, pp. 3293–3303, 2012
  * *C. Debbaut and D. De Wilde contributed equally to this study*
- R. Xing, D. De Wilde, G. McCann, Y. Ridwan, J. T. Schrauwen, A. F. van der Steen, F. J. Gijsen and K. van der Heiden, 'Contrast-enhanced micro-CT imaging for wall shear stress computation in murine carotid arteries', *Molecular Imaging and Biology*, Submitted

I

Studying atherosclerosis in mice

Chapters

Chapter 1

Atherosclerosis

1.1 The human cardiovascular system

A basic understanding of the anatomy and physiology of the cardiovascular system is indispensable for a clear understanding of the current work. This introductory section will therefore summarise the most relevant parts. This section is mainly based on the next sources[*] [†] [‡] [§], which give a more complete overview of the human anatomy and physiology.

1.1.1 General overview

The human body is a complex system. Structurally the body is organised on different levels including: the chemical level (individual molecules), the cellular level (individual cells), the tissue level (e.g. connective tissue, endothelium, ...), the organ level (e.g. stomach, heart, ...) and the organ system level (e.g. muscular system, skeletal system, ...). For a correct functioning

[*] E. N. Marieb and K. Hoehn, 'Anatomy & Physiology', Pearson In. Pearson Benjamin Cummings, 2008

[†] F. H. Martini, J. L. Nath and E. F. Bartholomew, 'Blood Vessels and Circulation', in *Fundamentals of Anatomy & Physiology*, 9th ed., Boston: Benjamin Cummings, 2012, ch. 21, pp. 707–764

[‡] M. Nair, 'The circulatory s ystem', in *Fundamentals of Anatomy and Physiology for Student Nurses*, I. Peate and M. Nair, Eds., Chichester: John Wiley & Sons, 2011, ch. 12, pp. 366–405

[§] S. Silbernagl and A. Despopoulos, 'Hart en bloedsomloop', in *SESAM Atlas van de fysiology*, 14th ed., Baarn: SESAM/HBuitgevers, 2007, ch. 8

of our body all these systems work together and each one of them fulfils a specific function. Together, these organ systems work towards the well-being of the human body (homeostasis) and they let us full-fill the necessary life functions such as maintaining boundaries (separate the internal environment from the external one), movement, responsiveness, digestion, metabolism, excretion, reproduction and growth [1].

One of the organ systems in the human body is the cardiovascular system. As the name suggests, the main parts of this system are the heart (cardio) and the blood vessels (vascular) together with the blood. The cardiovascular system is a complex distribution system of nutrients, gases, waste products, hormones and other substances. The blood also transports the specialised cells of the immune system that defend the body against infection and disease. The function of the cardiovascular system is vital and a cell that is deprived from blood flow may die in a matter of minutes.

The cardiovascular system of a male adult contains 5-6 litres of blood and an adult female 4-5 litres. When centrifuged, the blood can be split in its 3 main components: plasma (~55%), the buffy coat(<1%) and the erythrocytes (red blood cells) (~45%). Together, the erythrocytes and the buffy coat are called the formed elements. The main component of blood plasma is water (~92%) and the other components are plasma proteins (~7%) and other solutes (~1%). The buffy coat consists of leukocytes and platelets [1], [2].

The heart is the central engine that drives the blood through the blood vessels. It is a 4 chamber organ that, from an engineering point of view, consists of two pumps placed in series. When the heart contracts, the blood is forced into the arterial network. The left atrium (LA) and the left ventricle (LV) (figure 1.1) together form one of the serial pumps, that supplies the oxygen-rich blood (bright red) to the different organs. The right atrium (RA) and right ventricle (RV) form the other pump, pumping the oxygen-poor blood towards the lungs.

The blood vessels are the piping of the human body. In an adult they stretch for about 100.000 km [1]. The blood vessels are divided in arteries, carrying the blood away from the heart, and veins, carrying the blood towards the heart. The blood vessel network is split in a pulmonary loop (the pulmonary circulation) connecting the right ventricle to the left atrium of the heart passing through the lungs. In this way, the oxygen poor blood that leaves the heart is oxygenated in the lungs and transported back to the heart. There, it enters the heart at the left atrium, ready to be sent into the systemic loop (systemic circulation). The systemic circulation connects the left ventricle to the right atrium of the heart. In the body, both circulations (systemic and pulmonary) together form a closed loop with the heart in the middle as a driving force pumping the blood.

1.1.2 The systemic circulation

The systemic circulation transports the oxygen rich blood towards the different organs of the human body. In resting conditions, the brain receives ~13%, the heart ~4%, the kidneys ~20%, abdominal organs ~24% and the skeletal muscles ~20% of the systemic blood flow [1]. This systemic circulation is shown in figure 1.1.

The major artery leaving the left ventricle is called the aorta. The aorta starts upward from the heart (ascending aorta) but then curves (in the aortic arch) downward towards the descending thoracic and abdominal aorta. From the aortic arch, the subclavian arteries originate, supplying blood towards the arms and hands. The carotid arteries also originate from the aortic arch and they supply blood to the brain and neck. Because they are the main region of interest in the current thesis, a more detailed schematic is drawn in figure 1.2. An anatomical drawing of the arteries in the right side of the head is given in figure 1.3.

1.1.3 Main arteries in the head and neck

Figure 1.2 shows an asymmetry present in the human body directly at the point where the carotid and subclavian arteries originate. On the one hand, the brachiocephalic trunk branches off the aorta, which is a very short artery. This artery branches shortly thereafter into the right subclavian and the right common carotid artery (CCA). On the other hand, the left CCA and left subclavian arteries have no part in common and they both branch off the aortic arch directly (in most people). At the superior border of the larynx (level of the "Adam's Apple") the CCA bifurcates into the external carotid artery (ECA) and the internal carotid artery (ICA). This bifurcation is called the carotid bifurcation. The ECA supplies most of the tissues of the head except the brain and the eye. Examples of tissues supplied by (branches of) the ECA are: the tongue, the skin and muscles of the face, the chewing muscles, ... The ICA on the other hand supplies more than 80% of the cerebrum of blood and also supplies the orbits. At the base of the skull, the ICA connects to the circle of Willis (cerebral arterial circle). This is an anastomosis that encircles the optic chiasma and the pituitary gland. It unites the anterior and posterior blood cerebrum blood supply, it equalises the blood pressure and most importantly it provides alternative pathways for the blood to reach the brain tissue. Anticipating further chapters, the carotid bifurcation is prone to stenosis which can (partially) occlude the blood flow. In this case the redundancy brought in the system by the circle of Willis is indispensable.

In figure 1.3 the precise anatomical location of the different arteries described in the previous paragraph is shown. Both of the common carotid arteries run parallel to the spine and trachea. At the carotid bifurcation the

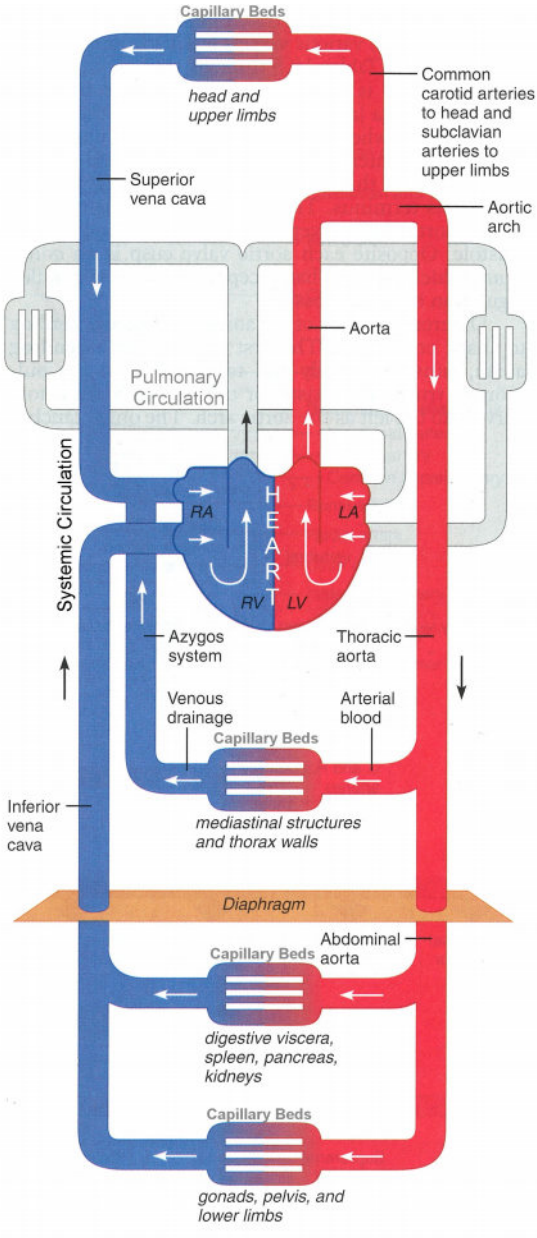

Figure 1.1: Schematic of the systemic circulation (adapted from [1]).

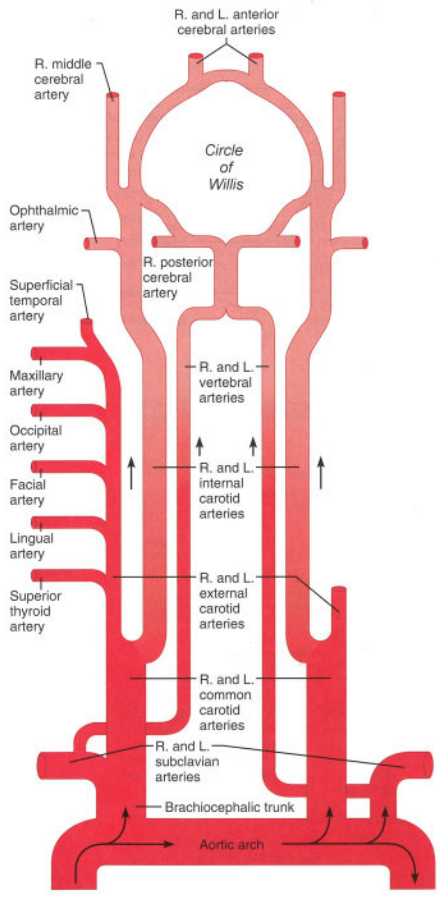

Figure 1.2: Schematic flowchart from the arteries in the neck and head (adapted from [1]).

ECA branches off anterior from the ICA. Downstream it clearly splits in arteries supplying the face and the scalp. The ICA enters the skull through the carotid canal and supplies blood to the cerebrum through an arterial network centred around the circle of Willis. The vertebral arteries root from the subclavian arteries and they ascend through the foramina in the transverse processes of the vertebrae. Within the skull the left and right vertebral arteries join again and connect to the circle of Willis through the basilar artery.

1.1.4 Structure of the arterial wall

The arterial wall consists of different constituents from which the most important ones are: endothelial cells (ECs), vascular smooth muscle cells (VSMCs), elastin and collagen. The ECs form an interface between the blood (inside

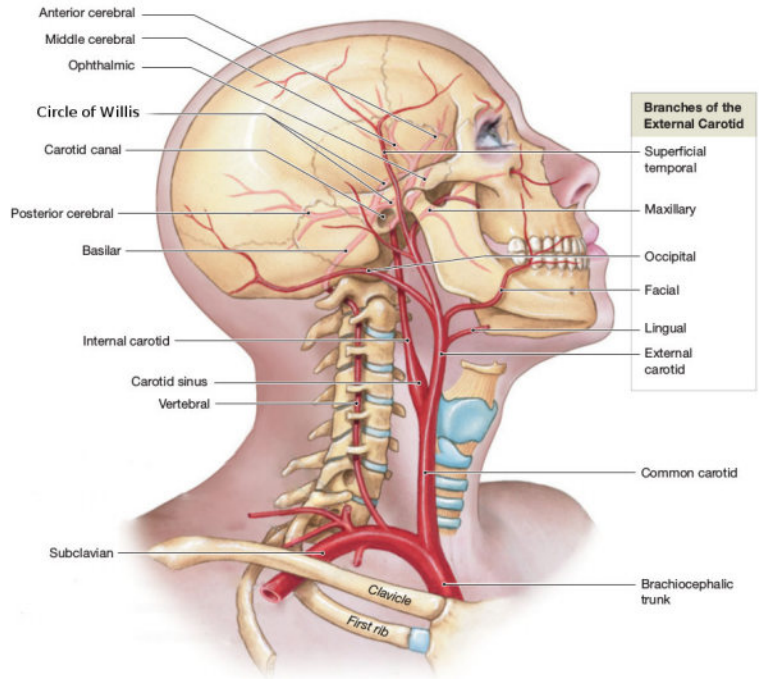

Figure 1.3: Drawing of the arteries in the head and neck, shown as seen from the right side (adapted from [2]).

the lumen) and the arterial wall. They serve as a selective barrier, but also produce vasoactive substances. The VSMCs are capable of contracting the vessel wall and they synthesise elastin and collagen fibres. Elastin is an elastic protein in connective tissues that forms elastic fibres together with a fibrillar component such as fibrillin. Elastin has no preferential direction with regard to load bearing. Collagen on the other hand has a preferential direction for bearing load. Collagen is present in a coiled up state and these fibres only bear a load when they are stretched completely. At high strains they have a high Young's modulus (3-9 GPa for a single molecule [5]) in comparison to elastin (0.4-1.2 MPa for a single fibre [5]) [5]–[8].

The structure of a general artery is shown in figure 1.4. Except for the smallest blood vessels, all blood vessels have three distinctive layers called tunica. The three layers are different on the cellular and protein level, resulting in a different proportion of the different constituents and thus in a different biomechanical behaviour. The same three layers are present in veins and arteries, but their relative size and importance differs. The three layers of a blood vessel are:

1. Tunica Externa (Adventitia)
   The tunica externa is the outer most layer of the blood vessel wall. It

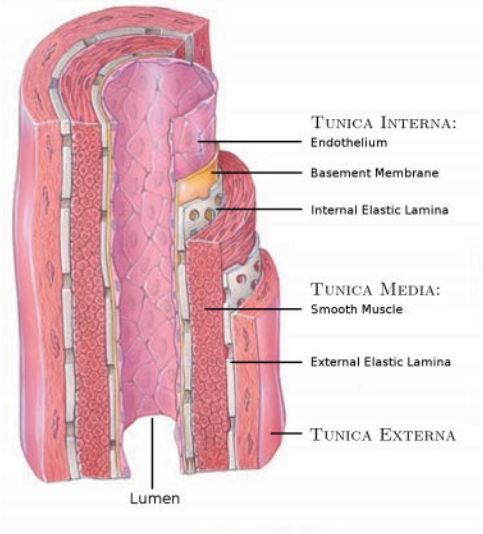

Figure 1.4: Different layers in the arterial wall (adapted from [3]).

mainly consists of collagen fibres that protect and reinforce the arterial wall. Nerve fibres and lymphatic vessels are present in this layer. In larger vessels the tunica externa also contains a network of tiny blood vessels, called the vasa vasorum supplying blood to the more external parts of the vessel wall.

2. Tunica Media (Media):
   In general, the tunica media is the bulkiest layer in arteries. For elastic arteries (see section 1.1.5), the high amount of elastin in the media provides the elasticity, which assures a continuous blood circulation. In muscular arteries (see section 1.1.5), the media mainly consists of VSMCs that can decrease the luminal diameter (vasoconstriction) or that can increase the luminal diameter (vasodilatation).

3. Tunica Interna (Interna):
   The most inner layer of the vessel wall contains simple squamous epithelium, called endothelium. These flat cells fit closely together to form a smooth surface to minimise the friction between the blood flow and the vessel wall. A subendothelial layer is present in vessels larger than 1mm diameter (humans) consisting of loose connective tissue and a basal membrane.

1.1.5 Different types of arteries

Although all the arteries are made of the three layers described in the previous paragraph (except the smallest arteries), they still differ in anatomy. These differences are illustrated in figure 1.5.

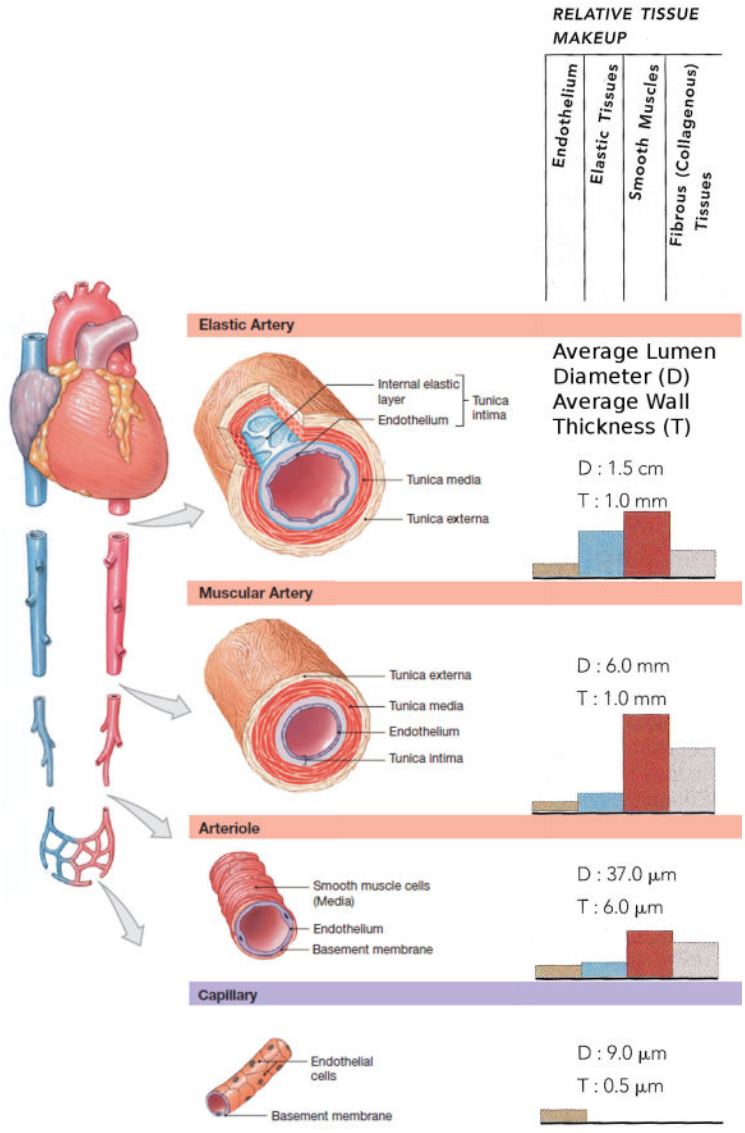

Figure 1.5: Structure of different blood vessels. A diagram of the cross-sectional views of different arteries and capillaries is drawn (adapted from [2]). Next to this, the relative tissue makeup for the different arteries is drawn in histograms (reproduced from [1]).

1. Elastic arteries
   The elastic arteries are the arteries near the heart. They are also called conducting arteries and the aorta and its main branches are classified in this category. Of all types of arteries, they have the largest amount of elastic tissues. They react as pressure reservoirs, buffering the blood flow by distending in systole.

2. Muscular arteries
   The muscular or distributing arteries deliver blood to specific organs. Of the different arterial types, they have relatively the thickest media. They play a more pronounced role in constriction because of the high number of VSMCs.

3. Arterioles
   On average arterioles have lumen diameter ranging from 0.3mm to 10μm [1]. In the larger arterioles all three layers are present in the vessel wall but in the smaller arterioles this is not the case. The smallest arterioles only consist of ECs with a small layer of smooth muscle cells.

4. Capillaries
   These are the smallest blood vessels (lumen diameter ranging from 8 to 10 μm [1]). The thin wall of the capillaries consists of only a very small tunica interna.

Carotid arteries (at least in humans) are of the elastic artery type. These conducting arteries have a low-resistance. Similar to the aorta the carotid arteries have a high buffering capacity that will play a crucial role in the models developed in chapters 8 and 9 on page 149 and on page 175.

1.1.6 Arterial blood pressure

The heart pumps the blood into the arteries by cycling through a contraction and a relaxation phase. When contracting, the ventriculo-arterial heart valves open and blood is pumped in the aorta (and pulmonary artery) which causes a peak in the pressure (systolic pressure). The aorta is an elastic artery, which reacts as a pressure reservoir. Therefore, the pressure decreases gradually and the aorta recoils during the relaxation of the heart (diastole) when the aortic valve is closed. The buffering of the aorta and other elastic arteries keeps the blood flowing further downstream. The buffering effect of the arteries is called the windkessel effect. This buffering converts the rapid, high-pressure pulsatile blood flow from the heart to slower, low-pressure blood flow in the capillaries. The pressure in the different vessels is plotted in figure 1.6.

For the different types of arteries, the individual area gradually decreases while the number of arteries increases exponentially. As a result, the total

cross-sectional area increases and reaches a maximum for the capillaries. This results in a lower pressure for the capillaries.

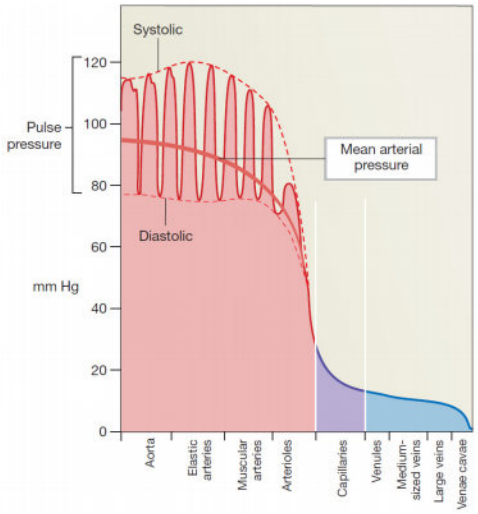

Figure 1.6: Pressures in the systemic circuit. Both the pulse pressure and the mean arterial pressure decrease downstream (reproduced from [2]).

1.2 Pathology: atherosclerosis

1.2.1 Introduction

Atherosclerosis has already been observed for centuries. The term "arteriosclerosis" was introduced by Jean Lobstein in 1829 [9]. In the 19th century, two well-known opposing schools of pathology studied atherosclerosis: the school of Rudolf Virchow in Berlin and the school of Carl von Rokitansky in Vienna [9]. Linguistically atherosclerosis is a combination of the Greek words *athēra* (*ἀθήρα*), meaning mush or gruel, and *sclerosis* meaning hardening. The two concepts appear to be contradictory but they describe the two main components of the atherosclerotic plaque. Atherosclerosis is a slowly progressing chronic inflammatory disease of the medium-sized and large arteries characterised by thickening of the arterial wall and the development of atherosclerotic plaques (see figure 1.8c on page 15) [10]–[12]. These atherosclerotic plaques consist of lipids accumulating in the arterial wall over time and are infiltrated by macrophages and other (pro-) inflammatory cells [13]–[15]. These lipids form an soft lipid-filled core in the plaque, described by the Greek word *athēra*. Over this plaque forms a hard and possibly thick fibrous cap, which is referred to by the *sclerosis* in the name of the disease [15], [16].

Atherosclerosis is a subgroup of the arteriosclerosis diseases. Arteriosclerosis is characterised by a reduction of the elasticity, hardening and thickening of the arterial wall. Next to atherosclerosis, marked by plaque formation, other pathologies of the arteriosclerosis family include: arteriolosclerosis (affects the small arteries and arterioles) and calcific sclerosis of Mönckeberg (calcific sclerosis) [15], [17].

Atherosclerosis is a very common disease that is the underlying cause in ischemic heart disease and stroke. Both of them are on the top of the causes of death worldwide figure 1.7. Especially in the industrialised countries such as the USA and (Western) Europe the incidence of atherosclerosis is high and a leading cause of death. The prevalence of the disease seems inversely proportional to the degree of wealth. The prevalence in the developing countries such as African countries is low, but it is also expected to become the leading cause of death in those countries by 2025 [15], [18]. Despite the omnipresence of atherosclerosis in the current time, it is already an "ancient" disease. It is described in medical works of the ancient Egyptians, Greek and Romans [18]. Moreover, atherosclerotic lesions have been found in Egyptian mummies [16], [18], [19].

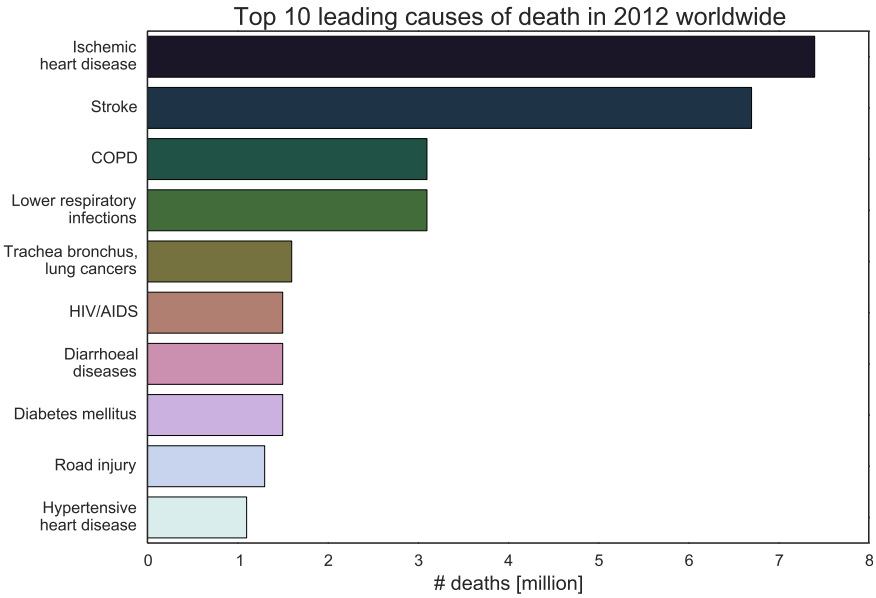

Figure 1.7: Top 10 leading causes of death in 2012 worldwide (adapted from [20]).

1.2.2 Pathogenesis

1.2.2.1 Initial steps of atherosclerosis formation

Several mechanisms occur at the same time when atherosclerosis develops and all these processes are cross-linked to each other. Historically, the accu-

mulation of lipids in the intimal layer has been emphasised [10], [11], [21], [22]. More recently the role of inflammation and the immune system in atherosclerosis development is gaining more attention from the scientific community [23]–[27].

The endothelial cell layer forms the barrier between the blood and the arterial wall. The offset of atherosclerosis starts with these endothelial cells. In normal conditions the endothelial layer resists the adhesion of leukocytes in the blood. Risk factors, however, can induce the expression of adhesion molecules such as vascular cell adhesion molecule-1 (VCAM-1)[28], [29]. This makes it possible for the monocytes to attach to the arterial wall. After the adhesion to the arterial wall, the monocytes enter the intima through diapedesis between the endothelial cells. This migration is likely partly stimulated by oxidized low density lipoprotein (oxLDL) (see next paragraph) [24], [28], [30].

Inflammatory stimuli such as dyslipidaemia, hypertension and wall shear stress (WSS), can lead to changes in permeability of the endothelium for low density lipoprotein (LDL). Structural changes and a reorientation of the endothelium have been shown for endothelium subject to low and oscillatory WSS, resulting in a higher permeability [31]. Both the ECs and the macrophages produce nitric oxide (NO), which is a potent oxidant. Once the LDL particles are present in the intimal layer, they can undergo oxidation to form oxLDL. Upon oxidation, LDL becomes cytotoxic and pro-inflammatory [32]. oxLDL can induce the expression of adhesion molecules and thus attract even more monocytes (differentiating to macrophages). This results in a positive feedback loop originates because the recruited inflammatory cells reinforce the oxidation of even more LDL [33].

Once inside the arterial intimal layer, the monocytes differentiate to macrophages and they take up the oxLDL molecules. In this way, the initial recruitment of macrophages can have a protective function because they remove the cytotoxic and pro-inflammatory oxLDL particles [34]. Yet, the consecutive, progressive accumulation of macrophages leads to atherosclerosis. Through accumulation of the LDL the macrophages become foam cells. These foam cells contain a massive amount of cholesterol esters. The macrophages that accumulate in the arterial wall release several molecules (growth factors and cytokines) to attract more macrophages and thus amplifying the inflammation. These foam cells also produce matrix metalloproteinases (MMP) which can degrade the extracellular matrix (ECM), that consists of collagen and elastin.

1.2.2.2 Progression of atherosclerosis

The simple fatty streak lesion, described in the previous section, transitions to a more complex lesion via the recruitment of VSMCs from the tunica media

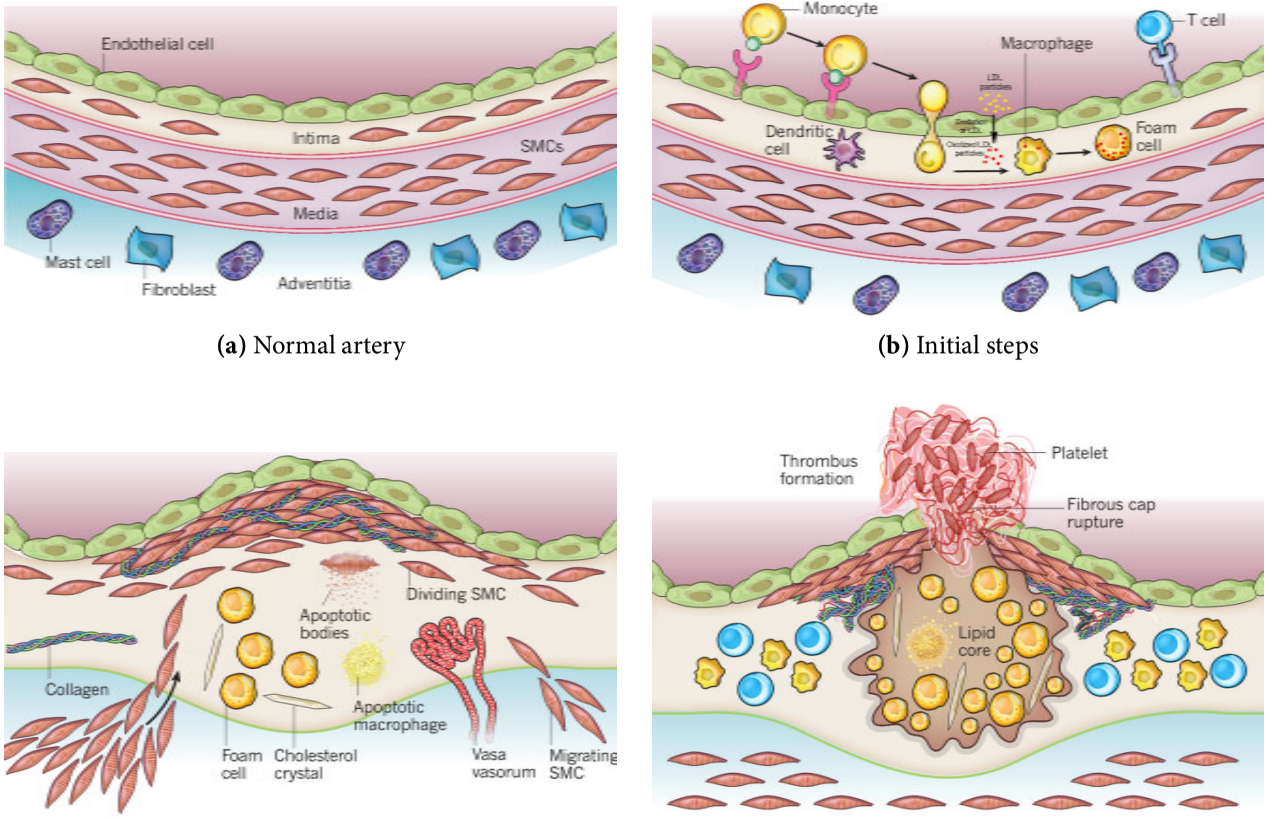

(a) Normal artery

(b) Initial steps

(c) Lesion progression

(d) Rupture/Thrombosis

Figure 1.8: Schematic representation of the different stages of atherosclerosis development. The most relevant processes are indicated in the figures(reproduced from [12]). (a) the normal arterial wall. (b) The initial steps of atherosclerosis are the adhesion of blood monocytes by the activated endothelium, infiltration and oxidation of LDL and the formation of foam cells(adapted from [12]). (c) After time a more advanced lesion develops which includes: migration from the VSMCs, neovascularization (vasa vasorum), formation of a fibrous cap, and a lipid/necrotic core. (d) Fibrous cap rupture that leads to thrombus formation.

towards the tunica interna (figure 1.8c). The fibroproliferative response of the VSMCs is normally responsible for the healing and repair after injury [32]. When the artery is damaged, VSMCs can switch from the "contractile" phenotype to the "synthetic" phenotype [35]. Due to this proliferation the VSMCs synthesise ECM proteins, including interstitial collagen and elastin. These proteins form (together with the VSMCs) the fibrous cap which is the second important component of an advanced atherosclerotic lesion next to the lipid core. The fibrous cap separates the lumen from the lipid in the lesion. It is possible that the inflammatory process (including LDL and macrophage infiltration) still continues after the cap formation. When this happens, the lesion will cycle through lipid accumulations and fibrous cap tissue formation, leading to an enlargement of the lesion [36].

In figure 1.8c it is also visible that the foam cells undergo a gradual transition during atherosclerotic plaque formation. Some of the LDL-rich macrophages die by apoptosis or necrosis. During necrosis their lipid content is released in the ECM. Together with the debris from the dead cells (also apoptosis (or cell death) from other cells including VSMCs occurs) this forms the so called necrotic core of the plaque. Cholesterol crystals can also be present in this region. The lipid core is the soft component in the plaque that does not provide mechanical stability and therefore destabilises the plaque [12], [32].

One last characteristic of advanced atherosclerotic plaque is the formation of new blood vessels or neovascularization. This intra-plaque angiogenesis is one of the hallmarks vulnerable plaques with a high risk of rupture (item (**E**) in section 1.2.4). The microvessels that originate from this neovascularization are fragile and leaky. As a consequence they leak plasma proteins, erythrocytes and inflammatory cells. This can result in an increased plaque progression [32].

1.2.2.3 Thrombosis and advanced lesions

There are different outcomes of atherosclerosis that lead to sudden fatal and non-fatal events. These different events are described in more detail in the next section (section 1.2.3). Classically most attention went to plaque rupture and this is plotted in figure 1.8d. If the (thin) fibrous cap ruptures, this can result in contact between the blood and the lipid core. Blood coagulation and thrombus formation can then occur. Several triggers can cause the rupture: blood pressure (BP), pulse pressure (PP), heart contraction (for coronary plaques), spasm, mechanical stress and haemodynamic shear stresses [37]–[39].

1.2.3 Paths to clinical complications

1.2.3.1 (Occlusive) thrombi

(Occlusive) thrombus (blood clot) formation can occur during plaque rupture section 1.2.3.2. However, thrombus formation can also occur without the presence of plaque rupture. In most of these cases the thrombus formation coexists with plaque erosion (limited to the endothelial cells covering the fibrous cap) or calcified nodules [40]–[42].

Thrombus formation in the carotid arteries can lead to ischemic stroke, cell death in the brain. Part of the brain is deprived from blood flow, due to the blocking of an artery by the thrombus . Carotid atherosclerosis contributes to at least 15-20% of all ischemic strokes [43]. Yearly ~795 000 US residents experience a stroke (both first attacks and recurrent attacks) [44]. Stroke was on the 4^{th} place of the deaths (by disease) in the US with an average of every 4min someone is dying of stroke in the US [44]. Worldwide stroke was ranked second (after ischemic heart disease: 7.4 million) on the numbers of deaths in 2012 with 6.7 million deaths (numbers of the World Health Organisation) [20]. Ischemic heart disease and stroke are accountable for the most deaths (places 1 and 2) worldwide for the lower-middle to higher income countries. Only for the low income countries lower respiratory infection, HIV/AIDS and diarrhoeal diseases were responsible for more deaths [20].

The damage of the stroke can be permanent (persistent, stable neurologic deficiency > 24h) or the ischemic event can only be temporary (transient ischemic attack (TIA) temporary loss of sensory or motor function <15min with complete recovery in 24h) [45]. The most common location for the occlusion to occur, is in the middle cerebral artery [46]. The symptoms include hemipareses (weakening of an entire side of the body, opposite to the side of the lesion location in the brain), hemisensory (loss of sensation on one side of the body) loss and aphasia (language disorder) [47].

1.2.3.2 Plaque rupture

Plaque rupture accounts for ~70% of the fatal acute myocardial infarctions (coronary plaques) [40]. As can be seen in figure 1.8d, the plaque rupture exposes the thrombogenic (high tendency for blood to form thrombi when in contact with this material) parts (from which the lipid core appears to be the most thrombogenic) of the plaque to the blood flow [39]. This is the first step in the activation of the clotting cascade leading to thrombus formation (see section 1.2.3.1). 70 to 80% of the coronary thrombi originate from plaque rupture [38]. The plaques prone to rupture do not always present a severe stenosis due to outward remodelling.

1.2.4 Vulnerable plaque

Historically, the term *vulnerable plaque* has been used for thin-cap fibroatheroma, which are plaques that are prone to rupture (for more details see next section). Yet, a new consensus was reached with regard to plaque vulnerability (mainly focused on coronary plaques) in 2 consensus articles [40], [48]. There are three main conclusions of this consensus: (i) not only rupture-prone plaques are vulnerable plaques, plaques with a high likelihood of rapid progression or thrombosis are also vulnerable; (ii) not only the vulnerable plaques but also vulnerable blood and vulnerable myocardium (coronary plaques) are important factors; (iii) quantitative methods to assess the risk of vulnerable plaque, blood and myocardium should be developed.

The classification as proposed in the consensus document by Naghavi *et al.* is shown in figure 1.9 and listed here [40]:

(**A**) *Rupture-prone*
These plaques are characterised by a large lipid core, a thin fibrous cap and macrophage infiltration. Both the thin cap and the large lipid core make this a mechanically unstable plaque. Macrophages (and other inflammatory cells) can secrete enzymes degrading the plaque matrix such as MMP [37].

(**B**) *Ruptured/healing*
A ruptured plaque with a non-occlusive thrombus present

(**C**) *Erosion-prone*
Dysfunctional endothelium is one of the markers of plaque vulnerability. These plaques have a higher risk for erosion of the EC layer.

(**D**) *Eroded*
Thrombosis is associated with plaque erosion of the ECs. Eroded plaques have an increased risk of thrombosis [41].

(**E**) *With intra-plaque haemorrhage*
Neovascularization can be present in complex lesions (figure 1.8c). When they leak red blood cells in the plaque this can indicate plaque vulnerability.

(**F**) *With calcified nodule*
Calcified nodules (near the surface) may form mechanical trigger points for plaque rupture and are an indicator of plaque vulnerability.

(**G**) *Critically stenotic*
Severe stenosis can lead to ischemia due to the reduced blood flow. Moreover, the high WSS at the cap raises the risk for thrombus formation [40].

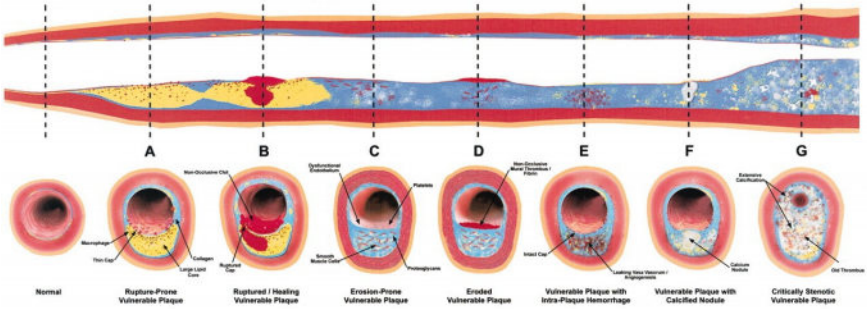

Figure 1.9: Different types of vulnerable plaque as cause of acute events (reproduced from [40]).

1.2.5 American Heart Association classification

In a series of three reports [10], [11], [21], the American Heart Association (AHA) Committee on Vascular Lesions has defined a numerical classification of the different types of the human atherosclerotic lesions based on the composition and structure of the lesions. In the first report, published in 1992, the normal arterial intima was defined, including the atherosclerosis-prone regions [10]. The second in the series, published in 1994, defines the initial, fatty streak and the intermediate lesions[11]. Finally, the third report (1995) defines the advanced lesions in terms of composition [21]. It is in this third report that the AHA classification system is introduced. This classification was generally accepted by the scientific community and used in numerous publications (3276 citations on Google scholar for the third and final report). Nonetheless, over time new data made it necessary to update the classification, which was done in 2000 by the AHA with a brief communication [22]. In this update 2 extra groups were added to the classification which results in 8 groups, shown in figure 1.10 and listed here [10], [11], [18], [21], [22], [49]:

I (Initial) Lesion
In the type I lesion, isolated foamy macrophages are present in the intima.

II (Fatty Streak) Lesion
The type II lesions are the first grossly visible lesions. They are characterised by mainly intracellular lipid accumulation. These lipids are present in the macrophage foam cells and under the form of lipid droplets in the VSMCs. Some extracellular lipid droplets can be present. Next to the macrophages, also lymphocytes can be present. Generally type I and type II are the only types of lesions found in children (although they may also occur in adults).

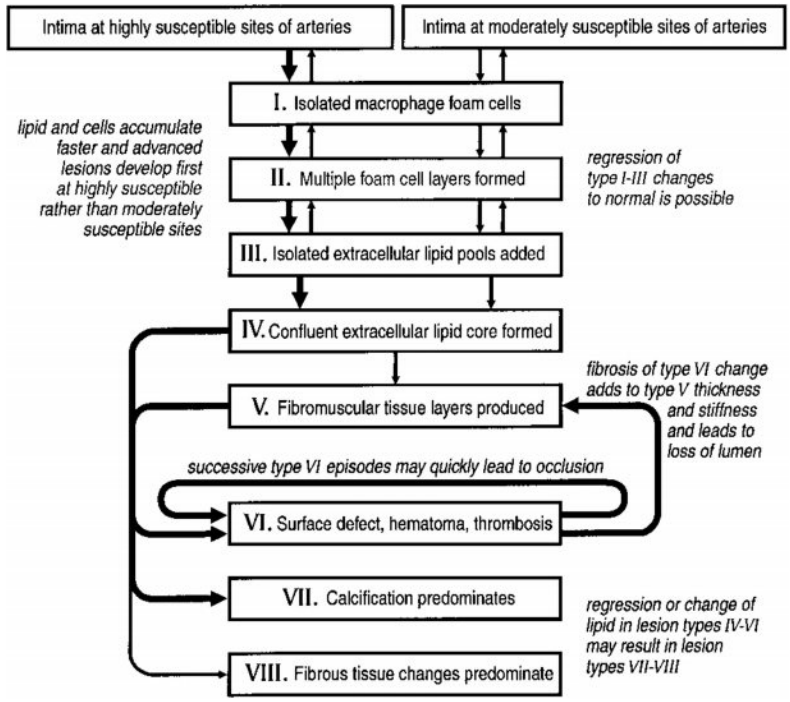

Figure 1.10: Classification of eight types of arterial wall lesions (reproduced from [21]).

III (Intermediate) Lesion

Type III atherosclerosis is an intermediate state between type II and type IV lesions. In this lesion type sets of extracellular lipid droplets are present. The coherence of some intimal VSMCs can be disrupted. For the first three types of lesions (I - III), the lesion is focal and relatively small. There are almost no changes present in either the composition of the matrix or architecture of the intima. The media is not affected in this stage of the disease.

IV (Atheroma) Lesion

This lesion type is the first advanced lesion type in this classification, because structural changes are present in the intima due to the formation of a lipid core. In the type IV lesions extracellular lipids accumulate in a well defined region in the intima forming a so called lipid core. These lipid cores are visible by the unaided eye on the histological coups. A thickening of the arterial wall is present due to the lipid cores. In most cases the lumen is not narrowed in this stage yet, due to the outward remodelling of the artery. From this stage on the damage in the arterial wall is irreversible and regression to lesion types I-III is not possible.

Via different pathways the type IV lesion can evolve to different more advanced lesion types (figure 1.10). From lesion type IV on clinical manifestations may be present. From this type of lesion on, the lumen of medium sized arteries can also be obstructed.

V (Fibromuscular) Lesion
In the type IV lesion, the lipid core is still mostly covered by intimal endothelial cells. When an increase in fibrous tissue together with VSMCs at the cover of this lipid core replaces this "normal" endothelial layer, the lesion has evolved to a type V lesion. The type V lesions are characterised by the striking amount of new fibrous connective tissue that is formed. These lesions can consist of multiple layers of lipid cores separated by fibrous tissue layers.

VI (Complicated) Lesion
Lesions of type IV and V can evolve in different lesion types. The complex lesions (VI) are characterised by either a surface defect (VIa), haematoma (VIb) or thrombosis (VIc). These are the three main pathways for type IV and V lesions to result in morbidity or mortality.

- VIa
  Both ulcerations and tears can penetrate the surface of the lesion, resulting in an surface disruption. Factors that facilitate these phenomena are: inflammatory cells in the lesion, structural weakness of the lesion and shear stresses.
- VIb
  Haemorrhage is mostly caused by tears in the surface of the lesion, it can also start due to an haemorrhage of the neovascularization in the lesion.
- VIc
  Thrombosis (the formation of blood clots), can be involved in these complex lesions. The thrombus can range from microscopic to clearly visible deposits. This thrombus formation can block the artery (occlusive thrombosis).

VII (Calcified) Lesion
Mineral deposits can replace the contents of the lipid core and calcified nodules. Plaques with predominant presence of calcifications are labelled as calcified (type VII) lesions. The presence of microcalcifications is one of the markers of plaque vulnerability. Plaques with macrocalcifications are more stable [15], [50].

VIII (Fibrotic) Lesion
Lesions with only a limited amount of lipids present but with abundant presence of fibrous tissue are called fibrotic lesions. They often occur in the arteries of the legs.

1.2.6 Risk factors

The most important risk factors are here briefly summarised. For a more detailed description the reader is referred to [15], [51]–[53].

1.2.6.1 Non modifiable

1. Gender
   Men are at higher risk for atherosclerosis compared to women [15], [52].

2. Age
   The atherogenic processes start already in childhood, but due the slowly progressing nature of this disease, clinical implication normally only occur from the fourth decade of life on (time from which type IV lesions are present [21]).

3. Race & Ethnicity
   Studies are showing that race is a possible risk factor for atherosclerosis. Both the prevalence and the locations of atherosclerosis development could be different between different populations [51].

4. Genetic Factors
   An active research field is the genetic influence on atherosclerosis development. Although genetics seem to have an influence, no strong association is found [51]. Yet, genetics play an important role in some of the modifiable risk factors such as: hypertension, diabetes and hypercholesterolemia.

1.2.6.2 Modifiable

1. Hypertension
   Hypertension mechanically stresses the arterial wall and may thus damage and weaken the arterial wall. Furthermore, hypertension and hyperlipidemia initiate similar responses of the arterial wall [54].

2. Dyslipidemia
   Dyslipidemia is an abnormally high amount of lipids and cholesterol in the blood. Plaque progression starts with the accumulation of lipids originating from the blood in the intimal layer of the arterial wall (section 1.2.5 on page 19). Mainly the LDL are responsible for this accumulation.

3. Cigarette Smoke
   Smoking is one of the strongest risk factors for peripheral artery disease (PAD) and it affects all phases of atherosclerosis. The precise mechanism is not fully known, but cigarette smoke increases inflammation, thrombosis, and oxidation of LDL cholesterol [53], [55].

4. Alcohol consumption
   The effect of alcohol intake is highly non-linear and the curve is J-shaped. Light drinkers have a lower risk for atherosclerosis compared to heavy drinkers and abstainers [29], [56], [57].

5. Diabetes Mellitus
   Diabetes mellitus increases the risk of developing atherosclerosis substantially. The metabolic abnormalities caused by diabetes, initiate mechanisms that contribute to vascular dysfunction [58].

6. Obesity
   Obesity is linked with a higher risk for cardiovascular diseases. Both in obesity and atherosclerosis lipids and inflammation are involved [33]. [59]

1.2.7 Role of haemodynamics in atherosclerosis

The aforementioned risk factors for atherosclerosis development are all systemic, meaning that they play a role over the entire vascular system. Nonetheless, atherosclerotic lesions are known to develop preferentially at arterial branches and curvatures[30], [60], [61]. What these locations have in common is the prevalence of spatially complex haemodynamics, with zones of flow recirculation. In some conditions, regions with (transiently) turbulent flow may be present.

In the 1970s, two different theories emerged aiming to explain this phenomenon. The high WSS hypothesis suggested that high WSS causes endothelial injury which forms the onset of atherosclerosis. The second hypothesis, proposed by Caro *et al.*, linked the initiation of atherosclerosis with low and oscillatory WSS [62], [63]. They linked haemodynamics and atherosclerotic plaque development by comparing cadaver human arteries with experimental flow studies in casts. Over time the low and oscillatory WSS hypothesis got generally accepted. Numerous studies have been performed since then to support this hypothesis [64]–[68].

The endothelium forms the interface between the lumen (blood flow) and the arterial wall. The flow exerts a shear force (called the WSS) on these endothelial cells, resulting in a shearing deformation of the ECs [28]. The endothelium responds to changes in WSS. Low and oscillatory WSS, induced

by the flow disturbances, leads to functional and structural changes of the endothelium. The shear rate is thus one of the determinants of vascular remodelling [31], [60], [69]–[72].

In normal physiological flow conditions with laminar uni-directional flow, the ECs have an elongated shape in the direction of the main flow direction. In regions with low, oscillatory and multi-directional flow regimes this alignment of the endothelium is lost. Several atheroprone pathways are activated in these ECs.

The magnitude of the WSS (~5 Pa)is only a fraction of the pressure magnitude (~10 000 Pa) [28]. Therefore the effect of WSS is amplified in the ECs by specialised cellular structures. Primary cilia at the luminal surface, are connected to the cytoskeleton and amplify the effect of WSS. In this manner, they raise the responsiveness of ECs to shear stress [28].

After the initial sensing, several signalling molecules are activated. The cytoskeleton forms the bond between the luminal surface with the sensing mechanisms and the locations where the various signalling molecules are formed. In this manner, the low and oscillatory WSS starts a cascade of mechanisms resulting in an atheroprone endothelial phenotype. Some of the major processes started are [66]:

- Enhanced uptake
  In the low WSS regions, the LDL permeability of the endothelium surface for LDL is increased [31], [73]. The ECs change shape to a more polygonal shape, which results in wider junctions between ECs[74]. A second pathway is the activation of sterol regulatory elements binding proteins, leading to an increased synthesis of LDL by the ECs [66].

- Enhanced LDL oxidation
  The oxidation of LDL to oxLDL (figure 1.8b) gets promoted by an upregulation of the main oxidative enzymes [66].

- Attenuation of NO release
  This is one of the earliest changes anteceding endothelial dysfunction. Endothelial NO release results in atheroprotective vascular relaxation and inhibits several atheroprone pathways: platelet activation, apoptosis and monocyte adhesion [75].

- Promotion of inflammation
  The infiltration of the arterial wall with leukocytes is one of the first steps of atherosclerosis development (section 1.2.2.1). The expression of VCAM-1 and other adhesion molecules, facilitating this leukocyte infiltration, is shown to be upregulated in low WSS regions [76], [77].

- Promotion VSMC migration, differentiation and proliferation
  The formation of a fibromuscular plaque (type V), is characterised by intimal infiltration of VSMCs that are dedifferentiated to the synthetic phenotype producing ECM proteins (section 1.2.2.2). This migration and proliferation is upregulated by low WSS by platelet-derived growth factor released by ECs[78].

- Promotion of ECM degradation
  MMP degrades the ECM (in the fibrous cap), which can lead to a rupture-prone vulnerable plaque (item (**A**) in section 1.2.4). It has been shown that low WSS upregulates the activity of these MMPs [66].

- Increased thrombogenicity
  Low WSS downregulates the expression of several anti-thrombotic molecules. Moreover, stagnation of the blood flow might facilitate the accumulation of thrombogenic factors at the arterial wall [66], [79].

Bibliography Chapter 1

[1] E. N. Marieb and K. Hoehn, 'Anatomy & Physiology', Pearson In. Pearson Benjamin Cummings, 2008.

[2] F. H. Martini, J. L. Nath and E. F. Bartholomew, 'Blood Vessels and Circulation', in *Fundamentals of Anatomy & Physiology*, 9th ed., Boston: Benjamin Cummings, 2012, ch. 21, pp. 707–764.

[3] M. Nair, 'The circulatory s ystem', in *Fundamentals of Anatomy and Physiology for Student Nurses*, I. Peate and M. Nair, Eds., Chichester: John Wiley & Sons, 2011, ch. 12, pp. 366–405.

[4] S. Silbernagl and A. Despopoulos, 'Hart en bloedsomloop', in *SESAM Atlas van de fysiology*, 14th ed., Baarn: SESAM/HBuitgevers, 2007, ch. 8.

[5] A. Tarakanova, S.-W. Chang and M. J. Buehler, 'Computational Materials Science of Bionanomaterials: Structure, Mechanical Properties and Applications of Elastin and Collagen Proteins', in *Handbook of Nanomaterial Properties*, B. Bhushan, D. Luo, S. R. Schricker, W. Sigmund and S. Zauscher, Eds., Berlin, Heidelberg: Springer Berlin Heidelberg, 2014, ch. 28, pp. 285–297.

[6] P. B. Dobrin, 'Mechanics of Normal and Diseased Blood Vessels', *Annals of Vascular Surgery*, vol. 2, no. 3, pp. 283–294, 1988.

[7] B. Trachet, 'The Role of Disturbed Hemodynamics in Aneurysm Formation in Mice', PhD thesis, Ghent University, 2012.

[8] A. J. Bank, H. Wang, J. E. Holte, K. Mullen, R. Shammas and S. H. Kubo, 'Contribution of Collagen, Elastin, and Smooth Muscle to In Vivo Human Brachial Artery Wall Stress and Elastic Modulus', *Circulation*, vol. 94, no. 12, pp. 3263–3270, 1996.

[9] C. Mayerl, M. Lukasser, R. Sedivy, H. Niederegger, R. Seiler and G. Wick, 'Atherosclerosis research from past to present—on the track of two pathologists with opposing views, Carl von Rokitansky and Rudolf Virchow', *Virchows Archiv*, vol. 449, no. 1, pp. 96–103, 2006.

[10] H. C. Stary, D. H. Blankenhorn, A. B. Chandler, S. Glagov, W. Insull Jr, M. Richardson, M. E. Rosenfeld, S. A. Schaffer, C. J. Schwartz and W. D. Wagner, 'A definition of the intima of human arteries and of its atherosclerosis-prone regions. A report from the Committee on Vascular Lesions of the Council on Arteriosclerosis, American Heart Association', *Arteriosclerosis, Thrombosis, and Vascular Biology*, vol. 12, no. 1, pp. 120–134, 1992.

[11] H. C. Stary, A. B. Chandler, S. Glagov, J. R. Guyton, W. Insull Jr, M. E. Rosenfeld, S. A. Schaffer, C. J. Schwartz, W. D. Wagner and R. W. Wissler, 'A definition of initial, fatty streak, and intermediate lesions of atherosclerosis. A report from the Committee on Vascular Lesions of the Council on Arteriosclerosis, American Heart Association', *Arteriosclerosis, Thrombosis, and Vascular Biology*, vol. 14, no. 5, pp. 840–856, 1994.

[12] P. Libby, P. M. Ridker and G. K. Hansson, 'Progress and challenges in translating the biology of atherosclerosis', *Nature*, vol. 473, no. 7347, pp. 317–325, 2011.

[13] W. Insull, 'The Pathology of Atherosclerosis: Plaque Development and Plaque Responses to Medical Treatment', *The American Journal of Medicine*, vol. 122, no. 1, S3–S14, 2009.

[14] P. Libby, 'Inflammation in atherosclerosis.' *Nature*, vol. 420, no. 6917, pp. 868–74, 2002.

[15] A. Marsico, 'Pathology of Atherosclerotic Disease', in *Atherosclerosis Disease Management*, New York, NY: Springer New York, 2011, pp. 71–85.

[16] A. R. Bond and C. L. Jackson, 'The fat-fed apolipoprotein E knockout mouse brachiocephalic artery in the study of atherosclerotic plaque rupture.' *Journal of biomedicine & biotechnology*, vol. 2011, p. 379 069, 2011.

[17] G. A. Fishbein and M. C. Fishbein, 'Arteriosclerosis: rethinking the current classification.' *Archives of pathology & laboratory medicine*, vol. 133, no. 8, pp. 1309–16, 2009.

[18] N. Carter-Monroe, S. K. Yazdani, E. Ladich, F. D. Kolodgie and R. Virmani, 'Introduction to the Pathology of Carotid Atherosclerosis: Histologic Classification and Imaging Correlation', in *Atherosclerosis Disease Management*, New York, NY: Springer New York, 2011, ch. 1, pp. 3–35.

[19] R. Magee, 'Arterial disease in antiquity.' *The Medical journal of Australia*, vol. 169, no. 11-12, pp. 663–6, 1998.

[20] World Health Organization, *The top 10 causes of death*, `http://www.who.int/mediacentre/factsheets/fs310/en/`, 2014.

[21] H. C. Stary, A. B. Chandler, R. E. Dinsmore, V. Fuster, S. Glagov, W. Insull Jr, M. E. Rosenfeld, C. J. Schwartz, W. D. Wagner and R. W. Wissler, 'A Definition of Advanced Types of Atherosclerotic Lesions and a Histological Classification of Atherosclerosis A Report From the Committee on Vascular Lesions of the Council Atherosclerotic Lesion Types Advanced by Histology', *Circulation*, vol. 92, pp. 1355–1374, 1995.

[22] H. C. Stary, 'Natural History and Histological Classification of Atherosclerotic Lesions : An Update', *Arteriosclerosis, Thrombosis, and Vascular Biology*, vol. 20, no. 5, pp. 1177–1178, 2000.

[23] P. Libby, 'Inflammation in Atherosclerosis', *Arteriosclerosis, Thrombosis, and Vascular Biology*, vol. 32, no. 9, pp. 2045–2051, 2012.

[24] P. Libby, 'Inflammation and cardiovascular disease mechanisms.' *The American journal of clinical nutrition*, vol. 83, no. 2, 456S–460S, 2006.

[25] L. G. Spagnoli, E. Bonanno, G. Sangiorgi and A. Mauriello, 'Role of Inflammation in Atherosclerosis', *Journal of Nuclear Medicine*, vol. 48, no. 11, pp. 1800–1815, 2007.

[26] B. Ludewig, R. M. Zinkernagel and H. Hengartner, 'Arterial Inflammation and Atherosclerosis', *Trends in Cardiovascular Medicine*, vol. 12, no. 4, pp. 154–159, 2002.

[27] B. W. Wong, A. Meredith, D. Lin and B. M. McManus, 'The Biological Role of Inflammation in Atherosclerosis', *Canadian Journal of Cardiology*, vol. 28, no. 6, pp. 631–641, 2012.

[28] F. Helderman, D. Segers, R. de Crom, B. P. Hierck, R. E. Poelmann, P. C. Evans and R. Krams, 'Effect of shear stress on vascular inflammation and plaque development.' *Current opinion in lipidology*, vol. 18, no. 5, pp. 527–533, 2007.

[29] J. M. Li and K. J. Mukamal, 'An update on alcohol and atherosclerosis', *Current Opinion in Lipidology*, vol. 15, no. 6, pp. 673–680, 2004.

[30] P. A. VanderLaan, 'Site Specificity of Atherosclerosis: Site-Selective Responses to Atherosclerotic Modulators', *Arteriosclerosis, Thrombosis, and Vascular Biology*, vol. 24, no. 1, pp. 12–22, 2004.

[31] A. M. Malek, S. L. Alper and S. Izumo, 'Hemodynamic shear stress and its role in atherosclerosis.' *JAMA : the journal of the American Medical Association*, vol. 282, no. 21, pp. 2035–2042, 1999.

[32] E. Falk, 'Pathogenesis of Atherosclerosis', *Journal of the American College of Cardiology*, vol. 47, no. 8, pp. C7–C12, 2006.

[33] V. Z. Rocha and P. Libby, 'Obesity, inflammation, and atherosclerosis', *Nature Reviews Cardiology*, vol. 6, no. 6, pp. 399–409, 2009.

[34] C. K. Glass and J. L. Witztum, 'Atherosclerosis: The Road Ahead', *Cell*, vol. 104, no. 4, pp. 503–516, 2001.

[35] D. A. Chistiakov, A. N. Orekhov and Y. V. Bobryshev, 'Vascular smooth muscle cell in atherosclerosis', *Acta Physiologica*, vol. 214, no. 1, pp. 33–50, 2015.

[36] A. Rudijanto, 'The role of vascular smooth muscle cells on the pathogenesis of atherosclerosis.' *Acta medica Indonesiana*, vol. 39, no. 2, pp. 86–93, 2007.

[37] G. Pasterkamp and E. Falk, 'Atherosclerotic plaque rupture: an overview', *Journal Of Clinical And Basic Cardiology*, vol. 3, no. 2, pp. 81–86, 2000.

[38] P. K. Shah, 'Mechanisms of plaque vulnerability and rupture', *Journal of the American College of Cardiology*, vol. 41, no. 4, S15–S22, 2003.

[39] D. E. Gutstein and V. Fuster, 'Pathophysiology and clinical significance of atherosclerotic plaque rupture.' *Cardiovascular research*, vol. 41, no. 2, pp. 323–33, 1999.

[40] M. Naghavi, 'From Vulnerable Plaque to Vulnerable Patient: A Call for New Definitions and Risk Assessment Strategies: Part I', *Circulation*, vol. 108, no. 14, pp. 1664–1672, 2003.

[41] A. Farb, A. P. Burke, A. L. Tang, Y. Liang, P. Mannan, J. Smialek and R. Virmani, 'Coronary Plaque Erosion Without Rupture Into a Lipid Core : A Frequent Cause of Coronary Thrombosis in Sudden Coronary Death', *Circulation*, vol. 93, no. 7, pp. 1354–1363, 1996.

[42] A. Lafont, 'Basic aspects of plaque vulnerability', *Heart*, vol. 89, no. 10, pp. 1262–1267, 2003.

[43] M. M. Mughal, M. K. Khan, J. K. DeMarco, A. Majid, F. Shamoun and G. S. Abela, 'Symptomatic and asymptomatic carotid artery plaque', *Expert Review of Cardiovascular Therapy*, vol. 9, no. 10, pp. 1315–1330, 2011.

[44] D. Mozaffarian, E. J. Benjamin, A. S. Go, D. K. Arnett, M. J. Blaha, M. Cushman, S. de Ferranti, J.-P. Despres, H. J. Fullerton, V. J. Howard, M. D. Huffman, S. E. Judd, B. M. Kissela, D. T. Lackland, J. H. Lichtman, L. D. Lisabeth, S. Liu, R. H. Mackey, D. B. Matchar, D. K. McGuire *et al.*, 'Heart Disease and Stroke Statistics–2015 Update: A Report From the American Heart Association', *Circulation*, vol. 131, no. 4, e29–e322, 2015.

[45] C. Daly and H. E. Rodriguez, 'Carotid Artery Occlusive Disease', *Surgical Clinics of North America*, vol. 93, no. 4, pp. 813–832, 2013.

[46] M. Paciaroni, G. Silvestrelli, V. Caso, F. Corea, M. Venti, P. Milia, N. Tambasco, L. Parnetti and V. Gallai, 'Neurovascular territory involved in different etiological subtypes of ischemic stroke in the Perugia Stroke Registry.' *European journal of neurology*, vol. 10, no. 4, pp. 361–5, 2003.

[47] W. Stetler, J. J. Gemmete, A. S. Pandey and N. Chaudhary, 'Endovascular Treatment of Carotid Occlusive Disease', *Neuroimaging Clinics of North America*, vol. 23, no. 4, pp. 637–652, 2013.

[48] M. Naghavi, 'From Vulnerable Plaque to Vulnerable Patient: A Call for New Definitions and Risk Assessment Strategies: Part II', *Circulation*, vol. 108, no. 15, pp. 1772–1778, 2003.

[49] R. Virmani, F. D. Kolodgie, a. P. Burke, A. Farb and S. M. Schwartz, 'Lessons From Sudden Coronary Death : A Comprehensive Morphological Classification Scheme for Atherosclerotic Lesions', *Arteriosclerosis, Thrombosis, and Vascular Biology*, vol. 20, no. 5, pp. 1262–1275, 2000.

[50] G. Pugliese, C. Iacobini, C. B. Fantauzzi and S. Menini, 'The dark and bright side of atherosclerotic calcification', *Atherosclerosis*, vol. 238, no. 2, pp. 220–230, 2015.

[51] M. H. Criqui and V. Aboyans, 'Epidemiology of Peripheral Artery Disease', *Circulation Research*, vol. 116, no. 9, pp. 1509–1526, 2015.

[52] M. Rodriguez-Flores, J. Rodriguez-Saldaña, C. Cantú-Brito, J. Aguirre-Garcia and G.-G. Alejandro, 'Prevalence and severity of atherosclerosis in different arterial territories and its relation with obesity', *Cardiovascular Pathology*, vol. 22, no. 5, pp. 332–338, 2013.

[53] A. W. Zieske, G. T. Malcom and J. P. Strong, 'Natural history and risk factors of atherosclerosis in childer and youth: the PDAY study', *Fetal & Pediatric Pathology*, vol. 21, no. 2, pp. 213–237, 2002.

[54] R. W. Alexander, 'Hypertension and the Pathogenesis of Atherosclerosis : Oxidative Stress and the Mediation of Arterial Inflammatory Response: A New Perspective', *Hypertension*, vol. 25, no. 2, pp. 155–161, 1995.

[55] J. a. Ambrose and R. S. Barua, 'The pathophysiology of cigarette smoking and cardiovascular disease', *Journal of the American College of Cardiology*, vol. 43, no. 10, pp. 1731–1737, 2004.

[56] P. da Luz and S. Coimbra, 'Wine, alcohol and atherosclerosis: clinical evidences and mechanisms', *Brazilian Journal of Medical and Biological Research*, vol. 37, no. 9, pp. 1275–1295, 2004.

[57] S. Kiechl, J. Willeit, G. Rungger, G. Egger, F. Oberhollenzer and E. Bonora, 'Alcohol Consumption and Atherosclerosis: What Is the Relation? : Prospective Results From the Bruneck Study', *Stroke*, vol. 29, no. 5, pp. 900–907, 1998.

[58] M. a. Creager, 'Diabetes and Vascular Disease: Pathophysiology, Clinical Consequences, and Medical Therapy: Part I', *Circulation*, vol. 108, no. 12, pp. 1527–1532, 2003.

[59] D. McNamara, 'Dietary cholesterol and atherosclerosis', *Biochimica et Biophysica Acta (BBA) - Molecular and Cell Biology of Lipids*, vol. 1529, no. 1-3, pp. 310–320, 2000.

[60] J. J. Chiu and S. Chien, 'Effects of disturbed flow on vascular endothelium: pathophysiological basis and clinical perspectives', *Physiological Reviews*, vol. 91, no. 1, pp. 327–387, 2011.

[61] P. F. Davies, D. C. Polacek, C. Shi and B. P. Helmke, 'The convergence of haemodynamics, genomics, and endothelial structure in studies of the focal origin of atherosclerosis.' *Biorheology*, vol. 39, no. 3-4, pp. 299–306, 2002.

[62] C. G. Caro, J. M. Fitz-Gerald and R. C. Schroter, 'Atheroma and Arterial Wall Shear Observation, Correlation and Proposal of a Shear Dependent Mass Transfer Mechanism for Atherogenesis', *Proceedings of the Royal Society B: Biological Sciences*, vol. 177, no. 1046, pp. 109–133, 1971.

[63] C. G. Caro, 'Discovery of the Role of Wall Shear in Atherosclerosis', *Arteriosclerosis, Thrombosis, and Vascular Biology*, vol. 29, no. 2, pp. 158–161, 2009.

[64] V. Peiffer, S. J. Sherwin and P. D. Weinberg, 'Does low and oscillatory wall shear stress correlate spatially with early atherosclerosis? A systematic review', *Cardiovascular Research*, vol. 99, no. 2, pp. 242–250, 2013.

[65] D. N. Ku, D. P. Giddens, C. K. Zarins and S. Glagov, 'Pulsatile flow and atherosclerosis in the human carotid bifurcation. Positive correlation between plaque location and low oscillating shear stress.' *Arteriosclerosis*, vol. 5, no. 3, pp. 293–302, 1985.

[66] Y. S. Chatzizisis, A. U. Coskun, M. Jonas, E. R. Edelman, C. L. Feldman and P. H. Stone, 'Role of endothelial shear stress in the natural history of coronary atherosclerosis and vascular remodeling: molecular, cellular, and vascular behavior.' *Journal of the American College of Cardiology*, vol. 49, no. 25, pp. 2379–93, 2007.

[67] T. Asakura and T. Karino, 'Flow patterns and spatial distribution of atherosclerotic lesions in human coronary arteries', *Circulation Research*, vol. 66, no. 4, pp. 1045–1066, 1990.

[68] A. Gnasso, C. Irace, C. Carallo, M. S. De Franceschi, C. Motti, P. L. Mattioli and A. Pujia, 'In Vivo Association Between Low Wall Shear Stress and Plaque in Subjects With Asymmetrical Carotid Atherosclerosis', *Stroke*, vol. 28, no. 5, pp. 993–998, 1997.

[69] N. Resnick, H. Yahav, a. Shay-Salit, M. Shushy, S. Schubert, L. C. Zilberman and E. Wofovitz, 'Fluid shear stress and the vascular endothelium: for better and for worse', *Prog.Biophys.Mol.Biol.*, vol. 81, pp. 177–199, 2003.

[70] R. S. Reneman, T. Arts and A. P. G. Hoeks, 'Wall shear stress–an important determinant of endothelial cell function and structure–in the arterial system in vivo. Discrepancies with theory.' *Journal of vascular research*, vol. 43, no. 3, pp. 251–69, 2006.

[71] P. F. Davies, 'Hemodynamic shear stress and the endothelium in cardiovascular pathophysiology', *Nature Clinical Practice Cardiovascular Medicine*, vol. 6, no. 1, pp. 16–26, 2008.

[72] P. F. Davies, J. a. Spaan and R. Krams, 'Shear Stress Biology of the Endothelium', *Annals of Biomedical Engineering*, vol. 33, no. 12, pp. 1714–1718, 2005.

[73] H. A. Himburg, D. M. Grzybowski, A. L. Hazel, J. A. LaMack, X.-M. Li and M. H. Friedman, 'Spatial comparison between wall shear stress measures and porcine arterial endothelial permeability.' *American journal of physiology. Heart and circulatory physiology*, vol. 286, no. 5, H1916–H1922, 2004.

[74] S. Chien, 'Molecular and mechanical bases of focal lipid accumulation in arterial wall', *Progress in Biophysics and Molecular Biology*, vol. 83, no. 2, pp. 131–151, 2003.

[75] K. S. Cunningham and A. I. Gotlieb, 'The role of shear stress in the pathogenesis of atherosclerosis', *Laboratory Investigation*, vol. 85, no. 1, pp. 9–23, 2005.

[76] J. Suo, D. E. Ferrara, D. Sorescu, R. E. Guldberg, W. R. Taylor and D. P. Giddens, 'Hemodynamic shear stresses in mouse aortas: implications for atherogenesis.' *Arteriosclerosis, thrombosis, and vascular biology*, vol. 27, no. 2, pp. 346–51, 2007.

[77] D. C. Chappell, S. E. Varner, R. M. Nerem, R. M. Medford and R. W. Alexander, 'Oscillatory Shear Stress Stimulates Adhesion Molecule Expression in Cultured Human Endothelium', *Circulation Research*, vol. 82, no. 5, pp. 532–539, 1998.

[78] J. Qiu, Y. Zheng, J. Hu, D. Liao, H. Gregersen, X. Deng, Y. Fan and G. Wang, 'Biomechanical regulation of vascular smooth muscle cell functions: from in vitro to in vivo understanding.' *Journal of the Royal Society, Interface / the Royal Society*, vol. 11, p. 20 130 852, 2014.

[79] C. L. Feldman, O. J. Ilegbusi, Z. Hu, R. Nesto, S. Waxman and P. H. Stone, 'Determination of in vivo velocity and endothelial shear stress patterns with phasic flow in human coronary arteries: A methodology to predict progression of coronary atherosclerosis', *American Heart Journal*, vol. 143, no. 6, pp. 931–939, 2002.

Chapter 2

Mouse models of atherosclerosis

2.1 Animal models of atherosclerosis

A variety of animal models has been used to study atherosclerosis. Up till now, no ideal animal model has been found that reflects all the stages found in human atherosclerosis. Next to the similar atherogenic process to humans, the ideal animal model would also permit an easy manipulation of the atherogenic process. The most extensively used animal models include: mice, rats, guinea pigs, pigs, hamsters, rabbits and non-human primates. Some of the main advantages and disadvantages of the most commonly used species are listed in table table 2.1. To induce the atherogenic process in these animal models some common methods are: cholesterol feeding [1]–[5] or surgically altered blood flow [6]–[8].

2.1.1 The rabbit

Rabbits do not develop atherosclerosis spontaneously but they are very susceptible to cholesterol manipulating diets [9]. The lipid metabolism of rabbits is much closer to humans than that of mice, explaining their extensive use [10]. The main disadvantage is that the lesions that rabbits develop are not as complex as the human atherosclerotic plaques. In comparison with mice, genetic manipulation of the rabbit is more difficult. Next to this, rabbits have a very low plasma level of hepatic lipase, which is an enzyme that modulates lipoprotein metabolism. Therefore, several studies support an anti-atherogenic role for this enzyme [11].

Table 2.1: Advantages and disadvantages of different animal models of atherosclerosis (adapted from [5] and [4]).

	Advantages	**Disadvantages**
Mouse	Easy breading Ease of genetic manipulation Low cost and maintenance Short generation time	No plaque instability✻ Monotypic HDL Small size → difficulties Limited complexity lesions
Rabbit	Good size Easy to keep and handle Cholesterol sensitive	Majority of circularing cholesterol is HDL Modest genetic modifications Hepatic lipase deficient
Pig	Human- like lipoprotein profile Humanoid lesions Experimental study of carotid stenting Size simplifies non-invasive measurements Vulnerable carotid plaques	Expensive Difficulties in care Longer time for diet induction No genetic modifications
Non-human Primates	Closest to human species Develop coronary lesions Spontaneous early stage lesions in some strains	Expensive No genetic modifications Ethical concerns Difficult to house and handle

✻ Except the recently developed ApoE$^{-/-}$ Fbn1$^{C1039G+/-}$ mouse model.

2.1.2 The pig

Pigs develop atherosclerosis spontaneously and this is further accelerated by feeding them an atherogenic diet. Their size makes it possible to harvest enough arterial material for analysis. The lipoprotein profile of pigs is similar to the human profile. 60% of the circulating lipoproteins are being transported as LDL in pigs which is close to the 63% in humans [4]. Next to this, both the cardiovascular system and the electro-physiological parameters of pigs closely resemble the human condition (more closely than the other laboratory animals except non-human primates). This makes it technically possible to perform surgical procedures including vascular stenting [12], [13], making it an ideal surgical model. Their main disadvantages are the relative long time for diet-induction and the high cost for their upkeep maintenance cost[4], [5].

2.1.3 Non-human primates

The non-human primates are attractive models for atherosclerosis because of their higher similarity to humans. Several different strains have been studied

with each of them their own advantages/specific results including: regression of atherosclerosis when put on a low-fat diet, more rapid atherosclerosis development, atherosclerosis development dependent on social status, spontaneous atherosclerosis development, fatal myocardial infarction, ... [14]–[16] However, there are some major disadvantages specific to this species. For example, ethical concerns with regard to their extinction hamper their usability. Next to this, the maintenance cost is very high, the experiments and atherosclerosis development take a long time. These are the main reasons why there is only a limited utility of non-human primates in the current research on atherosclerosis[4], [5].

2.2 Mouse models of atherosclerosis

The mouse has become the predominately used animal model for atherosclerosis research [17]. Compared to the large animal models mice are much cheaper to purchase, feed and house in appropriate conditions. This enables the use of a larger number of animals when this is advantageous or needed to get statistically robust data. Normally the atherosclerosis develops in a much shorter time frame for mice compared to bigger animals. More recently, this has been even further facilitated by the ability to genetically modify mice.

Similar like humans, mice have approximately 30.000 genes of which approximately 95% are shared with humans [18]. Since 2006, scientists have been working together in the Knockout Mouse Project, with the goal to develop a knockout mouse model for every gene. In a knockout mouse model, a specific gene is disabled. The goal of the Knockout Mouse Project is to produce a phenotype of 5000 knockout mice by 2016 [19]–[21]. Together with the high amount of different inbred strains that are available this provides a second major advantage. All these mice have different genetic backgrounds and thus present a unique means to link the different genes and their expression to their role in the atherogenic process. Thus the extensive knowledge about the mouse genome and the relatively easy genetic modification of mice play a crucial role in linking genetics with atherosclerosis.

Although these are all arguments in favour of the mouse as a model for atherosclerosis there are also some important differences between murine and human atherosclerosis (see table 2.2). First, a different haemodynamic environment is present with for example a much higher heart rate (HR) and much smaller dimensions for mice. Secondly, the lipid profile of mice is very different from the lipid profile of humans. Humans carry most of the plasma cholesterol on LDL while for mice this is mainly on HDL. For humans this HDL even has an atheroprotective effect. Furthermore, the murine lesions are showing less complex phenotypes and in most mouse models no spontaneous plaque rupture is present [9].

Table 2.2: Differences between mice and humans relevant for atherosclerosis (adapted from [5]).

	Mice	Humans
HR	> 300 bpm	70-100 bpm
Total plasma cholesterol	50-100 mg/dl (wild type)	150-300 mg/dl
Major lipoprotein	HDL	LDL
Development time	Months (genetically modified)	Years
Spontaneous rupture	no*	yes

* Except the recently developed ApoE$^{-/-}$ Fbn1$^{C1039G+/-}$ mouse model.

2.2.1 Surgically manipulated models

The current thesis studies the link between the WSS related to flow patterns and atherosclerosis development in mice. Specifically for this purpose a different approach for atherosclerosis research with mice as laboratory animals has been applied regularly in literature: the surgically manipulated flow models. The goal of these manipulations can be twofold: directly manipulating the WSS patterns and/or accelerating the atherosclerosis process.

In the arteriovenous fistula model, the CCA is connected directly, end-to-side, to the neighbouring vein resulting in an increased blood flow [22]. This model is used to study the influence of high levels of WSS. Next to this, ligation models of the CCA are commonly used in mice with complete CCA or partial ligation. Several partial ligation models have been described that (partially) ligate one or some arteries: CCA [7], [23], ECA [24]–[27], ICA[25]–[27] and occipital artery [27]. Depending on the ligation site, different zones with low and/or oscillatory shear stress and optionally vulnerable plaques occur. These models were used to study molecular mechanisms involving atherosclerotic plaque development.

Another approach is the insertion of a cast around the CCA. Several cast models with a different design were developed. Thüsen *et al.* developed the first constrictive cast which induced a 30% luminal stenosis in the common carotid artery (figure 2.1a). As a result, the WSS decreased upstream of the cast resulting in the rapid development of atherosclerosis. However, the induced plaques showed a relatively stable phenotype with low lipid, high smooth muscle cell and high collagen content [8], [28].

In the tapered cast model, developed by Cheng *et al.*, three different regimes of WSS are obtained: (i) a low WSS region upstream of the cast, (ii) an elevated WSS region inside the cast and (iii) a low and oscillatory WSS

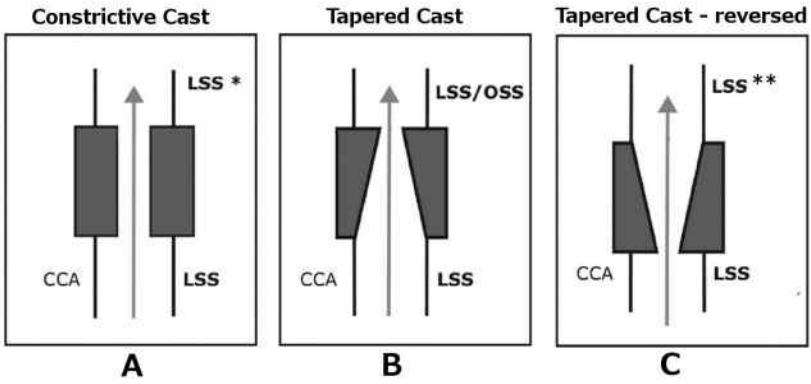

Figure 2.1: Different CCA casting methods used in mouse models. a) The constrictive cast with two low shear stress zones (LSS) (* level of WSS dependent on the degree of constriction). b) The tapered cast model with low shear stress (LSS) proximal and low and oscillatory shear stress (OSS) distal to the cast. c) The reversed tapering cast with low shear stress proximal and distal to the cast. (** only steady state simulations were performed so no information on oscillatory behaviour). Overview adapted from [8].

region downstream of the cast due to flow separation [29], [30] (figure 2.1b). Remarkably, the plaques in the proximal region were larger, showed more outward remodelling and contained more lipids and fewer smooth muscle cells. In this region intraplaque haemorrhage was observed. Therefore Cheng *et al.* concluded that a vulnerable plaque phenotype was present in the proximal region [8], [29], [30].

Another variation on the tapered cast was suggested by Mohri *et al.* They compared WSS patterns and uptake of macromolecules in the arterial wall for the previously described tapering cast in the conventional direction and a reversed implantation (figure 2.1c). The pattern of the macromolecule uptake was not reversed between both cases, suggesting that the underlying mechanism is not entirely explained by mechanic stresses in the arterial wall. On the other hand, for the reversed implantation case an elevated uptake was found in a wide downstream region without remarkable flow patterns in the computational fluid dynamics (CFD) simulations. This suggests that haemodynamic WSS cannot entirely explain the found patterns [31].

2.2.2 Different mouse strains used in atherosclerosis research

Similar to rats, mice are highly resistant to atherosclerosis and are thus, in principle, not the best animal model to model atherosclerosis. However, several inbred strains were developed with different degrees of susceptibility to atherosclerosis.

2.2.2.1 C57BL/6J

The C57BL/6J model is at the same time one of the strains most susceptible to diet-induced atherosclerosis and one of the most commonly used strains in laboratory animal research. One of the advantages is that a high quality sequence and analysis of the genome of this strain is available and published thanks to the Mouse Genomes Project [32], [33]. When they are fed a very high cholesterol diet, they develop atherosclerotic lesions that histologically differ from the human lesion [9]. Only the early stages of the atherosclerotic lesions such as fatty streaks can be induced [4]. Next to this, the location of the lesions is restricted to the aortic root, even after a prolonged feeding of the cholesterol high diet [17]. This limits the usability of this mouse model together with the fact that the plaques remain small in these mice.

2.2.2.2 LDLR$^{-/-}$

The low density lipoprotein receptor knockout (LDLR$^{-/-}$) mouse model is a model where the LDL receptor is knocked out. In humans, this mutation leads to a pronounced hypercholesterolemia with a dramatic phenotype usually resulting in a myocardial infarction in the second decade of life [17], [34]. In mice, this mutation blocks the clearance of the LDL through the LDL receptor, resulting to moderate LDL accumulations when on a normal chow diet and in severe LDL accumulations when on a western type diet. Compared to the apolipoprotein E knockout (ApoE$^{-/-}$) mouse (next section), this strain has a less severe phenotype [35]. The phenotype of the lesions in this mouse model is limited to AHA types I-IV [36].

2.2.2.3 ApoE$^{-/-}$

Apolipoprotein E (ApoE) is a glycoprotein that is synthesised in the liver, brain, and other tissues in both humans and mice [9]. This glycoprotein is present on the surface of several lipoproteins including very low density lipoprotein (VLDL) and HDL but not on the surface of LDL. The ApoE molecule is important for the lipoprotein metabolism and allows uptake in the liver.

In 1992, the ApoE$^{-/-}$ mouse model was generated by several groups, which was a breakthrough for the use of mice as a laboratory animal for atherogenesis [37]–[39]. The ApoE$^{-/-}$ mice have five times higher amount of plasma cholesterol levels compared to their littermates. Even more important, in C57BL/6J mice the highest amount of plasma cholesterol is present as HDL while for the ApoE$^{-/-}$ strain this has shifted to VLDL.

This mouse model is the most used mouse model in the present. An important factor is that this genetic manipulation has no effect on the fertility or birth weight compared to normal mice [40]. The progression of lesions

has been described when feeding either a normal chow diet or a western-type diet (figure 2.3). However, despite the genetic homogeneity and controlled condition, a considerable variation is present in atherosclerotic lesion size [35].

Similar to human plaques, the lesions in ApoE$^{-/-}$ mice tend to develop at vascular branching points. Complex lesions have been found in the aortic sinus, several regions of the aorta including the ascending region, the arch, and the renal area, and the innominate and coronary vessels [9], [17]. The precise locations have been mapped by Nakashima *et al.* for the ApoE$^{-/-}$ mouse model and by VanderLaan *et al.* for the LDLR$^{-/-}$ mouse model [41], [42]. The plaque locations for the ApoE$^{-/-}$ mouse model are shown in figure 2.2.

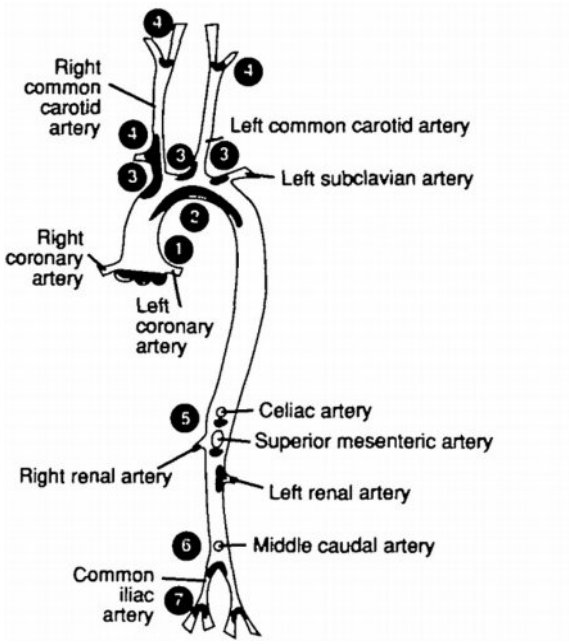

Figure 2.2: Atheroprone regions in the ApoE$^{-/-}$ mouse model vasculature: (1) aortic root, (2) lesser curvature of the aortic arch, (3) branches of the thoracic aorta, (4) carotid arteries, (5) principal branches of the abdominal aorta, (6) aortic bifurcation and (7) iliac arteries (reproduced from [41])

Still, caution has to be taken when translating results from murine plaque localisation studies to the human setting. In figure 2.2 it is clearly visible that plaques occur at the aortic root in ApoE$^{-/-}$ (and also in LDLR$^{-/-}$) mice. In humans this is not a common location for atherosclerosis [43], except perhaps for patients with familial hypercholesterolaemia [44]. When assessing the position of lesions relative to the branching point as a function of age in more

detail, Weinberg [45] described how human lesions (located at the intercostal branches of the aorta) progress from a downstream location (infancy) via a lateral location towards an upstream location (adult) based on experiments done by Sloop *et al.* [46]. At an old age, the lesions are all located all around the sidebranch (giving it the appearance of a volcano pattern) [45]. ApoE$^{-/-}$ mice predominantly show the volcano pattern, with plaque being present both up- and downstream from the sidebranch [43]. Unlike in humans, no change in pattern was observed with ageing in ApoE$^{-/-}$ mice [43], [45]. Both the presence of plaque in the aortic root in mice and the absence of changing lesion patterns with age show that there are important differences between plaque locations in mice and humans.

A diagram showing the evolution of the atherosclerotic plaques in ApoE$^{-/-}$ mice when on either a normal Chow diet or a western-type diet is shown in figure 2.3. The western-type diet accelerates the development of atherosclerotic plaques. And in contrast to C57BL/6J mice, that only develop early stage foam cell lesions, the ApoE$^{-/-}$ mouse model also develops more advanced fibrous plaques and plaques showing necrotic cores [36], corresponding to type V plaques (AHA classification) [36]. Spontaneous rupture and thrombus formation of complex plaques, which are commonly seen in humans, have not been demonstrated for ApoE$^{-/-}$ mice or at very low incidence rates (and neither for the C57BL/6J or LDLR$^{-/-}$ mice). Only in the brachiocephalic artery spontaneous plaque rupture has been reported (ApoE$^{-/-}$ when on a high fat diet) [40].

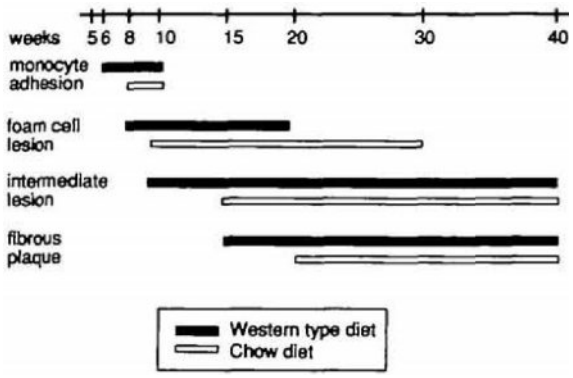

Figure 2.3: Diagram showing plaque development in ApoE$^{-/-}$ mice (reproduced from [41])

Next to the development of atherosclerosis, the knockout of the ApoE gene also results in: elevated cardiac output, elevated pulse wave velocity, reduced vascular elasticity, reduced vascular compliance and cardiac hypertrophy [47]

2.2.2.4 *ApoE$^{-/-}$ Fbn1$^{C1039G+/-}$*

The most severe limitation of the previously described mouse models is that spontaneous plaque rupture does not occur (regularly). Therefore, researchers had to resort to mechanical injury of the arterial wall or surgical methods to achieve plaque rupture [48]–[50] (for the surgical methods see section 2.2.1).

This led to the development of a new atherosclerotic mouse model at the University of Antwerp. For this purpose, ApoE$^{-/-}$ mice were crossbred with C1039G+/- mice to obtain mice showing both mutations (apolipoprotein E deficient and fbn1 heterogeneous (ApoE$^{-/-}$ Fbn1$^{C1039G+/-}$)). The C1039G+/- mutation in the fibrillin-1 (Fbn1) gene leads to Marfan syndrome, a genetic disorder of the connective tissue that results in fragmentation of the elastic fibres [51]. In humans, this leads to decreased arterial compliance, an increased risk for tear and rupture, aortic dilatation, bone overgrowth, joint laxity and scoliosis [52].

Both ageing and atherosclerosis lead to structural and functional changes in the elastic fibres. Similarly, C1039G+/- mutation leads to a fragmentation of the elastic Fbn1 fibres and thus an increased stiffness. This increased arterial stiffness is an important predictor of cardiovascular events. Combining the atheroprone ApoE$^{-/-}$ mice with this model of increased arterial stiffness resulted in a mouse model with a more severe atherosclerotic phenotype compared to the ApoE$^{-/-}$ mouse model [51].

The ApoE$^{-/-}$ Fbn1$^{C1039G+/-}$ mouse model develops highly unstable plaques with plaque rupture. This mouse model also shows many features of the human end-stage atherosclerosis (listed in section 1.2.4 on page 18): thin fibrous cap with loss of collagen fibres, presence of intraplaque microvessels and haemorrhage, outward remodelling, enlarged necrotic core resulting in plaque rupture, myocardial infarction, stroke and sudden death. Plaque rupture was observed in this study [53] in 50 % of the brachiocephalic arteries and 70 % of the proximal ascending aortas. Moreover, presence of fibrin deposits and thrombi, suggesting plaque rupture, were found in the coronary and carotid arteries[53]. Therefore, this mouse model is well suited for further research on the mechanisms of plaque rupture and potential therapeutic targets [51], [53]–[56].

2.3 The murine cardiovascular system

The mouse heart is about the same size as a pencil eraser and weighs ~100-200 mg [57]. The resting HR for mice is between 500 and 600 bpm (above 750 bpm is considered non-physiological)[58]. The challenges for measurements in the murine cardiovascular system become clear when comparing an average

mouse (of ~25g) with a dog of 25 kg. The body weight decreases 1000 fold, the surface area decreases 100 fold and the linear dimensions decrease 10 times [58].

Scaling laws have been proposed to link the different values of certain haemodynamic parameters between different animals. These allometric laws relate the body mass (M_b) with specific haemodynamic parameters such as for example the HR (see equation (2.1)). Body-mass exponents (c) for different haemodynamic parameters are listed in table 2.3.

$$HR \propto {M_b}^c \tag{2.1}$$

For the current thesis, these body-mass exponents, described by Weinberg *et al.* [59] (for the aorta), can be used to indicate the main differences in the haemodynamic environment between mice and humans before any numerical modelling has been performed. The Reynolds number describes the relative importance of the inertial forces compared to the viscous forces [60]. The body-mass exponent indicates that the murine Reynolds numbers are lower compared to the human blood flow. Therefore, the viscous forces are more important in the murine blood flow. This will lead to a more stabilised flow with less perturbations and recirculations (see chapters 8 and 9).

The Womersley number describes the unsteady nature of flow [61]. The lower Womersley number in mice indicates that the transient inertial forces are smaller (in comparison to the viscous forces) than in the human haemodynamics.

Langille approximated the WSS body-mass exponent to be -0.2 (based on body-mass exponents of 0.8 and 1/3 for resting blood flow and arterial radius

Table 2.3: Body-mass exponents for different haemodynamic parameters (adapted from [59]). The body-exponent is defined in equation (2.1).

Haemodynamic parameter	Body-mass exponent, c
Cardiac output✳	0.75
Heart rate✳	-025
Aortic diameter✳	0.375
Mean aortic blood velocity✦	0
TAWSS✦	-0.375
Aortic Reynolds number✦	0.375
Aortic Womersley parameter✦	0.25

✳ Literature values (see [59])
✦ Derived from the first three entries

respectively) [62]. Westerhof *et al.* on the other hand, approximated the WSS body-mass exponent to be -0.25 (based on c of 3/4 and 1/3 for blood flow and radius respectively) [63]. Based on the c values for cardiac output and aortic diameter in table 2.3, Weinberg *et al.* found the c for time averaged wall shear stress (TAWSS) to be -0.375 [59]. The TAWSS is the average WSS over a complete heart cycle. As described by Weinberg *et al.*, this means that the expected TAWSS in mice is about 20 times bigger compared to the TAWSS found in humans. Finally, Greve *et al.* experimentally found a value for the WSS c of -0.38 [64], which gives an 18 fold difference in WSS between mice and humans. Although the exact c-value differs between those publications, a substantially higher WSS value compared to human WSS values can thus be expected.

The aortic arch with the main arteries going to the head is shown in figure 2.4. First the brachiocephalic trunk branches off the arch of the aorta. Downstream, this artery splits in the right subclavian and the right common carotid arteries. On the left side, the left CCA and the left subclavian artery both branch off the aorta directly.

Both common carotid arteries split further downstream in the internal and the external carotid artery (see figure 2.5). This bifurcation is the main interest in the current research. The external carotid arteries mainly supply blood to the face and the neck. The internal carotid arteries mainly supply blood to the brain through the circle of Willis. In mice the blood flow to the brain only accounts for ~3.5% of the cardiac output (for humans this is ~14%). The lower amount of blood flowing to the brain is likely due to the smaller brain size per body weight[57].

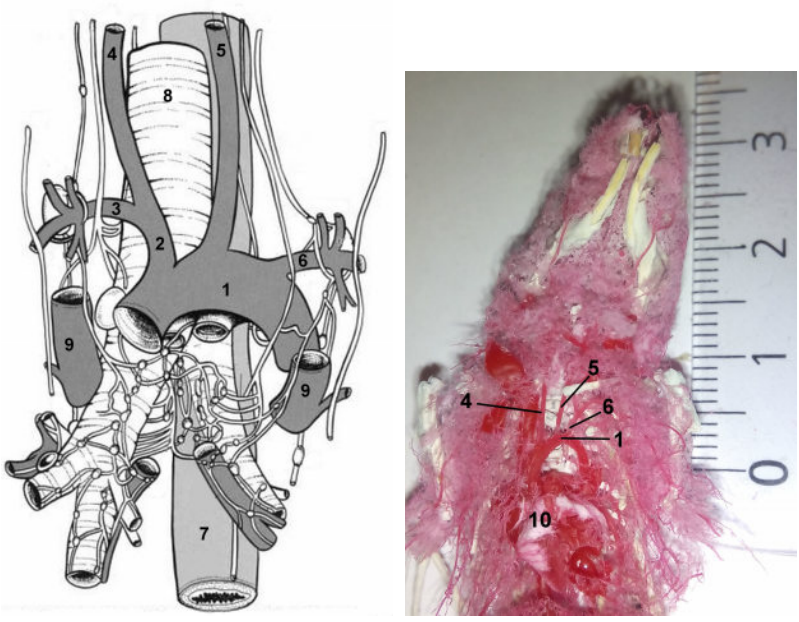

(a) Schematic **(b)** Photo of a cast

1. Aortic Arch
2. Brachiocephalic Trunk
3. Right Subclavian Artery
4. Right Common Carotid Artery
5. Left Common Carotid Artery
6. Left Subclavian Artery
7. Esophagus
8. Trachea
9. Internal Jugular Vein
10. Heart

Figure 2.4: Ventral view of the arteries at the aortic arch. (a) Schematic representation of the main arteries (adapted from [65]). (b) Photo of a corrosion cast of the arterial network.

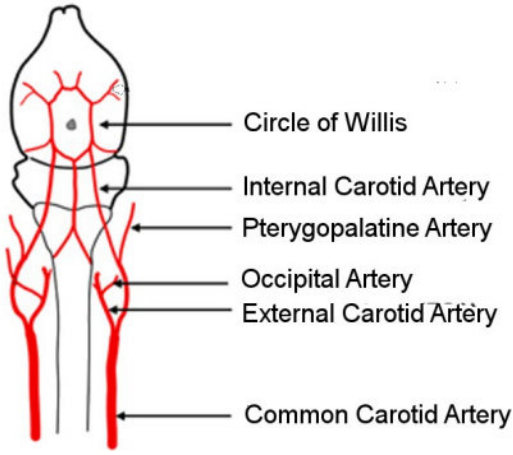

Figure 2.5: Schematic overview of the murine carotid arteries supplying the brain with blood (adapted from [66]).

Bibliography Chapter 2

[1] R. G. Gerrity, 'The role of the monocyte in atherogenesis: II. Migration of foam cells from atherosclerotic lesions.' *The American journal of pathology*, vol. 103, no. 2, pp. 191–200, 1981.

[2] S. J. Daley, E. E. Herderick, J. F. Cornhill and K. A. Rogers, 'Cholesterol-fed and casein-fed rabbit models of atherosclerosis. Part 1: Differing lesion area and volume despite equal plasma cholesterol levels', *Arteriosclerosis, Thrombosis, and Vascular Biology*, vol. 14, no. 1, pp. 95–104, 1994.

[3] G. S. Getz, 'Diet and Murine Atherosclerosis', *Arteriosclerosis, Thrombosis, and Vascular Biology*, vol. 26, no. 2, pp. 242–249, 2005.

[4] L. Xiangdong, L. Yuanwu, Z. Hua, R. Liming, L. Qiuyan and L. Ning, 'Animal models for the atherosclerosis research: a review', *Protein & Cell*, vol. 2, no. 3, pp. 189–201, 2011.

[5] G. S. Getz and C. a. Reardon, 'Animal Models of Atherosclerosis', *Arteriosclerosis, Thrombosis, and Vascular Biology*, vol. 32, no. 5, pp. 1104–1115, 2012.

[6] A. Kamiya and T. Togawa, 'Adaptive regulation of wall shear stress to flow change in the canine carotid artery.' *The American journal of physiology*, vol. 239, no. 1, H14–H21, 1980.

[7] A. Kumar and V. Lindner, 'Remodeling With Neointima Formation in the Mouse Carotid Artery After Cessation of Blood Flow', *Arteriosclerosis, Thrombosis, and Vascular Biology*, vol. 17, no. 10, pp. 2238–2244, 1997.

[8] L. C. Winkel, A. Hoogendoorn, R. Xing, J. J. Wentzel and K. Van der Heiden, 'Animal models of surgically manipulated flow velocities to study shear stress-induced atherosclerosis', *Atherosclerosis*, vol. 241, no. 1, pp. 100–110, 2015.

[9] J. Jawien, R. Nastalek, R. Korbut, J. Jawień, P. Nastałek and R. Korbut, 'Mouse models of experimental atherosclerosis', *journal of physiology and pharmacology*, vol. 55, no. 3, pp. 503–517, 2004.

[10] L.-M. Houdebine, 'The Mouse as an Animal Model for Human Diseases', in *The Laboratory Mouse*, Elsevier, 2004, pp. 97–110.

[11] S. Santamarina-Fojo, H. González-Navarro, L. Freeman, E. Wagner and Z. Nong, *Hepatic lipase, lipoprotein metabolism, and atherogenesis*, 2004.

[12] T. Kuehne, M. Saeed, C. B. Higgins, K. Gleason, G. A. Krombach, O. M. Weber, A. J. Martin, D. Turner, D. Teitel and P. Moore, 'Endovascular stents in pulmonary valve and artery in swine: feasibility study of MR imaging-guided deployment and postinterventional assessment.' *Radiology*, vol. 226, no. 2, pp. 475–81, 2003.

[13] P. H. Rolland, A.-B. Charifi, C. Verrier, H. Bodard, A. Friggi, P. Piquet, G. Moulin and J.-M. Bartoli, 'Hemodynamics and Wall Mechanics after Stent Placement in Swine Iliac Arteries: Comparative Results from Six Stent Designs1', *Radiology*, vol. 213, no. 1, pp. 229–246, 1999.

[14] S. B. Andrus and G. V. Mann, 'Xanthomatosis and atherosclerosis produced by diet in an adult rhesus monkey.' *The Journal of laboratory and clinical medicine*, vol. 48, no. 4, pp. 533–50, 1956.

[15] M. L. Armstrong and D. D. Heistad, 'Animal models of atherosclerosis.' *Atherosclerosis*, vol. 85, no. 1, pp. 15–23, 1990.

[16] C. A. Shively, T. C. Register and T. B. Clarkson, 'Social Stress, Visceral Obesity, and Coronary Artery Atherosclerosis in Female Primates', *Obesity*, vol. 17, no. 8, pp. 1513–1520, 2009.

[17] A. Daugherty, 'Mouse models of atherosclerosis.' *The American journal of the medical sciences*, vol. 323, no. 1, pp. 3–10, 2002.

[18] E. C. Bryda, 'The Mighty Mouse: The Impact of Rodents on Advances in Biomedical Research', *Missouri medicine*, vol. 110, no. 3, pp. 207–211, 2013.

[19] C. P. Austin, J. F. Battey, A. Bradley, M. Bucan, M. Capecchi, F. S. Collins, W. F. Dove, G. Duyk, S. Dymecki, J. T. Eppig, F. B. Grieder, N. Heintz, G. Hicks, T. R. Insel, A. Joyner, B. H. Koller, K. C. K. Lloyd, T. Magnuson, M. W. Moore, A. Nagy *et al.*, 'The Knockout Mouse Project', *Nature Genetics*, vol. 36, no. 9, pp. 921–924, 2004.

[20] R. E. Braun, S. Murray, K. Svenson, R. Taft and J. Ndukum, *KNOCKOUT MOUSE PROJECT (KOMP)*, `https://www.jax.org/research-and-faculty/tools/knockout-mouse-project`, 2015.

[21] UCDavis, *KOMP Repository: Knockout Mouse Project*, `https://www.komp.org/index.php`, 2015.

[22] Y. Castier, S. Lehoux, Y. Hu, G. Foteinos, G. Fonteinos, a. Tedgui and Q. Xu, 'Characterization of neointima lesions associated with arteriovenous fistulas in a mouse model', *Kidney International*, vol. 70, no. 2, pp. 315–320, 2006.

[23] P. C. CHANG, H. L. WU, H. C. LIN, K. C. WANG and G. Y. SHI, 'Human plasminogen kringle 1-5 reduces atherosclerosis and neointima formation in mice by suppressing the inflammatory signaling pathway', *Journal of Thrombosis and Haemostasis*, vol. 8, no. 1, pp. 194–201, 2010.

[24] A. W. Holt and D. A. Tulis, 'Experimental Rat and Mouse Carotid Artery Surgery: Injury and Remodeling Studies', *ISRN Minimally Invasive Surgery*, vol. 2013, pp. 1–10, 2013.

[25] D. Nam, C.-W. Ni, A. Rezvan, J. Suo, K. Budzyn, A. Llanos, D. G. Harrison, D. P. Giddens and H. Jo, 'A Model of Disturbed Flow-Induced Atherosclerosis in Mouse Carotid Artery by Partial Ligation and a Simple Method of RNA Isolation from Carotid Endothelium', *Journal of Visualized Experiments*, no. 40, 2010.

[26] D. Nam, C.-W. Ni, A. Rezvan, J. Suo, K. Budzyn, A. Llanos, D. Harrison, D. Giddens and H. Jo, 'Partial carotid ligation is a model of acutely induced disturbed flow, leading to rapid endothelial dysfunction and atherosclerosis', *AJP: Heart and Circulatory Physiology*, vol. 297, no. 4, H1535–H1543, 2009.

[27] C. J. Sullivan, 'Flow-Dependent Remodeling in the Carotid Artery of Fibroblast Growth Factor-2 Knockout Mice', *Arteriosclerosis, Thrombosis, and Vascular Biology*, vol. 22, no. 7, pp. 1100–1105, 2002.

[28] J. H. von der Thüsen, T. J. van Berkel and E. a. Biessen, 'Induction of rapid atherogenesis by perivascular carotid collar placement in apolipoprotein E-deficient and low-density lipoprotein receptor-deficient mice.' *Circulation*, vol. 103, no. 8, pp. 1164–1170, 2001.

[29] C. Cheng, R. de Crom, R. van Haperen, F. Helderman, B. Mousavi Gourabi, L. C. a. van Damme, S. W. Kirschbaum, C. J. Slager, A. F. W. van der Steen and R. Krams, 'The role of shear stress in atherosclerosis: action through gene expression and inflammation?', *Cell biochemistry and biophysics*, vol. 41, no. 2, pp. 279–294, 2004.

[30] C. Cheng, D. Tempel, R. van Haperen, A. van der Baan, F. Grosveld, M. J. A. P. Daemen, R. Krams and R. de Crom, 'Atherosclerotic lesion size and vulnerability are determined by patterns of fluid shear stress.' *Circulation*, vol. 113, no. 23, pp. 2744–2753, 2006.

[31] Z. Mohri, E. M. Rowland, L. A. Clarke, A. De Luca, V. Peiffer, R. Krams, S. J. Sherwin and P. D. Weinberg, 'Elevated Uptake of Plasma Macromolecules by Regions of Arterial Wall Predisposed to Plaque Instability in a Mouse Model', *PLoS ONE*, vol. 9, no. 12, e115728, 2014.

[32] D. J. Adams, A. G. Doran, J. Lilue and T. M. Keane, 'The Mouse Genomes Project: a repository of inbred laboratory mouse strain genomes.' *Mammalian genome : official journal of the International Mammalian Genome Society*, 2015.

[33] R. H. Waterston, K. Lindblad-Toh, E. Birney, J. Rogers, J. F. Abril, P. Agarwal, R. Agarwala, R. Ainscough, M. Alexandersson, P. An, S. E. Antonarakis, J. Attwood, R. Baertsch, J. Bailey, K. Barlow, S. Beck, E. Berry, B. Birren, T. Bloom, P. Bork *et al.*, 'Initial sequencing and comparative analysis of the mouse genome.' *Nature*, vol. 420, no. 6915, pp. 520–562, 2002.

[34] M. S. Brown and J. L. Goldstein, 'Lipoprotein receptors: therapeutic implications.' *Journal of hypertension. Supplement : official journal of the International Society of Hypertension*, vol. 8, no. 1, S33–S36, 1990.

[35] J. F. Bentzon and E. Falk, 'Atherosclerotic lesions in mouse and man: is it the same disease?', *Current opinion in lipidology*, vol. 21, no. 5, pp. 434–440, 2010.

[36] S. C. Whitman, 'A practical approach to using mice in atherosclerosis research.' *The Clinical biochemist. Reviews*, vol. 25, no. 1, pp. 81–93, 2004.

[37] J. a. Piedrahita, S. H. Zhang, J. R. Hagaman, P. M. Oliver and N. Maeda, 'Generation of mice carrying a mutant apolipoprotein E gene inactivated by gene targeting in embryonic stem cells.' *Proceedings of the National Academy of Sciences of the United States of America*, vol. 89, no. 10, pp. 4471–4475, 1992.

[38] N. Maeda, *Development of apolipoprotein E-deficient mice*, 2011.

[39] A. S. Plump, J. D. Smith, T. Hayek, K. Aalto-Setälä, A. Walsh, J. G. Verstuyft, E. M. Rubin and J. L. Breslow, 'Severe hypercholesterolemia and atherosclerosis in apolipoprotein E-deficient mice created by homologous recombination in ES cells.' *Cell*, vol. 71, no. 2, pp. 343–353, 1992.

[40] A. R. Bond and C. L. Jackson, 'The fat-fed apolipoprotein E knockout mouse brachiocephalic artery in the study of atherosclerotic plaque rupture.' *Journal of biomedicine & biotechnology*, vol. 2011, p. 379 069, 2011.

[41] Y. Nakashima, A. S. Plump, E. W. Raines, J. L. Breslow and R. Ross, 'ApoE-deficient mice develop lesions of all phases of atherosclerosis throughout the arterial tree', *Arteriosclerosis, Thrombosis, and Vascular Biology*, vol. 14, no. 1, pp. 133–140, 1994.

[42] P. A. VanderLaan, 'Site Specificity of Atherosclerosis: Site-Selective Responses to Atherosclerotic Modulators', *Arteriosclerosis, Thrombosis, and Vascular Biology*, vol. 24, no. 1, pp. 12–22, 2004.

[43] C. J. McGillicuddy, M. J. Carrier and P. D. Weinberg, 'Distribution of lipid deposits around aortic branches of mice lacking LDL receptors and apolipoprotein E.' *Arteriosclerosis, thrombosis, and vascular biology*, vol. 21, pp. 1220–1225, 2001.

[44] S. Ishibashi, J. L. Goldstein, M. S. Brown, J. Herz and D. K. Burns, 'Massive xanthomatosis and atherosclerosis in cholesterol-fed low density lipoprotein receptor-negative mice.' *Journal of Clinical Investigation*, vol. 93, no. 5, pp. 1885–1893, 1994.

[45] P. D. Weinberg, 'Disease patterns at arterial branches and their relation to flow.' *Biorheology*, vol. 39, no. 3-4, pp. 533–7, 2002.

[46] G. D. Sloop, R. S. Perret, J. S. Brahney and M. Oalmann, 'A description of two morphologic patterns of aortic fatty streaks, and a hypothesis of their pathogenesis', *Atherosclerosis*, vol. 141, no. 1, pp. 153–160, 1998.

[47] C. J. Hartley, A. K. Reddy, S. Madala, B. Martin-McNulty, R. Vergona, M. E. Sullivan, M. Halks-Miller, G. E. Taffet, L. H. Michael, M. L. Entman and Y. X. Wang, 'Hemodynamic changes in apolipoprotein E-knockout mice.' *American journal of physiology. Heart and circulatory physiology*, vol. 279, no. 5, H2326–H2334, 2000.

[48] G. S. van Bochove, R. Straathof, R. Krams, K. Nicolay and G. J. Strijkers, 'MRI-determined carotid artery flow velocities and wall shear stress in a mouse model of vulnerable and stable atherosclerotic plaque.' *Magnetic Resonance Materials in Physics, Biology and Medicine*, vol. 23, no. 2, pp. 77–84, 2010.

[49] Y.-C. Chen, A. V. Bui, J. Diesch, R. Manasseh, C. Hausding, J. Rivera, I. Haviv, A. Agrotis, N. M. Htun, J. Jowett, C. E. Hagemeyer, R. D. Hannan, A. Bobik and K. Peter, 'A Novel Mouse Model of Atherosclerotic Plaque Instability for Drug Testing and Mechanistic/Therapeutic Discoveries Using Gene and microRNA Expression Profiling.' *Circulation research*, vol. 113, no. 3, pp. 252–265, 2013.

[50] M. Ni, W. Q. Chen and Y. Zhang, 'Animal models and potential mechanisms of plaque destabilisation and disruption.' *Heart*, vol. 95, no. 17, pp. 1393–1398, 2009.

[51] J. L. Van Herck, G. R. De Meyer, W. Martinet, C. E. Van Hove, K. Foubert, M. H. Theunis, S. Apers, H. Bult, C. J. Vrints and A. G. Herman, 'Impaired Fibrillin-1 Function Promotes Features of Plaque Instability in Apolipoprotein E-Deficient Mice', *Circulation*, vol. 120, no. 24, pp. 2478–2487, 2009.

[52] H. C. Dietz, 'Marfan Syndrome', in *GeneReviews*, 15, R. A. Pagon, M. P. Adam, H. H. Ardinger, S. E. Wallace, A. Amemiya, L. J. Bean, T. D. Bird, C.-T. Fong, R. J. Smith and K. Stephens, Eds., Seattle, 2001.

[53] C. Van der Donckt, J. L. Van Herck, D. M. Schrijvers, G. Vanhoutte, M. Verhoye, I. Blockx, A. Van Der Linden, D. Bauters, H. R. Lijnen, J. C. Sluimer, L. Roth, C. E. Van Hove, P. Fransen, M. W. Knaapen, A.-S. A.-S. Hervent, G. W. De Keulenaer, H. Bult, W. Martinet, A. G. Herman and G. R. Y. De Meyer, 'Elastin fragmentation in atherosclerotic mice leads to intraplaque neovascularization, plaque rupture, myocardial infarction, stroke, and sudden death.' *European heart journal*, vol. 36, no. 17, pp. 1049–1058, 2014.

[54] C. Van der Donckt, L. Roth, G. Vanhoutte, I. Blockx, D. Bink, K. Ritz, I. Pintelon, J.-P. Timmermans, D. Bauters, W. Martinet, M. Daemen, M. Verhoye and G. R. Y. De Meyer, 'Fibrillin-1 impairment enhances blood–brain barrier permeability and xanthoma formation in brains of apolipoprotein E-deficient mice', *Neuroscience*, vol. 295, pp. 11–22, 2015.

[55] L. Roth, D. Van Dam, C. Van der Donckt, D. M. Schrijvers, K. Lemmens, I. Van Brussel, P. P. De Deyn, W. Martinet and G. R. Y. De Meyer, 'Impaired gait pattern as a sensitive tool to assess hypoxic brain damage in a novel mouse model of atherosclerotic plaque rupture', *Physiology & Behavior*, vol. 139, pp. 397–402, 2015.

[56] L. Roth, M. Rombouts, D. M. Schrijvers, K. Lemmens, G. W. De Keulenaer, W. Martinet and G. R. De Meyer, 'Chronic intermittent mental stress promotes atherosclerotic plaque vulnerability, myocardial infarction and sudden death in mice', *Atherosclerosis*, vol. 242, no. 1, pp. 288–294, 2015.

[57] V. Komarek, 'Normative Biology, Husbandry, and Models - Mouse Physiology', in *The Mouse in Biomedical Research*, II, vol. III, Elsevier, 2007, ch. 2, pp. 23–90.

[58] L. H. Michael, G. E. Taffet, N. G. Frangogiannis, M. L. Entman and C. J. Hartley, 'The Cardiovascular System', in *The Laboratory Mouse*, 2004, pp. 207–224.

[59] P. D. Weinberg and C. Ross Ethier, 'Twenty-fold difference in hemodynamic wall shear stress between murine and human aortas', *Journal of Biomechanics*, vol. 40, no. 7, pp. 1594–1598, 2007.

[60] O. Reynolds, 'On the Dynamical Theory of Incompressible Viscous Fluids and the Determination of the Criterion', *Philosophical Transactions of the Royal Society A: Mathematical, Physical and Engineering Sciences*, vol. 186, pp. 123–164, 1895.

[61] J. R. Womersley, 'Method for the calculation of velocity, rate of flow and viscous drag in arteries when the pressure gradient is known', *The Journal of Physiology*, vol. 127, no. 3, pp. 553–563, 1955.

[62] B. L. Langille, 'Remodeling of developing and mature arteries: endothelium, smooth muscle, and matrix.' *Journal of cardiovascular pharmacology*, vol. 21 Suppl 1, S11–7, 1993.

[63] N. Westerhof, N. Stergiopulos and M. I. Noble, 'Snapshots of Hemodynamics: An Aid for Clinical Research and Graduate Education', ser. Basic Science for the Cardiologist 1. Boston, MA: Springer US, 2005, vol. 18.

[64] J. M. Greve, A. S. Les, B. T. Tang, M. T. Draney Blomme, N. M. Wilson, R. L. Dalman, N. J. Pelc and C. a. Taylor, 'Allometric scaling of wall shear stress from mice to humans: quantification using cine phase-contrast MRI and computational fluid dynamics.' *American journal of physiology. Heart and circulatory physiology*, vol. 291, no. 4, H1700–8, 2006.

[65] V. Komárek, 'Normative Biology, Husbandry, and Models - Gross Anatomy', in *The Mouse in Biomedical Research*, 2007, ch. 1, pp. 1–22.

[66] O. Engel, S. Kolodziej, U. Dirnagl and V. Prinz, *Modeling stroke in mice - middle cerebral artery occlusion with the filament model.* 2011.

Chapter 3

Imaging atherosclerosis in mice

3.1 Introduction

In the current chapter, the preclinical imaging techniques that were applied during the current work are introduced: ultrasound (US) and micro-computed tomography (μCT) imaging. For both imaging techniques the basic imaging principles are explained.

3.2 Ultrasound imaging in mice

The current section gives an overview of the physical principles and the different imaging modalities in ultrasound (US) imaging. This part is mainly based on these sources [*] [†] [‡] [§].

3.2.1 General US principle

US imaging is a non-ionising imaging technique that uses acoustic waves beyond the audible range. Medical US is similar to radar systems, where

[*] A. Swillens, 'A multiphysics model for improving the ultrasonic assessment of large arteries', PhD thesis, Ghent University, 2010

[†] J. E. Aldrich, 'Basic physics of ultrasound imaging', *Critical Care Medicine*, vol. 35, no. Suppl, S131–S137, 2007

[‡] R. W. Cootney, 'Ultrasound Imaging: Principles and Applications in Rodent Research', *ILAR Journal*, vol. 42, no. 3, pp. 233–247, 2001

[§] V. Chan and A. Perlas, 'Basics of Ultrasound Imaging', in *Atlas of Ultrasound-Guided Procedures in Interventional Pain Management*, S. N. Narouze, Ed., New York, NY: Springer New York, 2011, ch. 2, pp. 13–20

information is gathered from wave propagation [5]. Most echo imaging is performed based on the pulse-echo imaging principle, with the working principle schematically shown in figure 3.1 [1], [5], [6].

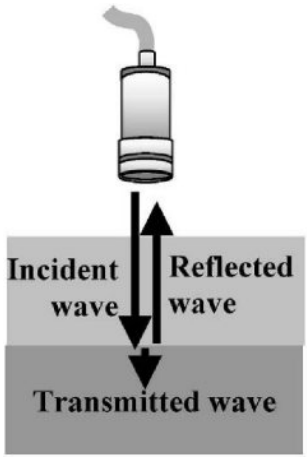

Figure 3.1: The general principle of pulse-echo ultrasound imaging. The transducer emits an ultrasonic wave. These waves travel through the tissues and get (partially) reflected back to the transducer (reproduced from [6]).

The imaging starts with the transducer, an array of piezoelectric crystals that convert electrical energy in mechanical energy (the reversed piezoelectric effect). This result in the emitting of longitudinal pressure pulses at ultrasonic frequency (typical US frequencies for applications in human imaging range from 2MHz to 10MHz [2]), but frequencies go up to 50 MHz for imaging in small animals. The speed of these waves (c) is determined by the compressibility (κ) and the density (ρ) of the tissue it travels through via equation:

$$c = \sqrt{\frac{1}{\rho\kappa}} \tag{3.1}$$

For most soft tissues this wave speed is around 1540m/s. When the ultrasonic waves travel through the tissue and encounter a change in acoustic impedance Z (Z=ρc with c the wave velocity), a part of the wave is reflected back towards the probe because of reflection and scattering. In figure 3.1, schematically two tissues with a different acoustic impedance (different gray values) are plotted. At the boundary between both tissues, the wave is (partially) reflected.

The reflected wave arrives back at the transducer under the form of a radio-frequent signal (in the frequency range normally used for radio communication). The transducer then acts as a receiver and converts the radio-frequent signal to an electric signal. The time delay (t) between the

emitted and received wave is related to the depth (d) of the reflection/scatter site using (with c the wave speed):

$$d = \frac{c\,t}{2} \tag{3.2}$$

Finally adequate processing is used to convert the radio-frequent signal in an US image.

During the transmit phase the transducer generates a signal that consists of two or three sound cycles with the same frequency. After this pulse, the transducer has to wait for the pulse to travel through the tissue, to be reflected back and to be received before the next pulse is sent. The pulse repetition frequency (PRF), are the number of pulses sent per unit of time and for normal medical applications the PRF ranges from 1 to 10 kHz [4]. In comparison to humans, mice have a heart rate that is about 10 times higher and the cardiovascular structures are about 10 times smaller (chapter 2). As a result the required temporal resolution is also higher compared to clinical imaging. The frame rate is mainly limited by the time that the ultrasonic waves need to travel through the tissue. Theoretically, the smaller imaging depth can make up for the higher frame rate needed [7].

3.2.2 Interaction between ultrasonic waves and tissue

Figure 3.2 summarises different interactions between tissue and ultrasonic waves:

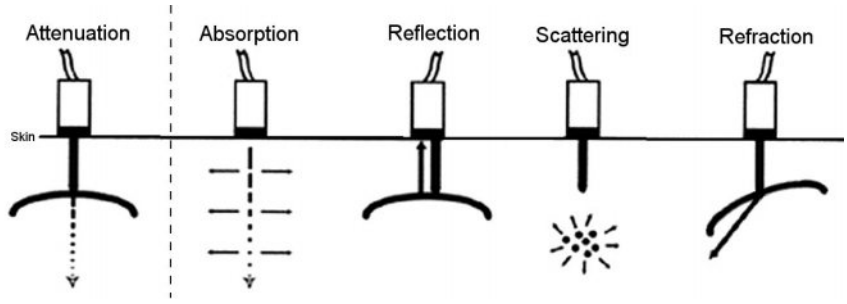

Figure 3.2: Different interactions between US waves and tissue (adapted from [8])

- **Attenuation** is the energy loss occurring when an ultrasonic beam propagates through a heterogeneous medium. Absorption, reflection, scattering and refraction are four mechanisms that divert energy of the incident beam and thus all four of them attribute to the attenuation of the beam. Overall, the attenuation of the beam is exponentially related to the frequency of the ultrasonic wave and the image depth.

- **Absorption** is the conversion of wave motion into heat and is probably the most important mechanism for attenuation.

- **Reflection** occurs when the wave reaches an interface between two objects that have a different acoustic impedance. For (specular) reflection to occur, these objects need to be bigger than the wave length of the pulse and need to have a relatively smooth surface. When the difference in acoustic impedance is small, only a small part of the energy will be reflected and most of the wave will propagate further into the tissue. If the difference in acoustic impedance is high, most of the US waves will be reflected as is the case for example when a wave travels from soft tissue to bone. Because almost the entire wave is reflected, no transmission occurs and a shadow is present in the image behind the bone. Specular reflection has a preferential direction. For beams with a normal angle of incidence, the wave is reflected back. If the incidence angle is different from 90°, the reflected beam leaves at an angle equal to the angle of incidence (similar to the reflection of light in a mirror). In this case, the reflected beam can be directed away from be transducer.

- **Scattering** occurs when the objects with a different acoustic impedance are smaller than the wave length of the pulse. Scattering is a more multi-directional phenomenon compared to reflection. Due to this scattering the intensity of the beam is reduced.

- **Refraction** is the change of direction of the beam after hitting an in interface between to tissues with a different wave speed. In medical applications refractions are most prominent at fat/soft tissue interfaces (c_{fat}~1450m/s and $c_{soft\ tissue}$~1540m/s) [4].

3.2.3 Different US imaging modalities

There are different imaging modes that can be obtained, depending on the processing of the signal measured with the transducer.

- **B-mode imaging** (Brightness Mode) (figure 3.3a): a view of the anatomical structures in the imaging plane.

- **Colour Doppler imaging** (figure 3.3b): the (blood flow) velocity field is plotted in a 2D colour frame. The velocity magnitude in the direction of the acoustic pulse (meaning the velocity in the direction from/to the transducer) is coloured according to the magnitude. By convention blue is flow away from the probe and red flow towards the probe.

- **M-mode imaging** (Motion Mode) (figure 3.3c): the variation over time of a single scan line. This mode can for example be used to quantify the distension of an artery.

- **Pulsed Doppler imaging** (figure 3.3d): the velocity of the scatterers (mainly red blood cells) in the direction defined by the pulse wave in a small control volume. The velocity in another direction (within the image plane) can be calculated with a goniometric correction factor (limited by a range of 30-40°).

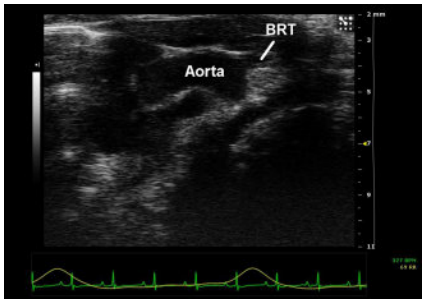

(a) B-mode

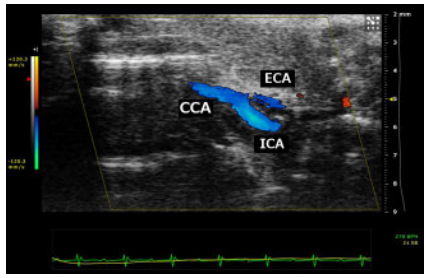

(b) Colour Doppler

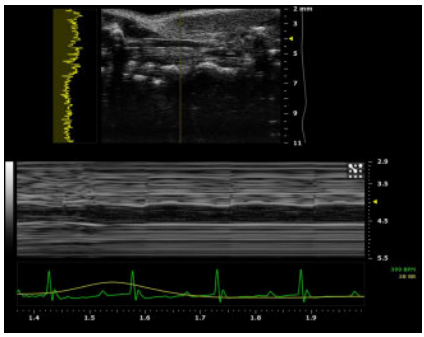

(c) M-mode

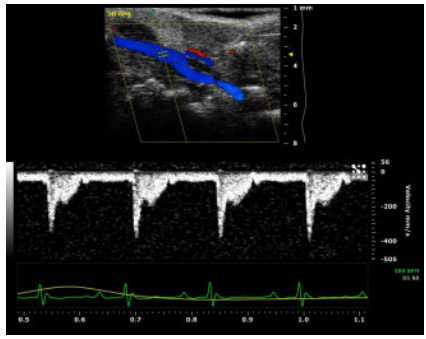

(d) Pulsed Doppler

Figure 3.3: Different US applications measured *in vivo* in mice. (a) B-mode longitudinal view of the aortic arch with the aorta and the brachiocephalic trunk (BRT) visible. (b) A Colour Doppler image showing the 1D velocity field of the carotid bifurcation. Blue indicates flow away from the probe. (c) A M-mode image showing the distension of a CCA over time. The location of the M-mode image is indicated with a dotted line in the top B-mode image in the same pane. (d) The Pulsed Doppler (PD) image showing the velocity of the blood flow in the control volume. The control volume (CCA) is plotted in the Colour Doppler image in the top of the same pane. An angle correction was performed to calculate the velocity in the direction of the dotted line (instead of the measured velocity in the direction of the beam).

A more thorough theoretical description of the several imaging techniques falls outside the scope of the current text. More information can be found in literature: general US [1], [2] or small animal ultrasound [3]. Examples of the 4 listed imaging modes are shown in figure 3.3.

3.2.4 The main challenge for small animal ultrasound: high frequency

In comparison to humans, the murine cardiovascular structures are about 10 times smaller (chapter 2). Because of the smaller size, a higher resolution is necessary. The axial resolution (resolution along the axis of the ultrasonic beam) depends on both the pulse length and the frequency (wavelength). If two objects are (axially) located closer than the pulse length, they are not discernible and are measured as one reflection. The lateral resolution (ability to discern two objects next to each other) is dependent on the frequency (wavelength) and the beam width [3].

Recently, dedicated scanners designed for small animal imaging were developed (Vevo 770, 2100 and 3100, VisualSonics, Toronto, Canada). These scanners enable the use of high-frequency probes (up to 70MHz). In the current work, measurements were performed using the Vevo 2100 system (maximal resolution axial-30μm and lateral-75μm) equipped with a linear array probe (MS550D, 22-55MHz). This system system has a better resolution and a higher detection rate of small structures (assessed through the detection of follicles within marmoset ovaries [9]) compared to clinical scanners.

On the other hand, the attenuation of the ultrasonic beam is also dependent on the frequency. The increase of attenuation limits the penetration depth of the ultrasonic wave at higher frequencies. This results in a frequency range between 20 and 56 MHz for dedicated small animal imaging systems.

3.2.5 The ultrasound measurements in practice

For the duration of the US measurements the mice were under anaesthesia with 1-1.5% isoflurane (for induction a dose of 5 % isoflurane was given). The mice were then fixated to the mouse handling table which is kept at a temperature of 40°C, to prevent a lowering of the body temperature. The body temperature was monitored with a rectal probe. The handling table has 4 electrocardiography (ECG) electrodes for the four paws to allow for monitoring of the HR and respiratory rate during the experiments. The mouse is fixated on the table and the probe is fixed on a clamp mounted on an integrated rail system. Both the position of the table (and thus the mouse) and the rail system can be changed. Micro-manipulator turning wheels allow the operator to fine tune the measurement position. The fixation of both the mouse (on the table) and the probe (on the rail system) keep the measurement plane position fixed during the measurement, which is essential for the visualisation/measurement in the small mice.

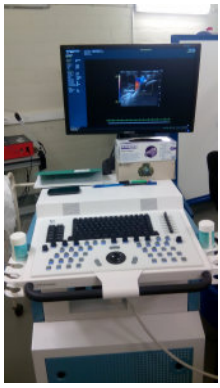

(a) Scanner

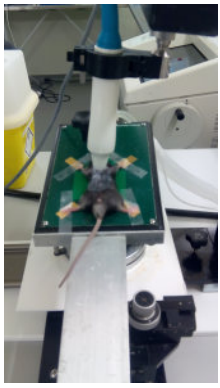

(b) Handling table

Figure 3.4: The setup of the US measurement setup for mice. (a) The Vevo2100 scanner (b) The mouse fixated on the handling table with the US probe in a clamp. The four paws are connected to electrodes to measure the ECG and the respiratory rate.

3.3 μCT imaging in mice

The current section focuses on working principle and the advantages / limitations of micro-computed tomography (μCT) with regard to the *in vivo* imaging of the murine vasculature. This section is mainly based on these sources [¶] [‖] [**] [††] [‡‡].

3.3.1 General μCT principle

In contrast to US, μCT is a medical imaging technique based on ionising radiation. A μCT scanner mainly consists of three parts (figure 3.5A):

- **The X-ray tube** is the source where the X-rays are generated. For most scanners, the electron beam is produced at the tip of a tungsten filament.

[¶] D. Clark and C. Badea, 'Micro-CT of rodents: State-of-the-art and future perspectives', *Physica Medica*, vol. 30, no. 6, pp. 619–634, 2014

[‖] S. J. Schambach, S. Bag, L. Schilling, C. Groden and M. a. Brockmann, 'Application of micro-CT in small animal imaging', *Methods*, vol. 50, no. 1, pp. 2–13, 2010

[**] H. Li, H. Zhang, Z. Tang and G. Hu, 'Micro-computed tomography for small animal imaging: Technological details', *Progress in Natural Science*, vol. 18, no. 5, pp. 513–521, 2008

[††] L. Nebuloni, G. A. Kuhn and R. Müller, 'A comparative analysis of water-soluble and blood-pool contrast agents for in vivo vascular imaging with micro-CT.', *Academic radiology*, vol. 20, no. 10, pp. 1247–55, 2013

[‡‡] B. Vandeghinste, 'Iterative Reconstruction in Micro-SPECT / CT : Regularized Sparse-View CT and Absolute In Vivo Multi-Isotope Micro-SPECT Quantification', thesis, Ghent University, 2014

A cone beam is generated (figure 3.5A) which speeds the measurement process up tremendously compared to a plane by plane measurement.

- **The object** (in the current thesis a mouse) that is scanned is placed in the middle of the scanner.

- **Detector** measures the X-rays that have penetrated through the object.

When the X-rays travel through the object, they get partially attenuated resulting in a lower amount of photon quanta measured by the detector. The total attenuation of a beam depends on the attenuation coefficients from all tissues it travelled through. Therefore, a single projection measurement has limited information.

To overcome this limitation, the scanner takes several projections for over at least 180° (see figure 3.5B). With respect to the rotation two different scanner geometries are present. For *ex vivo* imaging most of the systems use a stationary X-ray tube and detector. Instead the specimen is rotated to measure projections at different angles. For most *in vivo* scanners, rotating the object is challenging because the object is a breathing mouse, and needs to be mechanically fixated. Thus, for most *in vivo* scanners both the X-ray tube and the detector are placed on a gantry and rotated around the object while the object does not move (see figure 3.5A).

The image reconstruction process then converts the projection data into a discrete tomographic representation of the object. The filtered back projection is the discretized version of the analytic solution of the reconstruction process. Feldkamp extended this algorithm to be able to deal with cone beams instead of planar beams [15]. A second family of algorithms applied for the image reconstruction are the iterative reconstruction methods. Such algorithms reconstruct the data by iteratively comparing the original projections with simulated re-projections of the reconstructed dataset. These iterative reconstruction methods can provide a better image quality compared to the filtered back projection because they are more robust for noise and other artefacts. A more in depth description of the different reconstruction methods is outside the scope of this text but this can be found in [16], [17].

In the current thesis the Iterative Maximum-likelihood Polychromatic Algorithm for CT (IMPACT) algorithm was used to reconstruct the μCT [18]. This iterative algorithm allowed to take the beam hardening due to the dense skull and spine bones into account. The X-rays are polychromatic and lower energy X-rays attenuate more rapidly when passing through (dense) tissue. Due to this beam hardening effect, the IMPACT algorithm is necessary to prevent dark(er) streaks originating from these dense structures from

occurring. To speed up the reconstructions, all data were first reconstructed at a lower resolution (0.2 mm isotropic voxel size), after which only the volume of interest (VOI) was reconstructed at a higher resolution (50 μm isotropic voxel size)[19]. In a μCT scan of the murine brain, this reduced the noise to 5.5% instead of 14.1% with the filtered back projection [20].

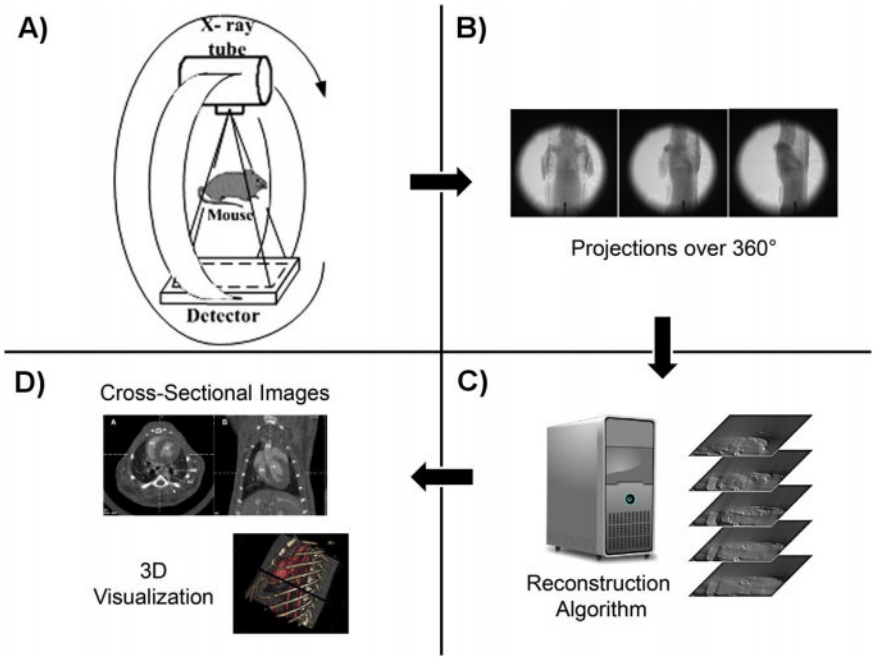

Figure 3.5: Schematic overview of the μCT imaging process. (A) The X-ray tube generates the X-rays that penetrate through the animal and get partially attenuated in the tissues. The detector measures the X-rays that travelled through the animal. (B)Both the X-ray tube and the detector rotate around the animal and measure a projection at different angles (ranging over at least 180°). (C) The projection information is processed by the reconstruction algorithm to generate the final images. (D) The reconstructed images can be visualised using cross-sectional images or 3D visualisations. The image was adapted from [10], [12].

After the reconstruction, a discrete 3D dataset of the attenuation is obtained. In most applications this attenuation is expressed in HU (Hounsfield units). The HU is calibrated so that the attenuation of air equals -1000 HU and the attenuation of water equals 0 HU (equation (3.3) with μ the attenuation coefficient).

$$\mathrm{CT}\,[\mathrm{HU}] = \frac{\mu - \mu_{water}}{\mu_{water}} \cdot 1000\mathrm{HU} \tag{3.3}$$

3.3.2 Interaction between X-rays and tissue

Figure 3.6 summarised the two main interaction mechanisms between X-rays and tissue with regard to μCT imaging.

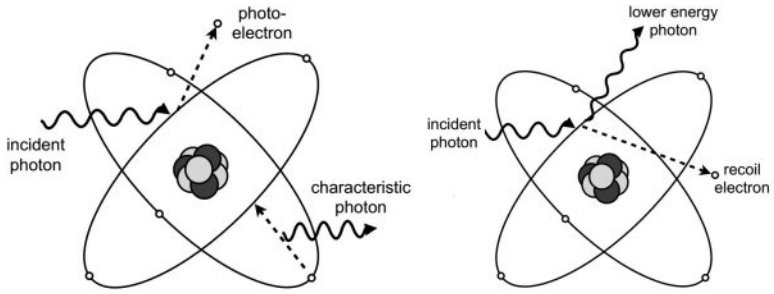

(a) photoelectric effect **(b)** Compton scattering

Figure 3.6: The two dominant interaction mechanisms between X-rays and tissue with regard to μCT are the photoelectric effect (a) and Compton scattering (b)[14]

- **Photoelectric Absorption** (figure 3.6a) occurs when an inner shell electron absorbs an incident photon. The electron is ejected from the atom if the energy of the incident photon is high enough. Afterwards, the vacant place is filled by an outer shell electron [14].

- **Compton Scattering** (figure 3.6b) occurs when the energy of the incident photon is substantially higher than the binding energy of the electron. The photon does not get absorbed completely, but keeps existing with a lower energy and is deflected (scattered) from its initial trajectory [14].

3.3.3 The main challenge for cardiovascular μCT: contrast

μCT does not provide sufficient soft tissue contrast to image the cardiovascular structures. Therefore, a specialised contrast agent with a high attenuation factor is needed. In the current clinical setting water-soluble (low molecular weight) agents are used to provide additional contrast for imaging of the vasculature. These contrast agents consist of organically bound iodine, which has a high atomic number and thus a high attenuation/contrast. They are excreted through renal filtration. In mice the rapid renal filtration accounts for a clearance of the contrast agent within seconds [10], [21]. Therefore in small animal μCT, especially when scanning at high resolution, most of the current systems are not able to visualise the vasculature using human tracers [13]. Some custom build systems are able to perform measurements in this short time frame [22], but the μCT scanner that was available for the research presented in this thesis (Triumph-II imaging system, TriFoil Imaging, Chatsworth, California, US) and most commercially available scanners have longer measurement times, which prevents this option. To overcome this limitation, a second family of contrast agents for cardiovascular μCT

imaging, has been developed: the blood-pool agent contrast agents. In 1998 Fenestra VC (ART Advanced Research Technologies Inc., Montreal, Canada), an iodinated contrast medium embedded in a lipidic formulation [23], was the first contrast agent in the blood-pool agent family [13]. The development of this and other blood-pool contrast agents facilitated the translation of clinical imaging to the preclinical setting.

More recently, larger nanoparticle metal-based agents became popular because of their higher attenuation than iodine. For example gold has a ~2.7 times higher contrast value compared to iodine per unit of weight[24]. As a result, smaller volumes need to be injected in the mice. Aurovist 15nm (Nanoprobes, Yaphank, New York, US) is gold particle based and ExiTron nano 12000 (Miltenyi Biotec, Berlin, Germany) is barium based.

Nebuloni *et al.* compared in an extensive study one water-soluble agent (Iomeron 400, Bracco, Italy) and 3 blood-pool agents: eXIA160XL Binitio Biomedical,Ottawa, Ontario, Canada), Aurovist 15nm and ExiTron nano 12000. Their conclusion was that Aurovist provided the best contrast but that a dark staining of the skin could limit follow up studies. ExiTron nano 12000 did not have this limitation and could therefore be an alternative for longitudinal monitoring [13].

Our lab has extensive experience with repeated measurements with Aurovist as a contrast agent[25]. The dark staining of the tail makes it more challenging, but not impossible, to inject the Aurovist at later time points. Therefore, for the μCT measurements done during the current work, Aurovist 15nm is used as a contrast agent.

3.3.4 The μCT measurements in practice

During the μCT measurements the mice were under 1-1.5% isoflurane anaesthesia and they were fixed at the animal holder of the μCTscanner. All μCT measurements were performed using a Triumph-II imaging system (TriFoil Imaging, Chatsworth, CA). First, a pre-contrast injection scan was taken at 50 μm resolution. Then, 100 μl/25g body weight Aurovist was injected, followed by the post-contrast injection scan. For both scans the scan time was around 20 min resulting in a scan time around 1 h (including animal preparation).

Figure 3.7: The setup of the μCT scanner (reproduced from [7]).

Bibliography Chapter 3

[1] A. Swillens, 'A multiphysics model for improving the ultrasonic assessment of large arteries', PhD thesis, Ghent University, 2010.

[2] J. E. Aldrich, 'Basic physics of ultrasound imaging', *Critical Care Medicine*, vol. 35, no. Suppl, S131–S137, 2007.

[3] R. W. Cootney, 'Ultrasound Imaging: Principles and Applications in Rodent Research', *ILAR Journal*, vol. 42, no. 3, pp. 233–247, 2001.

[4] V. Chan and A. Perlas, 'Basics of Ultrasound Imaging', in *Atlas of Ultrasound-Guided Procedures in Interventional Pain Management*, S. N. Narouze, Ed., New York, NY: Springer New York, 2011, ch. 2, pp. 13–20.

[5] S. Vandenberghe, H. Hallez, R. Declerck and J. Cornelis, *Biomedical signals and images (course notes)*, Gent, 2010.

[6] T. M. Robinson, 'Basic Principles of Ultrasound', in *Physics for Medical Imaging Applications*, Y. Lemoigne, A. Caner and G. Rahal, Eds., Dordrecht: Springer Netherlands, 2007, pp. 101–110.

[7] B. Trachet, 'The Role of Disturbed Hemodynamics in Aneurysm Formation in Mice', PhD thesis, Ghent University, 2012.

[8] K. Pichamuthu, *ICU sonography: Demystifying sonology in intensive care*, `http://www.criticalecho.com/category/image-galleries/tutorial-images`, 2015.

[9] C. M. Moran, S. D. Pye, W. Ellis, A. Janeczko, K. D. Morris, A. S. McNeilly and H. M. Fraser, 'A comparison of the imaging performance of high resolution ultrasound scanners for preclinical imaging.' *Ultrasound in medicine & biology*, vol. 37, no. 3, pp. 493–501, 2011.

[10] D. Clark and C. Badea, 'Micro-CT of rodents: State-of-the-art and future perspectives', *Physica Medica*, vol. 30, no. 6, pp. 619–634, 2014.

[11] S. J. Schambach, S. Bag, L. Schilling, C. Groden and M. a. Brockmann, 'Application of micro-CT in small animal imaging', *Methods*, vol. 50, no. 1, pp. 2–13, 2010.

[12] H. Li, H. Zhang, Z. Tang and G. Hu, 'Micro-computed tomography for small animal imaging: Technological details', *Progress in Natural Science*, vol. 18, no. 5, pp. 513–521, 2008.

[13] L. Nebuloni, G. A. Kuhn and R. Müller, 'A comparative analysis of water-soluble and blood-pool contrast agents for in vivo vascular imaging with micro-CT.' *Academic radiology*, vol. 20, no. 10, pp. 1247–55, 2013.

[14] B. Vandeghinste, 'Iterative Reconstruction in Micro-SPECT / CT : Regularized Sparse-View CT and Absolute In Vivo Multi-Isotope Micro-SPECT Quantification', thesis, Ghent University, 2014.

[15] L. a. Feldkamp, L. C. Davis and J. W. Kress, 'Practical cone-beam algorithm', *Journal of the Optical Society of America*, vol. 1, no. 6, pp. 612–619, 1984.

[16] A. C. Kak and M. Slaney, 'Principles of Computerized Tomographic Imaging'. IEEE Press, 1988.

[17] M. Beister, D. Kolditz and W. A. Kalender, 'Iterative reconstruction methods in X-ray CT', *Physica Medica*, vol. 28, no. 2, pp. 94–108, 2012.

[18] B. De Man, J. Nuyts, P. Dupont, G. Marchal and P. Suetens, 'An iterative maximum-likelihood polychromatic algorithm for CT.' *IEEE transactions on medical imaging*, vol. 20, no. 10, pp. 999–1008, 2001.

[19] A. Ziegler, T. Nielsen and M. Grass, 'Iterative reconstruction of a region of interest for transmission tomography', *Medical Physics*, vol. 35, no. 4, pp. 1317–27, 2008.

[20] B. Vandeghinste, D. De Wilde, C. der Donckt, G. De Meyer, P. Segers, R. Van Holen, S. Vandenberghe and C. Vanhove, 'In vivo mouse cerebral plaque visualisation with micro-CT', in *World Molecular Imaging Congress, Abstracts*, 2013.

[21] Ming De Lin, Lutao Ning, C. Badea, N. Mistry, Yi Qi and G. Johnson, 'A High-Precision Contrast Injector for Small Animal X-Ray Digital Subtraction Angiography', *IEEE Transactions on Biomedical Engineering*, vol. 55, no. 3, pp. 1082–1091, 2008.

[22] S. J. Schambach, S. Bag, C. Groden, L. Schilling and M. A. Brockmann, 'Vascular imaging in small rodents using micro-CT', *Methods*, vol. 50, no. 1, pp. 26–35, 2010.

[23] J. P. Weichert, F. T. Lee, M. A. Longino, S. G. Chosy and R. E. Counsell, 'Lipid-based blood-pool CT imaging of the liver', *Academic Radiology*, vol. 5, S16–S19, 1998.

[24] H. L. Grinstaff and M. W., 'X-Ray Computed Tomography Contrast Agents', 3. 2014, vol. 113, pp. 1641–1666.

[25] B. Trachet, M. Renard, G. De Santis, S. Staelens, J. De Backer, L. Antiga, B. Loeys and P. Segers, 'An Integrated Framework to Quantitatively Link Mouse-Specific Hemodynamics to Aneurysm Formation in Angiotensin II-infused ApoE -/- mice.' *Annals of biomedical engineering*, vol. 39, no. 9, pp. 2430–2444, 2011.

II

Computational techniques to study arterial haemodynamics

Chapters

Chapter 4

Numerical simulations of arterial haemodynamics: Surpassing measurement limitations

4.1 Introduction

The WSS exerted at the EC is the main biomechanical interaction that the blood flow has with the ECs (see chapter 1). However, to be able to assess the WSS and related metrics (see chapter 5), the flow velocity field needs to be known in great detail. The small size and the high HR of mice make this impossible to measure and thus numerical methods such as computational fluid dynamics (CFD) are applied to calculate the WSS with a high accuracy.

For simple cases, the equations describing the physical laws of fluid flow and deformation of solids can be solved analytically. For real *in vivo* applications this is generally not the case because of several reasons: (i) complex geometry, (ii) complex boundary conditions and (iii) complex properties of the fluid (blood) and solid (arterial wall). For these more complex cases CFD or computational solid mechanics (CSM) provide a solution. These simulations approximate the solution by discretization of the governing partial differential equations (PDEs).

Both the temporal and the spatial domain are discretized. For the spatial discretization, the domain is split in different cells (elements) and nodes called the computational mesh. After this spatial discretization the physics laws can be described using a Lagrangian, Eulerian or arbitrary Lagrangian-Eulerian

(ALE) approach. These three techniques are schematically represented in figure 4.1.

- **Lagrangian** (figure 4.1a) This method is mostly used for CSM. The nodes of the mesh follow the material during the deformation over time. The main advantage is that free surfaces and interfaces can be tracked easily over time[1].

- **Eulerian** (figure 4.1b) This method is widely used for CFD calculations. As illustrated in figure 4.1b, the material moves over time but this motion is not followed by the computational mesh: mesh points do not move over time. Large displacements of the particles can be simulated particularly well with this method [1].

- **ALE** (figure 4.1c) With this technique, the nodes of the computational mesh are allowed to move at an arbitrary speed, different from the particle speed. For fluid-structure interaction (FSI) simulations, this technique is one of the possibilities to be able to deal with the presence of both fluids and solids. This technique is applied to the fluid domain of the FSI simulations in this thesis and more detail will be presented in section 4.4.4.

The remainder of this chapter is mainly based on * †.

4.2 Computational Fluid Dynamics

4.2.1 Navier-Stokes equations

Isothermal fluid flow is described by two principles: *conservation of mass* and *conservation of momentum*. Together they are called the Navier-Stokes equations.

4.2.1.1 Conservation of mass

The conservation of mass formulates that no mass is generated or lost during fluid flow. Mathematically this principle can be expressed by the following equation:

$$\frac{\partial \rho_f}{\partial t} + \nabla \cdot (\rho_f \vec{v}_f) = 0 \tag{4.1}$$

*J. Degroote, 'Partitioned Simulation of Fluid-Structure Interaction', *Archives of Computational Methods in Engineering*, vol. 20, no. 3, pp. 185–238, 2013

†A. Quarteroni and L. Formaggia, 'Mathematical Modelling and Numerical Simulation of the Cardiovascular System', in *Handbook of Numerical Analysis*, October, P. G. Ciarlet and J. L. Lions, Eds., vol. 12, Amsterdam: Elsevier, 2004, pp. 3–127

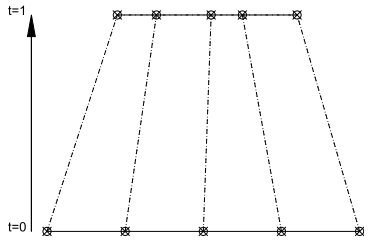

(a) Lagrangian

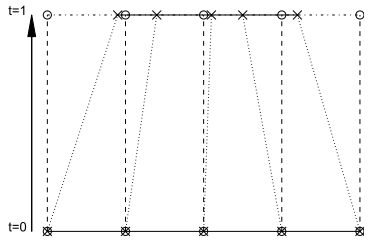

(b) Eulerian

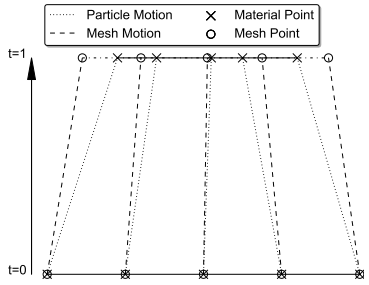

(c) ALE

Figure 4.1: Different formulations of the partial differential equation based on mesh motion. (a) In the Lagrangian description, the mesh (◯) motion follows the material (x) motion. (b) In the Eulerian description, the mesh does not move. Due to material motion, material points can move from one mesh cell to another. (c) In the ALE description, the mesh moves with an arbitrary speed, not necessary equal to the material speed. Similar to the Eulerian description, material can move between mesh cells (adapted from [1]).

In these equations ρ_f expresses the density of the fluid and $\vec{v}_f$ the fluid velocity. In the case of incompressible fluid flow, ρ_f is constant and thus equation (4.1) simplifies to:

$$\nabla \cdot \vec{v}_f = 0 \tag{4.2}$$

4.2.1.2 Conservation of momentum

Newton's second law of motion is generally known in the form $M \cdot \vec{a} = \vec{F}$ with $\vec{F}$ force, M mass and $\vec{a}$ acceleration. For the fluid flow this law is expressed as the second Navier-Stokes equation:

$$\rho_f \frac{\partial \vec{v}_f}{\partial t} + \rho_f \vec{v}_f \cdot \nabla \vec{v}_f = \nabla \cdot \bar{\sigma}_f + \vec{f}_f \tag{4.3}$$

In this equation the forces are grouped as:

surface forces stresses experienced by the fluid and expressed by the Cauchy stress tensor $\bar{\sigma}_f$

body forces ($\vec{f}_f$) external forces applied to the fluid for example gravity

For the simulation of the blood flow in the carotid artery of a mouse, this equation can be simplified further. The body forces are omitted because the gravity is negligible compared to the surface forces. Next to this, the conservation of mass for incompressible fluids further simplifies this equation resulting in:

$$\rho_f \frac{\partial \vec{v}_f}{\partial t} + \rho_f \nabla \cdot \left(\vec{v}_f \vec{v}_f\right) = \nabla \cdot \bar{\sigma}_f \tag{4.4}$$

4.2.2 Constitutive law

Equations (4.2) and (4.4) are the equations used to describe the fluid flow. But these equations are not closed yet. In the current form, the velocity components ($\vec{v}_f$) and the components of the Cauchy stress tensor ($\bar{\sigma}_f$) are the unknowns. Yet only 4 equations are available: the conservation of mass and the 3 components (x, y and z) for the conservation of momentum. Therefore the components of the Cauchy stress tensor need to be linked to kinematic quantities, in particular the velocity field, for us to be able to solve this system [3].

The Cauchy stress tensor can be split in the (internal) pressure P_f and the shear stresses. These shear stresses ($\bar{\tau}_f$) arise from the viscous forces. In reality blood is a non-Newtonian fluid (the viscosity is dependent on the shear rate) [4]. However, in the current work blood will be modelled as a Newtonian fluid for simplicity, thus assuming a constant viscosity independent of the shear rate. Under the assumption of Newtonian fluid, the Cauchy stress tensor ($\bar{\sigma}_f$) is given by the following constitutive law:

$$\bar{\sigma}_f = -P_f \bar{I} + \bar{\tau}_f = -P_f \bar{I} + 2\mu \bar{\varepsilon}_f \tag{4.5}$$

In this equation $\bar{I}$ is the identity tensor and the strain rate tensor ($\bar{\varepsilon}_f$) is calculated by (with $\vec{v}_f$ the fluid velocity):

$$\bar{\varepsilon}_f = \frac{1}{2}\left[\nabla \vec{v}_f + \left(\nabla \vec{v}_f\right)^T\right] \tag{4.6}$$

This constitutive law (equations (4.5) and (4.6)) can be used for substitution of the Cauchy stress tensor components in the conservation of momentum equation (4.4) leading to:

$$\rho_f \frac{\partial \vec{v}_f}{\partial t} + \rho_f \nabla \cdot \left(\vec{v}_f \vec{v}_f\right) = \nabla \cdot \left(-P_f \bar{I} + \mu \nabla \vec{v}_f + \mu \left(\nabla \vec{v}_f\right)^T\right) \tag{4.7}$$

This results in 4 equations (the conservation of mass equation (4.2) and 3 components of the conservation of momentum equation (4.7)) with only 4 unknowns (P and 3 components of $\vec{v}_f$). This set of equations is closed and can then be solved numerically.

4.2.3 Solution of the fluid mechanics equations

The current section describes the methodology followed in this thesis to solve the fluid mechanics problem. The reader should take into account that this is only one of several possibilities.

In the current work, the spatial domain is discretized using the Eulerian formulation (section 4.1) for the CFD simulations (for FSI simulations see section 4.4.4). After the domain is split in different cells, the finite volume method (FVM) was applied using Fluent 14.5 (Ansys, Canonsburg, USA). The FVM is a possible method to solve the PDEs. In the FVM method, the mesh is considered as a set of small control volumes. In Fluent all the quantities (including pressures and velocities) are then stored in the centre of this control volume (cell). For the solution the face centred values (needed to solve the set of equations) are constructed using interpolation [5]–[7].

The time is discretised using an implicit second order backward discretisation scheme. As an example, the discretization of a general first order PDE (equation (4.8a)) is given in equation (4.8b).

$$\frac{\partial \phi}{\partial t} = F(\phi) \tag{4.8a}$$

$$\frac{3\phi^{n+1} - 4\phi^n + \phi^{n-1}}{2\Delta t} = F(\phi^{n+1}) \tag{4.8b}$$

In this equation, ϕ is a general scalar quantity, ϕ^n the value at the current time step, ϕ^{n-1} the value at the previous time step and ϕ^{n+1} the value at the next time step. The value ϕ^{n+1} is still unknown at this stage. F is a generic function that includes any space discretization. This method is called implicit because the value ϕ^{n+1} is only present implicitly and dependent on the unknown values of ϕ^{n+1} in the neighbouring cells through $F(\phi^{n+1})$. This

scheme therefore results in a set of equations that needs to be solved iteratively at every time point until convergence is reached.

A more detailed description of the solution method is beyond the scope of this work. For a more detailed explanation the reader is referred to the manual or the theory guide of Fluent [7].

4.3 Computational Solid Mechanics

One of the differences with CFD simulations is that in CSM simulations normally the Lagrangian approach is followed (figure 4.1a). Therefore, in this paragraph the equations are presented in the Lagrangian form. The material derivative (also called Lagrangian derivative) is the time derivative in a Lagrangian frame. This derivative of a general function f can be calculated using (with $\vec{v}_s$ the velocity of the solid):

$$\frac{\mathrm{D}f}{\mathrm{D}t} = \frac{\partial f}{\partial t} + \vec{v}_s \cdot \nabla f \tag{4.9}$$

4.3.1 Conservation of momentum

In CSM the displacement or the deformation ($\vec{u}$) is determined by the Cauchy momentum equation:

$$\rho_s \frac{\mathrm{D}^2\vec{u}_s}{\mathrm{D}t^2} = \vec{f}_s + \nabla \cdot \bar{\sigma}_s \tag{4.10}$$

In this formula ρ_s is the density of the solid, $\vec{f}_s$ the body forces and $\bar{\sigma}_s$ the Cauchy stress tensor of the solid. Similar to the fluid flow problem, we will ignore the body forces because the gravity (= $\vec{f}_s$) is low compared to the other forces involved. Next to this, equation (4.10) differs from the fluid momentum equation (equation (4.3)) by the Lagrangian formulation visible in the use of the material derivative.

4.3.2 Constitutive law

Similar as to the fluid case, constitutive laws are needed to close the equations. For fluid flow, these constitutive laws express $\bar{\sigma}_f$ in function of the gradient of the velocity. In solid mechanics the constitutive law links the stress tensor with the gradient of the deformation ($\nabla\vec{u}_s$). The mass and momentum equations for solid and fluid mechanics are the same, but the different constitutive laws result in major differences [3].

To derive the constitutive laws, we need the deformation gradient tensor ($\bar{F}$) which is defined in function of the reference coordinates ($\vec{X}$) and the coordinates during deformation ($\vec{x}$). Suppose a material point p of a solid

body B has coordinates $\vec{X}$ in the reference configuration. When the body deforms, the coordinates change to $\vec{x}$. The deformation gradient is then defined in equation (4.11). In other words, the deformation gradient projects the vector $\mathrm{d}\vec{X}$, pointing from p to a neighbouring point q in the reference configuration, onto the vector $\mathrm{d}\vec{x}$, pointing from p to q in the deformed configuration: $\mathrm{d}\vec{x} = \bar{F}.\mathrm{d}\vec{X}$

$$\bar{F} = \frac{\partial \vec{x}}{\partial \vec{X}} \tag{4.11}$$

Furthermore we note the determinant of $\bar{F}$ as J. J expresses the relative change of an infinitesimal volume around a material point p and is a measure for local material compression.

In large deformation theory, the constitutive laws are expressed in function of the second Piola-Kirchhoff stress tensor ($\bar{S}_s$) instead of the Cauchy stress tensor ($\bar{\sigma}_s$). When they are defined using $\bar{S}_s$, the Green-Lagrange strain tensor ($\bar{\varepsilon}_s$) is applied to define the strain. The second Piola-Kirchhoff stress tensor and the Green-Lagrange strain are defined in function of the Cauchy stress ($\bar{\sigma}_s$), the displacement ($\vec{u}$), the deformation gradient tensor ($\bar{F}$) and its determinant (J) as:

$$\bar{S}_s = J\bar{F}^{-1}\bar{\sigma}_s\bar{F}^{T} \tag{4.12a}$$

$$\bar{\varepsilon}_s = \left[\nabla\vec{u}_s + \left(\nabla\vec{u}_s\right)^T + \left(\nabla\vec{u}_s\right)^T \nabla\vec{u}_s\right] \tag{4.12b}$$

For hyperelastic materials (such as the models used in this thesis), the constitutive law is regularly defined in its integral form using the strain energy density function (W). During deformation this function W defines the elastic strain potential energy per unit of initial (undeformed) volume. Different material models are then defined by describing their different W.The link between $\bar{S}_s$ and $\bar{\varepsilon}_s$ can then be expressed as [8], [9]:

$$\bar{S}_s = \frac{\partial W}{\partial \bar{\varepsilon}_s} \tag{4.13}$$

For example for the Arruda-Boyce model the strain energy density function is defined as [10]–[12]:

$$W = Nk_B\theta\sqrt{n}\left[\beta\lambda_{chain} - \sqrt{n}\ln\left(\frac{\sinh\beta}{\beta}\right)\right] \tag{4.14}$$

This model was originally developed to describe the mechanics of rubber-like materials that consist of a network of linked polymeric chains. In the previous equation several physical and material dependent constants are included to mimic reality: the number of chain segments (n), the Boltzmann constant (k_B), the temperature in Kelvin (θ) and the number of polymeric / rubber chains (N). λ_{chain} and β are given by:

$$\lambda_{chain} = \sqrt{\frac{I_1}{3}} \tag{4.15a}$$

$$\beta = \mathcal{L}^{-1}\left(\frac{\lambda_{\text{chain}}}{\sqrt{n}}\right) \tag{4.15b}$$

In these equations I_1, is the first invariant (trace) of the left Cauchy – Green deformation tensor (= $\bar{F}\bar{F}^T$) and $\mathcal{L}^{-1}$ is the inverse Langevin function.

Together with the conservation of momentum, the constitutive law closes the governing equations. The CSM model can then be solved to calculate the deformation of the solid material.

4.3.3 Solution of the solid mechanics equations

Both the standalone CSM simulations and the CSM simulations that are part of the FSI protocol made use of the Lagrangian formulation. A finite element method (FEM) approach in Abaqus Standard (Simulia, Johnston, USA) was used to solve the equations. The solution domain is discretized based on a piecewise representation of the basis functions. The computational mesh splits the domain into a set of elements and in every element the solution is formulated in function of the basic functions. This is conceptually different from the FVM method used for the CFD in section 4.2.3 on page 75, where in every cell the solution is only represented by the central value. In the FEM method the basic function approximation is known, which includes more information compared to the FVM applied in the CFD simulations[6], [13], [14].

The time domain is discretised using a first order implicit backward discretisation scheme. In this scheme, the time derivative of equation (4.10) can be expressed using[15]:

$$\dot{\vec{u}}_s\big|_{t+\Delta t} = \frac{\vec{u}_s\big|_{t+\Delta t} - \vec{u}_s\big|_t}{\Delta t} \tag{4.16a}$$

$$\ddot{\vec{u}}_s\big|_{t+\Delta t} = \frac{\dot{\vec{u}}_s\big|_{t+\Delta t} - \dot{\vec{u}}_s\big|_t}{\Delta t} \tag{4.16b}$$

As for the fluid mechanics problem, this is an implicit scheme that needs to be solved iteratively at every time point.

A more detailed description of the solution procedure followed by Abaqus Standard is outside the scope of this text and can be found in the *Abaqus Theory Guide* [15].

4.4 Fluid Structure Interaction

This section describes the coupling of the CFD and CSM solver using the coupling code Tango developed by prof. Joris Degroote at Ghent University. An in depth analysis is beyond the scope of the current work, only a summary of the work of prof. Degroote is presented. For a more detailed overview the reader is referred to the original articles describing the coupling code and comparing different FSI methodologies [2], [16]–[18].

4.4.1 Equilibrium conditions

After solving the Navier-Stokes equations for the fluid domain (section 4.2.1) and the solid domain equations (section 4.3.1), we still need to describe what is happening at the interface of both domains. In CFD simulations, the no-slip boundary condition at physical borders (walls) is commonly applied, which translates to a zero velocity at the boundary. In FSI simulations the no-slip boundary condition means that the velocity of the fluid is equal to the velocity of the solid at the interface.

$$\vec{v}_f = \frac{\mathrm{d}\vec{u}_s}{\mathrm{d}t} \tag{4.17}$$

At the interface the traction forces also have to be in equilibrium (with $\vec{n}$ the normal of the element on the interface pointing outward of the respective domain).

$$\bar{\sigma}_f \cdot \vec{n}_f = -\bar{\sigma}_s \cdot \vec{n}_s \tag{4.18}$$

4.4.2 Monolithic or partitioned FSI approach

FSI simulations combine the fluid and solid mechanics simulations. When they are combined in a monolithic approach, the fluid and solid mechanics equations are solved simultaneously. This approach takes the mutual influence directly into account which has a beneficial influence on the stability. Furthermore, no coupling iterations are needed.

On the other hand it is also possible to solve the fluid and solid mechanics equations separately, which is called a partitioned approach. Over the years highly specialised and well known codes have been developed to solve

either the fluid or the solid mechanics equations efficiently. When using the partitioned approach, these highly optimised codes can be applied, possibly resulting in a higher efficiency. The partitioned approach also adds more flexibility because it can more easily be adapted to other codes.

At the interface between the fluid and the solid, Dirichlet-Neumann boundary conditions are used to describe the problem. For the flow solver, the displacement (or velocity) at the interface is applied (Dirichlet boundary condition) according the the CSM results. For the solid solver, the traction exerted by the fluid at the solid elements at the interface is applied for the CSM (Neumann boundary condition).

For the current work a strongly coupled partitioned approach was applied: Tango [2]. For an in depth comparison between the partitioned approach of Tango and a monolithic approach, the reader is referred to [16].

4.4.3 Explicit or Implicit coupling

Most partitioned FSI simulation approaches can be grouped in either explicitly (=weakly) coupled or implicitly coupled formulations (although other formulations exist). In explicit coupled codes, only one coupling iteration is performed (fluid ⇒ solid ⇒ next time step) and thus the solid and fluid equations are only solved once for each time step. As a result the equilibrium conditions (section 4.4.1) are not exactly imposed [2].

In Tango the fluid and solid equations are implicitly coupled. For each time step the equilibrium conditions are imposed at both the fluid and the solid solver. An iterative process (the coupling iterations) between both solvers (fluid and solid) based on the interface- quasi-Newton with inverse Jacobian from a least-squares model (IQN-ILS) iteration scheme [16] is applied to ensure convergence. This ensures the equilibrium of the displacements and forces at the interface for every time step.

For every time step several solid and fluid simulations are performed. In the previous section, it was mentioned that displacement and traction are exchanged at the surface between the CFD and CSM simulations. Using an interface- quasi-Newton with inverse Jacobian from a least-squares model (IQN-ILS) iteration scheme, the coupling code Tango determines the equilibrium state for this exchange at the interface at every time step [2], [16].

4.4.4 Arbitrary Lagrangian-Eulerian formulation

In figure 4.2, the mesh deformation is schematically drawn for FSI simulations using the ALE description for the fluid domain and the Lagrangian description for the solid domain. The Lagrangian description makes sure that the solid mesh is attached to the structure (grey) and the mesh thus deforms along with the movement of solid particles (dots) in figure 4.2.

For the fluid flow a strict Eulerian formulation is no longer sufficient, because the fluid domain is deforming. This deformation is due to the motion of the solid (arterial wall) and the fluid domain needs to stay in contact with the deforming solid (at least in the application of blood flow in arteries).

In this work, the fluid equations were expressed using an ALE approach. As can be seen in figure 4.2, the fluid mesh has the same velocity at the interface as the solid mesh. To avoid excessive distortion of the fluid mesh, the fluid mesh velocity at the interface is extended to the whole fluid domain mesh for example by a spring-based model. This models the edges of the mesh as springs with a stiffness inversely proportional to the edge length [2]. As a result the fluid mesh deforms with a different velocity compared to the fluid motion (figure 4.2b).

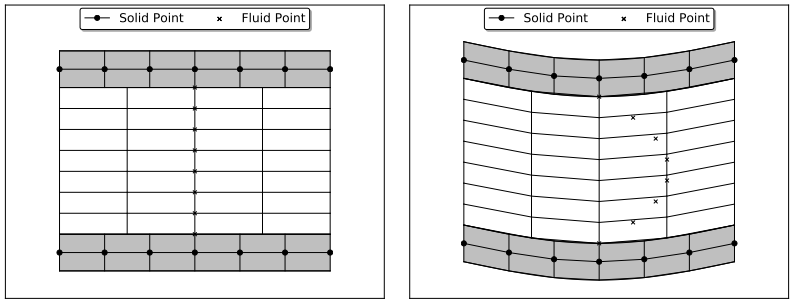

(a) t = 0 **(b)** t = ΔT

Figure 4.2: Schematic drawing of the ALE (fluid) and Lagrangian (structure) grid motion during the FSI simulations. The original meshes (a) and the meshes at a later time point (b) are plotted. The solid mesh (grey) deforms together with the structure (Lagrangian formulation). For the fluid mesh, the deformation of the mesh happens with a deformation different from the fluid deformation (ALE). At the interface the solid and fluid meshes move with the same velocity.

The disadvantages of the ALE formulation only occur at high deformations of the structure or when the topology changes (for example closing of a valve). In these cases, the extension of the displacement of the fluid grid at the interface to the rest of the fluid grid will lead to a low quality, highly skewed, distorted mesh. In the research presented in this thesis, the deformations are low and no topological changes occur so the ALE formulation causes no problems. Another advantage of the ALE approach is that the time-dependent WSS can be quantified easily. These time-dependent changes of WSS influence the EC at the solid surface (see chapter 5 on page 85). Because the fluid mesh follows the solid motion at the interface, it is possible to link WSS, which is a property of the fluid domain, with specific locations at the arterial wall, in the solid domain.

Bibliography Chapter 4

[1] J. Donea, A. Huerta, J.-P. Ponthot and A. Rodriguez-Ferran, 'Arbitrary Lagrangian-Eulerian Methods', in *Encyclopedia of Computational Mechanics*, E. Stein, R. de Borst and T. J. R. Highes, Eds., Volume 1: Chichester, UK: John Wiley & Sons, Ltd, 2004, ch. 14, pp. 413–437.

[2] J. Degroote, 'Partitioned Simulation of Fluid-Structure Interaction', *Archives of Computational Methods in Engineering*, vol. 20, no. 3, pp. 185–238, 2013.

[3] A. Quarteroni and L. Formaggia, 'Mathematical Modelling and Numerical Simulation of the Cardiovascular System', in *Handbook of Numerical Analysis*, October, P. G. Ciarlet and J. L. Lions, Eds., vol. 12, Amsterdam: Elsevier, 2004, pp. 3–127.

[4] D. Katritsis, L. Kaiktsis, A. Chaniotis, J. Pantos, E. P. Efstathopoulos and V. Marmarelis, 'Wall shear stress: theoretical considerations and methods of measurement.' *Progress in cardiovascular diseases*, vol. 49, no. 5, pp. 307–329, 2007.

[5] B. Trachet, J. Bols, G. De Santis, S. Vandenberghe, B. Loeys and P. Segers, 'The Impact of Simplified Boundary Conditions and Aortic Arch Inclusion on CFD Simulations in the Mouse Aorta: A Comparison With Mouse-specific Reference Data', *Journal of Biomechanical Engineering*, vol. 133, no. 12, p. 121 006, 2011.

[6] J. Peiró and S. Sherwin, 'Finite Difference, Finite Element and Finite Volume Methods for Partial Differential Equations', in *Handbook of Materials Modeling*, S. Yip, Ed., vol. M, Dordrecht: Springer Netherlands, 2005, pp. 2415–2446.

[7] ANSYS Inc. (US), *ANSYS Fluent Theory Guide*, 2013.

[8] K. J. Willam, 'Constitutive modele for engineering materials', *Encyclopedia of Physical Science & Technology*, vol. 3, pp. 603–633, 2002.

[9] J. Degroote, *Fluid-Structure Interaction (course notes)*, Gent, 2012.

[10] J. Bols, 'Numerical Modelling of the Fluid-Structure Interaction in Complex Vascular Geometries', PhD thesis, Ghent, 2014.

[11] B. Trachet, J. Bols, J. Degroote, B. Verhegghe, N. Stergiopulos, J. Vierendeels and P. Segers, 'An Animal-Specific FSI Model of the Abdominal Aorta in Anesthetized Mice', *Annals of Biomedical Engineering*, vol. 43, no. 6, pp. 1298–1309, 2015.

[12] E. M. Arruda and M. C. Boyce, 'A three-dimensional constitutive model for the large stretch behavior of rubber elastic materials', *Journal of the Mechanics and Physics of Solids*, vol. 41, no. 2, pp. 389–412, 1993.

[13] F. J. Sayas, *A gentle introduction to the Finite Element Method An introduction*, http://www.math.udel.edu/~fjsayas/anIntro2FEM.pdf, 2008.

[14] *What is the difference between FEM, FVM and FDM?*, http://www.cfd-online.com/Wiki/General_CFD_FAQ#What_is_the_difference_between_FEM.2C_FVM_and_FDM.3F, 2013.

[15] Simulia, *Abaqus Theory Guide*, 2015.

[16] J. Degroote, K.-J. Bathe and J. Vierendeels, 'Performance of a new partitioned procedure versus a monolithic procedure in fluid–structure interaction', *Computers & Structures*, vol. 87, no. 11-12, pp. 793–801, 2009.

[17] J. Degroote, R. Haelterman, S. Annerel, P. Bruggeman and J. Vierendeels, 'Performance of partitioned procedures in fluid–structure interaction', *Computers & Structures*, vol. 88, no. 7-8, pp. 446–457, 2010.

[18] J. Degroote and J. Vierendeels, 'Multi-solver algorithms for the partitioned simulation of fluid-structure interaction', *Computer Methods in Applied Mechanics and Engineering*, vol. 200, no. 25-28, pp. 2195–2210, 2011.

Chapter 5

Haemodynamic wall parameters:

From simulations to physiology

5.1 Introduction

Perhaps the most important step in the CFD (section 4.2 on page 72) or FSI (section 4.4 on page 79) tool chain is to translate the calculations into physiologically relevant results and metrics. CFD is a tool used in a lot of different engineering fields. It is generally accepted that haemodynamics play a crucial role in atherosclerosis development, with especially the blood flow close to the arterial wall being important. The shear stress is the frictional force per unit area that the blood flow exerts on the arterial wall, and it is an essential biomechanical stimulus of the blood flow on the EC. As described in section 1.2.7 on page 23, low and oscillatory WSS sets off several molecular pathways leading to atherosclerosis development. Throughout the years, several haemodynamic wall parameters (HWPs) have been defined which all aimed to quantitatively link the haemodynamics with atherosclerosis development through an objective quantification of flow/WSS properties. In the next part of this chapter, the most important HWPs are listed, subdivided into three main groups: the magnitude-based, the gradient-based and the harmonic based HWPs.

We will illustrate the different HWPs using a dataset that has been generated as part of this PhD thesis (simulations of a carotid bifurcation in

an ApoE$^{-/-}$ mouse, mouse 3L). In chapter 8 on page 149, a more complete overview of the FSI methodology and results is given.

5.2 Wall shear stress

The shear stress (τ) exerted on the arterial wall is proportional to the local velocity (u) gradient (shear rate) with the dynamic viscosity (μ) being the proportionality constant - equation (5.1). In this equation y is the direction perpendicular to the arterial surface.

$$\tau = \mu \frac{\partial u}{\partial y}\bigg|_{y=0} \tag{5.1}$$

The WSS is the tangential force exerted by the flowing blood on the arterial surface per unit of area. The main problem, however, is that the shear rate in equation (5.1) can not be measured directly.

The simplest method of estimating the WSS is assuming Poiseuille flow. This assumption is justified in case of: circular tube (rigid walls), steady state flow (no time dependence), Newtonian behaviour of the fluid (constant viscosity) and sufficiently low Reynolds number (Re $\ll$ 1900 for pipe flow [1]) to ensure laminar flow. In that case, the velocity profile is parabolic (figure 5.1) and equation (5.1) simplifies to the Hagen-Poiseuille formula (equation (5.2)) [2]. It should be stressed that these assumptions are strict, which practically renders them unusable for complex flow fields in the vicinity of, for example, bifurcations, stenoses and aneurysms.

$$\tau = \frac{4\mu Q}{\pi R^3} \tag{5.2}$$

Another possibility to obtain WSS, is to measure the velocity field (flow field) with high accuracy and to calculate the WSS directly from the shear rate (equation (5.1)). Magnetic resonance imaging (MRI) and US are the main imaging modalities used for this kind of studies in humans [2], [4], [5]. However, the usability of these methods is limited in mice. van Bochove *et al.* applied an MRI approach to the casted CCA in mice (tapered cast section 2.2.1). They only estimated WSS at peak flow [6] and their method is not applicable to more complex geometries such as bifurcations.

The challenging measurements needed to apply equation (5.1) directly are one of the reasons why CFD or FSI models are used for WSS studies. These simulations allow to calculate the time dependent WSS vector in complex geometries and to derive several HWPs that take the time dependency into account.

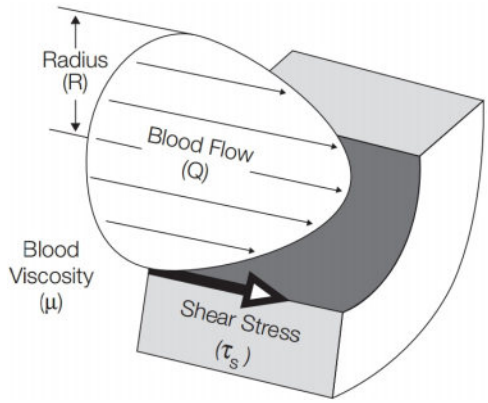

Figure 5.1: Schematic representation of the wall shear stress (reproduced from [3]).

5.3 Magnitude-based HWP

5.3.1 Time averaged wall shear stress (TAWSS)

The TAWSS is calculated by averaging the norm of the time dependent wall shear vector ($\vec{\tau}$) over time (one heart cycle - T) - equation (5.3).

$$\text{TAWSS} = \frac{1}{T}\int_0^T \|\vec{\tau}\| \, \mathrm{d}t \tag{5.3}$$

Figure 5.2a shows the TAWSS for the example murine carotid bifurcation. It is clearly visible that the ECA for this specific bifurcation has the lowest TAWSS value from the three branches and the ICA the highest. Within both the ECA and ICA, the lowest value of the TAWSS occurs at the outer bend of the bifurcation.

5.3.2 Oscillatory shear index (OSI)

Next to the average value of the WSS, also its fluctuating nature has an important influence. It is generally accepted that atheroprone regions are characterised by low and oscillatory shear stress [7]. The oscillatory shear index (OSI) was originally proposed by Ku *et al.* to describe this oscillatory character [8], [9]. The OSI also has an average value over the whole heart-cycle and can be calculated using equation (5.4).

$$\text{OSI} = \frac{1}{2}\left(1 - \frac{\left\|\int_0^T \vec{\tau}\,\mathrm{d}t\right\|}{\int_0^T \|\vec{\tau}\| \, \mathrm{d}t}\right) \tag{5.4}$$

The OSI value is limited to the range [0,1/2]. When almost no oscillations are present the OSI will have a value close to 0. In the case a purely oscillatory flow

is present (for example a sinusoidal-wave), the OSI will reach the maximum value of 1/2. As can be seen in figure 5.2b, the zone with a high OSI in the murine carotid bifurcation is found mainly at the outer side of the ECA sinus. This overlaps with the low TAWSS region.

5.3.3 Relative residence time (RRT)

Himburg *et al.* showed that the residence time of particles near the wall is inversely correlated with both the TAWSS and OSI. The relative residence time (RRT) can be calculated using equation (5.5). When the oscillatory flow component is low, the OSI is small (close to 0). In that case, OSI only has a small influence on equation (5.5) and RRT. However, when OSI approaches its limit of 0.5, its influence increases significantly.

$$\mathrm{RRT} \sim \frac{1}{(1 - 2 \cdot \mathrm{OSI}) \cdot \mathrm{TAWSS}} \tag{5.5}$$

The RRT is calculated from both TAWSS and OSI. Because both HWPs show a similar (but inverse) distribution in the example carotid bifurcation, RRT shows a highly similar spatial distribution as both previous HWPs (figure 5.2c).

5.3.4 Transverse wall shear stress (transWSS)

The previous HWPs (TAWSS, OSI and RRT) do not take into account the multi-directionality of the flow and can thus not differentiate between uni-axial and multi-directional flow. However, it has been hypothesised that this multi-directionality has influence on the endothelial permeability [10]. More recently, Wang *et al.* showed *in vitro* that flow perpendicular to the EC alignment activates pro-inflammatory pathways [11]. Therefore, the previously introduced metrics may not include all the relevant information about the WSS.

To include the multi-directionality of the shear stress, the transverse wall shear stress (transWSS) metric has been proposed by Peiffer *et al.* [12]. The transWSS is calculated as the time average of the WSS component perpendicular to the average shear stress vector. The average shear stress vector ($\vec{\tau}_{mean}$) is calculated using equation (5.6b) and the transWSS using equation (5.6a). The value of transWSS ranges between 0 and TAWSS. The transWSS can differentiate between multi-directional (high transWSS) and uni-directional flow (transWSS close to 0), but it can not differentiate between purely forward and flow reversions in unidirectional flow, in contrast to the OSI. Therefore, the transWSS can be used to complement the other metrics. Mohamied *et al.* showed that the transWSS correlates with the atherosclerotic lesions in the aortic branch ostia in rabbit aortas [13].

$$\text{transWSS} = \frac{1}{T}\int_0^T \left|\vec{\tau} \bullet \left(\vec{n} \times \frac{\vec{\tau}_{mean}}{\|\vec{\tau}_{mean}\|}\right)\right| \mathrm{d}t \tag{5.6a}$$

$$\text{with} \qquad \vec{\tau}_{mean} = \int_0^T \vec{\tau}\,\mathrm{d}t \tag{5.6b}$$

When comparing transWSS (figure 5.2d) with the other magnitude-based HWPs (figures 5.2a to 5.2c) for the example case of the mouse carotid bifurcation, the different overall pattern of the transWSS map stands out. While the TAWSS, OSI and RRT mainly suggest the outer side of the ECA sinus to be the atheroprone region, this zone is not highlighted by the transWSS. The zones characterised by a high transWSS, are closer to the inner side of the bifurcation. These zones spread out to both the lateral and the medial side of the arteries.

5.3.5 Other magnitude-based metrics

There are several other metrics that can be defined based on the magnitude of the WSS vector [14]–[16]. In the current thesis, however, we will focus on the ones listed above. Morbiducci *et al.* proposed a topology driven approach to project the WSS vector on the secondary and main flow directions [14]. The splitting is based on the centreline of the vasculature, which identifies the main flow direction. However, for trivial flows (laminar flows, following the centreline direction) this approach is equivalent to the approach followed by Peiffer *et al.* for the transWSS [12].

The directional oscillatory shear index (DOSI) was proposed by Chakraborty *et al.*, as another method to take the multi-directionality into account of flow. This metric been developed specifically for the unique flow patterns in an orbital shaker. The DOSI is based on a splitting of the OSI in its two principal directions. It differentiates between uniaxial oscillations (DOSI = 1) and oscillations equal in both principal directions (DOSI =0) [17].

5.3.6 Comparison of the magnitude-based HWP

In figure 5.3 a schematic overview is given over different flow conditions that can occur in an artery. The influence of the WSS in these conditions on the calculated magnitude-based HWPs is schematically plotted. The TAWSS does not include any directionality information. Therefore, the TAWSS can not differentiate between the different flow conditions and is equal in all three cases. The OSI is able to differentiate between purely forward flow (figure 5.3a) and pulsatile flow (figure 5.3b). However, OSI can not differentiate between uniaxial (figure 5.3b) and multi-directional pulsations (figure 5.3c). The

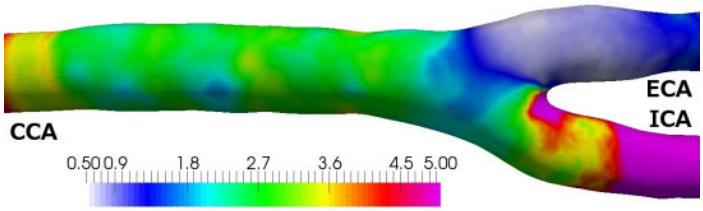

(a) TAWSS [Pa]

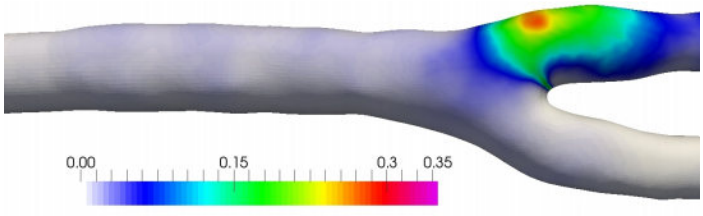

(b) OSI

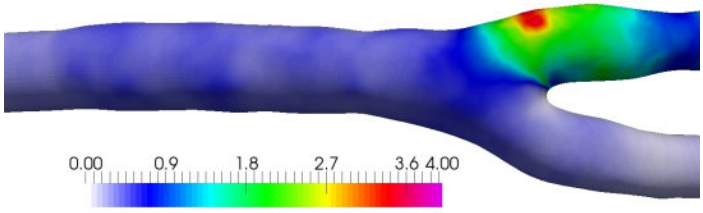

(c) RRT

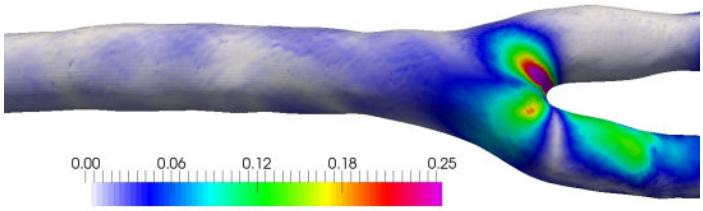

(d) transWSS [Pa]

Figure 5.2: The magnitude-based HWP in the murine carotid bifurcation

RRT is related to both the TAWSS and the OSI and can therefore also not differentiate multi-directional pulsatile flow. Since the transWSS takes the WSS component perpendicular to the main flow direction into account, it highlights regions with WSS in the secondary direction (at an angle of 90°). As a consequence the transWSS is not able to discriminate flow pulsations in the main flow direction.

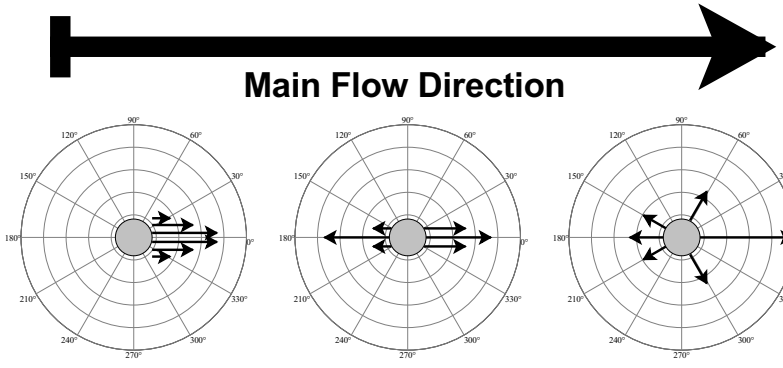

(a) Purely forward **(b)** Oscillatory **(c)** Multi-directional

	Purely forward	**Pulsatile**	**Multi-directional**
TAWSS	2.5	2.5	2.5
OSI	0	0.4	0.4
RRT~	0.4	2	2
transWSS	0	0	0.85

Figure 5.3: Comparison of different flow environments of endothelial cells with the same TAWSS. The influence of the flow environments on the different magnitude-based HWP is listed. (a) Purely forward flow regime. (b) Pulsatile flow regime with reversal. (c) Multi-directional disturbed flow regime (inspired by [12]).

5.4 Harmonic-based HWP

5.4.1 Dominant harmonic (DH)

The response of the vascular endothelium to shear stress is frequency-dependent [18]. This led to the development of metrics that include this extra piece of information. Himburg *et al.* introduced the dominant harmonic (DH), which identifies the zones where the endothelium is subject to higher frequency shear forces. After applying a Fourier analysis (FFT) to the magnitude of the WSS, the dominant harmonic is used to calculate the DH (equation (5.7)). In this formula ω_0 is the fundamental frequency and n the harmonic index so

that $n \cdot \omega_0$ indicates the n^{th} harmonic. Himburg *et al.* showed that the zones with a high harmonic content corresponds to regions with a low mean shear stress [19].

$$DH = n \ni \max\left(F\left(n\omega_0\right)\right) \quad , \quad F \equiv FFT\left(\|\vec{\tau}\|\right) \quad , \quad \omega_0 = \frac{2\pi}{T} \tag{5.7}$$

Only a very small zone with an elevated DH was present (at the stagnation point of the flow) in the murine carotid bifurcation.

5.4.2 Harmonic index (HI)

Gelfand *et al.* proposed the harmonic index (HI) as a HWP that includes the frequency-dependence [20]. This metric is defined as the harmonic amplitude of the oscillatory components over the total harmonic amplitude (including the mean, constant component), as shown in equation (5.8).

$$HI = \frac{\sum_{n=1}^{\infty} F\left(n\omega_0\right)}{\sum_{n=0}^{\infty} F\left(n\omega_0\right)} \quad , \quad F \equiv FFT\left(\|\vec{\tau}\|\right) \quad , \quad \omega_0 = \frac{2\pi}{T} \tag{5.8}$$

In comparison with DH, this metric has a continuous value rendering it a more appropriate choice to study the harmonic content of the WSS in the murine carotid bifurcation. In figure 5.4a, it can be seen that the HI parameter has a very smooth distribution. Globally, it highlights the same region (outer bend of the ECA) as the classical magnitude based HWPs for the simulated case.

5.4.3 Axial harmonic-based HWP

Lee *et al.* did not find the correspondence between low TAWSS and high DH in the human carotid bifurcation [21], in contrast with the results of Himburg *et al.* [19] in the iliac artery in pigs. A possible reason is the highly uni-axial flow in the porcine iliac artery in contrast to the more multi-axial flow of the human carotid bifurcation. Therefore, Lee *et al.* proposed to use the axial dominant harmonic (DH-axial) and axial harmonic index (HI-axial) instead of the DH and HI in this more multi-axial flow case [21]. Both axial metrics are calculated as their "normal" counterparts, except that the instantaneous wall shear vector projected on the average wall shear vector is used. This can be seen in equation (5.9b). The flow in the murine carotid bifurcation is highly uniaxial and thus the HI-axial and HI show a very similar pattern.

$$DH = n \ni \max\left(F\left(n\omega_0\right)\right) \quad , \quad F \equiv FFT\left(\vec{\tau} \bullet \vec{\tau}_{mean}\right) \quad , \quad \omega_0 = \frac{2\pi}{T} \tag{5.9a}$$

$$HI = \frac{\sum_{n=1}^{\infty} F(n\omega_0)}{\sum_{n=0}^{\infty} F(n\omega_0)} \quad , \quad F \equiv FFT\left(\vec{\tau} \bullet \vec{\tau}_{mean}\right) \quad , \quad \omega_0 = \frac{2\pi}{T} \tag{5.9b}$$

$$\text{with} \qquad \vec{\tau}_{mean} = \int_0^T \vec{\tau}\, dt \tag{5.9c}$$

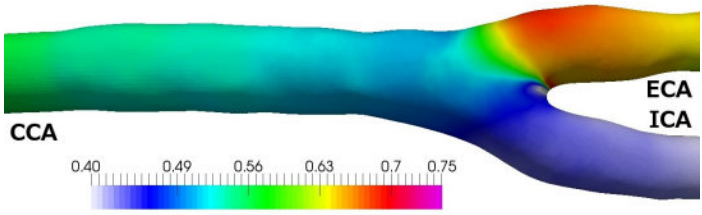

(a) HI

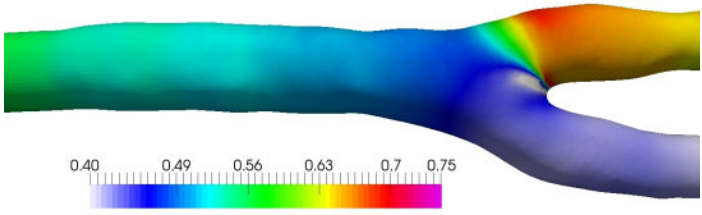

(b) HI-axial

Figure 5.4: The HI in the murine carotid bifurcation

5.5 Gradient based HWP

The tension exerted on the EC is expressed by the spatial gradient of the WSS (wall shear stress spatial gradient (WSSG): equation (5.10a)) [22]. Changes in the directionality can be quantified by the wall shear stress angle gradient (WSSAG) [16], [23]. In the WSSAG formula (equation (5.10b)), the WSS values in the surface mesh element (el) centroid and the surface mesh element nodes of the numerical grid are used. Moreover, (peak) temporal gradient of the WSS (wall shear stress temporal gradient (WSST): equation (5.10c)) has been proposed as a metric [24].

$$\text{WSSG} = \sqrt{\left(\left|\frac{\partial \vec{\tau}}{\partial x}\right|\right)^2 + \left(\left|\frac{\partial \vec{\tau}}{\partial y}\right|\right)^2 + \left(\left|\frac{\partial \vec{\tau}}{\partial z}\right|\right)^2} \tag{5.10a}$$

$$\text{WSSAG} = \frac{1}{T}\int_0^T \left|\frac{1}{A_i}\iint \nabla\phi_j \, dA_i\right| dt \tag{5.10b}$$

$$\text{with} \quad \phi_j = cos^{-1}\left(\frac{\vec{\tau}_i \cdot \vec{\tau}_j}{\|\vec{\tau}_i\| \cdot \|\vec{\tau}_j\|}\right) \quad , \quad i \equiv el\ centroid \quad , \quad j \equiv el\ node$$

$$\text{WSST} = max\left(\left|\frac{\partial \|\vec{\tau}\|}{\partial t}\right|\right) \tag{5.10c}$$

These parameters form a different approach to quantify the influence of WSS on the EC and were not considered in this thesis. First, Lee *et al.* showed that they are highly correlated to the other HWPs in the human carotid bifurcation [21]. Secondly, TAWSS showed to have a higher sensitivity for identifying zones prone to atherosclerosis compared to the (time averaged) WSSG in the human left coronary artery [25]. Moreover, Knight *et al.* noted that there are different definitions of the discrete WSSG in use. This distantiates the gradient values from the biological processes and limits their usefulness for practical use [26].

Bibliography Chapter 5

[1] O. Reynolds, 'On the Dynamical Theory of Incompressible Viscous Fluids and the Determination of the Criterion', *Philosophical Transactions of the Royal Society A: Mathematical, Physical and Engineering Sciences*, vol. 186, pp. 123–164, 1895.

[2] D. Katritsis, L. Kaiktsis, A. Chaniotis, J. Pantos, E. P. Efstathopoulos and V. Marmarelis, 'Wall shear stress: theoretical considerations and methods of measurement.' *Progress in cardiovascular diseases*, vol. 49, no. 5, pp. 307–329, 2007.

[3] A. M. Malek, S. L. Alper and S. Izumo, 'Hemodynamic shear stress and its role in atherosclerosis.' *JAMA : the journal of the American Medical Association*, vol. 282, no. 21, pp. 2035–2042, 1999.

[4] P. J. Brands, A. P. Hoeks, L. Hofstra and R. S. Reneman, 'A noninvasive method to estimate wall shear rate using ultrasound', *Ultrasound in Medicine & Biology*, vol. 21, no. 2, pp. 171–185, 1995.

[5] R. Stokholm, S. Oyre, S. Ringgaard, H. Flaagoy, W. Paaske and E. Pedersen, 'Determination of Wall Shear Rate in the Human Carotid Artery by Magnetic Resonance Techniques', *European Journal of Vascular and Endovascular Surgery*, vol. 20, no. 5, pp. 427–433, 2000.

[6] G. S. van Bochove, R. Straathof, R. Krams, K. Nicolay and G. J. Strijkers, 'MRI-determined carotid artery flow velocities and wall shear stress in a mouse model of vulnerable and stable atherosclerotic plaque.' *Magnetic Resonance Materials in Physics, Biology and Medicine*, vol. 23, no. 2, pp. 77–84, 2010.

[7] E. Cecchi, C. Giglioli, S. Valente, C. Lazzeri, G. F. Gensini, R. Abbate and L. Mannini, 'Role of hemodynamic shear stress in cardiovascular disease', *Atherosclerosis*, vol. 214, no. 2, pp. 249–256, 2011.

[8] D. N. Ku, D. P. Giddens, C. K. Zarins and S. Glagov, 'Pulsatile flow and atherosclerosis in the human carotid bifurcation. Positive correlation between plaque location and low oscillating shear stress.' *Arteriosclerosis*, vol. 5, no. 3, pp. 293–302, 1985.

[9] X. He, 'Pulsatile Flow in the Human Left Coronary Artery Bifurcation: Average Conditions', *Journal of Biomechanical Engineering*, vol. 118, no. 1, pp. 74–82, 1996.

[10] D. E. McMillan, 'Blood flow and the localization of atherosclerotic plaques', *Stroke*, vol. 16, no. 4, pp. 582–587, 1985.

[11] C. Wang, B. M. Baker, C. S. Chen and M. A. Schwartz, 'Endothelial Cell Sensing of Flow Direction', *Arteriosclerosis, Thrombosis, and Vascular Biology*, vol. 33, no. 9, pp. 2130–2136, 2013.

[12] V. Peiffer, S. J. Sherwin and P. D. Weinberg, 'Computation in the rabbit aorta of a new metric - the transverse wall shear stress - to quantify the multidirectional character of disturbed blood flow.' *Journal of biomechanics*, vol. 46, no. 15, pp. 2651–2658, 2013.

[13] Y. Mohamied, E. M. Rowland, E. L. Bailey, S. J. Sherwin, M. a. Schwartz and P. D. Weinberg, 'Change of Direction in the Biomechanics of Atherosclerosis', *Annals of Biomedical Engineering*, vol. 43, no. 1, pp. 16–25, 2015.

[14] U. Morbiducci, D. Gallo, S. Cristofanelli, R. Ponzini, M. a. Deriu, G. Rizzo and D. a. Steinman, 'A rational approach to defining principal axes of multidirectional wall shear stress in realistic vascular geometries, with application to the study of the influence of helical flow on wall shear stress directionality in aorta', *Journal of Biomechanics*, vol. 48, no. 6, pp. 899–906, 2015.

[15] C. Karmonik, C. Yen, O. Diaz, R. Klucznik, R. G. Grossman and G. Benndorf, 'Temporal variations of wall shear stress parameters in intracranial aneurysms–importance of patient-specific inflow waveforms for CFD calculations.' *Acta neurochirurgica*, vol. 152, no. 8, 1391–8, discussion 1398, 2010.

[16] S. Hyun, C. Kleinstreuer and J. P. Archie, 'Hemodynamics analyses of arterial expansions with implications to thrombosis and restenosis', *Medical Engineering and Physics*, vol. 22, pp. 13–27, 2000.

[17] A. Chakraborty, S. Chakraborty, V. R. Jala, B. Haribabu, M. K. Sharp and R. E. Berson, 'Effects of biaxial oscillatory shear stress on endothelial cell proliferation and morphology', *Biotechnology and Bioengineering*, vol. 109, no. 3, pp. 695–707, 2012.

[18] H. A. Himburg, S. E. Dowd and M. H. Friedman, 'Frequency-dependent response of the vascular endothelium to pulsatile shear stress.' *American journal of physiology. Heart and circulatory physiology*, vol. 293, no. 1, H645–H653, 2007.

[19] H. A. Himburg and M. H. Friedman, 'Correspondence of low mean shear and high harmonic content in the porcine iliac arteries.' *Journal of biomechanical engineering*, vol. 128, no. 6, pp. 852–856, 2006.

[20] B. D. Gelfand, F. H. Epstein and B. R. Blackman, 'Spatial and spectral heterogeneity of time-varying shear stress profiles in the carotid bifurcation by phase-contrast MRI', *Journal of Magnetic Resonance Imaging*, vol. 24, no. 6, pp. 1386–1392, 2006.

[21] S.-W. Lee, L. Antiga and D. A. Steinman, 'Correlations among indicators of disturbed flow at the normal carotid bifurcation.' *Journal of biomechanical engineering*, vol. 131, no. 6, p. 061 013, 2009.

[22] M. Lei, C. Kleinstreuer and G. Truskey, 'A focal stress gradient-dependent mass transfer mechanism for atherogenesis in branching arteries', *Medical Engineering & Physics*, vol. 18, no. 4, pp. 326–332, 1996.

[23] P. W. Longest and C. Kleinstreuer, 'Computational haemodynamics analysis and comparison study of arterio-venous grafts.' *Journal of medical engineering & technology*, vol. 24, no. 3, pp. 102–10, 2000.

[24] M. Ojha, 'Wall shear stress temporal gradient and anastomotic intimal hyperplasia', *Circulation Research*, vol. 74, no. 6, pp. 1227–1231, 1994.

[25] F. Rikhtegar, J. a. Knight, U. Olgac, S. C. Saur, D. Poulikakos, W. Marshall, P. C. Cattin, H. Alkadhi and V. Kurtcuoglu, 'Choosing the optimal wall shear parameter for the prediction of plaque location—A patient-specific computational study in human left coronary arteries', *Atherosclerosis*, vol. 221, no. 2, pp. 432–437, 2012.

[26] J. Knight, U. Olgac, S. C. Saur, D. Poulikakos, W. Marshall, P. C. Cattin, H. Alkadhi and V. Kurtcuoglu, 'Choosing the optimal wall shear parameter for the prediction of plaque location-A patient-specific computational study in human right coronary arteries.' *Atherosclerosis*, vol. 211, no. 2, pp. 445–450, 2010.

III

Pathophysiology of atherosclerosis in mouse models: imaging results

Chapters

Chapter 6

Assessment of carotid anatomy and (patho)physiology using ultrasound

6.1 Mice included in this study

In the next sections, an overview is presented of the results of the small animal US measurements that were performed in the context of this thesis. Female ApoE$^{-/-}$ (n=9) and their ApoE$^{-/-}$ Fbn1$^{C1039G+/-}$ (n=14) littermates were studied. They were fed a Western-type diet (TD88137, Harlan Teklad, Madison, WI) for up to 20 weeks, starting at an age of 6 weeks. All experiments were conducted according to the European Commission guidelines and were approved by the Animal Ethics Committee of Ghent University.

Table 6.1: Overview of the number of mice included in the measurement protocol. The columns are grouped in time after the start of the diet (starting at an age of 6 weeks).

	W0	W5	W10	W15	W20
ApoE$^{-/-}$	9	8	8	8	8
ApoE$^{-/-}$ Fbn1$^{C1039G+/-}$	14	13	12	11	8

The animals underwent a 5-weekly measurement protocol consisting of either solely US or US and μCT. The drop-out of animals with time is because of sudden death or because of euthanasia for ethical reasons (weight loss or

signs of stress: panting, head tilt, a hunched body posture, and immobility). The sudden deaths were related to the severe phenotype [1], while some deaths occurred because of a combination of the severe phenotype and the anaesthesia. The total amount of mice included at each time points is listed in table 6.1.

For the statistical analysis a linear mixed model (LMM) approach was applied. This is a modelling strategy to determine which fixed factors, i.e. grouping variables, have a significant outcome on the measurements. The different grouping factors were: time after the start after the diet (weeks 0, 5, 10, 15 or 20), the strain (ApoE$^{-/-}$ or ApoE$^{-/-}$ Fbn1$^{C1039G+/-}$) and the side of the measurement (left or right).

A short introduction to the LMM is added in Appendix A. The analysis was performed in SPSS Statistics 22 (IBM, Armonk, NY, US). Results were deemed significant if $p<0.05$ and highly significant for $p<0.01$. To compare individual groups, the estimated marginal means of the fitted models were compared using Bonferroni correction (where applicable).

6.2 Carotid flow velocities

The pulsed wave Doppler ultrasound (PW Doppler US) signal (velocity of the red blood cells in the control volume) was obtained from the CCA, the ECA and the ICA branches. The maximum envelope of this signal was tracked in an application written in Matlab (Mathworks, Natick, Massachusetts, USA) (see figure 6.1a). A 3-cycle (based on tracking of the QRS-complex at the ECG signal) averaged curve was constructed to further limit noise (figure 6.1b). From this curve, the systolic velocity (V_{sys}) was obtained as the maximum of the curve; the end-diastolic velocity (V_{ed}) was obtained by selecting the minimum velocity located before the foot of the flow wave. Finally, the cycle averaged value of the velocity (V_{avg}) was calculated.

Common carotid artery

For the CCA an overview of the measured velocities is given in figure 6.2. In panel A) the V_{sys} (top, $\triangle$), V_{avg} (middle, $\bigcirc$) and the V_{ed} (bottom, $\triangledown$) are shown for the ApoE$^{-/-}$ mice (blue). During the heart cycle, the velocity will range from the V_{ed} to the V_{sys} velocity and cycle through the light blue shaded area in figure 6.2 A). For the ApoE$^{-/-}$ Fbn1$^{C1039G+/-}$ mice, the results are plotted in red in figure 6.2B. On average, over time a small decrease in V_{sys} is visible (time is a significant grouping factor for V_{sys}: $p<0.01$), but neither V_{avg} nor V_{ed} change over time ($p>0.05$). To allow for an easy visual comparison of both strains of mice, the ApoE$^{-/-}$ Fbn1$^{C1039G+/-}$ results are plotted in a lighter shade on the ApoE$^{-/-}$ panel (A) and vice versa. The

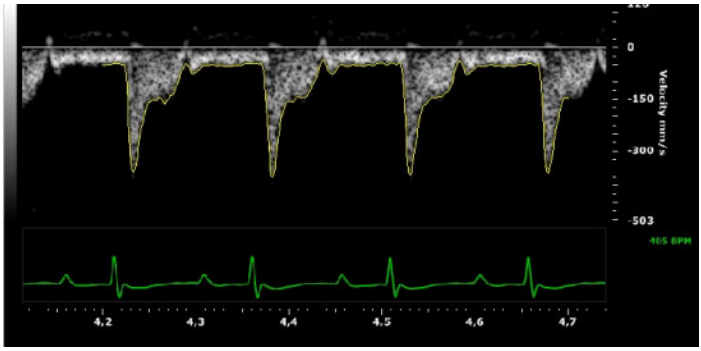

(a) Tracking of the PW Doppler US signal (yellow-line)

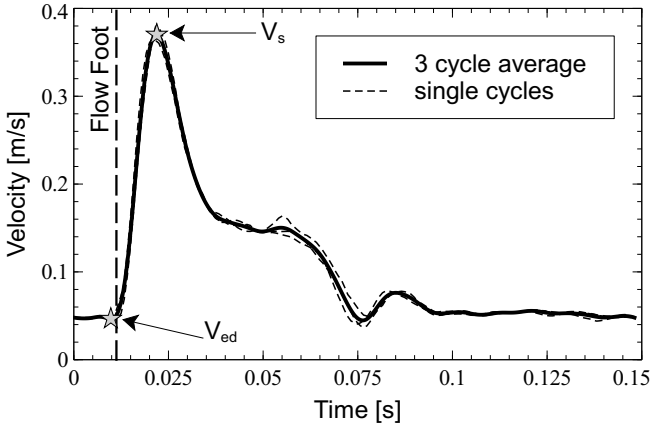

(b) Calculating 3-cycle average

Figure 6.1: Post-processing of the PW Doppler US signal in Matlab. (a) Tracking of the maximum envelope of the PW Doppler US signal (yellow-line) for an example CCA. A sudden increase in intensity is detected by the algorithm. Afterwards, limited Savitzky-Golay-filtering was applied to filter out the high-frequent scatter noise. (b) The three cycle average (thick solid line) is taken of the individual curves (thin dashed lines) to further reduce the noise. The V_{sys}, V_{ed} and the location of the flow foot are calculated automatically.

estimated marginal mean (LMM) values for the V_{sys} are 0.316 and 0.272 for the ApoE$^{-/-}$ and the ApoE$^{-/-}$ Fbn1$^{C1039G+/-}$ strain respectively and this difference is highly significant ($p<0.01$). The plots also show that the three velocity profile parameters are the same for both strains at weeks 0 and 20 but that for the other time points, the blood velocity is lower in the ApoE$^{-/-}$ Fbn1$^{C1039G+/-}$ strain (for V_{sys} $p<0.05$, $p=0.11$ and $p<0.05$ for weeks 5, 10 and 15 – t-test on the left / right aggregated data). Strain is a significant grouping variable for V_{sys} ($p<0.05$) and V_{ed} ($p<0.01$) but not significant for V_{avg} ($p=0.05$).

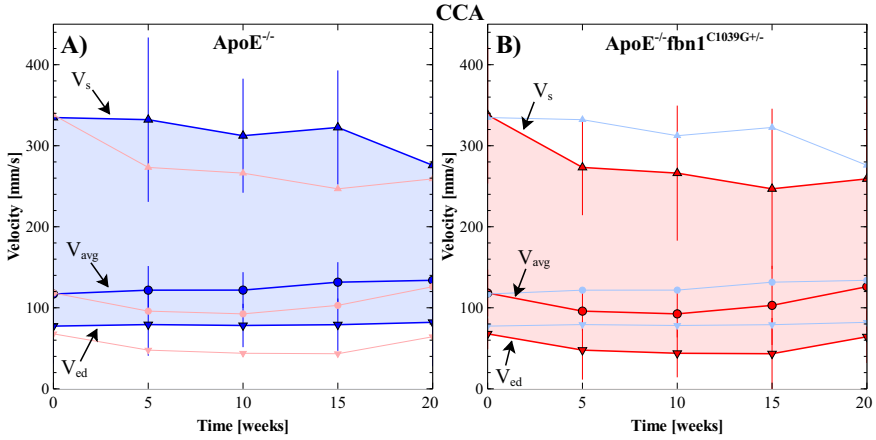

Figure 6.2: Evolution of the measured velocity in the CCA. The measured velocities for the ApoE$^{-/-}$ mice are plotted in blue on the left and for the ApoE$^{-/-}$ Fbn1$^{C1039G+/-}$ in red on the right. The other strain is plotted in a lighter tint for an easy comparison. The systolic velocity (V_{sys}-△), the average velocity (V_{avg}-◯) and the end diastolic velocity (V_{ed}-▽) are plotted.

External carotid artery

The velocity in the ECA branch (figure 6.3) is lower compared to the CCA (V_{sys} of 0.12 vs. 0.30 m/s) and this difference is highly significant ($p<0.01$ – paired t-test after aggregating time and side). For the ECA both the ApoE$^{-/-}$ (panel A) and ApoE$^{-/-}$ Fbn1$^{C1039G+/-}$ mice (panel B), show a clear increase in blood velocity over time (time grouping $p<0.01$ for V_{sys}, V_{avg} and V_{ed}). Next to this, the difference between V_{sys} and V_{ed} also increases. In the figure this is clearly shown by the widening of the coloured band. The difference between the estimated means for the ApoE$^{-/-}$ and the ApoE$^{-/-}$ Fbn1$^{C1039G+/-}$ strain is small but significant for the V_{sys} (0.121 vs. 0.107m/s; $p<0.05$ – LMM). Both V_{avg} (0.042 vs. 0.036 m/s; $p=0.01$ – LMM) and V_{ed} (0.018 vs. 0.010 m/s; $p<0.01$ – LMM) are more clearly lower for the ApoE$^{-/-}$ Fbn1$^{C1039G+/-}$ strain. Strain is a significant grouping variable for both V_{avg} - $p<0.05$ and V_{ed} - $p<0.05$.

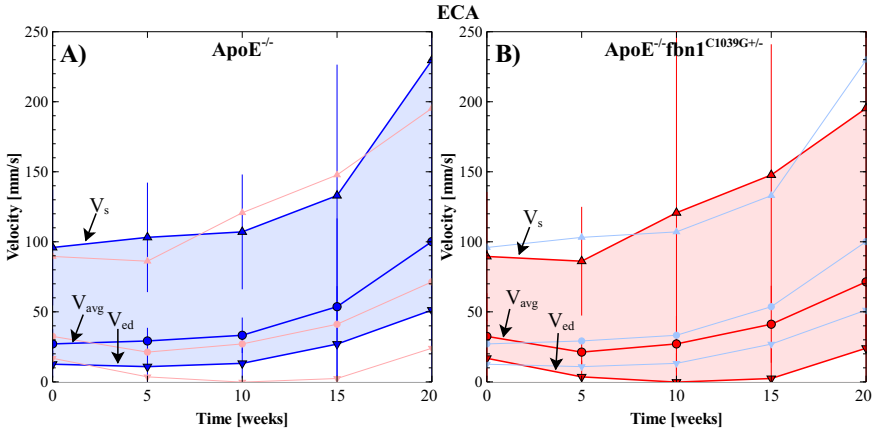

Figure 6.3: Evolution of the measured velocity in the ECA. The measured velocities for the ApoE$^{-/-}$ mice are plotted in blue on the left and for the ApoE$^{-/-}$ Fbn1$^{C1039G+/-}$ in red on the right. The other strain is plotted a lighter tint for an easy comparison. The systolic velocity (V_{sys}-△), the average velocity (V_{avg}-◯) and the end diastolic velocity (V_{ed}-▽) are plotted.

Internal carotid artery

The amplitude of the measured ICA velocity (0.27 m/s - Figure 6.4) is much closer to the CCA velocity (0.30 m/s) compared to the ECA velocity (0.12 m/s). The difference between CCA-ICA is not significant (p=0.055) while the difference between ICA-ECA is highly significant (p<0.01 – paired t-test after aggregating over time and side). At baseline (week 0), the velocity measured in the ApoE$^{-/-}$ Fbn1$^{C1039G+/-}$ mice (panel B) is clearly lower than the velocity measured in the ApoE$^{-/-}$ mice (panel A) (p<0.01 for V_{sys} – t-test aggregated over side). The increase in velocity over time that was visible in the ECA, is also present in the ICA (time is a highly significant (p<0.01) grouping factor for the three measures). This increase is more outspoken in the ApoE$^{-/-}$ Fbn1$^{C1039G+/-}$ strain (interaction between time and strain is significant p=0.011 in the LMM), resulting in an higher velocity in the ApoE$^{-/-}$ Fbn1$^{C1039G+/-}$ mice at week 20 compared to the ApoE$^{-/-}$ mice (but not significant p=0.09 for V_{sys} – t-test after aggregating over side). Nonetheless, it is important to keep in mind that the variability of the data also increases over time, resulting in higher error bars at these time points. Especially in the ApoE$^{-/-}$ Fbn1$^{C1039G+/-}$ strain, the V_{sys} rises more compared to the V_{ed}. This results in a broader range of velocities within one heart cycle.

Overview

An overview of the significance of the different grouping factors in the LMM is given in table 6.2. Side (left or right) did not influence any of the measured velocity parameters in any of the branches.

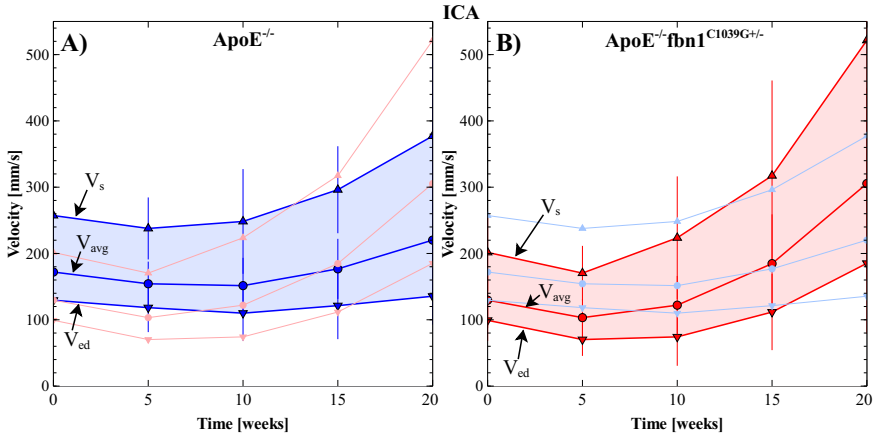

Figure 6.4: Evolution of the measured velocity in the ICA. The measured velocities for the ApoE$^{-/-}$ mice are plotted in blue on the left and for the ApoE$^{-/-}$ Fbn1$^{C1039G+/-}$ in red on the right. The other strain is plotted in a lighter tint for an easy comparison. The systolic velocity (V_{sys}-△), the average velocity (V_{avg}-◯) and the end diastolic velocity (V_{ed}-▽) are plotted.

Table 6.2: For every velocity parameter a LMM was applied to test if it has a significant influence. For the V_{sys}, V_{avg} and V_{ed} the significance is listed of the three grouping variables: time, strain and side.

	time	strain	side
	V_{sys}		
CCA	.003**	.039*	.276
ECA	.000**	.203	.169
ICA	.000**	.000**	.143
	V_{avg}		
CCA	.530	.050	.200
ECA	.000**	.031*	.291
ICA	.000**	.000**	.232
	V_{ed}		
CCA	.207	.004**	.917
ECA	.003**	.034*	.132
ICA	.000**	.001**	.981

* Significant ($p<0.05$)
** Highly significant ($p<0.01$)

The significant influence of time and strain (in most cases in table 6.2), is likely linked to atherosclerosis development. Both strains of mice develop atherosclerotic plaques, resulting in a narrowing of the lumen leading to a locally increased blood velocity. In chapter 7 we will show that atherosclerotic plaque development and stenosis mainly occurs in the ECA and ICA and only to a lesser extent in the CCA (close to the carotid bifurcation) in mice. The decrease in cross sectional area of the lumen of the ICA and ECA is likely a reason for this increased velocity. Next to this, plaques in the ApoE$^{-/-}$ Fbn1$^{C1039G+/-}$ mice are more pronounced than in the ApoE$^{-/-}$ mice [1]–[3] which is a possible reason for the steeper increase in velocity in the ICA for the ApoE$^{-/-}$ Fbn1$^{C1039G+/-}$ mice.

On the other hand, especially the ApoE$^{-/-}$ Fbn1$^{C1039G+/-}$ mice also show other haemodynamics-related symptoms, such as: ventricular dysfunction, myocardial infarction, cardiac hypertrophy, disturbed cerebral flow and brain hypoxia [1]. It is therefore also possible that the reduced cardiac function in the ApoE$^{-/-}$ Fbn1$^{C1039G+/-}$ mice partially explains the lower blood flow and thus lower blood velocity. This is especially the case for measurements in the CCA, where the occurrence of plaque is lesser compared to the ECA and ICA. On the other hand, a (partial) occlusion in the brain can increase the downstream resistance and thus also offer a possible explanation for the reduced blood velocity.

6.3 Resistivity (RI) and Pulsatility (PI) indices

Definition of the RI and PI

The resistivity index (RI) and pulsatility index (PI) are commonly used in literature to quantify flow velocity profiles and express downstream properties [4]–[8]. Both indices are calculated based on the V_{sys}, V_{ed} and V_{avg}.

$$\text{Resistive Index} = \frac{V_{sys} - V_{ed}}{V_{sys}} \tag{6.1a}$$

$$\text{Pulsatility Index} = \frac{V_{sys} - V_{ed}}{V_{avg}} \tag{6.1b}$$

Resistivity index

The RI results are plotted in figure 6.5. The scatter for every bar is big compared to the differences that occur. The figure shows that the on average the RI is lower for the ICA (0.58) compared to the other two branches (CCA-0.78 and ECA-0.89). All three paired comparisons for 2 RI locations were highly significant ($p<0.01$ – paired t-test after aggregating side and time). The LMM

did not reveal a statistical significant effect of the grouping factor strain for the CCA or the ICA measurements ($p>0.05$). However, for the ECA measurements strain was a statistically significant ($p<0.05$) grouping factor. Over time, the differences are small, with only for the ICA a consistent increase in both strains. Yet, time showed to be a significant factor for the ECA RI ($p<0.05$) and a highly significant factor for the ICA RI ($p<0.01$).

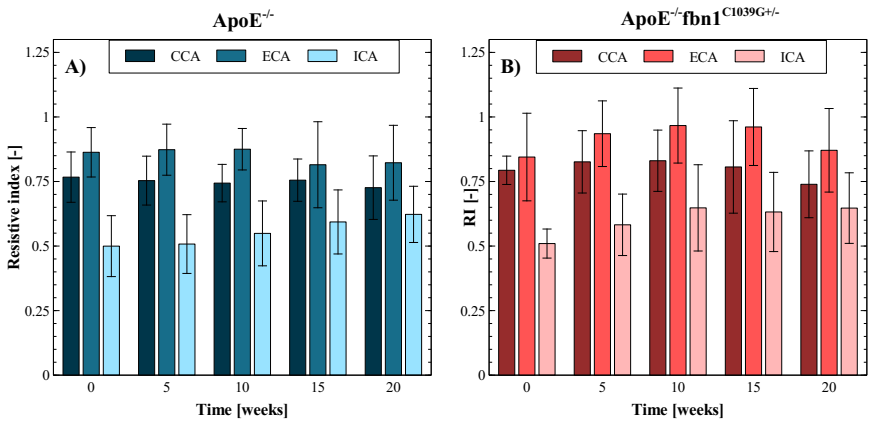

Figure 6.5: Overview of the resistivity index (RI) for both the (A-blue) ApoE$^{-/-}$ and the (B-red) ApoE$^{-/-}$ Fbn1$^{C1039G+/-}$ mice. The CCA, ECA and ICA are shaded from dark to light.

Pulsatility index

In comparison with the RI, the same trends are visible for the PI (figure 6.6). The ECA has the highest value (3.76), the CCA the middle value (2.12) and ICA the lowest (0.97). The average differences between all three locations were significant ($p<0.01$ – paired t-test after aggregating over time and side). For the ApoE$^{-/-}$ Fbn1$^{C1039G+/-}$ strain, the CCA/ECA values are higher and the ICA values lower. The differences are larger compared to the RI, but the error bars (standard deviation) have increased accordingly. As a result the grouping according to strain did not have significant influence on the PI for any of the branches. Time was a significant grouping factor for all three branches were the PI was calculated.

Overview

For both the RI and the PI, the side of the measurement did not have a significant influence on the result (table 6.3).

6.4 Carotid diameters

The inner diameter was measured in the three branches of the carotid bifurcation with motion mode ultrasound (M-mode US). For this goal, the RF data

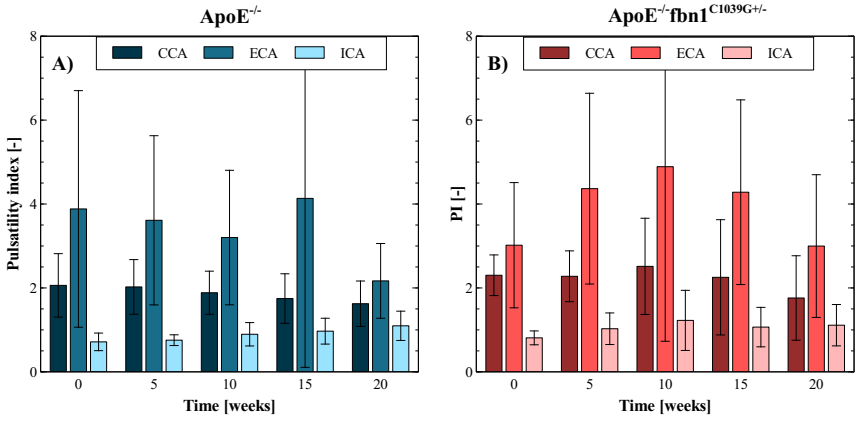

Figure 6.6: Overview of the pulsatility index (PI) for both the (A-blue) ApoE$^{-/-}$ and the (B-red) ApoE$^{-/-}$ Fbn1$^{C1039G+/-}$ mice. The CCA, ECA and ICA are shaded from dark to light.

Table 6.3: For both the PI and the RI the influence of the three grouping variables is listed: time, strain and side.

	PI			RI		
	time	**strain**	**side**	**time**	**strain**	**side**
CCA	.003**	.252	.203	.231	.195	.965
ECA	.001**	.125	.070	.018*	.029*	.885
ICA	.000**	.100	.542	.000**	.138	.137

* Significant ($p<0.05$)
** Highly significant ($p<0.01$)

of the M-mode measurements was tracked using the algorithm described by Rabbe *et al.* [9]. The exact value of the diameter is highly dependent on the exact location of the measurement. Plaques that show signs of inward remodelling will result in a significant narrowing of the lumen. In the measurements the diameter is measured in a region were no or minimal inward remodelling was visible. Nevertheless, the results should be interpreted with care.

Common carotid artery

For the CCA, the measured diameters (d_{max}, d_{avg} and d_{min}) are shown in figure 6.7. The measured diameters of the ApoE$^{-/-}$ and ApoE$^{-/-}$ Fbn1$^{C1039G+/-}$ mice are very similar (strain is no significant grouping factor for the CCA diameter $p>0.05$). Further, there is almost no change in diameter visible over time (time is no significant grouping factor $p>0.05$). At week 20 of the

ApoE$^{-/-}$ Fbn1$^{C1039G+/-}$ mice, there is a (small) increase in diameter from week 15. However, this increase is smaller than the standard deviation of the measurements and is thus not significant (d_{max} p=0.20 – paired t-test after aggregating over side). The difference between d_{max} and d_{min} is also similar for both strains (p=0.49 – t-test after aggregating over side and time).

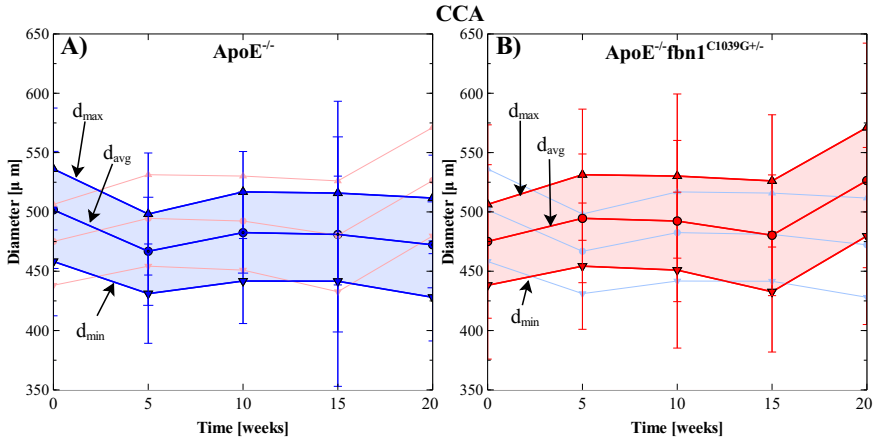

Figure 6.7: Evolution of the measured diameter in the CCA. The measured diameter for the ApoE$^{-/-}$ mice are plotted in blue (A) and for the ApoE$^{-/-}$ Fbn1$^{C1039G+/-}$ in red (B). The other strain is plotted a lighter tint for an easy comparison. The maximum diameter (d_{max}-△), the average diameter (d_{avg}-◯) and the minimum diameter (d_{min}-▽) are plotted.

External carotid artery

In figure 6.8, the diameters of the ECA are shown. The average ECA diameter is smaller (d_{max}:410 μm) than the CCA (d_{max}:524 μm) (p<0.05 — paired t-test after aggregating time and side). Also for the ECA there is no clear difference visible between the ApoE$^{-/-}$ and the ApoE$^{-/-}$ Fbn1$^{C1039G+/-}$ mice (p>0.05 for strain as grouping factor – LMM). From week 10 on, there is a small decrease in diameter visible for both strains (time is a significant grouping factor for d_{max}, d_{avg} and d_{min} p<0.05). The difference between the maximum and minimum diameter is smaller in the ECA compared to the CCA (p<0.01 — paired t-test after aggregating time and side).

Internal carotid artery

Finally, the diameter results for the ICA are plotted in figure 6.9. The d_{max} of the ICA (379μm) is a little smaller than the d_{max} of the ECA (410μm) (p<0.01 – paired t-test after aggregating time and side). Between species and over time there is not much change. Although, similar to the CCA case, there is also an increase in diameter present at week 20.

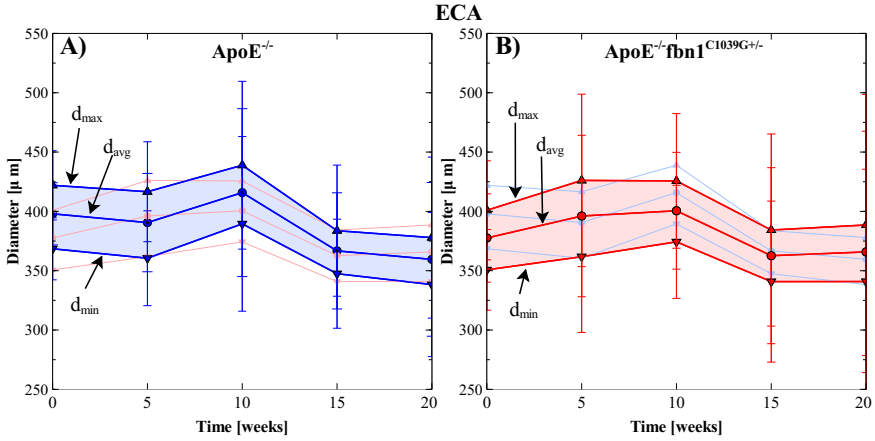

Figure 6.8: Evolution of the measured diameter in the ECA. The maximum diameter (d_{max}-△), the average diameter (d_{avg}-◯) and the minimum diameter (d_{min}-▽) are plotted.

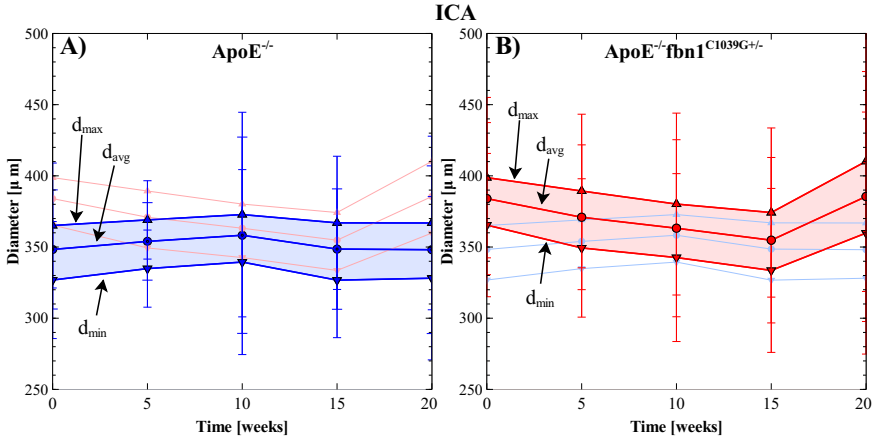

Figure 6.9: Evolution of the measured diameter in the ICA. The maximum diameter (d_{max}-△), the average diameter (d_{avg}-◯) and the minimum diameter (d_{min}-▽) are plotted.

Overview

Remarkably, side was a significant ($p<0.05$) grouping factor for the CCA-d_{max} (Table 6.4). As described in the previous paragraphs, the differences for the measured diameters, with regard to the different grouping factors, were smaller compared to the velocity measurements. This results in less significant factors for the measured diameter (table 6.4). The only consistent significant grouping factor is the time for the ECA branch. In a further chapter (chapter 7) it will be shown that the atherosclerotic plaque development influences the ECA the most and that the plaque is much less localised there. The ECA plaque has a more spread out phenotype. Therefore, this might be an explanation why only in the ECA a clear decrease was visible. As a reminder, the diameter was measured in a part of the artery where the least lumen narrowing was visible.

Table 6.4: LMM analysis of the maximum (d_{max}), average (d_{avg}) and minimum (d_{min}) measured using M-mode US. For the different grouping factors, their statistical significance is show.

	time	**strain**	**side**
		d_{max}	
CCA	.093	.140	.049*
ECA	.009**	.405	.159
ICA	.951	.174	.656
		d_{avg}	
CCA	.308	.241	.130
ECA	.017*	.261	.111
ICA	.953	.242	.607
		d_{min}	
CCA	.594	.324	.385
ECA	.047*	.191	.088
ICA	.898	.278	.556

* Significant ($p<0.05$)
** Highly significant ($p<0.01$)

6.5 Carotid distensibility

The distension is calculated according to equation 6.2 [10] and is an indication of the local functional stiffness of the artery (although pressure is required to

truly assess stiffness).

$$dist = \frac{d_{\max} - d_{\min}}{d_{\min}} \tag{6.2}$$

An overview of the resulting distension is plotted in figure 6.10. The global averages for the CCA, ECA and ICA are: 18.0, 14.0 and 11.4%. The distension of the CCA is thus on average higher than the distension of the ECA or ICA. The pairwise comparisons of the three locations are highly significant ($p<0.01$ – paired t-test after aggregating side and time). The estimated means for the ApoE$^{-/-}$ and ApoE$^{-/-}$ Fbn1$^{C1039G+/-}$ mice are similar: 18 vs. 18.2 ($p=0.783$ - CCA), 13.3 vs. 14.2 ($p=0.277$ - ECA) and 11.4 vs. 11.3% ($p=0.838$ - ICA). Time is a significant grouping factor for the distensibility of the CCA ($p<0.01$) and the ECA ($p<0.05$) but not for the ICA ($p=0.097$).

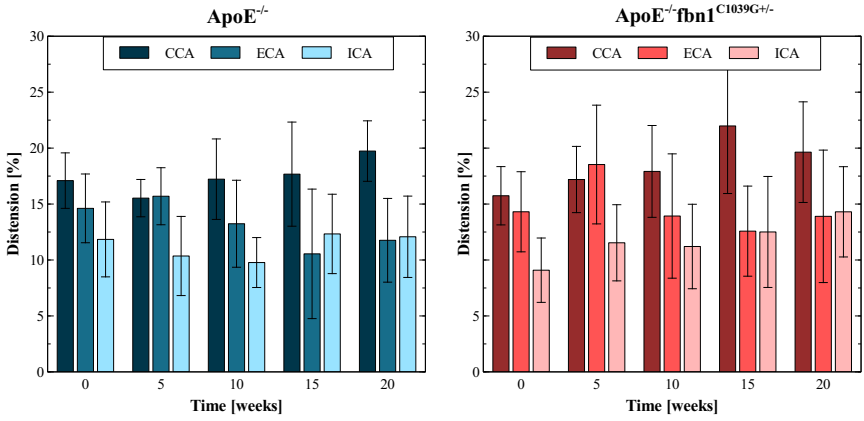

Figure 6.10: Overview of the distention in the three main branches of the carotid bifurcation. On the left (blue) the ApoE$^{-/-}$ mice are shown and on the right (red) the ApoE$^{-/-}$ Fbn1$^{C1039G+/-}$ mice. On the x-axis the results are grouped according to the timing of the measurement. The CCA, ECA and ICA are show coloured from dark to light.

6.6 Conclusion

This chapter presented an overview of the US measurements in both ApoE$^{-/-}$ and ApoE$^{-/-}$ Fbn1$^{C1039G+/-}$ mice. For the ECA and ICA an increase in velocity over time was present. Overall, the velocities measured in the carotid bifurcations of ApoE$^{-/-}$ Fbn1$^{C1039G+/-}$ mice were a little bit (but significantly) lower than the velocities of ApoE$^{-/-}$ mice. However, in ApoE$^{-/-}$ Fbn1$^{C1039G+/-}$ mice the velocity increased more over time for the ECA and

ICA. Both the RI and the PI were similar for both strains. Next to this, the diameter measurements (M-mode US) were also similar for both strains. Only the small decrease of the ECA diameter was significant. Finally, no significant difference between ApoE$^{-/-}$ and ApoE$^{-/-}$ Fbn1$^{C1039G+/-}$ mice was found with regard to the distensibility of the carotid arteries. The distensibility of the CCA was markedly higher compared to the ECA and ICA.

Overall, we can conclude that the bulk flow (velocity) and distension parameters assessed by US did not show distinct differences between both strains. A more detailed study of the local haemodynamics is needed to assess the influence of haemodynamics on atherosclerotic plaque development.

Bibliography Chapter 6

[1] C. Van der Donckt, J. L. Van Herck, D. M. Schrijvers, G. Vanhoutte, M. Verhoye, I. Blockx, A. Van Der Linden, D. Bauters, H. R. Lijnen, J. C. Sluimer, L. Roth, C. E. Van Hove, P. Fransen, M. W. Knaapen, A.-S. A.-S. Hervent, G. W. De Keulenaer, H. Bult, W. Martinet, A. G. Herman and G. R. Y. De Meyer, 'Elastin fragmentation in atherosclerotic mice leads to intraplaque neovascularization, plaque rupture, myocardial infarction, stroke, and sudden death.' *European heart journal*, vol. 36, no. 17, pp. 1049–1058, 2014.

[2] D. De Wilde, B. Trachet, C. Van der Donckt, B. Vandeghinste, B. Descamps, C. Vanhove, G. R. Y. De Meyer and P. Segers, 'Vulnerable plaque detection and quantification with gold particle-enhanced computed tomography in atherosclerotic mouse models.' *Molecular imaging*, vol. 14, pp. 9–19, 2015.

[3] J. L. Van Herck, G. R. De Meyer, W. Martinet, C. E. Van Hove, K. Foubert, M. H. Theunis, S. Apers, H. Bult, C. J. Vrints and A. G. Herman, 'Impaired Fibrillin-1 Function Promotes Features of Plaque Instability in Apolipoprotein E-Deficient Mice', *Circulation*, vol. 120, no. 24, pp. 2478–2487, 2009.

[4] M. Schöning, J. Walter, P. Scheel, M. Schoning, J. Walter and P. Scheel, 'Estimation of cerebral blood flow through color duplex sonography of the carotid and vertebral arteries in healthy adults', *Stroke*, vol. 25, no. 1, pp. 17–22, 1994.

[5] T. Okura, 'Intrarenal and carotid hemodynamics in patients with essential hypertension', *American Journal of Hypertension*, vol. 17, no. 3, pp. 240–244, 2004.

[6] J. Jung, J. Chang, S. Oh and M. Choi, 'Spectral Doppler ultrasound in the major arteries of normal conscious immature micropigs', *Journal of Veterinary Science*, vol. 11, no. 2, p. 155, 2010.

[7] S. Manabe, T. Okura, S. Watanabe and J. Higaki, 'Association between carotid haemodynamics and inflammation in patients with essential hypertension', *Journal of Human Hypertension*, vol. 19, no. 10, pp. 787–791, 2005.

[8] P. Wohlfahrt, A. Krajcoviechova, M. Jozifova, O. Mayer, J. Vanek, J. Filipovsky, S. Laurent and R. Cifkova, 'Large artery stiffness and carotid flow pulsatility in stroke survivors.' *Journal of hypertension*, vol. 32, no. 5, 1097–103, discussion 1103, 2014.

[9] S. I. Rabben, S. Bjærum, V. Sørhus and H. Torp, 'Ultrasound-based vessel wall tracking: An auto-correlation technique with RF center frequency estimation', *Ultrasound in Medicine and Biology*, vol. 28, no. 4, pp. 507–517, 2002.

[10] P. Segers, S. I. Rabben, J. De Backer, J. De Sutter, T. C. Gillebert, L. Van Bortel, P. Verdonck, S. Inge, J. D. Backer, J. D. Sutter, T. C. Gillebert, L. V. Bortel and P. Verdonck, 'Functional analysis of the common carotid artery: relative distension differences over the vessel wall measured in vivo', *Journal of Hypertension*, vol. 22, no. 5, pp. 973–981, 2004.

Chapter 7

Gold particle–enhanced μCT: vulnerable plaque detection and quantification *

7.1 Introduction

Cardiovascular disease is the leading cause of morbidity and mortality in the developed countries [1], with atherosclerosis often being the underlying cause of myocardial infarction and stroke. Atherosclerosis is a slowly progressing chronic inflammatory disease of the medium-sized and large arteries and characterised by the development of atherosclerotic plaques. One of the major emerging clinical challenges is the need to differentiate between vulnerable plaques, which are likely to cause embolic stroke upon rupture and thus need immediate treatment, and stable plaques, which do not cause an immediate threat. Traditionally, the ApoE$^{-/-}$ deficient mouse model is the most popular mouse model to study atherosclerotic plaque at a pre-clinical stage [2]–[5]. When fed a Western type diet, these mice develop stable atherosclerotic plaques. Recently, ApoE$^{-/-}$ Fbn1$^{C1039G+/-}$ mice have been described as a novel mouse model for vulnerable plaques and plaque rupture

*This chapter is based on the work: D. De Wilde, B. Trachet, C. Van der Donckt, B. Vandeghinste, B. Descamps, C. Vanhove, G. R. Y. De Meyer and P. Segers, 'Vulnerable plaque detection and quantification with gold particle-enhanced computed tomography in atherosclerotic mouse models.' *Molecular imaging*, vol. 14, pp. 9–19, 2015

[6], [7]. A heterozygous mutation in the Fbn1 gene leads to fragmentation of the elastic fibres in the artery wall. When fed a Western type diet, vulnerable plaque formation occurs, including intraplaque neovascularization, intraplaque haemorrhage and plaque rupture.

Both stable and unstable plaques consist of lipids accumulating in the artery wall and are infiltrated by macrophages and other inflammatory cells. Since the presence of a high number of macrophages is one of the indications of a more severe, unstable plaque phenotype [8], macrophage quantification is a main target for molecular small animal imaging strategies [9]. For example, ultra-small superparamagnetic iron oxide particles have been used to detect the macrophages present in plaques with MRI [10]–[13], and so has the vascular cell adhesion molecule-1. This molecule has been targeted with superparamagnetic peptide-functionalised nanoparticles for MRI [14], [15] and with lipid-shelled microbubbles for ultrasound imaging [16]. Furthermore 18fluorodeoxyglucose (FDG) positron emission tomography (PET)- computed tomography (CT) imaging has been used to visualise plaque-related inflammation [17], [18].

However, the (through-plane) resolution of the used scanners, mainly MRI and PET, is limited for capturing the presence of atherosclerotic plaques in the carotid bifurcation of mice [19]. Therefore, plaque imaging is often restricted to anatomical images obtained by CT in combination with (iodinated) contrast agents, in which narrowing of the lumen indicates the presence of a plaque [20]. Enhancing anatomical CT with molecular imaging could help to better understand the processes taking place *in vivo* during the formation of atherosclerotic plaques. For this purpose N1177, a suspension of crystalline iodinated particles dispersed with surfactant, has been explored in rabbits [21], [22]. High-risk, macrophage-rich atherosclerotic plaques could be detected with CT resolution, but unfortunately the half-life of water-soluble iodine contrast agents is too short to be used with a single bolus injection in mice [23]. Accordingly, there is a need for a high-precision μCT scan protocol that allows detection of macrophages in murine plaques as a marker of plaque vulnerability.

In the present study, we show that Aurovist (Nanoprobes, Yaphank, NY), a recently introduced μCT contrast agent, can be used as a 'tracing marker' for macrophages. Aurovist consists of 15 nm gold particles with a polyethylene glycol coating, which increases its circulation time by partial switching its elimination pathways from the reticuloendothelial system to the mononuclear phagocyte system. Details on the mechanism of action and the biodistribution of the contrast agent are found in [23]–[26]. ApoE$^{-/-}$ mice, developing stable plaques, and ApoE$^{-/-}$ Fbn1$^{C1039G+/-}$ mice, developing vulnerable plaques, were injected with Aurovist and scanned with μCT at three

consecutive time points. Animals were sacrificed and dissected carotid arteries were investigated with histology, confirming that Aurovist is phagocytized by macrophages that accumulate within the atherosclerotic plaque. Furthermore, we propose a novel methodology to quantify Aurovist/macrophage accumulation *in vivo*, along the carotid bifurcation. A significant difference in macrophage accumulation was found between mice with stable and mice with vulnerable plaques.

7.2 Materials and Methods

7.2.1 Mice

Female ApoE$^{-/-}$ Fbn1$^{C1039G+/-}$ mice [7] (n=14) and their ApoE$^{-/-}$ littermates (n=9, 6 weeks old) were fed a Western type diet (TD88137, Harlan Teklad, Madison, Wis, USA) for up to 20 weeks. The mice were kept under environmentally controlled conditions (12h normal light/dark cycles, 20-23°C and 50% relative humidity) with food and water ad libitum. They were housed in groups of 4-8 animals in well-ventilated cages with appropriate cage enrichment. All the experiments were conducted according to the ethics committee guidelines and were approved by the animal ethics committee of Ghent University.

7.2.2 In vivo imaging at week 10, 15 and 20

The animals underwent contrast-enhanced μCT scans at weeks 10, 15 and 20 after the start of the diet. Anaesthesia was induced using a mixture of medical oxygen and 5% isoflurane, reduced to 1-1.5% during the scan. A first μCT scan (termed the pre-contrast μCT measurement)(see figure 7.1 A) was acquired using a Triumph-II imaging system (TriFoil Imaging, Chatsworth, CA, USA). After this measurement, the animal bed was moved out of the scanner and 100 μl/25g body weight Aurovist was injected [27] in the tail vein through a previously inserted catheter to avoid animal movement. Immediately after this injection, the animal was translated back to its initial position in the scanner and a post-contrast μCT measurement was taken (see figure 7.1 B). The μCT scan settings were set to a 50 μm focal spot size, 50 μm detector pixel size, 1024 projections, 3.5 times magnification, 500 μA tube current, 75 kVp tube voltage and a continuous rotation mode. The acquisition region of interest spanned the entire volume between the root of the aorta and approximately half of the skull.

7.2.3 Histologic examination

After euthanasia or sudden death, mice were dissected and the aorta (including the brachiocephalic and carotid arteries) was isolated. Arteries

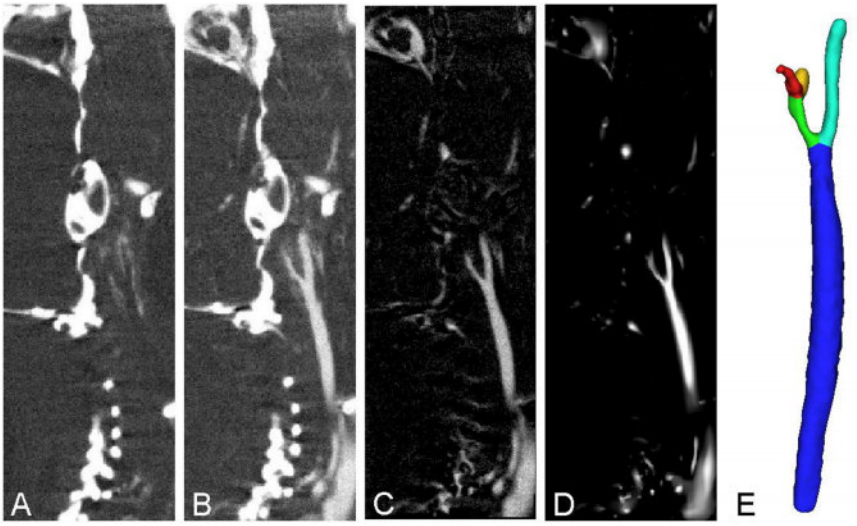

Figure 7.1: Overview of the measured and post-processed images. Images represent the right carotid bifurcation of an ApoE$^{-/-}$ Fbn1$^{C1039G+/-}$ mouse on a Western type of diet for 20 weeks. (A) The pre-contrast measured μCT dataset where the contrast agent accumulation in the artery wall is clearly visible around the bifurcation. (B) Post-contrast injection image showing the vasculature. (C) The angiographic image, constructed by subtracting the registered pre-contrast image from the post-contrast image. The vasculature is clearly visible in this image. (D) The vesselness filtered angiographic image showing higher contrast for the vasculature. This facilitates the initialisation of the segmentation process. (E) Segmentation of the right carotid bifurcation depicting the CCA (blue), the ECA (cyan), the first part of the ICA (green), part of the stapedial artery (SA) (red) and the second part of the ICA (orange).

were fixed in 4% formaldehyde (pH 7.4) for 24 h, processed and embedded in paraffin. Histological analysis was performed on serial cross sections (5μm) of the proximal ascending aorta, brachiocephalic and carotid arteries. Macrophages were determined by immunohistochemistry using anti-Mac-3 antibody (Pharmingen, San Diego, CA). Secondary antibody was species-appropriate horseradish peroxidase-conjugates (Vector Laboratories, Burlingame, CA). 3-amino-9-ethyl-carbazole (Vector Laboratories) was used as a chromogen. Images were acquired with the Universal Grab 6.1 (IDL) software (Exelis, Boulder, CO, USA) using an Olympus BX40 microscope (Tokyo, Japan). Images were quantified using ImageJ software (NIH, `http://imagej.nih.gov/ij/`).

7.2.4 Segmentation and image processing

The IMPACT algorithm [28] was used to reconstruct the CT data, in order to reduce the effect of beam hardening due to the dense skull bone. To speed

up the reconstructions, all data were first reconstructed at a lower resolution (0.2 mm isotropic voxel size), after which only the VOI around the carotid arteries was reconstructed at a higher resolution (50 μm isotropic voxel size) [29]. This method was applied to both the pre- and post-contrast datasets.

To get rid of misalignment between the pre- and post-contrast image, an image registration step was applied based on the BRAINSfit toolbox [30] in 3D slicer4 (`www.slicer.org`)[31]. The following parameters were inserted in the rigid registration algorithm: number of samples=300000, spline grid size= 14, 10, 12, number of iterations=1000, linear interpolations, minimum step length= 0.000001, number of histogram bins=200 and number of matchpoints=40. The pre-contrast injection image was set as the moving image. After automatic registration the 3Dslicer-chequerboard module was used to visually inspect the registration results and if there was a residual misalignment the dataset was removed from the database. Subsequently, an angiographic image was constructed by subtracting the registered pre-contrast image from the post-contrast image (figure 7.1 C). A vesselness-enhanced image (figure 7.1 D) was constructed based on the angiographic image. To that end a Frangi vesselness filter was applied in the Vascular Modeling Toolkit (VMTK) (`www.vmtk.org`) [32] with parameters: α 0.3, β 500 and γ 200. For the algorithm 10 logarithmically spaced steps between 0.05 and 0.5 mm were taken.

The left and right carotid arteries were segmented with the levelset segmentation algorithm of VMTK [33]. First an initial levelset was segmented based on the vesselness-enhanced image. The CCA, ECA and ICA were initially segmented by repeated executions of the colliding fronts algorithm, which returns a branch of the vascular network between a source and a target point. The threshold level was taken to be 40 HU but manually adapted between 30 HU and 50 HU to get rid of noise or nearby veins if needed. The ICA was segmented beyond the emerging of the SA and the first part of the SA was also segmented (see figure 7.1 E). The ECA was segmented as far as the bifurcation into the maxillary and superficial temporal arteries. After the initialisation an evolution step based on the angiographic image was carried out. The parameters for this step were: propagation weight=1, curvature weight=0.4, advection weight=0.6, edge weight=0 and number of iterations=200. The resulting surface was consecutively remeshed, smoothed and remeshed again in VMTK to get an optimal surface representation. For the first remeshing the area of the triangles was taken to be between 500 and 300 μm^2. Afterwards smoothing was performed with a passband of 0.1 and 30 iterations. For the final remeshing, the triangle area ranged between 150 and 50 μm^2. Based on the calculated centreline the carotid bifurcation was split in its 3 branches (CCA, ECA and ICA).

7.2.5 Quantifying macrophage presence within the lumen area

The next step was to quantify the presence of contrast agent in the arterial wall on the pre-contrast images (i.e. with contrast agent originating from injections at previous time points). In principle, this is only relevant for data measured at weeks 15 and 20, but pre-contrast scans at week 10 were also processed to serve as controls (since there should be no contrast detected). To allow a smoother integration, the registered pre-contrast image was resampled to a resolution of 0.025 mm. Subsequently, the volume inside the segmented carotid arteries was masked on the resampled pre-contrast image using the vtkImageStencil tool of Visualization Toolkit (VTK) (`www.vtk.org`). The carotid bifurcation was cut out of the segmented surface by cutting the three branches based on the length of the ICA (between the carotid bifurcation and the SA bifurcation). The ICA was cut at 95% of its length, the ECA was cut at the point where it reached the length of the ICA and the CCA was cut at 2 times the length of the ICA. For every triangle of the surface mesh at the carotid bifurcation, the normal was calculated in pyFormex (`www.nongnu.org/pyformex/`) (figure 7.2 A). These normals were uniformly sampled at 100 points over a total length of 0.3 mm. The sample points were classified to have an increased intensity, indicating the presence of contrast agent, if the image intensity was higher than a cutoff value of 350 HU. Based on the volume mask we verified that every point was located outside the artery. Finally, for every surface triangle the relative number of selected high-intensity points on the corresponding normal was expressed divided by the total amount of points outside the artery (figure 7.2 B). Thus, we obtained a clear visual representation of the presence of contrast agent near the boundary of the lumen. Finally, we quantified the results as follows: every surface element in which more than 25% of the points of its surface normal had elevated intensity values was categorised to the increased intensity group, while all other elements were categorised in the normal intensity group. Subsequently, for every bifurcation branch (CCA, ECA and ICA) the contrast-enhanced area and the contrast-enhanced area fraction (CAF) ($CAF\%_{area}$), were calculated.

7.2.6 Quantifying macrophage presence along the centreline

Because the $ApoE^{-/-}$ $Fbn1^{C1039G+/-}$ mice develop a high degree of stenosis in the carotid arteries over time, only considering the luminal surface holds the risk of a bias. Stenosis will reduce the internal area of the artery wall, which leads to an underestimation of the influence of these regions when using an area-averaged value. To circumvent this risk, the contrast-enhanced regions were mapped to the centreline of the lumen, since the centreline length is not affected by the presence of stenosis. For this operation, the centreline was calculated, resampled to 0.05 mm and split into branches in VMTK.

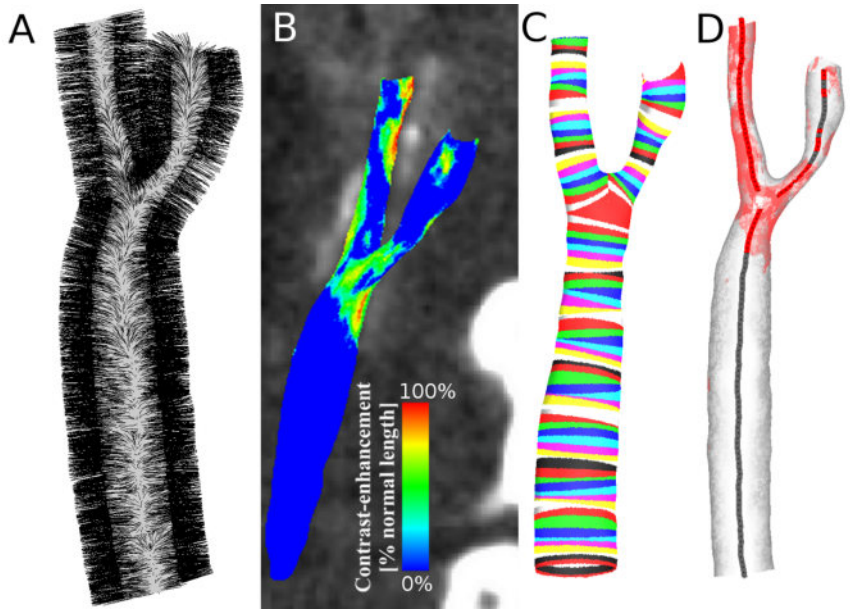

Figure 7.2: Overview of the different steps involved in the quantification of the contrast-enhanced regions. (A) This panel shows 1 out of 10 calculated normals (black) perpendicular to the lumen surface (grey). (B) The amount of points along each normal with an intensity higher than 350 HU indicates the regions with contrast agent present. (C) The luminal area is split in rings with an average width of 0.05 mm to map the contrast-enhanced regions along the length of the arteries. (D) The surface zones with contrast agent present along more than 25% of the normals, are indicated in red. After the splitting of the lumen area in rings, a ring was selected to belong to the contrast-enhanced group if more than 10% of the surface showed contrast. The affected regions of the centrelines are indicated in red, the unaffected regions in grey.

For every segment of the centreline, the corresponding part of the luminal wall was selected in pyFormex by cutting the entire luminal surface with two planes, thus splitting the total geometry into rings with an average width of 0.05 mm (figure 7.2 C). Again, we categorised the data and considered each segment to belong to the contrast group if the outer contrast-enhanced lumen area in the corresponding ring segment was more than 10% of the total lumen ring segment area (figure 7.2 D). Similar to the method proposed by Brown et al. with regard to calcification of plaques [34], we were thus able to track the presence of contrast agent along the centreline. Finally, we calculated for every branch for what distance along the centreline contrast agent was present: contrast-enhanced length fraction (CLF), (CLF [$\%_{\text{length}}$]).

7.2.7 Statistical analysis[†]

The same statistical analysis was performed for the CAF [$\%_{area}$] and CLF[$\%_{length}$]. Genotype was taken as a between-subject factor because the mice were grouped accordingly (ApoE$^{-/-}$ or ApoE$^{-/-}$ Fbn1$^{C1039G+/-}$). In addition, the measured dataset was split by 3 within-subject factors namely: time (week 15 or week 20), side (left or right carotid bifurcation) and location (CCA, ECA or ICA). The measurements at week 10 were used to validate the process and did not receive a contrast injection at a previous time point; therefore these measurements were not included in this analysis. The statistical analysis was performed in SPSS Statistics 22 (IBM, Armonk, NY, USA). The preferred test for this type of dataset is the general linear model with repeated measures. However, for this test only the subjects (mice) for whom all measurements are available are taken into account, which reduced the dataset to 3 ApoE$^{-/-}$ and 6 ApoE$^{-/-}$ Fbn1$^{C1039G+/-}$ mice. Hence, we decided to use a linear mixed model in which the within-subject variables are included as repeated measurements. This test can handle missing values, so no measured data was excluded. We opted for an autoregressive heterogeneous covariance structure for the residuals after minimising the information criteria for different covariance structures. A random effect, with scaled identity as covariance type and including the intercept, was added for the mice identities to account for the random mice selection out of the population for this study. Next, a type-III type of sum of squares was chosen. Finally, a full factorial analysis was performed for the four factors namely, strain, time, side and location.

7.2.8 Testing for operator independence

To verify the operator independence of the proposed methodology, the operator dependent segmentation step was performed (blinded) by a second operator. From these second set of segmentations, further operator independent processing steps resulted in a new set of CAF and CLF values. The correlation between the results of both operators for CAF and CLF was calculated, as we tested for equivalence of the average values of both datasets using a two one-sided paired T-tests approach [35] (Microsoft Excel).

7.3 Results

7.3.1 Available datasets for analysis

One ApoE$^{-/-}$ and two ApoE$^{-/-}$ Fbn1$^{C1039G+/-}$ mice died or were euthanized for ethical reasons before they reached week 10 of the diet. Signs of severe

[†]This research has benefited from a statistical consultation with Ghent University FIRE (Fostering Innovative Research based on Evidence)

pain and distress, which led to the euthanasia, included panting, head tilt, a hunched body posture and immobility. Therefore at the first imaging time point 8 ApoE$^{-/-}$ and 12 ApoE$^{-/-}$ Fbn1$^{C1039G+/-}$ mice were still included in the study. Afterwards 4 more ApoE$^{-/-}$ Fbn1$^{C1039G+/-}$ died or were euthanized before the end of the experiment. Two measurements failed because of a human error. Next to this, in six cases the registration of the pre- and post-contrast image failed due to motion artefacts. Finally, only a portion of the right ECA of two ApoE$^{-/-}$ mice at week 20 could be resolved, due to severe stenosis, and only the left carotid bifurcation was thus included at this time point. In summary, the analysis includes 14, 8 and 14 ApoE$^{-/-}$ carotid bifurcations (left and right) at week 10, 15 and 20 respectively. For the ApoE$^{-/-}$ Fbn1$^{C1039G+/-}$ mice, 20, 16 and 14 bifurcations were available for analysis at these time points.

7.3.2 Histology

As a first step we investigated whether the injected Aurovist particles can be used as a tracing marker for macrophage presence. The Mac-3 stain in figure 7.3 shows a representative example of macrophage infiltration (in red) in different areas of an atherosclerotic plaque (panels A and B). Aurovist particles (visible on the Mac-3 stain as black dots) are abundantly present in macrophage-rich regions (panels C, D) as well as in the plaque necrotic cores (panels E, F). We hypothesise that in the hours and days after Aurovist injection, macrophages phagocytize the Aurovist particles and migrate to inflamed zones within the plaque. At the necrotic cores, Aurovist particles accumulate yet no macrophages can be detected on the Mac-3 stain. We hypothesise that Aurovist particles at this location have been released by necrotic macrophages that are no longer visible on the Mac3 stain (loss of epitope). We conclude that Aurovist can be used in combination with μCT as an *in vivo* tracer for macrophage presence.

7.3.3 Validation test for false positive results at week 10

The results at week 10 served to validate the performance of the proposed framework with regard to false positives (contrast-enhanced locations found), as these animals did not receive any prior contrast injection. The maximum value for an individual mouse at week 10 of the CAF was 0.15, 1.17 and 0.22 $\%_{\text{area}}$ for the CCA, ECA and ICA respectively. For the CLF these values were respectively 0.00, 3.36 and 0.00 $\%_{\text{length}}$. Averaged over the whole group, the false positives for the CCA and the ICA were smaller than 0.02%$_{area/length}$. For the ECA the average false positives were 0.077$\%_{\text{area}}$ and 0.18$\%_{\text{length}}$ mainly because of the presence of a tracheal cartilage ring in the image field in one animal. Both measures are thus reasonably robust but fail in the rare case that a trachea cartilaginous ring is present in the region of interest.

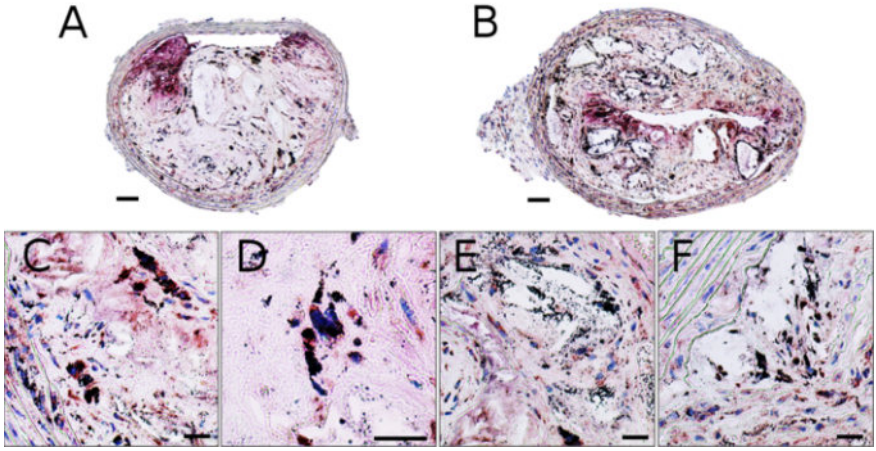

Figure 7.3: (A-B) Mac-3 stain showing a representative example of macrophage infiltration in different areas of an atherosclerotic plaque of an ApoE$^{-/-}$ Fbn1$^{C1039G+/-}$ mouse. Macrophages are stained in red while Aurovist particles are visible as black dots. Aurovist particles are abundantly present in macrophage-rich regions such as the plaque shoulder as well as in the plaque necrotic cores. (C-D) Detailed images show how macrophages have engulfed Aurovist particles. (E-F) In the necrotic cores Aurovist particles accumulate yet no macrophages can be detected on the Mac3 stain. Scale bars of A and B are 200 μm and scale bars of C-F are 50 μm.

7.3.4 Quantification of contrast-enhancement in the arterial branches: CAF and CLF

Table 7.1 quantifies the CAF [$\%_{area}$] for every separate branch of the bifurcation (CCA, ECA and ICA). In both ApoE$^{-/-}$ and ApoE$^{-/-}$ Fbn1$^{C1039G+/-}$ mice, the highest contrast agent uptake occurred in the ECA, both at week 15 and week 20. In both mouse models there was an increase over time, especially in the ApoE$^{-/-}$ model where a 4-fold increase in contrast uptake between week 15 and 20 could be observed. The increase in the ApoE$^{-/-}$ Fbn1$^{C1039G+/-}$ model was less pronounced, with a 200% increase for the CCA and ICA, and a 50% increase in the CCA. This is, however, mainly due to the already higher extent of contrast agent uptake at week 15 in the ApoE$^{-/-}$ Fbn1$^{C1039G+/-}$ mice. The statistical CAF analysis in different branches revealed that time (week 15-week 20) and location (CCA, ECA or ICA) are highly significant factors ($p<0.01$). Genotype (ApoE$^{-/-}$ or ApoE$^{-/-}$ Fbn1$^{C1039G+/-}$) has a higher p-value but is still a significant factor ($p<0.05$). No difference was found between the left or right side ($p=0.745$). Finally, the interaction between the factors time and location was also highly significant ($p<0.01$). This supports the trends shown in table 7.1. The estimated averages showed that on average, ApoE$^{-/-}$ mice had 14.2$\%_{area}$ less contrast-enhanced area compared to ApoE$^{-/-}$ Fbn1$^{C1039G+/-}$ mice and this effect was significant ($p<0.05$). At week 15, the affected area was

smaller than at week 20 with an average difference of 19.6%$_{area}$ ($p<0.01$). The differences between the locations in both strains were also highly significant ($p<0.01$): the contrast-enhanced area in the CCA was smaller compared to the ECA (32.3%$_{area}$) or to the ICA (13.6%$_{area}$).

Table 7.1: The CAF [%$_{area}$] with the standard deviation at the different branches.

	ApoE$^{-/-}$		
	CCA	ECA	ICA
w15	2.77 ± 3.33	12.56 ± 10.32	4.20 ± 2.97
w20	11.70 ± 18.23	51.74 ± 27.68	27.11 ± 24.56
	ApoE$^{-/-}$ Fbn1$^{C1039G+/-}$		
	CCA	ECA	ICA
wk15	8.02 ± 5.94	40.35 ± 26.53	18.98 ± 15.81
wk20	18.05 ± 18.22	64.55 ± 24.16	43.27 ± 20.98

The results depicted in table 7.2 represent the CLF expressed in %$_{length}$ for the three different branches (CCA, ECA and ICA). These results are similar to the results shown in table 7.1. However, the absolute values are higher, since this way of calculating contrast agent accumulation attributes a higher weight to regions where contrast agent is present only partially around the circumference. These results are summarised in figure 7.4. A marked increase in Aurovist accumulation can be observed from week 15 (cross hatched bars) to week 20 (bars without hatching). The statistical analysis of the CLF yields slightly different results compared to the CAF. Time and location are still highly significant ($p<0.01$) but in this case genotype is also highly significant. Still there is no statistical indication of a difference between left and right ($p=0.609$). Furthermore the interaction between time and location remains highly significant. Finally the interaction between genotype and location, which was almost significant in the CAF, became significant ($p<0.05$) for the CLF. The ApoE$^{-/-}$ mice have on average 20.7%$_{length}$ smaller contrast accumulations ($p<0.01$) compared to ApoE$^{-/-}$ Fbn1$^{C1039G+/-}$ mice. From week 15 to week 20 the model estimated average growth of the contrast deposits is 30.5%$_{length}$. Moreover the CLF in the CCA is 51.3%$_{length}$ lower compared to the ECA, and 32.0%$_{length}$ lower compared to the ICA (both $p<0.01$). For both the CAF and the CLF, the statistical tests show that there is a significant difference between both groups of mice. We can conclude that on average the ApoE$^{-/-}$ Fbn1$^{C1039G+/-}$ mice have more contrast accumulation, that there is a significant growth in accumulation over time and that it is very location dependent.

Table 7.2: The CLF [$\%_{length}$] with the standard deviation at the different branches.

	$ApoE^{-/-}$		
	CCA	ECA	ICA
w15	10.23 ± 17.23	40.87 ± 21.75	11.31 ± 10.79
w20	23.51 ± 28.77	82.30 ± 25.61	67.44 ± 33.43
	$ApoE^{-/-}$ $Fbn1^{C1039G+/-}$		
	CCA	ECA	ICA
wk15	15.78 ± 10.10	75.65 ± 36.17	48.57 ± 34.64
wk20	39.34 ± 12.93	95.32 ± 12.77	87.88 ± 17.71

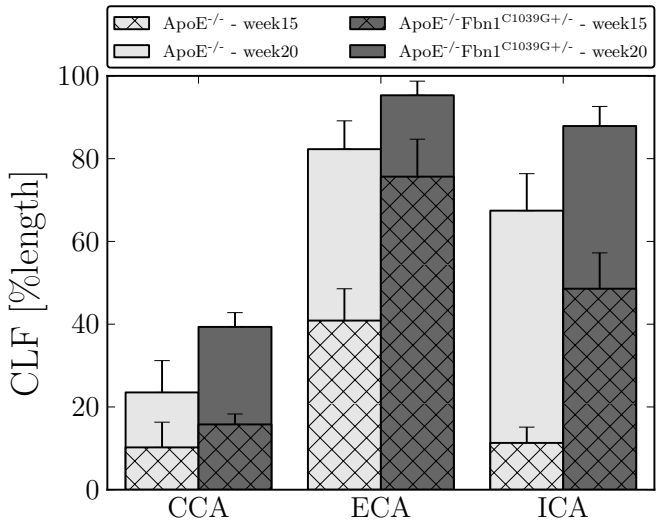

Figure 7.4: The length of the centreline of each branch where contrast agent is present (CLF) [$\%_{length}$].

7.3.5 Testing for operator independence

The resulting CAF and CLF values were compared for 2 sets of segmentations, executed by 2 different operators. The correlation between both CAF datasets was 0.993 and for the CLF it was 0.986. The mean difference between both CAF datasets was smaller than $1\%_{area}$ ($p<0.001$). For CLF, the mean difference is smaller than $5\%_{length}$ ($p<0.001$).

7.3.6 Qualitative visualisation of the contrast-enhanced regions

The quantitative results described above are further illustrated by graphical representations of the precise contrast-enhanced locations. Figure 7.5 shows a representative example of an $ApoE^{-/-}$ mouse at week 15 and week 20. At week

15 there were only small regions where contrast-enhancement was visible. The two largest regions were located in the ECA. At week 20 the shape of the contrast-enhanced area had changed, with contrast-enhanced zones at regions of the ECA, ICA and CCA close to the bifurcation. In figure 7.6, similar images are shown for an ApoE$^{-/-}$ Fbn1$^{C1039G+/-}$ mouse at weeks 15 and 20. In this case, the shape of the contrast-enhanced area was similar for both time points, with Aurovist present along the entire ECA and ICA and in the part of the CCA closest to the carotid bifurcation. However, the contrast-enhanced area was significantly increased at week 20, confirming the quantitative results indicated in table 7.1.

7.3.7 Precise locations of contrast-enhanced regions in both groups of mice

On top of the quantitative and qualitative analysis, the proposed framework also allows for an exact and detailed visualisation of the locations of Aurovist accumulation. The first row of figure 7.7 (panels A and B) shows the number of cases for which Aurovist was present in the CCA as a function of the distance to the bifurcation. The distance is zero (right side of the x-axis) at the bifurcation and decreases downstream from there. On the left side (panel A) the values for the ApoE$^{-/-}$ mice are shown and on the right side (panel B) the values for the ApoE$^{-/-}$ Fbn1$^{C1039G+/-}$ mice can be found. For both cases the status is pictured with circles at week 15 and with crosses at week 20. A first striking feature is that the contrast preferentially builds up near the bifurcation and is more or less confined to this region, especially for the ApoE$^{-/-}$ Fbn1$^{C1039G+/-}$ mice. For the ECA, shown in the second row in figure 7.7 (panels C and D), the contrast agent is much less restricted to a specific region. On an average basis the locations are more or less uniform along the inspected length of the artery. Finally for the ICA, shown in the third row in figure 7.7 (panels E and F), the contrast agent is mostly located near the bifurcation at week 15, with a gradual decrease downstream. At week 20 however it evolved to a state where the Aurovist was more equally distributed along the whole artery, confirming earlier results.

7.4 Discussion

In this study, we investigated contrast-enhanced, *in vivo* μCT imaging to visualise macrophage infiltration over time in murine atherosclerotic plaques. The technique was validated with histology and applied in a longitudinal study including both ApoE$^{-/-}$ mice, a model for stable atherosclerotic plaque, and ApoE$^{-/-}$ Fbn1$^{C1039G+/-}$ mice, a model for vulnerable atherosclerotic plaque. We used two different methods to quantify the contrast accumulated in the atherosclerotic plaque: the CAF for the contrast-enhanced area fraction

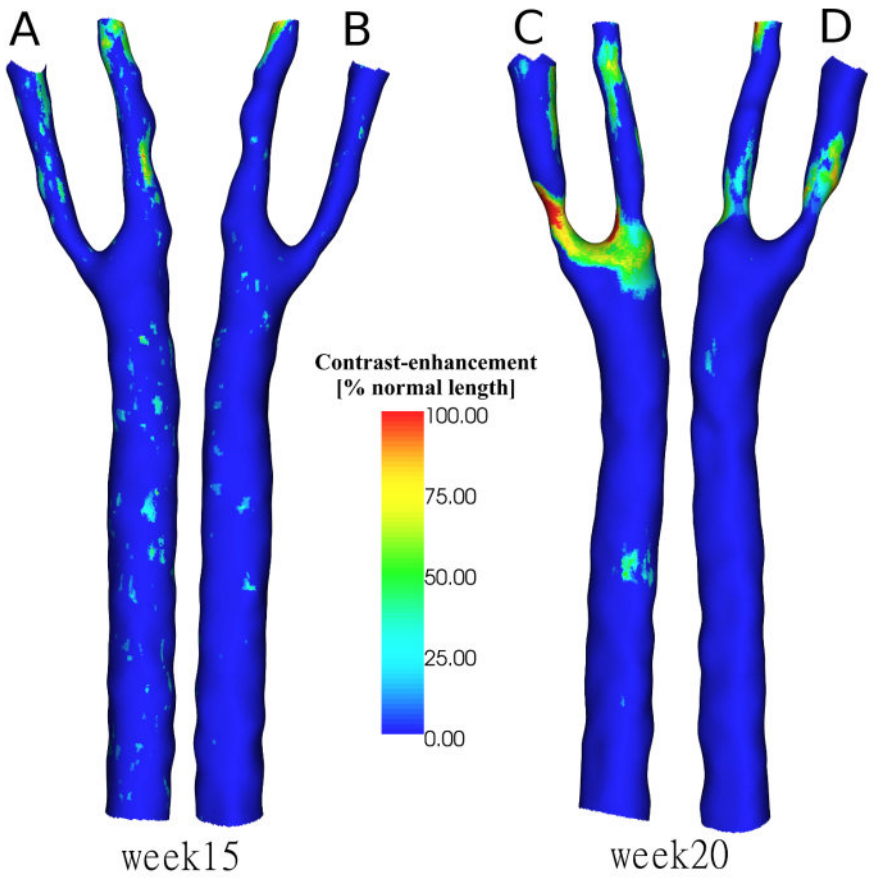

Figure 7.5: Contrast-enhanced regions around the carotid bifurcation of an ApoE$^{-/-}$ mouse at weeks 15 and week 20 after the start of the diet. At week 15 both the medial side of the carotid bifurcation (A) and the lateral side (B) only show small zones with little contrast-enhancement. These zones are preferably located at the ECA. The contrast-enhanced regions have grown over time and are at week 20 (C-D) merely located in the ECA and ICA. They are mainly situated at the medial side (C) compared to the lateral side (D).

and the CLF for the contrast-enhanced centreline length fraction of the branches along the carotid bifurcation. We visualised and quantified the different contrast-enhanced locations, and found significant differences in macrophage infiltration between time points and between mouse models.

7.4.1 Contrast agent accumulation and distribution

We observed a significant growth of contrast-enhanced (and thus macrophage-infiltrated) regions over time in both mouse models and these regions were significantly larger in ApoE$^{-/-}$ Fbn1$^{C1039G+/-}$ mice compared to

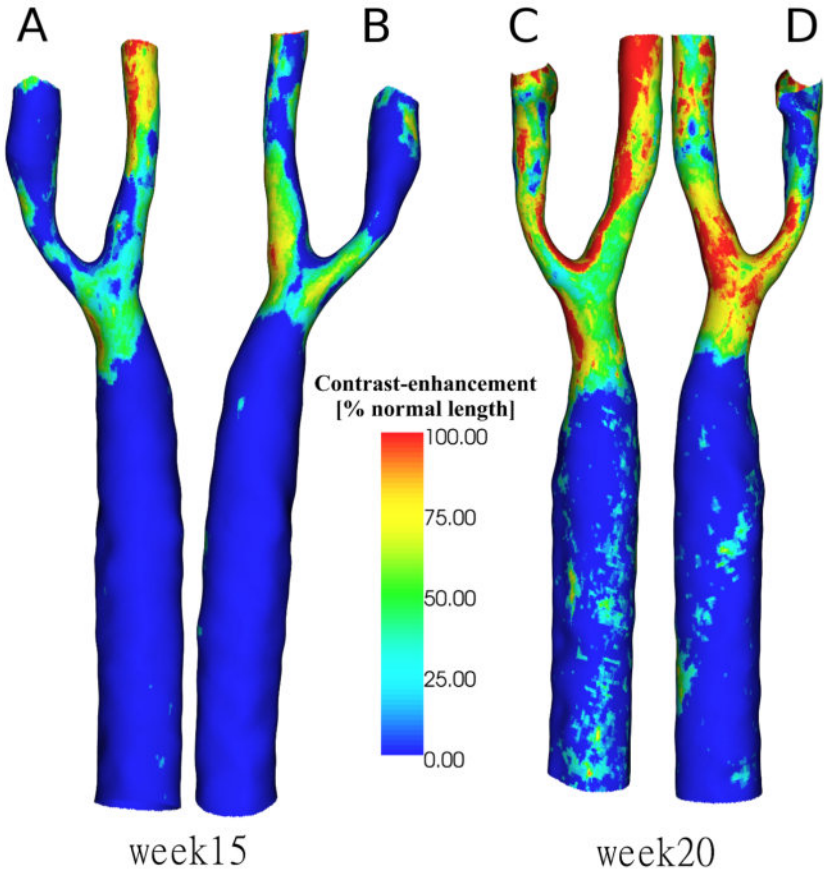

Figure 7.6: Contrast-enhanced regions around the carotid bifurcation of an ApoE$^{-/-}$ Fbn1$^{C1039G+/-}$ mouse at weeks 15 and 20. (A-B) At week 15 regions with contrast-enhancement are visible in the last part of the CCA, in the first part of the ICA and along the ECA. These regions span both the medial (A) and the lateral (B) side of the carotid bifurcation. (C-D) At week 20 the area with contrast-enhancement has increased. It are still the same zones as at week 15 but they have considerably grown in size. Especially in the ECA contrast-agent is present along whole the length. The contrast agent is present around the whole bifurcation and thus spans both the medial (C) and the lateral (D) side.

ApoE$^{-/-}$ mice. Nevertheless, interesting geometrical differences could be observed between different branches. In the ApoE$^{-/-}$ Fbn1$^{C1039G+/-}$ mice the CAF and CLF increased significantly from week 15 to week 20 at both ICA and CCA, while only a small increase was noticeable at the ECA. This could be explained by the fact that in about 75% of the ApoE$^{-/-}$ Fbn1$^{C1039G+/-}$ mice the contrast agent was already present along the entire ECA at week 15. Therefore,

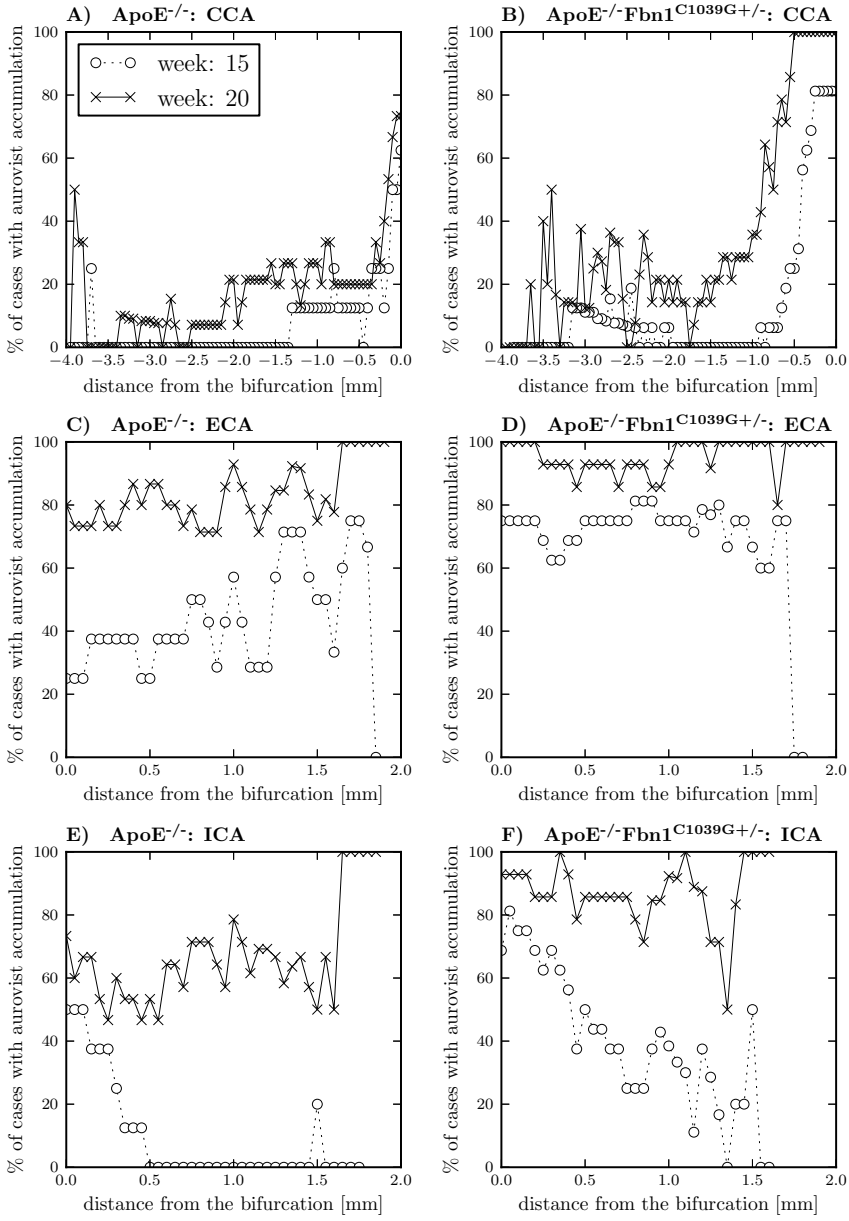

Figure 7.7: Localisation of Aurovist at the different branches. At the horizontal axis the distance, sampled at 0.05mm, from the bifurcation is depicted and on the vertical axis the percentage of cases with Aurovist at that precise location is shown. The occurrence of Aurovist at every location was determined by projecting the lumen surface contrast agent plot on the centreline. The first row (panels A and B) shows the CCA, the second row (panels C and D) the ECA and the third row (panels E and F) the ICA. On the left hand side (panels A, C and D), the ApoE$^{-/-}$ mice, and on the right hand side (panels B, D and F) the ApoE$^{-/-}$ Fbn1$^{C1039G+/-}$ mice are shown. For every case the comparison was made between the situation at week 15 (circles) and week 20 (crosses).

there was only little space for an expansion of the contrast-enhanced region along the lumen over time, as it occurred in the other two branches. Another interesting observation in this respect was that in both mouse models, at both time points, a larger part of the ECA and ICA was contrast-enhanced compared to the CCA. Moreover, the contrast-enhanced regions in the CCA were localised near the bifurcation whereas the contrast-enhanced regions in ECA and ICA were smeared out away from the bifurcation. Likely, the latter can be linked to flow haemodynamics, since locations of low and oscillatory flow are known to promote macrophage infiltration [36], [37]. Since the flow distally to the bifurcation is likely to be more disturbed, flow perturbations will induce more spread-out flow patterns in the ECA and ICA. In the CCA on the other hand, the blood flow reaches a stagnation point at the bifurcation and little flow perturbations occur upstream. We conclude that macrophage infiltration occurs with similar geometrical patterns but different intensities in both mouse models, and that the ECA is exposed to macrophage infiltration at an earlier time point than the other two branches.

The study does not include control animals not developing atherosclerosis. Note, however, that the animals included can, to a certain extent, be used as their own controls. It is known that atherosclerosis develops only in a later stage in the central section of the common carotid artery. This is consistent with our observation that no contrast accumulation was visible, in neither ApoE$^{-/-}$ nor ApoE$^{-/-}$ Fbn1$^{C1039G+/-}$ mice at week 15 (figure 7.7 panels a and b – dotted lines with circles) at the proximal end of the CCA.

7.4.2 Advantages: imaging technique

The present methodology enabled the use of a high-resolution μCT scanner for molecular imaging of the location of macrophages in atherosclerotic plaques in the carotid bifurcation of mice. This enables the measurement of plaque development very precisely, which was not possible with standard, purely anatomical μCT imaging. Moreover, it allows longitudinal *in vivo* studies of the inflammation process in the artery wall in mice. Therefore, this methodology has potential to be used in preclinical studies on plaque development or plaque stabilising therapeutics. To the best of our knowledge no such technique currently exists in mice.

7.4.3 Advantages: post-processing

The processing and quantification of the data has advantages as well. We described a method to Colour-code contrast-enhanced areas on the luminal surface, which gives a clear overview of all the targeted areas (figure 7.5 and figure 7.6). This allows the demonstration of small location shifts of the longitudinal data and is an excellent technique to follow-up individual cases. For example, in figure 7.6 the contrast-enhanced regions for the ApoE$^{-/-}$

Fbn1$^{C1039G+/-}$ mouse clearly originate at the outer bends of the bifurcation at week 15 but at week 20 they also span the inner side. Another asset of this method is the user-independency. Only for the segmentation of the arterial geometry interaction of the user was necessary, by selecting points inside the arterial network. The operator dependency study, however, showed that operator dependency in this step is likely to have only a very small influence on the resulting CAF and the CLF values. For the more critical selection of contrast-enhanced regions, no interaction was needed. In the future, as segmentation- and/or imaging-techniques evolve, the segmentation would probably evolve more towards automatic algorithms where (almost) no user interaction will be needed.

7.4.4 Limitations

The main limitation of the scanning protocol is that two μCT scans are needed, a pre- and a post- contrast injection scan, at every time point. First of all, this doubles the amount of scans which have to be successful for one measurement dataset. Moreover, rigid image registration is an effective way of removing translations between both scans but it cannot remove animal repositioning effects, between the pre- and post-contrast injection scan at the same time point. In the current study, this accounted for 6 failures out of 50 measurements. As such, measures to limit animal motion in between scans are warranted. The duration of every scan was around 20 min, so one option is to reduce the scan time by using another scan protocol or scanner to reduce the amount of registration failures. Another option is to use a more advanced registration method with more degrees of freedom for example a deformable method, which can take into account movements of the mouse [38].

The repeated injections of Aurovist do not seem to have an effect on the animal welfare [23] or plaque development. However, due to the need for pre- and a post-contrast injection scans, the animals get twice as much radiation. In this study, the mice were scanned 6 times spread out over 10 weeks, with an estimated total radiation dose of 6Gy. Therefore, we cannot rule out radiation dose induced morbidity and mortality. Moreover, it has been shown in literature that (high) radiation doses accelerate the development of inflammatory, macrophage-rich lesions in ApoE$^{-/-}$ mice [39], [40]. It is therefore important to optimise protocols in terms of radiation dose and number of intermediate time points as well as required image quality.

A larger sample size would result in a smoother curve for the localisation of the contrast agent in the different branches (figure 7.7). The applied framework lacks inherent information about the depth of the contrast accumulations as long as they are closer than the threshold value of 0.3 mm

to the lumen surface. Therefore, it is a useful tool to determine the size and location of the areas with contrast agent, but is less suited to study outward or inward remodelling related processes occurring in atherosclerotic plaque development.

In the present study, there was a time difference of 5 weeks between consecutive measurements. The Aurovist stayed inside the lumen for more than 24 h but afterwards gradually decreased. During this time the Aurovist was taken up by macrophages and migrated to the atherosclerotic plaque regions. However, it is possible that these macrophages migrated and mixed with macrophages that had migrated at a later time point.

Finally, we chose to express the contrast-enhanced regions in terms of influenced luminal area and influenced artery length. As a side effect of this choice, the inner curve of the bifurcation can be taken into account twice. If the curve is sharp enough, the surface normals of both the ECA and ICA will penetrate this region. However, this effect only plays a role for a small fraction of the surface and does not affect the meaning of the influenced area, since this is the transition between both branches.

7.5 Conclusion

We propose Aurovist-enhanced μCT as a promising new tool to visualise macrophage infiltration *in vivo* in preclinical small animal research. By using histology, we showed that Aurovist coincides with macrophages using histology, and developed a methodology to quantify Aurovist presence within atherosclerotic plaques based on *in vivo* μCT images. We applied this methodology in a longitudinal follow-up study in two different mouse models for atherosclerotic plaque. We observed a significant growth of contrast-enhanced (and thus macrophage-infiltrated) regions over time in both mouse models and these regions were significantly larger in ApoE$^{-/-}$ Fbn1$^{C1039G+/-}$ mice (a model for vulnerable plaque) compared to ApoE$^{-/-}$ mice (a model for stable plaque). Regional differences in macrophage distribution over different branches suggested that local haemodynamics affect macrophage infiltration. The developed methodology will be used in the future to perform more in depth research on the presence of macrophages in cardiovascular disease in mice.

7.6 μCT imaging beyond the carotid arteries: the brain vasculature

In this section, a short exploration to the brain vasculature will be taken, demonstrating the possibility to visualise the cerebral vasculature using the

μCT measurements that were taken. No extra measurements were performed for these results, just another VOI was selected in the measurement domain and further post processing of the measurements was performed. Visualisation of the brain vasculature may be of interest because it has been shown that hypoxia and disturbed blood flow occurs in the ApoE$^{-/-}$ Fbn1$^{C1039G+/-}$ brain (based on MRI and histology) [6].

7.6.1 Constructing an angiographic image of the murine brain

The technical description of how to construct this angiographic image is equal or very similar to the methodology used in the previous sections (section 7.2.4) to construct the angiographic image of the carotid bifurcation. The measured pre- and post-contrast injection images are cropped to only contain the skull. These images are shown in figures 7.8a and 7.8b for an example animal.

After cropping, a first step is to register both images, as the animal might have moved in between both scans due to the necessity to translate the mouse out of the scanner for the contrast injection. The BRAINSfit toolbox [30] in 3D slicer4 (`www.slicer.org`)[31] was used to apply a rigid registration. The parameters used were: number of samples=300000, spline grid size= 14, 10, 12, number of iterations=1000, linear interpolations, minimum step length= 0.000001, number of histogram bins=200 and number of matchpoints=40. The pre-contrast injection image was set as the moving image. By subtracting the pre-contrast injection image from the post-contrast injection image, an angiographic image (figure 7.8c) could be constructed. These images can be used directly to visualise the whole brain vasculature using volume renderings. A volume rendering with the vasculature in yellow/red and the bone (skull) in blue is shown in figure 7.9.

7.6.2 Segmenting the brain vasculature

In a next step, the cerebral arteries can be segmented from the angiographic image. Probably due to the high density of the surrounding skull, the image quality is not perfect inside the skull and the arteries are rather noisy (shown in figure 7.8c). Thus, a vesselness enhancement filter was applied to facilitate the segmentation initialisation. In the VMTK(`www.vmtk.org`), a Frangi vesselness filtered image was constructed with parameters: α 0.3, β 500, γ 150. The radius of the filter varied between 0.05 and 0.7 mm.

For the initialisation of the vesselness enhanced image, an isosurface algorithm was applied. This was followed by an evolution step based on the original angiographic image. For this step, the parameters were: propagation weight=0, curvature weight=0.4, advection weight=0.6, edge weight=0 and number of iterations=500. The skull was segmented on a single thresholding

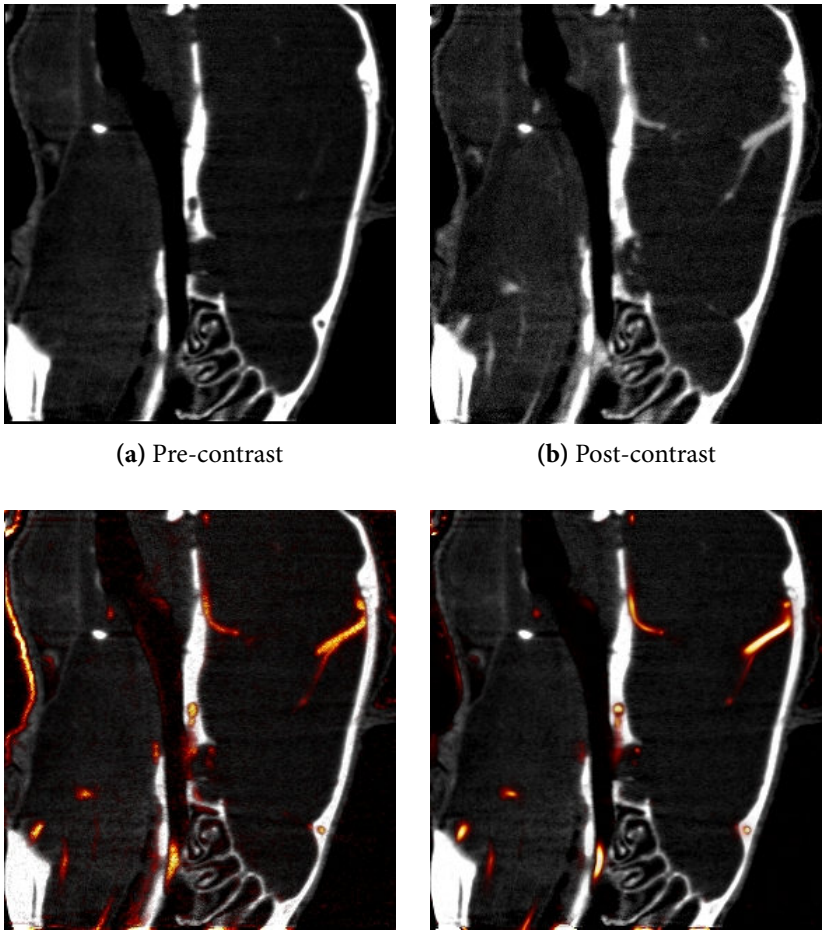

(a) Pre-contrast

(b) Post-contrast

(c) Subtracted (red)

(d) Frangi filtered (red)

Figure 7.8: Creating an angiographic image of the murine cerebral vasculature. (a) the pre-contrast injection image with only the skull visible. (b) the post-contrast injection image with both vasculature and skull visible. (c) the subtracted, angiographic image (red) in an overlay on the pre-contrast injection image (white, skull). (d) result after applying a Frangi filter to the angiographic image.

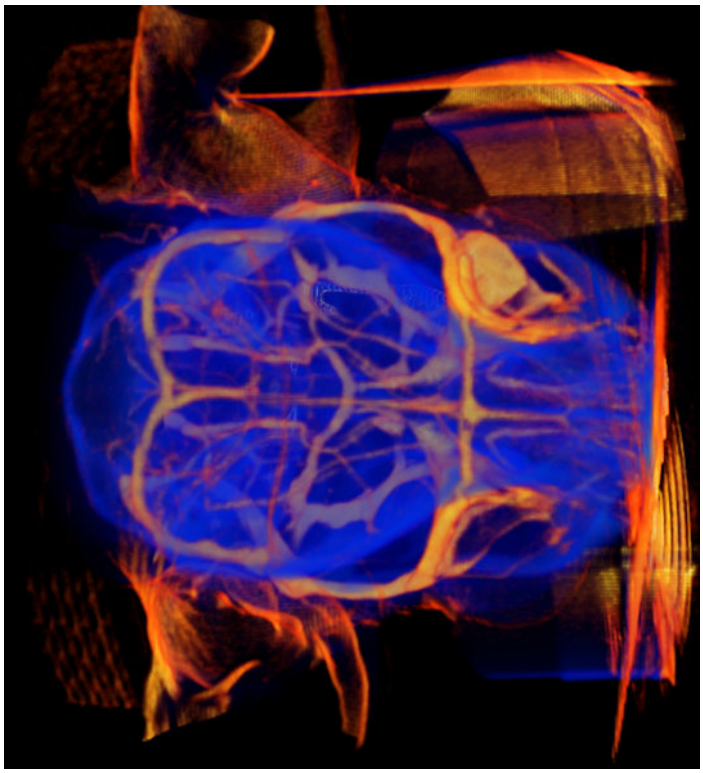

(a) Dorsal

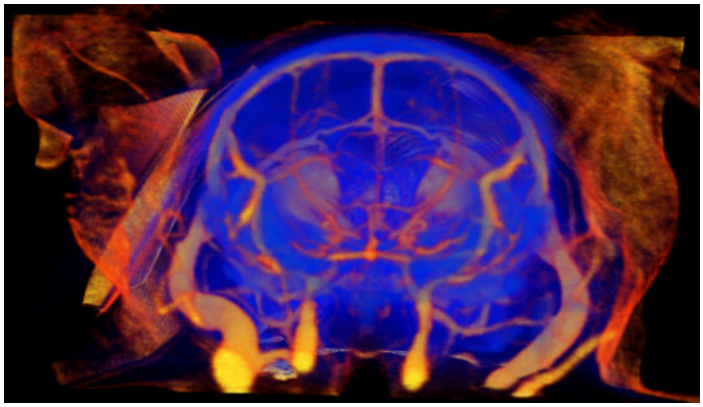

(b) Posterior

Figure 7.9: The murine brain vasculature assessed with gold-nanoparticle-enhanced enhanced μCT. A volume rendering of the dorsal (a) and the posterior (b) view. The vasculature is shown in red and the skull in blue.

and propagation step with a lower threshold of 700 HU. An example segmentation result is shown in figure 7.10. In figure 7.10a, the circle of Willis is clearly visible in the middle of the image.

7.6.3 Contrast accumulation in the brain vessels

As explained in more detail in chapter 7 on page 117, the contrast agent from the injections of weeks 10 and 15 accumulates in the macrophages in atherosclerotic plaques and is therefore visible on the μCT image at week 20. Similarly, contrast agent accumulations from previous injections are visible in the brain. The blue structures in figure 7.10, are present in virtually all mice. Their anatomical location suggests that this is possibly the choroid plexus. The choroid plexus is a structure that is mainly involved in the production of cerebrospinal fluid and that stands into close contact with leaky vessels [41]. However, it has been shown that xanthomas (accumulation of lipid rich macrophages) are located near the choroid plexus in both $ApoE^{-/-}$ and $ApoE^{-/-}$ $Fbn1^{C1039G+/-}$ mice [42]. The current results are still preliminary and further investigation is needed before any conclusion can be made.

In addition to the contrast accumulations described in the previous paragraph, 3 animals also showed signs of contrast accumulation at another location (green on figure 7.10). The origin of the contrast is not clear. It could also indicate the presence of a xanthoma or it could be plaque content from a plaque rupture that occurred for example at the level of the carotid bifurcation. Without further histological examination it is not possible to draw any conclusions, but we do consider it as an interesting observation, worth reporting

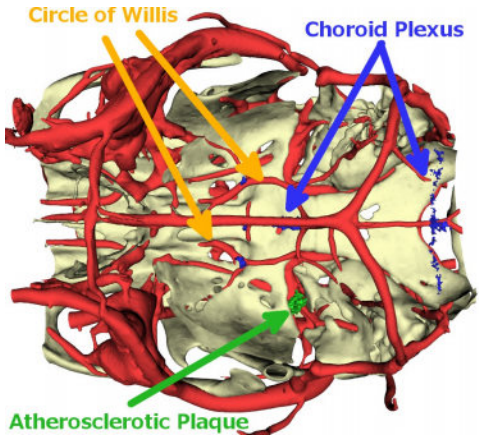

(a) Dorsal

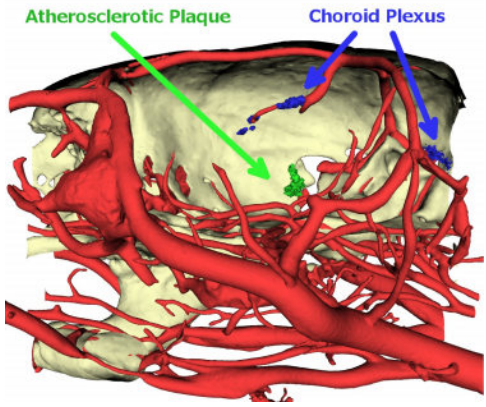

(b) Lateral

Figure 7.10: The segmented murine brain vasculature assessed with gold-nanoparticle-enhanced enhanced μCT. Contrast remaining from previous injections is visible in 2 regions presumed to be: the atherosclerotic plaque (green) and the choroid plexus (blue). The dorsal (a) and the lateral (b) view are shown.

Bibliography Chapter 7

[1] P. Libby, 'Inflammation in atherosclerosis.' *Nature*, vol. 420, no. 6917, pp. 868–74, 2002.

[2] A. A. Pendse, J. M. Arbones-Mainar, L. A. Johnson, M. K. Altenburg and N. Maeda, 'Apolipoprotein E knock-out and knock-in mice: atherosclerosis, metabolic syndrome, and beyond.' *Journal of lipid research*, vol. 50 Suppl, no. December 2008, S178–S182, 2009.

[3] S. C. Whitman, 'A practical approach to using mice in atherosclerosis research.' *The Clinical biochemist. Reviews*, vol. 25, no. 1, pp. 81–93, 2004.

[4] A. Daugherty, 'Mouse models of atherosclerosis.' *The American journal of the medical sciences*, vol. 323, no. 1, pp. 3–10, 2002.

[5] J. Jawien, R. Nastalek, R. Korbut, J. Jawień, P. Nastałek and R. Korbut, 'Mouse models of experimental atherosclerosis', *journal of physiology and pharmacology*, vol. 55, no. 3, pp. 503–517, 2004.

[6] C. Van der Donckt, J. L. Van Herck, D. M. Schrijvers, G. Vanhoutte, M. Verhoye, I. Blockx, A. Van Der Linden, D. Bauters, H. R. Lijnen, J. C. Sluimer, L. Roth, C. E. Van Hove, P. Fransen, M. W. Knaapen, A.-S. A.-S. Hervent, G. W. De Keulenaer, H. Bult, W. Martinet, A. G. Herman and G. R. Y. De Meyer, 'Elastin fragmentation in atherosclerotic mice leads to intraplaque neovascularization, plaque rupture, myocardial infarction, stroke, and sudden death.' *European heart journal*, vol. 36, no. 17, pp. 1049–1058, 2014.

[7] J. L. Van Herck, G. R. De Meyer, W. Martinet, C. E. Van Hove, K. Foubert, M. H. Theunis, S. Apers, H. Bult, C. J. Vrints and A. G. Herman, 'Impaired Fibrillin-1 Function Promotes Features of Plaque Instability in Apolipoprotein E-Deficient Mice', *Circulation*, vol. 120, no. 24, pp. 2478–2487, 2009.

[8] A. P. Burke, A. Farb, G. T. Malcom, Y. H. Liang, J. Smialek and R. Virmani, 'Coronary risk factors and plaque morphology in men with coronary disease who died suddenly.' *The New England journal of medicine*, vol. 336, no. 18, pp. 1276–82, 1997.

[9] F. A. Jaffer and P. Libby, 'Molecular Imaging of Atherosclerosis', in *Molecular imaging: principles and practice*, R. Weissleder, B. D. Ross, A. Rehemtulla and S. S. Gambhir, Eds., 1st ed., Shelton: People's Medical Publishing House, 2010, ch. Molecular, pp. 960–979.

[10] S. G. Ruehm, C. Corot, P. Vogt, S. Kolb and J. F. Debatin, 'Magnetic Resonance Imaging of Atherosclerotic Plaque With Ultrasmall Superparamagnetic Particles of Iron Oxide in Hyperlipidemic Rabbits', *Circulation*, vol. 103, no. 3, pp. 415–422, 2001.

[11] J. B. Morris, A. R. Olzinski, R. E. Bernard, K. Aravindhan, R. C. Mirabile, R. Boyce, R. N. Willette and B. M. Jucker, 'p38 MAPK inhibition reduces aortic ultrasmall superparamagnetic iron oxide uptake in a mouse model of atherosclerosis: MRI assessment.' *Arteriosclerosis, thrombosis, and vascular biology*, vol. 28, no. 2, pp. 265–71, 2008.

[12] Y. Watanabe and M. Nagayama, 'MR plaque imaging of the carotid artery.' *Neuroradiology*, vol. 52, no. 4, pp. 253–74, 2010.

[13] S. A. Schmitz, S. E. Coupland, R. Gust, S. Winterhalter, S. Wagner, M. Kresse, W. Semmler and K.-J. Wolf, 'Superparamagnetic Iron Oxide–Enhanced MRI of Atherosclerotic Plaques in Watanabe Hereditable Hyperlipidemic Rabbits', *Investigative Radiology*, vol. 35, no. 8, pp. 460–471, 2000.

[14] M. Michalska, L. Machtoub, H. D. Manthey, E. Bauer, V. Herold, G. Krohne, G. Lykowsky, M. Hildenbrand, T. Kampf, P. Jakob, A. Zernecke and W. R. Bauer, 'Visualization of vascular inflammation in the atherosclerotic mouse by ultrasmall superparamagnetic iron oxide vascular cell adhesion molecule-1-specific nanoparticles.' *Arteriosclerosis, thrombosis, and vascular biology*, vol. 32, no. 10, pp. 2350–7, 2012.

[15] C. Burtea, S. Ballet, S. Laurent, O. Rousseaux, A. Dencausse, W. Gonzalez, M. Port, C. Corot, L. Vander Elst and R. N. Muller, 'Development of a magnetic resonance imaging protocol for the characterization of atherosclerotic plaque by using vascular cell adhesion molecule-1 and apoptosis-targeted ultrasmall superparamagnetic iron oxide derivatives.' *Arteriosclerosis, thrombosis, and vascular biology*, vol. 32, no. 6, e36–48, 2012.

[16] B. A. Kaufmann, J. M. Sanders, C. Davis, A. Xie, P. Aldred, I. J. Sarembock and J. R. Lindner, 'Molecular imaging of inflammation in atherosclerosis with targeted ultrasound detection of vascular cell adhesion molecule-1.' *Circulation*, vol. 116, no. 3, pp. 276–84, 2007.

[17] C. Wenning, C. Kloth, M. T. Kuhlmann, A. H. Jacobs, O. Schober, S. Hermann and M. a. Schäfers, 'Serial F-18-FDG PET/CT distinguishes inflamed from stable plaque phenotypes in shear-stress induced murine atherosclerosis.' *Atherosclerosis*, vol. 234, no. 2, pp. 276–82, 2014.

[18] A. Broisat, S. Hernot, J. Toczek, J. De Vos, L. M. Riou, S. Martin, M. Ahmadi, N. Thielens, U. Wernery, V. Caveliers, S. Muyldermans, T. Lahoutte, D. Fagret, C. Ghezzi and N. Devoogdt, 'Nanobodies targeting mouse/human VCAM1 for the nuclear imaging of atherosclerotic lesions.' *Circulation research*, vol. 110, no. 7, pp. 927–37, 2012.

[19] Y. S. Chatzizisis, R. Blankstein and P. Libby, 'Inflammation goes with the flow: Implications for non-invasive identification of high-risk plaque', *Atherosclerosis*, vol. 234, no. 2, pp. 476–478, 2014.

[20] M. L. James and S. S. Gambhir, 'A molecular imaging primer: modalities, imaging agents, and applications.' *Physiological reviews*, vol. 92, no. 2, pp. 897–965, 2012.

[21] F. Hyafil, J. C. Cornily, J. E. Feig, R. Gordon, E. Vucic, V. Amirbekian, E. a. Fisher, V. Fuster, L. J. Feldman and Z. a. Fayad, 'Noninvasive detection of macrophages using a nanoparticulate contrast agent for computed tomography.' *Nature medicine*, vol. 13, no. 5, pp. 636–41, 2007.

[22] J. L. Van Herck, G. R. Y. De Meyer, W. Martinet, R. a. Salgado, B. Shivalkar, R. De Mondt, H. Van De Ven, A. Ludwig, P. Van Der Veken, L. Van Vaeck, H. Bult, A. G. Herman and C. J. Vrints, 'Multi-slice computed tomography with N1177 identifies ruptured atherosclerotic plaques in rabbits.' *Basic research in cardiology*, vol. 105, no. 1, pp. 51–9, 2010.

[23] L. Nebuloni, G. A. Kuhn and R. Müller, 'A comparative analysis of water-soluble and blood-pool contrast agents for in vivo vascular imaging with micro-CT.' *Academic radiology*, vol. 20, no. 10, pp. 1247–55, 2013.

[24] Q.-Y. Cai, S. H. Kim, K. S. Choi, S. Y. Kim, S. J. Byun, K. W. Kim, S. H. Park, S. K. Juhng and K.-H. Yoon, 'Colloidal Gold Nanoparticles as a Blood-Pool Contrast Agent for X-ray Computed Tomography in Mice', *Investigative Radiology*, vol. 42, no. 12, pp. 797–806, 2007.

[25] Y. Liu, K. Ai and L. Lu, 'Nanoparticulate X-ray computed tomography contrast agents: from design validation to in vivo applications.' *Accounts of chemical research*, vol. 45, no. 10, pp. 1817–1827, 2012.

[26] G. Sonavane, K. Tomoda and K. Makino, 'Biodistribution of colloidal gold nanoparticles after intravenous administration: Effect of particle size', *Colloids and surfaces. B, Biointerfaces*, vol. 66, no. 2, pp. 274–280, 2008.

[27] B. Trachet, M. Renard, G. De Santis, S. Staelens, J. De Backer, L. Antiga, B. Loeys and P. Segers, 'An Integrated Framework to Quantitatively Link Mouse-Specific Hemodynamics to Aneurysm Formation in Angiotensin II-infused ApoE -/- mice.' *Annals of biomedical engineering*, vol. 39, no. 9, pp. 2430–2444, 2011.

[28] B. De Man, J. Nuyts, P. Dupont, G. Marchal and P. Suetens, 'An iterative maximum-likelihood polychromatic algorithm for CT.' *IEEE transactions on medical imaging*, vol. 20, no. 10, pp. 999–1008, 2001.

[29] A. Ziegler, T. Nielsen and M. Grass, 'Iterative reconstruction of a region of interest for transmission tomography', *Medical Physics*, vol. 35, no. 4, pp. 1317–27, 2008.

[30] H. J. Johnson, G. Harris, K. Williams, H. J. Johnson, G. Harris and S. Pieper, 'BRAINSFit : Mutual Information Rigid Registrations of Whole-Brain 3D Images , Using the Insight Toolkit', *The Insight Journal*, pp. 1–10, 2007.

[31] A. Fedorov, R. Beichel, J. Kalpathy-Cramer, J. Finet, J.-C. Fillion-Robin, S. Pujol, C. Bauer, D. Jennings, F. Fennessy, M. Sonka, J. Buatti, S. Aylward, J. V. Miller, S. Pieper and R. Kikinis, '3D Slicer as an image computing platform for the Quantitative Imaging Network.' *Magnetic resonance imaging*, vol. 30, no. 9, pp. 1323–41, 2012.

[32] L. Antiga, M. Piccinelli, L. Botti, B. Ene-Iordache, A. Remuzzi and D. a. Steinman, 'An image-based modeling framework for patient-specific computational hemodynamics.' *Medical & biological engineering & computing*, vol. 46, no. 11, pp. 1097–1112, 2008.

[33] M. Piccinelli, A. Veneziani, D. A. Steinman, A. Remuzzi and L. Antiga, 'A framework for geometric analysis of vascular structures: application to cerebral aneurysms.' *IEEE transactions on medical imaging*, vol. 28, no. 8, pp. 1141–55, 2009.

[34] E. R. Brown, R. A. Kronmal, D. A. Bluemke, A. D. Guerci, J. J. Carr, J. Goldin and R. Detrano, 'Coronary calcium coverage score: determination, correlates, and predictive accuracy in the Multi-Ethnic Study of Atherosclerosis.' *Radiology*, vol. 247, no. 3, pp. 669–75, 2008.

[35] S. J. Richter and C. Richter, 'A Method for Determining Equivalence in Industrial Applications', *Quality Engineering*, vol. 14, no. 3, pp. 375–380, 2002.

[36] Y. S. Chatzizisis, A. U. Coskun, M. Jonas, E. R. Edelman, C. L. Feldman and P. H. Stone, 'Role of endothelial shear stress in the natural history of coronary atherosclerosis and vascular remodeling: molecular, cellular, and vascular behavior.' *Journal of the American College of Cardiology*, vol. 49, no. 25, pp. 2379–93, 2007.

[37] A. Seneviratne, M. Hulsmans, P. Holvoet and C. Monaco, 'Biomechanical factors and macrophages in plaque stability.' *Cardiovascular research*, vol. 99, no. 2, pp. 284–93, 2013.

[38] F. P. M. Oliveira and J. M. R. S. Tavares, 'Medical image registration: a review.' *Computer methods in biomechanics and biomedical engineering*, vol. 17, no. 2, pp. 73–93, 2014.

[39] F. A. Stewart, S. Heeneman, J. te Poele, J. Kruse, N. S. Russell, M. Gijbels and M. Daemen, 'Ionizing Radiation Accelerates the Development of Atherosclerotic Lesions in ApoE-/- Mice and Predisposes to an Inflammatory Plaque Phenotype Prone to Hemorrhage', *The American Journal of Pathology*, vol. 168, no. 2, pp. 649–658, 2006.

[40] D. L. Tribble, M. H. Barcellos-Hoff, B. M. Chu and E. L. Gong, 'Ionizing Radiation Accelerates Aortic Lesion Formation in Fat-Fed Mice via SOD-Inhibitable Processes', *Arteriosclerosis, Thrombosis, and Vascular Biology*, vol. 19, no. 6, pp. 1387–1392, 1999.

[41] H. Wolburg and W. Paulus, *Choroid plexus: Biology and pathology*, 2010.

[42] C. Van der Donckt, L. Roth, G. Vanhoutte, I. Blockx, D. Bink, K. Ritz, I. Pintelon, J.-P. Timmermans, D. Bauters, W. Martinet, M. Daemen, M. Verhoye and G. R. Y. De Meyer, 'Fibrillin-1 impairment enhances blood–brain barrier permeability and xanthoma formation in brains of apolipoprotein E-deficient mice', *Neuroscience*, vol. 295, pp. 11–22, 2015.

IV

Role of wall shear stress in the pathophysiology of atherosclerosis in mouse models

Chapters

Chapter 8

Assessment of shear stress metrics using mouse-specific FSI simulations *

8.1 Introduction

Mouse models are often used to study the development of atherosclerosis, due to their rapid development of atherosclerotic plaques. In particular, ApoE$^{-/-}$ knockout mice have been reported to develop spontaneous diet-induced plaques, which have morphological resemblance to human plaques [1]–[3]. It is generally accepted that shear stresses, imposed by the blood flow on the endothelial cells, play a crucial role in the onset of atherosclerosis. This hypothesis has been extensively studied and validated in humans [4], [5] and animal models [6], [7], as well as in surgically altered flow conditions *in vivo* [8], [9]. However, the smaller dimensions and the higher heart rate in mice make measurements to calculate the shear stress challenging. Although the Hagen-Poiseuille formula may provide an estimate of the order of magnitude of wall shear stress, its accuracy is expected to be low in bifurcation regions (e.g. carotid bifurcation) where the blood flow is more complex. Alternatively, the wall shear rate can be calculated from an MRI measurement of the velocity

*This chapter is based on the work: D. De Wilde, B. Trachet, N. Debusschere, F. Iannaccone, A. Swillens, J. Degroote, J. Vierendeels, G. R. De Meyer and P. Segers, 'Assessment of shear stress related parameters in the carotid bifurcation using mouse-specific FSI simulations', *Journal of Biomechanics*, In press, 2015

field in the murine CCA [10]. Nevertheless, spatial resolution is still limited and the temporal resolution of MRI does not allow capturing complex flow oscillations in the mouse carotid.

In order to overcome these limitations, computational fluid dynamics (CFD) simulations have been used to calculate WSS. Several derived parameters such as the TAWSS, the OSI [11] and RRT [12] have been proposed to serve as indicators plaque initiation regions [13]. These parameters have been studied in the murine aortic arch, CCA and/or the abdominal aorta [14]–[22], in relation to both plaque and aneurysm development. Moreover, altered shear stress patterns induced via surgical implantation of a tapering cast around the murine right CCA have been assessed with CFD [23]). CFD simulations, however, assume rigid walls and do not take the volume buffering in the arteries into account. Fluid-structure interaction (FSI) simulations add the wall movement through combined computational solid mechanics (CSM) and CFD simulations. This approach makes the simulations more complex and time consuming, but leads to more realistic simulations as we recently demonstrated in an FSI model of the abdominal aorta of the mouse [24].

In the current study, we show that the rigid wall assumption of CFD simulations hampers the application of realistic flow boundary conditions at the carotid bifurcation in mice. Therefore, we performed FSI simulations of 8 carotid bifurcations (left and right) in 4 ApoE$^{-/-}$ mice, using mouse specific geometries and boundary conditions measured *in vivo*.

8.2 Methods

8.2.1 Mice

Data were acquired in 4 female ApoE$^{-/-}$ mice, fed a Western type diet (TD88137, Harlan Teklad, Madison, Wis, USA) ad libitum from the age of 6 weeks until 16 weeks. The mice were housed in groups of 4-8 animals in well-ventilated cages. Their cages were kept under controlled environmental conditions, resulting in a 12h normal light/dark cycle, a temperature of 20-23°C and a 50% relative humidity. All the experiments were conducted according to the EC guidelines and were approved by the animal ethics committee of Ghent University. The data represents a subgroup of a larger study, with the complete protocol described in [25].

8.2.2 Measurements

8.2.2.1 Ultrasound measurements

Animals underwent an imaging protocol at week 16 consisting of ultrasound examination and a contrast-enhanced μCT protocol. US imaging was performed using a high-frequency US scanner (Vevo 2100, Visualsonics, Toronto,

Canada) equipped with a linear array probe (MS550D, 22-55MHz). A single operator (DDW) performed all measurements. The mice were secured in a supine position while monitoring the ECG, the respiratory rate and the body temperature under 1-1.5% isoflurane anaesthesia. Flow velocities were assessed using PW Doppler US measurements proximal to the bifurcation in the CCA and distal to the bifurcation (outflows) at the ECA and ICA. radio frequency (RF) M-mode US measurements were performed at CCA, ECA and ICA. The distance of these ultrasonic measurement locations to the bifurcation was measured.

8.2.2.2 μCT measurements

After the US examination, anaesthesia was maintained, and the mice immediately underwent a contrast-enhanced μCT scan using a Triumph-II imaging system (TriFoil Imaging, Chatsworth, CA, USA). First, 100 μl/25g body weight Aurovist (Nanoprobes, Yaphank, NY, USA) was injected in the tail vein (Wathen et al., 2013). The scanner settings were set to 50 μm focal spot size, 50 μm detector pixel size, 3.5 times magnification, 500 μA tube current, 75 kVp tube voltage, 1024 projections and a continuous rotation mode.

8.2.3 Processing of the measurements

8.2.3.1 Ultrasound processing

The outer envelope of the Doppler spectrum was tracked using an application written in Matlab (Mathworks, Natick, Massachusetts, USA). The diameter distension was obtained using an ultrasonic vessel wall tracking algorithm as described by Rabben *et al.* [26]. A flowchart of the processing of the measurements is given in figure 8.1. Signals were cycle-averaged (minimally 3 cycles) based on the R-peak of the ECG. The velocity and diameter signals were time-aligned (since a non-consistent time-offset was detected between both signals) by shifting the diameter distension waveforms. This was done automatically as part of the ln(D)U method for local wave speed assessment [27], [28]. The time shift for which the ln(D)U-loop fitted best to the theoretical straight line in the early systolic region was selected by minimising the L2-norm of the difference between the measured data and the linear fit, divided by the number of sample points in the selected upslope region.

8.2.3.2 μCT processing

The Iterative Maximum-likelihood Polychromatic Algorithm for CT was applied to reconstruct the μCT data at a 0.05 mm isotropic voxel size [29]. Mimics (Materialise, Leuven, Belgium) was used to semi-automatically segment the three branches of the carotid bifurcation, CCA, ECA and ICA.

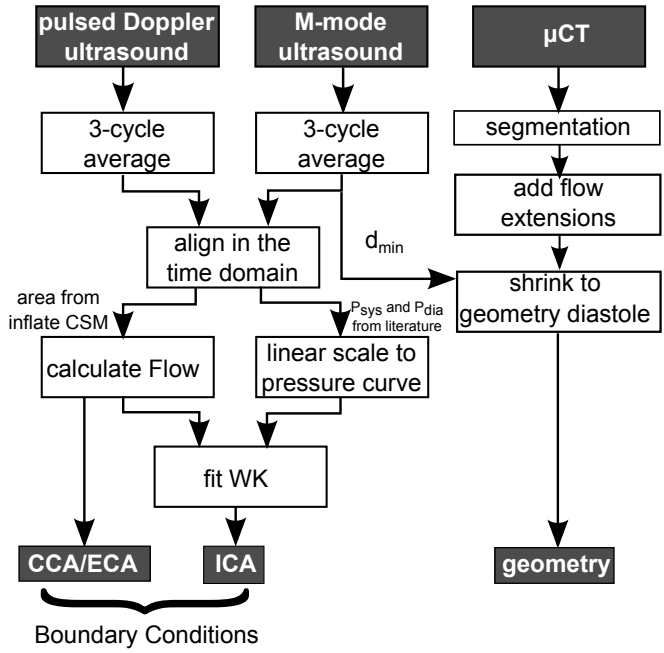

Figure 8.1: Overview of the processing of the measurement data. The US measurements were used to generate mouse specific boundary conditions for the flow simulations. From the μCT measurement, the diastolic geometry of the carotid bifurcation was created.

The workflow was based on thresholding and region growing steps, combined with manual editing where needed. Afterwards, flow extensions with a length equal to the diameter of the arteries were added in the VMTK (`www.vmtk.org`). In the end, the segmented geometry was shrunk to the diastolic radius measured with M-mode US (with a rescale factor of 0.8, 0.84, 0.84 and 0.88 for the four mice). The final result was inspected visually by plotting the segmented contours on the μCT images.

8.2.4 Creating a volume mesh using the XTM method

From the resulting STL-surface, a volume mesh was constructed in pyFormex (`http://www.nongnu.org/pyformex/`) using the Extended TreeMesh method (XTM) [30]. This meshing method results in a high-quality unstructured hexahedral mesh, with the cells aligned along the predominant direction of flow. A mesh sensitivity study was performed to assure that the 90% percentile of the TAWSS, OSI and RRT were converged. The 10% percentile of the TAWSS (TAWSS-low) was also included to assure low TAWSS were correctly calculated. Convergence was obtained with 303k cells as depicted in figure 8.2 a). Meshes of the arterial wall were generated assuming a wall thickness of 10% of the local luminal diameter and 3 cell layers in the

radial direction [24]. The structural meshes contained around 65k cells and convergence was assured using the 90% percentile of maximum displacement figure 8.2 b). Figure 8.3 depicts the fluid mesh (white) and the structural mesh (grey) for a representative geometry.

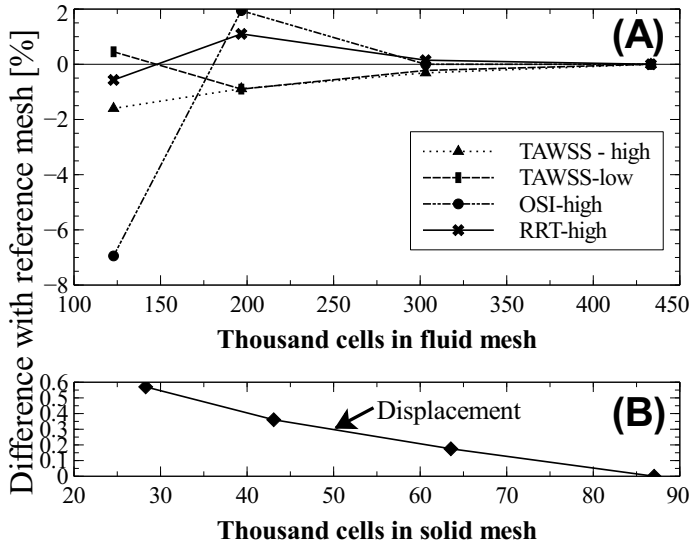

Figure 8.2: (A) Results of the mesh convergence study for the fluid domain. Convergence of the high values (90% percentile) of the TAWSS, OSI and RRT are plotted. For the TAWSS also the low values (10% percentile) values are considered. The difference with the values of the reference mesh (433k cells) is shown. For 300k cells convergence is reached. (B) The 90% percentile of the maximum displacement for the solid domain convergence study with respect to the reference value (87k cells mesh).

8.2.5 The Wall Mechanics problem

The CSM simulations were performed using the commercial finite element solver Abaqus Standard via an implicit (backward-Euler) time integration scheme.

8.2.5.1 Material Model Parameter Fitting

The blood vessel wall was modelled as an incompressible hyperelastic Arruda-Boyce material [24], with material parameters fitted to measurement data. The material parameter fitting procedure is illustrated in figure 8.4: an idealised cylindrical CCA geometry X_{cyl} was constructed using the following dimensions (averaged on 8 carotids): inner diastolic radius of 0.215 mm, wall thickness of 10% of the diameter, spring constant k_s of 1e6 Pa/m (to model external tissue; see further). The Arruda-Boyce λ_m parameter was set to

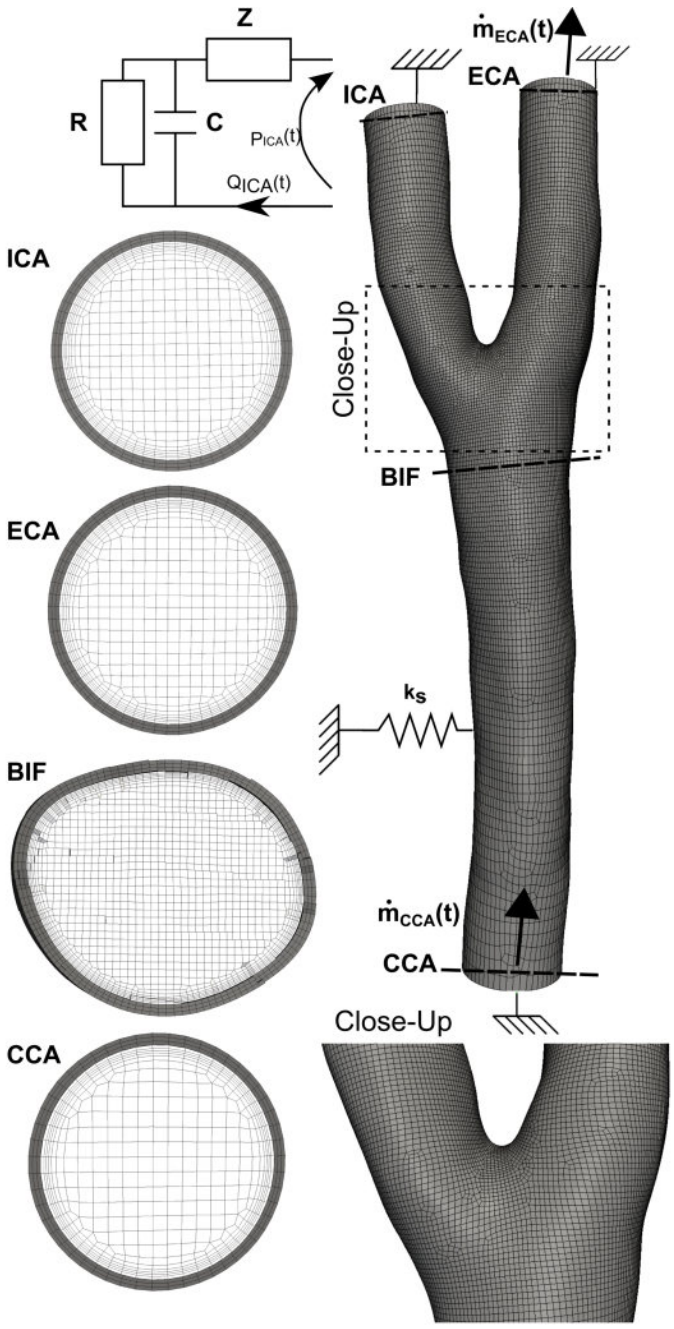

Figure 8.3: The fluid mesh (white) and structural mesh (grey) constructed with the XTM algorithm. The boundary conditions for both the CFD and CSM simulations are also schematically represented.

1.01 [24]. For the shear modulus μ an iterative optimisation procedure was performed based on the initial shear modulus μ^o and the average measured systolic radius of 0.24716 mm. Applying the axial prestress and diastolic inflate backwards incremental method (BI) (see below) and a static structural simulation with a systolic pressure load of P_{sys}=119 mmHg [31], the simulated systolic diameter could be calculated as a function of the material parameter guess μ^i and was compared to the peak of the distension waveform. The material model optimisation resulted in a value of 9516 Pa for μ^*. The same parameter value was used for all 8 simulations.

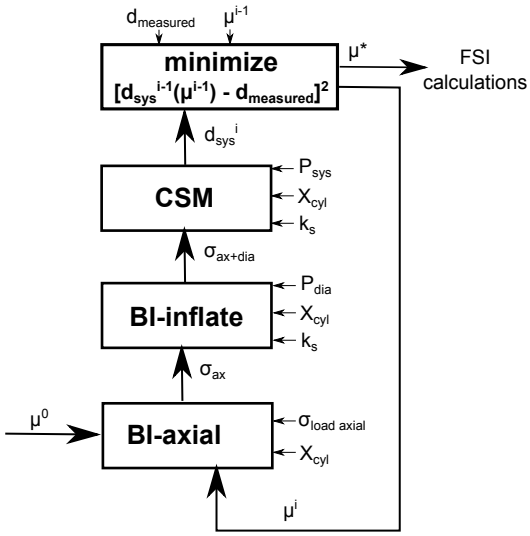

Figure 8.4: Flowchart of the material parameter optimisation. For this parameter optimisation loop, an average CCA cylindrical geometry (X_{cyl}) was pre-loaded with the axial prestress ($\sigma_{load\ axial}$) and the diastolic pressure P_{dia}. The systolic distension d_{sys} was calculated by applying the systolic pressure P_{sys}. The material model parameter was optimised iteratively so that d_{sys} equalled the measurement.

8.2.5.2 External tissue support

The stabilising influence of external tissue was modelled using spring elements at the outer wall surface [32], as plotted schematically at the bottom of figure 8.5 b). This resulted in around 20k springs per model (ranging from 18k to 23k springs). The results are independent of the exact amount of springs due to the adaptation of the spring constant to the local cell area. Assuming that the tissue pressure of mice and humans is similar, the spring constant k_s as given by [32] in humans (1e4 Pa/m) rescales to a value of approximately 1e6 Pa/m in mice (tissue pressure = k_s*distension, with the distension of the aorta artery in humans (2.3 mm) [33] being about 50 times higher than the murine carotid artery distension).

8.2.5.3 *Initial stresses*

To account for the diastolic *in vivo* stress state, the BI method was applied [34], [35] (figure 8.5 b). In short, this is an iterative approach that starts from the deformed geometry, to find the internal stresses under a load. The resulting stress state in the original geometry is in equilibrium with the applied load, leading to no further displacements. We first applied an axial prestress of 100 kPa ($\sigma_{\text{load axial}}$) to the cross section of the CCA while fixing the ECA and ICA outlets (schematic overview: figure 8.5 a - bottom). This is a stress value in between the low and medium extension found in [36]. The forward calculation steps of the BI method were performed using the commercial finite element solver Abaqus Standard (Simulia, Johnston, USA). The axial load was smoothly increased to 100 kPa in 10 steps and kept constant afterwards [34].

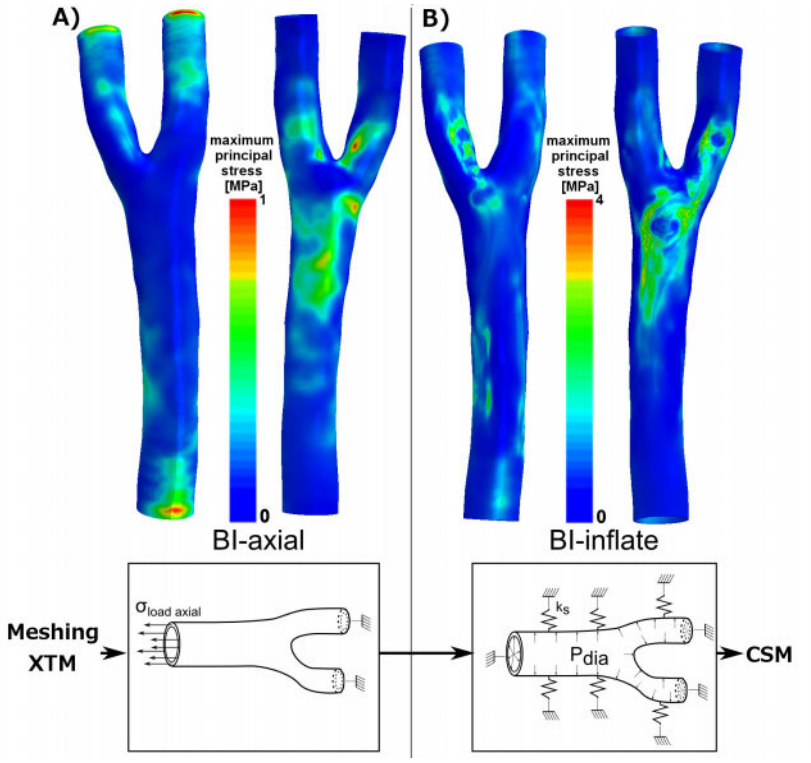

Figure 8.5: The two BI steps (BI-axial and BI-inflate) to calculate the *in vivo* stress state. (A) The maximal principal stress in the carotid bifurcation under an axial prestress with the original geometry, calculated with the BI-axial step. (B) The *in vivo* stress state, under a combined load of an axial prestress and a diastolic pressure, calculated with the second BI step, BI-inflate. The resulting stress field was used as an initial condition for the following CSM step and the final FSI calculations.

Secondly, a diastolic pressure (P_{dia}) of 87 mmHg [31] was added by performing a second BI calculation with altered loads and boundary conditions. At the inner surface of the artery, the pressure was increased in 50 steps from zero to a value of 87 mmHg. This time, only radial movement was allowed at the three boundaries: CCA, ECA and ICA. The stress field resulting from the axial prestress procedure (σ_{ax}) was applied as an initial condition to the BI-inflate step. Because no axial displacement was allowed, the axial pre-stress could not relax and remained present in the solution. The external tissue was modelled with springs, as explained previously (schematic overview: figure 8.5 b – bottom). The convergence criteria were: 1e-6m maximum displacement, 1e-11m L2 norm of the displacement and 1 Pa for the L2 norm of the difference in maximal principal stresses between two iterations. This second BI step resulted in the *in vivo* stresses (σ_{ax+dia}) in the geometry under a combined axial prestress and a diastolic pressure load. How both BI steps fit into the general work flow, is indicated in figure 8.6.

8.2.6 The Flow Mechanics Problem

All flow simulations were performed with the finite volume solver Fluent 14.5 (Ansys, Canonsburg, USA). The density of the blood was set to 1060kg/m^3 with a constant dynamic viscosity of 3.5mPas [16], [19], [37]. The SIMPLE algorithm with second-order upwind discretization was used for the pressure-velocity coupling and the momentum equations, respectively. For the time integration, a second order implicit discretization scheme was used. Convergence was reached when the continuity and momentum relative residuals dropped below 1e-6. For the FSI-simulations, a spring analogy was used to move the interior grid nodes of the fluid domain at an arbitrary velocity (arbitrary Lagrangian–Eulerian method).

8.2.6.1 Boundary conditions

Mass flow inlets were used at the inlet (CCA) and one outlet (ECA), while a windkessel model was imposed at the ICA outlet. As blood flow velocity $U_b(t)$ was measured rather than mass flow, rescaling was mandatory. To calculate the instantaneous average velocity over the cross-section, the maximum velocity was divided by 2, assuming a parabolic flow profile at the measuring location (which was confirmed a posteriori by the simulations). As also the cross section varied throughout the cardiac cycle, a structural simulation was performed inflating the prestressed geometries according to the pressure curve. The cross-sectional area at the location of the flow velocity measurements was exported. The mean velocity curve was then multiplied with the cross sectional area curve and the density of 1060 kg/m^3 to calculate the mass flow profile at these locations.

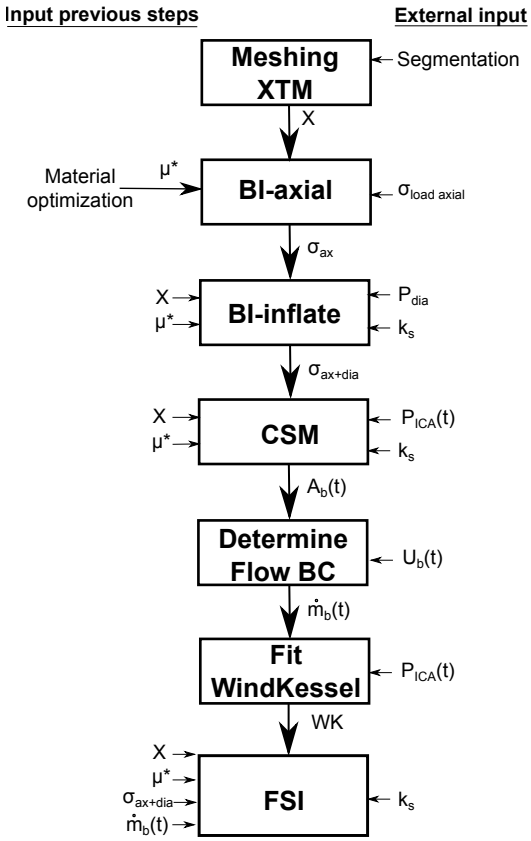

Figure 8.6: Flowchart depicting the followed methodology for the FSI simulations. First, the segmented geometry was meshed with the XTM. Using the optimised parameter μ^* (see material optimisation flowchart figure 8.4), the *in vivo* stress state under an axial stress load ($\sigma_{\text{load axial}}$) and a diastolic pressure (P_{dia}) was calculated with two BI steps (BI-axial and BI-inflate). The areas of the lumen boundaries was approximated by inflating the bifurcations according to the pressure profile. Based on the resulting areas (A_b) and the measured US velocity (U_b), the mass flow ($\dot{m}_b$) at the boundaries was determined. Finally the ICA windkessel was fitted to the pressure (P_{ICA}) and flow profile ($\dot{m}_b$).

Due to measuring errors and assumptions in the data processing, the time-averaged mass flow balance in the model (cycle-averaged difference between in- and outflow) was not completely fulfilled. As we estimated the CCA measurement to be the most accurate, a scaling factor c was applied to the ICA and ECA mass flows such that averaged over a heart cycle $\dot{m}_{\text{CCA-meas}} = c^{te\star}(\dot{m}_{\text{ECA-meas}}+\dot{m}_{\text{ICA-meas}})$. Note that only the rescaled ECA flow is directly imposed as boundary condition. The average correction factor for the measured ECA and ICA flow was 1.20±0.22 (ranging from 0.9469 to 1.6839).

For the FSI simulations, a three element windkessel model [38] was applied at the ICA outlet (figure 8.3). Model parameters were fitted in Matlab by minimising the difference between a target pressure curve and the pressure curve predicted by the windkessel model, when imposing the rescaled ICA flow. The target pressure curve was approximated by linearly rescaling the measured diameter distension waveform to the assumed *in vivo* diastolic and systolic pressures $P_{\text{ICA}}(t)$ (87/ 119 mmHg) [31]. As such, the global pressure in the model is not a priori prescribed, but will be determined by the imposed inlet and outlet flow, the 3-element windkessel model parameters and the properties of the arterial wall.

8.2.7 FSI coupling

The in house developed code Tango was applied to couple the flow and structural solvers for describing the FSI problem. At the interface a new prediction of the location was made with an IQN-ILS algorithm based on the previous positions calculated by the structural solver [39]. At each time step coupling iterations between both solvers were performed to meet equilibrium at the interface.

8.2.8 HWP

Derived haemodynamic wall parameters include the TAWSS, OSI and RRT [11]–[13].

$$\text{TAWSS} = \frac{1}{T}\int_0^T \|\vec{\tau}\|\,\mathrm{d}t \tag{8.1a}$$

$$\text{OSI} = \frac{1}{2}\left(1 - \frac{\left\|\int_0^T \vec{\tau}\,\mathrm{d}t\right\|}{\int_0^T \|\vec{\tau}\|\,\mathrm{d}t}\right) \tag{8.1b}$$

$$\text{RRT} \sim \frac{1}{(1-2\cdot\text{OSI})\cdot\text{TAWSS}} \tag{8.1c}$$

$\vec{\tau}$ is the instantaneous wall shear stress vector and T the period of the cardiac cycle. In the case of FSI simulations where the arterial wall was

moving, a local coordinate system was constructed at every interface node using pyFormex moving with the arterial wall. The wall shear stress was expressed in this local frame of reference.

8.3 Results

8.3.1 Fitting the Windkessel model

The fitting of the Windkessel model resulted in the following values: Z= 1603.8±755.0 mmHg/mm/s, R= 8147.4±1491.1 mmHg/mm/s and C = 8.22E-06±2.61E-06 ml/mmHg. The diastolic pressure at the inlet was 91.2±2.4 mmHg (averaged over the 8 simulations), while the systolic pressure was 118.3±4.9 mmHg (table 8.1). The pressure drop over the carotid artery was 1.99+/-0.40 mmHg between CCA – ECA and 2.52±0.71 mmHg between CCA – ICA.

8.3.2 The simulated flow field

Figure 8.7 displays simulated pressure and flow waveforms for a representative case (mouse2, right bifurcation), as extracted from the cross-sections indicated in figure 8.8. The flow profile is highly laminar with no recirculation present around the bifurcation for any of the cases with the boundary condition (BC) extracted from the measurements (under anaesthesia). In diastole only a small amount of mass flow is present in the ECA, and the highest velocities are visible in the ICA at both time points. The displacement (figure 8.8 b) is smooth over the entire bifurcation with the highest displacement present at the bifurcation itself.

The simulated flow at the ICA agrees very well with the flow directly derived from the measurements (figure 8.9). In a CFD approach, the ICA-flow would equal the difference between inflow at CCA and outflow via the ECA, which would result in a much more peaked waveform due to the lack of buffering in systole (figure 8.9).

8.3.3 Results for the HWP

Flow derived indices are displayed in figure 8.10 (TAWSS), figure 8.11 (OSI) and figure 8.12 (RRT) for all eight simulated cases. Despite differences in absolute values of TAWSS, a similar spatial distribution of the lowered (blue) and elevated TAWSS (red) is present in all cases (figure 8.10). The high velocity in the ICA results in an elevated TAWSS compared to the CCA. A region with a lowered TAWSS (in blue) was present at the outer bend of the ECA. The OSI is highest mainly at the outer bend of the ECA zone but stays more localised compared to the TAWSS (figure 8.11). This trend continues in the RRT pattern shown in figure 8.12. In mice 2 and 3, the higher RRT value at the outer bend of the ECA is most pronounced, but only in mouse 3R (right bifurcation) this spans the whole ECA.

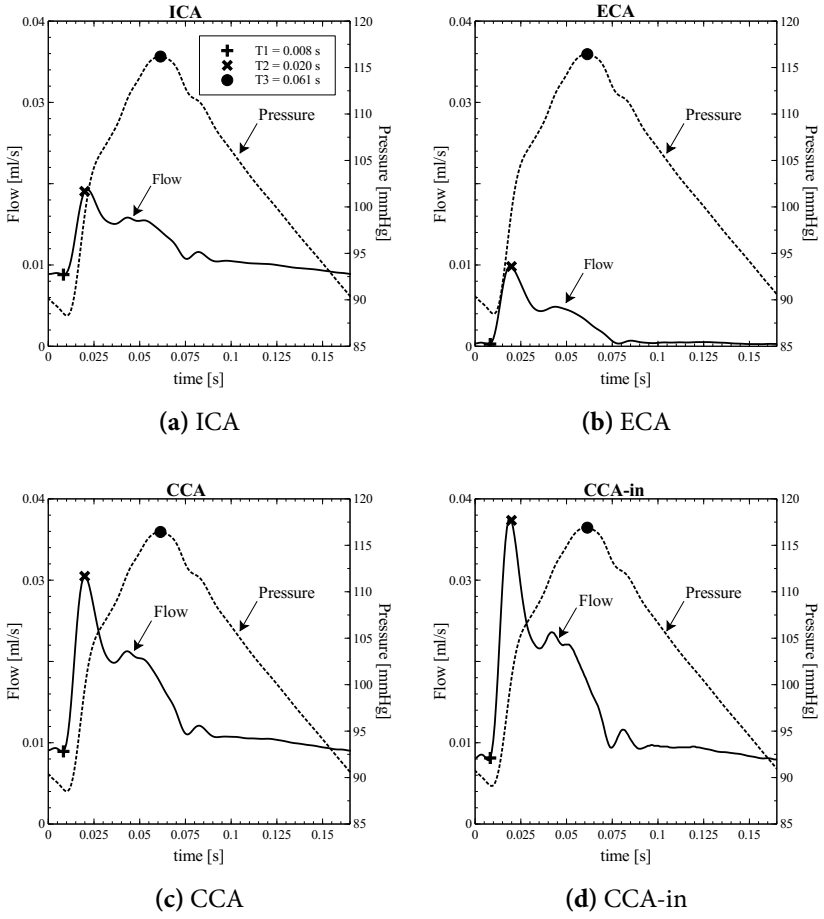

Figure 8.7: The calculated pressure and flow profiles in an example bifurcation at four different locations: (a) ICA,(b) ECA,(c) CCA, (d) CCA-in. (a-c) are taken close to the bifurcation and (d) at the inlet. The precise locations are shown in figure 8.8. The CCA buffers the flow, resulting in a less peaked flow profile at the CCA compared to the CCA-in. The flow in the ECA is small compared to the flow through the ICA.

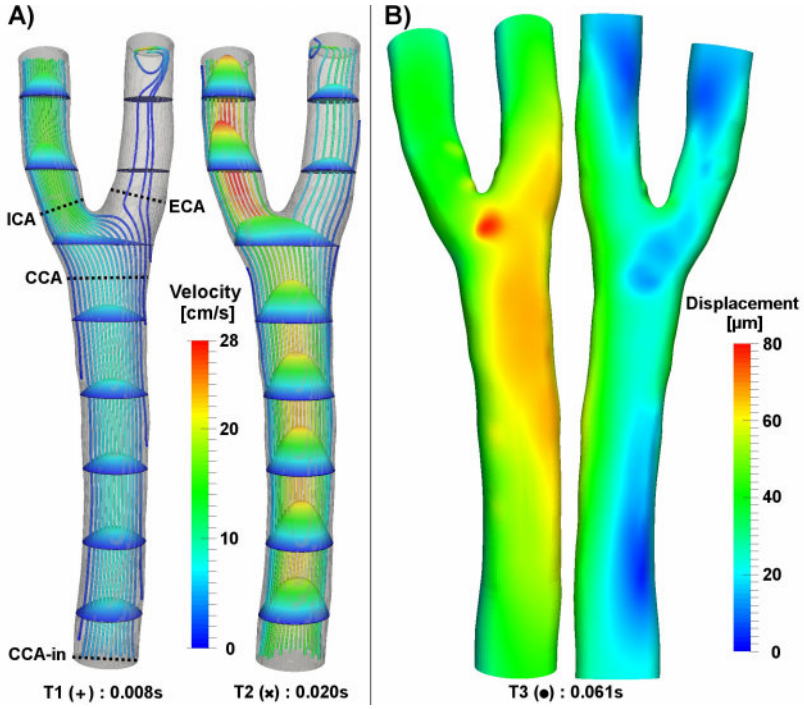

Figure 8.8: (A) The velocity fields at end diastole (+ in figure 8.7) and peak velocity (x). Laminar flow, without recirculation at the bifurcation is visible. (B) The displacement at peak pressure is largest at the bifurcation (•).

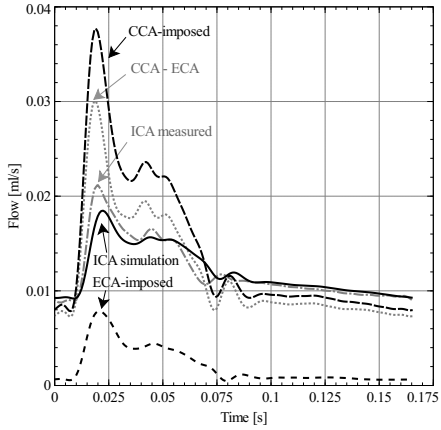

Figure 8.9: Comparison of the different flow profiles at the boundaries. For the CCA and ECA, the imposed flow profiles are plotted. The ICA measured flow, after correcting for the flow imbalance, is the target flow profile for the simulations. The FSI simulation resulted in an ICA flow profile (ICA simulation) that corresponds well with this profile. CFD simulations would neglect the buffering of the bifurcation and would have resulted in an ICA flow equal to QCCA-QECA

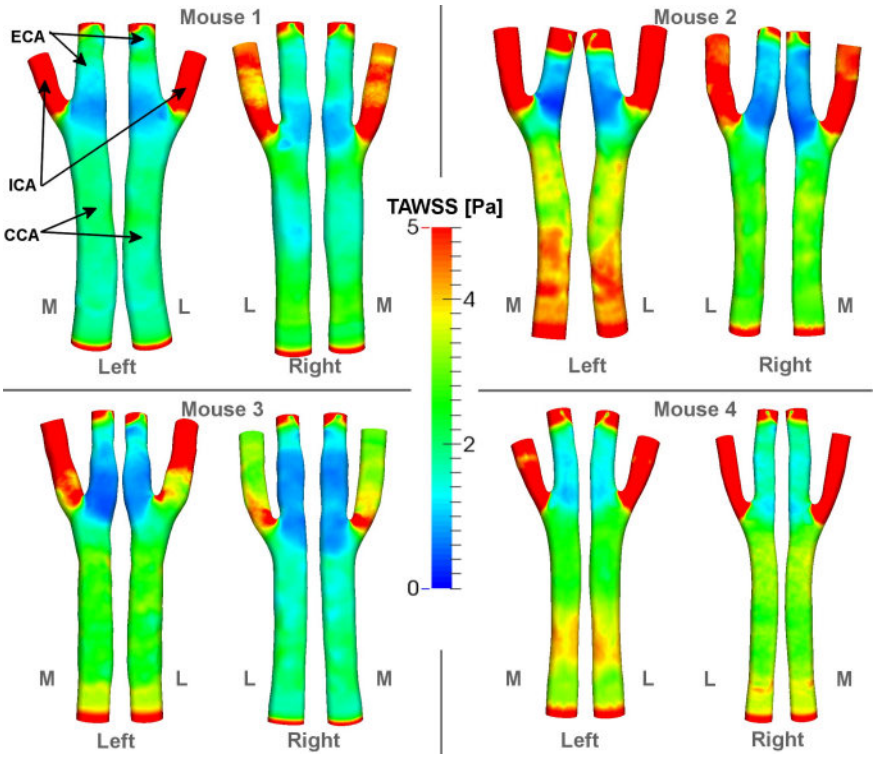

Figure 8.10: The TAWSS result from the FSI simulations of all the different bifurcations, medial (M) and lateral (L) views. Differences in absolute values between different bifurcations are present. However, the qualitative patterns are similar for all bifurcations.

8.4 Discussion

In this study, an FSI model of the carotid bifurcation was developed for the left and right carotid of 4 ApoE$^{-/-}$ mice, providing, to the best of our knowledge, the first estimates of wall shear stress distributions along the mouse carotid artery that take into account the buffering capacity of the walls. The model was animal-specific in terms of carotid geometries and imposed flow boundary conditions; the material model was tuned to averaged diameter distension measurements in the animal cohort.

In order to determine haemodynamic wall parameters, a realistic simulation of the blood flow is important. We are convinced that accounting for the fluid-structure interaction is of added value as it allows for a volume buffering in systole and a much more natural application of the boundary conditions. This is best illustrated in figure 8.9, where it is shown that merely using the difference between CCA inflow and ECA outflow to retrieve the ICA outflow (as is the case in CFD) leads to waveforms differing much more

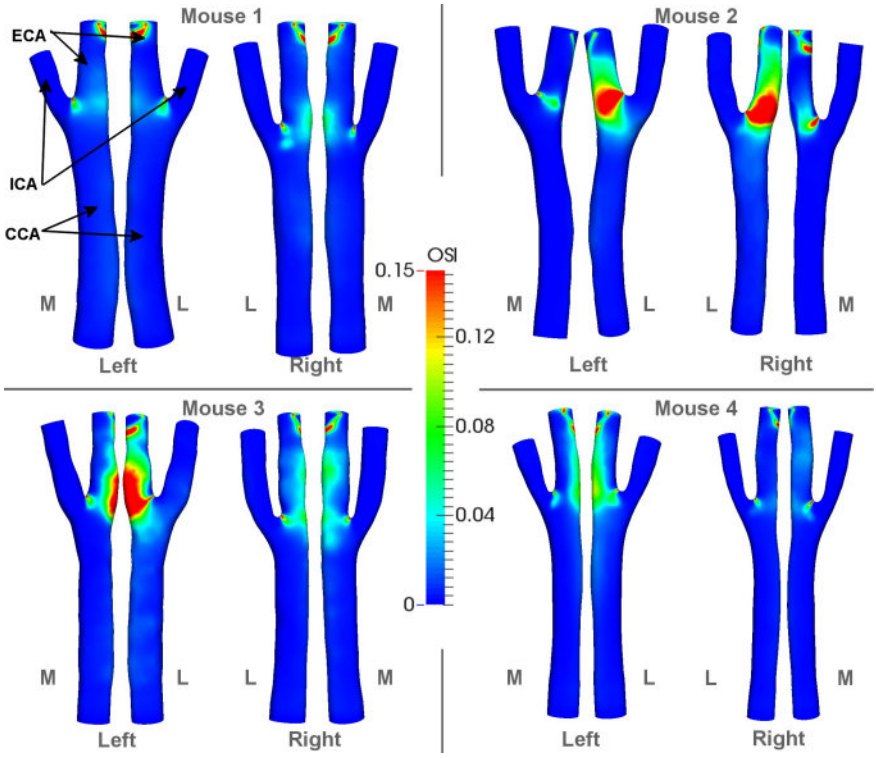

Figure 8.11: The OSI result from the FSI simulations of all the different bifurcations, medial (M) and lateral (L) views.

Table 8.1: Pressures [mmHg] and distensions [%] at the boundaries of the FSI simulations.

	CCA	ECA	ICA
Pulse Pressure - FSI	27.2±7.0	27.3±6.8	27.1±6.9
P_{dia} - FSI	91.2±2.4	90.5±2.3	89.8±2.5
P_{sys} - FSI	118.3±4.9	117.8±4.8	117.0±4.7
Distension - FSI	9.4±1.5	10.1±1.3	8.2±1.3
Distension - Measured	16.2±2.8	11.7±4.1	8.4±3.2

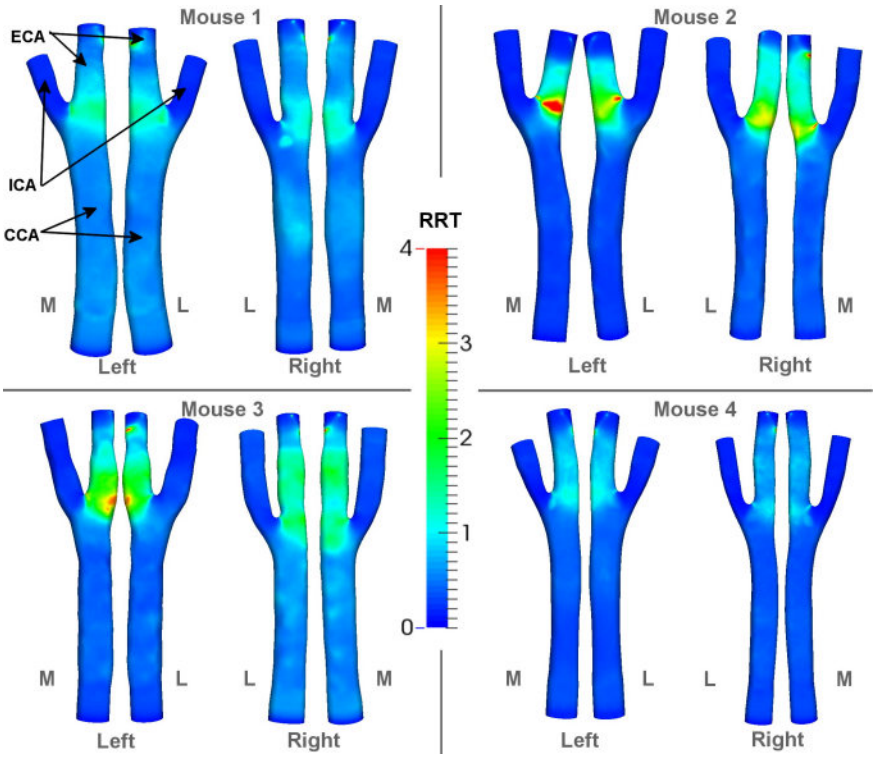

Figure 8.12: The RRT result from the FSI simulations of all the different bifurcations, medial (M) and lateral (L) views.

from the measured waveform than the one retrieved in the FSI simulations (L2-norm difference of 0.1330±0.0317 ml/s vs. 0.0111±0.0039 ml/s). Both approaches can also be compared with the pulsatility index (PI), defined as $(U_{sys}\text{-}U_{ed})/U_{mean}$ with U_{sys} the systolic, U_{ed} the end diastolic and U_{mean} the average outflow velocity. The pulsatility index (PI) at the ICA obtained by CFD (1.86±0.300) is considerably higher than the measured value of 0.777±0.164 which again was much better replicated by the FSI simulations (0.555±0.180). A full overview of the measured PI of all mice is given in section 6.3 on page 107.

In humans, flow separation and recirculation in the carotid bifurcation have been reported in 99 out of 100 subjects [40]. None of the 8 simulated murine carotid bifurcations, however, presented flow separation (neither in the FSI, nor in CFD simulations). It has been reported that the critical Reynolds number, below which no recirculation is present, is geometry dependent [41]. The Reynolds numbers in mice are much lower than in humans, and are lower in the carotid arteries than in the central aorta. Our simulations resulted in a Reynolds number of 12.7±2.9 (peak systole). Womersley numbers

were 0.46±0.03 at the CCA inlet. Note, however, that simulations were done in animals not showing any signs of plaque. As demonstrated in the aorta [15], the presence of plaque may lead to geometrical discontinuities that can induce local flow recirculation zones. Another explanation might be that the (flow) boundary conditions are based on US measurements performed while the mice were under anaesthesia. Mohri *et al.* showed that flow recirculations are present in the casted carotid artery, when simulating highly locomotor active mice by adapting the boundary conditions [23]. The influence of the anaesthesia and the locomotor activity is studied in more detail in chapter 9.

The main interest of the current research is the influence of the flow on the arterial wall through the WSS. The influence of these flow recirculations is minimal because the magnitude of the WSS vector is low at these location (with or without recirculations). Therefore, based on the single case that we computed, we can presume that the influence of the anaesthesia onto the HWPs is minimal when a normalisation is used to take the lower overall WSS into account.

Overall, the patterns of TAWSS and RRT were quite consistent between animals. Only for the CCA of mouse1 L/R and mouse3 R, the global TAWSS is lower compared to the other mice. This is consistent with the calculation of the TAWSS based on the Poiseuille flow assumption [42], which is lower for these CCA (between 3.3 and 4.7 Pa) compared to the other CCA (between 6.1 and 9.2 Pa). However, the locations where TAWSS is lowest (blue in figure 8.10) are similar in all mice: the outer bends of the ECA branch of the bifurcation. It was also observed that TAWSS in the ECA is lower compared to the ICA and CCA due to the lower flow.

Setting up and tuning the animal specific model is largely dependent on the haemodynamic measurements that are much more challenging in mice than in humans. Direct measurement of the flow in the murine CCA using MRI is possible but results in limited spatial (50x50x500 μm) and temporal (27 timeframes/cardiac cycle) resolution [10]. We determined the flow by multiplying the PW Doppler US velocity with the cross-sectional assuming a parabolic profile. As can be seen from figure 8.8 on page 162, the parabolic flow profile is a reasonable assumption for the CCA and for the side branches when measuring far enough downstream. Probably the largest error source is the angle correction of the PW Doppler US velocities, especially for the ICA and ECA measurements. To guarantee a correct mass balance over the bifurcation, we decided to apply a rescaling factor at the outflow velocity waveforms of the ECA and ICA outlets. On the other hand, the smaller magnitude of the ECA blood velocity and the higher penetration depth to reach the ICA are arguments to select either the ECA or the ICA as the least accurate measurement. Therefore we decided to distribute the error equally

over both branches. The high average flow correction factor (1.20±0.22) is mainly explained by the large correction for case 1L (1.68). Therefore, the results for bifurcation 1L should be interpreted with caution. When omitting that case, the average correction factor is 1.13±0.23, which is in the same order of magnitude as previous performed studies [19], [24].

A major drawback of our study is the absence of pressure measurements, which are still extremely challenging in mice. In our experience, non-invasive (tail-cuff) pressure data show large variability and we judged them insufficiently accurate, while invasive pressure measurements imply sacrificing the animal. We therefore decided to generate a pseudo pressure waveform based on rescaling the M-mode US diameter distension to a pressure range that was previously reported [31]. Although the high correlation between the measured and simulated distension curves justifies this choice, a mouse specific measurement would have further improved the simulations.

As described in the methods section, we applied a shrinking step after the initial segmentation based on the μCT images. This was necessary to account for the arterial pulsation/movement during the μCT measurements, and the partial volume effect, resulting in a gradual intensity transition from artery to surrounding tissue. With an extra shrinking step added to the measured diastolic diameter (M-mode US), we verified that these artefacts did not artificially inflate the geometry. The final segmentation was visually inspected on the μCT image. In the future, cardiac gated μCT [43] might circumvent the necessity of this step.

The material model used in these simulations is fairly simple. It does not include anisotropy, neither does it account for the layering of the arterial wall. We also assumed a fixed ratio between local radius and wall thickness. Given the focus of the study on flow-derived parameters, any material model providing a realistic degree of wall distension over the physiological pressure range would suit our purpose. Our choice for the Arruda-Boyce model is mainly driven by the model simplicity, with hyper-elastic behaviour achieved by fitting only one model parameter. We did, however, include the supporting effect of surrounding tissue in the simulations. This, together with the implementation of the axial prestress improved both the realism and the stability of the simulations compared to previous FSI simulations of the murine vasculature [24].

In the present study, we focused on advancing our computational biomechanics approach, and we have implemented a methodology that allows assessing carotid haemodynamics and derived flow-related parameters in what we think is a fairly realistic way. Overall, the zones of low TAWSS corresponded with the areas in which plaque development was found (chapter 7). In

chapter 10 the spatial correlation between these fluid mechanical parameters and plaque development and progression is studied.

8.5 Conclusion

We have presented mouse specific FSI simulations of eight carotid bifurcations of 4 ApoE$^{-/-}$ mice. A realistic wall movement was obtained by including the axial prestress, the *in vivo* stress state and the support of the surrounding tissue. The calculated haemodynamic wall parameters identified the sinus of the ECA at the bifurcation as the region that would be exposed most to an atherosclerosis-promoting haemodynamic environment.

Bibliography Chapter 8

[1] J. Jawien, R. Nastalek, R. Korbut, J. Jawień, P. Nastałek and R. Korbut, 'Mouse models of experimental atherosclerosis', *journal of physiology and pharmacology*, vol. 55, no. 3, pp. 503–517, 2004.

[2] A. A. Pendse, J. M. Arbones-Mainar, L. A. Johnson, M. K. Altenburg and N. Maeda, 'Apolipoprotein E knock-out and knock-in mice: atherosclerosis, metabolic syndrome, and beyond.' *Journal of lipid research*, vol. 50 Suppl, no. December 2008, S178–S182, 2009.

[3] S. C. Whitman, 'A practical approach to using mice in atherosclerosis research.' *The Clinical biochemist. Reviews*, vol. 25, no. 1, pp. 81–93, 2004.

[4] D. N. Ku, D. P. Giddens, C. K. Zarins and S. Glagov, 'Pulsatile flow and atherosclerosis in the human carotid bifurcation. Positive correlation between plaque location and low oscillating shear stress.' *Arteriosclerosis*, vol. 5, no. 3, pp. 293–302, 1985.

[5] J. E. Moore, C. Xu, S. Glagov, C. K. Zarins and D. N. Ku, 'Fluid wall shear stress measurements in a model of the human abdominal aorta: oscillatory behavior and relationship to atherosclerosis.' *Atherosclerosis*, vol. 110, no. 2, pp. 225–240, 1994.

[6] V. Peiffer, S. J. Sherwin and P. D. Weinberg, 'Computation in the rabbit aorta of a new metric - the transverse wall shear stress - to quantify the multidirectional character of disturbed blood flow.' *Journal of biomechanics*, vol. 46, no. 15, pp. 2651–2658, 2013.

[7] T. Thim, M. K. Hagensen, E. Falk, A. Hørlyck, W. Y. Kim, A. K. Niemann, S. A. Thrysøe, L. Drouet, W. P. Paaske and H. E. Bøtker, 'Wall shear stress and local plaque development in stenosed carotid arteries of hypercholesterolemic minipigs', *Journal of Cardiovascular Disease Research*, vol. 3, no. 2, pp. 76–83, 2012.

[8] C. Cheng, D. Tempel, R. van Haperen, A. van der Baan, F. Grosveld, M. J. A. P. Daemen, R. Krams and R. de Crom, 'Atherosclerotic lesion size and vulnerability are determined by patterns of fluid shear stress.' *Circulation*, vol. 113, no. 23, pp. 2744–2753, 2006.

[9] L. C. Winkel, A. Hoogendoorn, R. Xing, J. J. Wentzel and K. Van der Heiden, 'Animal models of surgically manipulated flow velocities to study shear stress-induced atherosclerosis', *Atherosclerosis*, vol. 241, no. 1, pp. 100–110, 2015.

[10] G. S. van Bochove, R. Straathof, R. Krams, K. Nicolay and G. J. Strijkers, 'MRI-determined carotid artery flow velocities and wall shear stress in a mouse model of vulnerable and stable atherosclerotic plaque.' *Magnetic Resonance Materials in Physics, Biology and Medicine*, vol. 23, no. 2, pp. 77–84, 2010.

[11] X. He, 'Pulsatile Flow in the Human Left Coronary Artery Bifurcation: Average Conditions', *Journal of Biomechanical Engineering*, vol. 118, no. 1, pp. 74–82, 1996.

[12] H. A. Himburg, D. M. Grzybowski, A. L. Hazel, J. A. LaMack, X.-M. Li and M. H. Friedman, 'Spatial comparison between wall shear stress measures and porcine arterial endothelial permeability.' *American journal of physiology. Heart and circulatory physiology*, vol. 286, no. 5, H1916–H1922, 2004.

[13] S.-W. Lee, L. Antiga and D. A. Steinman, 'Correlations among indicators of disturbed flow at the normal carotid bifurcation.' *Journal of biomechanical engineering*, vol. 131, no. 6, p. 061 013, 2009.

[14] P. Assemat, J. A. Armitage, K. K. Siu, K. G. Contreras, A. M. Dart, J. P. Chin-Dusting and K. Hourigan, 'Three-dimensional numerical simulation of blood flow in mouse aortic arch around atherosclerotic plaques', *Applied Mathematical Modelling*, vol. 38, no. 17-18, pp. 4175–4185, 2014.

[15] P. Assemat, K. K. Siu, J. Armitage, S. N. Hokke, A. Dart, J. Chin-Dusting and K. Hourigan, 'Haemodynamical stress in mouse aortic arch with atherosclerotic plaques: Preliminary study of plaque progression', *Computational and Structural Biotechnology Journal*, vol. 10, no. 17, pp. 98–106, 2014.

[16] A. Feintuch, P. Ruengsakulrach, A. Lin, J. Zhang, Y.-Q. Zhou, J. Bishop, L. Davidson, D. Courtman, F. S. Foster, D. A. Steinman, R. M. Henkelman and C. R. Ethier, 'Hemodynamics in the mouse aortic arch as assessed by MRI, ultrasound, and numerical modeling.' *American journal of physiology. Heart and circulatory physiology*, vol. 292, no. 2, H884–H892, 2007.

[17] Y. Hoi, Y.-Q. Zhou, X. Zhang, R. M. Henkelman and D. A. Steinman, 'Correlation between local hemodynamics and lesion distribution in a novel aortic regurgitation murine model of atherosclerosis.' *Annals of biomedical engineering*, vol. 39, no. 5, pp. 1414–22, 2011.

[18] Y. Huo, X. Guo and G. S. Kassab, 'The flow field along the entire length of mouse aorta and primary branches.' *Annals of biomedical engineering*, vol. 36, no. 5, pp. 685–699, 2008.

[19] B. Trachet, M. Renard, G. De Santis, S. Staelens, J. De Backer, L. Antiga, B. Loeys and P. Segers, 'An Integrated Framework to Quantitatively Link Mouse-Specific Hemodynamics to Aneurysm Formation in Angiotensin II-infused ApoE -/- mice.' *Annals of biomedical engineering*, vol. 39, no. 9, pp. 2430–2444, 2011.

[20] B. Trachet, A. Swillens, D. Van Loo, C. Casteleyn, A. De Paepe, B. Loeys and P. Segers, 'The influence of aortic dimensions on calculated wall shear stress in the mouse aortic arch.' *Computer methods in biomechanics and biomedical engineering*, vol. 12, no. 5, pp. 491–499, 2009.

[21] B. Vandeghinste, B. Trachet, M. Renard, C. Casteleyn, S. Staelens, B. Loeys, P. Segers and S. Vandenberghe, 'Replacing vascular corrosion casting by in vivo micro-CT imaging for building 3D cardiovascular models in mice.' *Molecular imaging and biology*, vol. 13, no. 1, pp. 78–86, 2011.

[22] Y.-C. Chen, A. V. Bui, J. Diesch, R. Manasseh, C. Hausding, J. Rivera, I. Haviv, A. Agrotis, N. M. Htun, J. Jowett, C. E. Hagemeyer, R. D. Hannan, A. Bobik and K. Peter, 'A Novel Mouse Model of Atherosclerotic Plaque Instability for Drug Testing and Mechanistic/Therapeutic Discoveries Using Gene and microRNA Expression Profiling.' *Circulation research*, vol. 113, no. 3, pp. 252–265, 2013.

[23] Z. Mohri, E. M. Rowland, L. A. Clarke, A. De Luca, V. Peiffer, R. Krams, S. J. Sherwin and P. D. Weinberg, 'Elevated Uptake of Plasma Macromolecules by Regions of Arterial Wall Predisposed to Plaque Instability in a Mouse Model', *PLoS ONE*, vol. 9, no. 12, e115728, 2014.

[24] B. Trachet, J. Bols, J. Degroote, B. Verhegghe, N. Stergiopulos, J. Vierendeels and P. Segers, 'An Animal-Specific FSI Model of the Abdominal Aorta in Anesthetized Mice', *Annals of Biomedical Engineering*, vol. 43, no. 6, pp. 1298–1309, 2015.

[25] D. De Wilde, B. Trachet, C. Van der Donckt, B. Vandeghinste, B. Descamps, C. Vanhove, G. R. Y. De Meyer and P. Segers, 'Vulnerable plaque detection and quantification with gold particle-enhanced computed tomography in atherosclerotic mouse models.' *Molecular imaging*, vol. 14, pp. 9–19, 2015.

[26] S. I. Rabben, S. Bjærum, V. Sørhus and H. Torp, 'Ultrasound-based vessel wall tracking: An auto-correlation technique with RF center frequency estimation', *Ultrasound in Medicine and Biology*, vol. 28, no. 4, pp. 507–517, 2002.

[27] J. Feng and A. W. Khir, 'Determination of wave speed and wave separation in the arteries using diameter and velocity', *Journal of Biomechanics*, vol. 43, no. 3, pp. 455–462, 2010.

[28] A. Swillens, L. Taelman, J. Degroote, J. Vierendeels and P. Segers, 'Comparison of non-invasive methods for measurement of local pulse wave velocity using fsi-simulations and in vivo data', *Annals of Biomedical Engineering*, vol. 41, no. 7, pp. 1567–1578, 2013.

[29] B. De Man, J. Nuyts, P. Dupont, G. Marchal and P. Suetens, 'An iterative maximum-likelihood polychromatic algorithm for CT.' *IEEE transactions on medical imaging*, vol. 20, no. 10, pp. 999–1008, 2001.

[30] J. Bols, L. Taelman, G. De Santis, J. Degroote, B. Verhegghe, P. Segers and J. Vierendeels, 'Unstructured hexahedral mesh generation of complex vascular trees using a multi-block grid-based approach', *Computer Methods in Biomechanics and Biomedical Engineering*, pp. 1–10, 2015.

[31] J. L. Van Herck, G. R. De Meyer, W. Martinet, C. E. Van Hove, K. Foubert, M. H. Theunis, S. Apers, H. Bult, C. J. Vrints and A. G. Herman, 'Impaired Fibrillin-1 Function Promotes Features of Plaque Instability in Apolipoprotein E-Deficient Mice', *Circulation*, vol. 120, no. 24, pp. 2478–2487, 2009.

[32] P. Moireau, N. Xiao, M. Astorino, C. A. Figueroa, D. Chapelle, C. A. Taylor and J.-F. Gerbeau, 'External tissue support and fluid-structure simulation in blood flows.' *Biomechanics and modeling in mechanobiology*, vol. 11, no. 1-2, pp. 1–18, 2012.

[33] F. Rengier, T. F. Weber, V. Henninger, D. Böckler, H. Schumacher, H. U. Kauczor and H. Von Tengg-Kobligk, 'Heartbeat-related distension and displacement of the thoracic aorta in healthy volunteers', *European Journal of Radiology*, vol. 81, no. 1, pp. 158–164, 2012.

[34] S. de Putter, B. J. B. M. Wolters, M. C. M. Rutten, M. Breeuwer, F. A. Gerritsen and F. N. van de Vosse, 'Patient-specific initial wall stress in abdominal aortic aneurysms with a backward incremental method.' *Journal of biomechanics*, vol. 40, no. 5, pp. 1081–1090, 2007.

[35] L. Speelman, E. M. H. Bosboom, G. W. H. Schurink, J. Buth, M. Breeuwer, M. J. Jacobs and F. N. van de Vosse, 'Initial stress and nonlinear material behavior in patient-specific AAA wall stress analysis', *Journal of Biomechanics*, vol. 42, no. 11, pp. 1713–1719, 2009.

[36] R. L. Gleason, E. Wilson and J. D. Humphrey, 'Biaxial biomechanical adaptations of mouse carotid arteries cultured at altered axial extension', *Journal of Biomechanics*, vol. 40, pp. 766–776, 2007.

[37] G. Chen, Y. Yin, B. Wang, P. Li, Q. Liu, G. You, J. Zhao, S. Xia, L. Zhao and H. Zhou, 'Impaired erythrocyte deformability in transgenic HO-1G143H mutant mice', *Transgenic Research*, vol. 24, no. 1, pp. 173–178, 2014.

[38] N. Westerhof, G. Elzinga and P. Sipkema, 'An artificial arterial system for pumping hearts.' *Journal of applied physiology (Bethesda, Md. : 1985)*, vol. 31, no. 5, pp. 776–781, 1971.

[39] J. Degroote, K.-J. Bathe and J. Vierendeels, 'Performance of a new partitioned procedure versus a monolithic procedure in fluid–structure interaction', *Computers & Structures*, vol. 87, no. 11-12, pp. 793–801, 2009.

[40] G. Schuierer and W. J. Huk, 'Diagnostic significance of flow separation within the carotid bifurcation demonstrated by digital subtraction angiography.' *Stroke*, vol. 21, no. 12, pp. 1674–1679, 1990.

[41] M. Motomiya and T. Karino, 'Flow patterns in the human carotid artery bifurcation', *Stroke*, vol. 15, no. 1, pp. 50–56, 1984.

[42] D. Katritsis, L. Kaiktsis, A. Chaniotis, J. Pantos, E. P. Efstathopoulos and V. Marmarelis, 'Wall shear stress: theoretical considerations and methods of measurement.' *Progress in cardiovascular diseases*, vol. 49, no. 5, pp. 307–329, 2007.

[43] C. Badea, L. W. Hedlund and G. A. Johnson, 'Micro-CT with respiratory and cardiac gating.' *Medical physics*, vol. 31, no. 12, pp. 3324–3329, 2004.

Chapter 9

Comparison of numerical methodologies to assess WSS

9.1 Introduction

The hypothesis that low and oscillatory WSS has an atheroprone effect on the endothelial cells lining the inner arterial wall is generally accepted [1]–[5] . In mouse models of atherosclerosis, it has been shown that atherosclerotic lesions preferentially develop at branching points, bifurcations and at the bends of arteries [6]. However, to the best of our knowledge, no study directly addressed the quantitative association between development of atherosclerosis and patterns of WSS on a within-subject bases in this animal model.

To be able to calculate murine WSS, highly accurate measurements of the blood velocity near the arterial wall are needed, which is extremely challenging [7]. A commonly used alternative is applying numerical modelling to calculate the velocity field and to derive WSS from the spatial velocity gradient perpendicular to the arterial wall. An important component of numerical simulations is the application of appropriate BCs. In most publications measurements of the bulk blood velocity are used at the in- and outlets of the region of interest, which are then applied as mouse specific BCs to ensure the validity of the calculations.

The simplest type of numerical simulations to calculate WSS in arteries are steady state CFD calculations [8]–[10]. In these calculations either the peak or mean velocity (or flow) is applied at the boundaries. The time dependence is ignored and a steady state flow condition is calculated. The WSS

pattern is afterwards calculated based on this flow field. Steady state CFD has been performed to link the WSS in the casted CCA to the uptake of plasma macromolecules[8] or the wall thickness [9].

Transient CFD simulations also take into account the time dependency of the blood flow. Typically the velocities (or flows) are measured during the heart cycle and these curves are imposed. The calculated WSS is now a function of time and therefore the TAWSS is calculated in most cases. These simulations make it possible to study the oscillatory behaviour of the flow and the WSS, which is also assumed to play an important role in the atheroprone effect of low WSS on the endothelium. Transient CFD simulations of the mouse vasculature have already been performed in many cases. The aorta was the main region of interest in most of these publications with the main regions of interest: the aortic arch [10]–[17] , the abdominal aorta [18]–[20] or the whole aorta (arch+abdominal) [21]–[23]. The most of these publications were mainly oriented towards the methodology and the feasibility to calculate WSS in mice [10]–[14], [18], [21]–[23]. In these publications, the found WSS patterns were not linked (quantitatively or qualitatively) to biological responses or processes. In the abdominal aorta, studies were focused on aneurysm progression and WSS has been linked to aneurysm progression in mice [19], [20]. With regard to atherosclerosis development, Assemat *et al.* linked different HWPs with plaque development. To achieve this goal, they virtually removed the plaque from the model to link pre-disease HWPs with plaque presence. Other studies linked HWPs with plaque progression markers such as presence of fat in the wall [24] or the expression of VCAM-1 [17]. In these studies, a between animals comparison was made, meaning that the HWPs were calculated in another group of animals compared to the group of animals used to determine the progression marker(s).

Feintuch *et al.* compared the steady state CFD WSS and the transient CFD TAWSS in the mouse aortic arch. Both metrics show a close agreement but a small difference in absolute value was present [10].

A further step to get even closer to reality is the inclusion of the mechanical behaviour of the arterial wall in the model, resulting in FSI simulations. In these models, the effect of the distension and buffering of the arteries is taken into account. Our group has done this for the mouse carotid arteries (chapter 8) [25] as part of this PhD thesis and the mouse abdominal aorta [26]. This adds an extra layer of complexity to the modelling methodology, but also results in more realistic results.

Important to keep in mind when interpreting data from these studies is the fact that most of these models are based on measurements obtained while the mice were under anaesthesia. Anaesthesia has an influence on

the cardiovascular parameters, resulting in a lowered mean arterial pressure (MAP), a lower cardiac output and blood flow and a lower HR [27], [28]. When the activity level of the mice increases, these parameters will increase even further. Mohri *et al.* showed that the increased blood velocity due to increased activity levels can considerably influence the flow patterns [8]. When under anaesthesia, flow recirculation is normally not visible in the murine vasculature [8]. Taking the effect of anaesthesia into account, considerably recirculation was observed in the modelled, casted murine carotid artery [8].

In the current chapter the different modelling methodologies are compared for a single carotid bifurcation (bifurcation 3L). Steady state CFD simulations are performed for both peak and mean velocity, as well as transient CFD simulations. The third investigated option is the FSI model setup discussed in the previous chapter (chapter 8 on page 149).

As performed by Mohri *et al.* [8], the influence of the anaesthesia is also investigated. The flow and HR (CFD and FSI) are rescaled to both the conscious-rest condition and the active condition (=high locomotor activity). For the FSI simulations the BP is also scaled to model the same conditions.

9.2 Methods

9.2.1 Experimental protocol

The study is based on data acquired in a female ApoE$^{-/-}$ mouse (mouse 3L), fed a Western type diet (TD88137, Harlan Teklad, Madison, Wis, USA) ad libitum from the age of 6 weeks until 16 weeks. The housing of the animal and all the experiments were conducted according to the EC guidelines and were approved by the animal ethics committee of Ghent University [25], [29].

At week 16 the mouse underwent an imaging protocol. Using a high-frequency US scanner (Vevo 2100, Visualsonics, Toronto, Canada) with a linear array probe (MS550D, 22-55MHz), the blood flow velocity was assessed in the CCA, ECA and ICA of the left carotid bifurcation with PW Doppler US. The distension of the artery was measured using M-mode US measurements.

A contrast-enhanced (100 μl/25g body weight Aurovist, Nanoprobes, Yaphank, NY, USA) μCT scan using a Triumph-II imaging system (TriFoil Imaging, Chatsworth, CA, USA) provided the geometrical information of the carotid bifurcation at a 50 μm resolution.

9.2.2 Post-processing of the measurements

The outer envelope of the Doppler signal and the diameter distension of the US measurements were tracked to obtain respectively the blood velocity and the diameter curve. For the three locations (CCA, ECA and ICA) both

signals were aligned in time. The measured velocity was rescaled to a mass flow and a flow correction factor of 1.1275 was applied to the ECA and ICA flow to make the total cycle mass-balance fit. More information about the post processing of the US measurements can be found in section 8.2.3.1 on page 151.

Mimics (Materialise, Leuven, Belgium) was used to semi-automatically segment the three branches of the carotid bifurcation, CCA, ECA and ICA from the μCT datasets. Flow extensions with a length equal to the diameter of the arteries were added in the VMTK (`www.vmtk.org`).Finally, the segmented geometry was shrunk to the diastolic radius measured with M-mode US, resulting in a shrinking factor of 0.84.

From the resulting STL-surface, a volume mesh of both the fluid (lumen) and the solid (arterial wall) domain was constructed using the XTM [30]. A mesh convergence study resulted in convergence for 300k fluid domain cells and 65k solid domain cells (section 8.2.4 on page 152) [25]. The wall thickness of the artery was assumed to be 10% of the local luminal diameter

9.2.3 Different numerical modelling techniques

9.2.3.1 Steady state CFD simulations

For the steady state CFD simulations 2 sets of BCs were applied: (i) the average velocity/flow of the three branches and (ii) the peak velocity of the three branches. For both cases, the mass flow of the three branches was calculated from the measurements, assuming a parabolic flow profile. At the CCA the calculated mass flow was applied. At the ECA and ICA the mass flow split was calculated and they were applied using outflow BCs with the constant outflow fraction. For the steady state simulations convergence was reached when the continuity and momentum residuals dropped below $1e^{-10}$.

9.2.3.2 Transient CFD simulations

For the transient CFD simulations a mass flow inlet was applied at both the CCA and the ECA (at the ECA the mass flow inlet behaved as an outflow). The ICA was modelled as a traction free outlet. For the transient CFD simulations a convergence criterion of $1e^{-10}$ was applied for both the continuity and the momentum equations.

9.2.3.3 Transient FSI simulations

The methodology for the FSI simulations is described more in depth in chapter 8 on page 149 [25]. In short, the same mass flow inlets as in the transient CFD simulations were applied. At the ICA a windkessel was implemented, with the parameters fitted to the measurements. The external tissue was modelled using linear springs [31]. The BI method was executed

sequentially to take axial and diastolic pre-stresses into account. The absolute coupling iterations convergence criteria for the residuals were set to 10^{-8}m for the displacement and 0.5Pa for the load at the interface.

9.2.3.4 Comparing results

For the WSS and the TAWSS, the absolute values were compared between the different simulations. To also be able to compare the patterns, the normalised values were also studied. The values were normalised by dividing the absolute values by the average value (over the whole bifurcation-surface). Because the OSI is a dimensionless number, the absolute values where compared and no normalisation was carried out.

9.2.4 Influence of anaesthesia and activity

An overview of the different parameters for the different calculated cases is given in table 9.1. This table is based on an experimental paper by Janssen *et al.* [27]. The *Anaesthesia* case is the physical condition of the mouse that was calculated in the previous chapter (chapter 8 on page 149). In this case, the measurements (performed while the mouse was under anaesthesia) were imposed as BCs directly as described in the previous paragraphs. This means that we are not calculating the "actual" physical condition of the mouse, but rather the physical state of the mouse while being under anaesthesia (hence the name *Anaesthesia*).

By estimating the effect of the anaesthetic, the physical state of the mouse under "normal" resting conditions (=awake but resting) can be determined. This is a better indication of the "real life", long term WSS that the ECs are subject to. In the study of Janssen *et al.*, the experiments were done at doses between 1% and 2 % isoflurane at two different universities. In the current study a dose of 1.5% was used and thus the values of Janssen *et al.* can be seen as the lower and the higher bound estimates of the influence of anaesthesia. Therefore, in the current chapter the most extreme values (lowest and highest influence of isoflurane found by Janssen *et al.*) will be investigated to estimate the influence of isoflurane. *Rest1* is the lower bound estimation of a mouse under conscious resting conditions (*Rest1*) [27]. For the same conscious resting conditions, *Rest2* is the higher bound estimation of the physical condition of the mouse (*Rest2*), adaptation from the *Anaesthesia* case with the 2% isoflurane rescaling factors. According to Janssen *et al.*, the changes under anaesthesia are: HR -11/38%, flow -5.4/42% and blood pressure -24% as lower and higher estimate of the influence of isoflurane anaesthesia (between 1 and 2% isoflurane). This results in scale factors for the flow of 1.06 and 1.72 for cases *Rest1* and *Rest2* respectively. The HR of our mouse specific measurements were also rescaled according to the percentage found by Janssen *et al.* These rescale factors for Q were applied to all simulations

(steady state CFD, transient CFD and FSI). The change in HR could only be taken into account for the transient (CFD and FSI) simulations.

Table 9.1: Adaptation of the BC to account for anaesthesia and activity.

Mouse 3L	scale factor Q	P_{sys}	P_{dia}	Ts	HR [bpm]
Anaesthesia	1.00	119	87	0.1719	349
Rest1	1.06	119	87	0.1530	392
Rest2	1.72	119	87	0.1066	563
Active1	2.04	156	114	0.1236	485
Active2	3.33	156	114	0.0861	697

The BP was not changed for the conscious resting state (*Rest1* and *Rest2*), because the measured values of van Herck *et al.* (used in our simulations: MAP=102± 2mmHg) [32] are already in the same order of magnitude as the conscious state measurements of Janssen *et al.* (MAP=105± 3mmHg) [27].

During a period of high locomotor activity (=active state), these parameters increase even further with the conscious resting case as a reference. Janssen *et al.* found this increase to be: HR +23.77%, blood flow +93% and BP +31.3%. This extra increase rescales case *Rest1* to case *Active1*. This means that *Active1* is a lower bound estimate of the active condition, with regard to the rescale factors to neutralise the influence of the anaesthesia on our initial measurements (done in case *Anaesthesia*). Similarly, *Active2* is the adaptation of case *Rest2* with regard to the influence of activity. With respect to the factor to neutralise the influence of anaesthesia *Active2* is an upper bound estimate. In the *Active* cases the HR, blood flow and the BP are increased. Once again, the change in HR could only be applied to the transient simulations (transient CFD and FSI) and the BP only for the FSI simulations.

For the CFD simulations, the BCs were simply scaled according to the factors of table 9.1. For the FSI simulations the first step was to recalculate the 3-element windkessel model based on the new, rescaled ICA flow and BP. It is important to note that the rescaled pressure is not applied explicitly, but implicitly through this windkessel. For both the CCA and ECA the rescaled mass flows are applied at the boundaries. This means that for the 4 extra cases (*Rest1/2* and *Active1/2*), we step into the previous explained FSI workflow in chapter 8 on page 149 at the determine flow BCs block in the diagram on figure 8.6 on page 158. The prestress calculation is not repeated, because the previously found stress-state at a pressure of 87 mmHg (= P_{dia}) is still valid. The new, higher windkessel pressure will result in an extra distension of the artery.

9.3 Results

9.3.1 Different simulation types

In figure 9.1, the flow across the different boundaries is plotted for the different simulation types. For both steady state simulations (figures 9.1a and 9.1b) all three boundary flows are applied directly (ECA and ICA through an outflow split). It is clearly visible that the ECA/ICA flow-split for the mean flow steady state CFD simulation (0.13/0.87) differs from the flow-split of the peak flow steady state CFD simulation (0.24/0.76). The transient CFD ICA flow (figure 9.1c) is much more peaked compared to the transient FSI ICA flow (figure 9.1d). When comparing the resulting ICA flow with the measured waveform, it is obvious that the FSI simulations approximate the measurements better compared to the CFD simulations.

Figure 9.2 shows the WSS distribution for the steady state CFD simulations (figures 9.2a and 9.2b) and the TAWSS for the transient simulations (figures 9.2a and 9.2b). The most striking, is the higher WSS of the peak velocity steady state CFD simulations. The other 3 simulation techniques (mean steady state CFD, transient CFD and transient FSI) show a similar WSS distribution

Figure 9.3 shows the normalised WSS for the steady state simulations (figures 9.3a and 9.3b) and the normalised TAWSS for the transient simulations (figures 9.3c and 9.3d) for the mouse under anaesthesia. The WSS and TAWSS values were divided by their mean values of respectively 3.25, 7.54, 3.42 and 2.85Pa to normalise them. The different normalised WSS patterns show very similar distributions.

The steady state CFD simulations do not take into account the time dependency of the flow and flow oscillations are not included in the modelling strategy. For the transient CFD and FSI simulations the oscillations were assessed and compared by means of the OSI (equation (8.1b) on page 159). For the CFD simulations the OSI was negligible with an average value of $1.3^{*}10^{-3}$ (figure 9.4a) and a maximum value of 0.166 (at the flow stagnation point). For the FSI simulations on the other hand, there was a clear increase in OSI at the outer side of the ECA sinus (figure 9.4b), increasing the average value to $2.46^{*}10^{-2}$ with a maximum value of 0.272.

9.3.2 Influence of anaesthesia and activity

9.3.2.1 TAWSS

Figure 9.5 shows the TAWSS plotted on the diastolic geometry for the FSI simulations of the 5 different physical conditions of the example mouse. With the rising activity level, the flow (see rescale factors in table 9.1) and thus

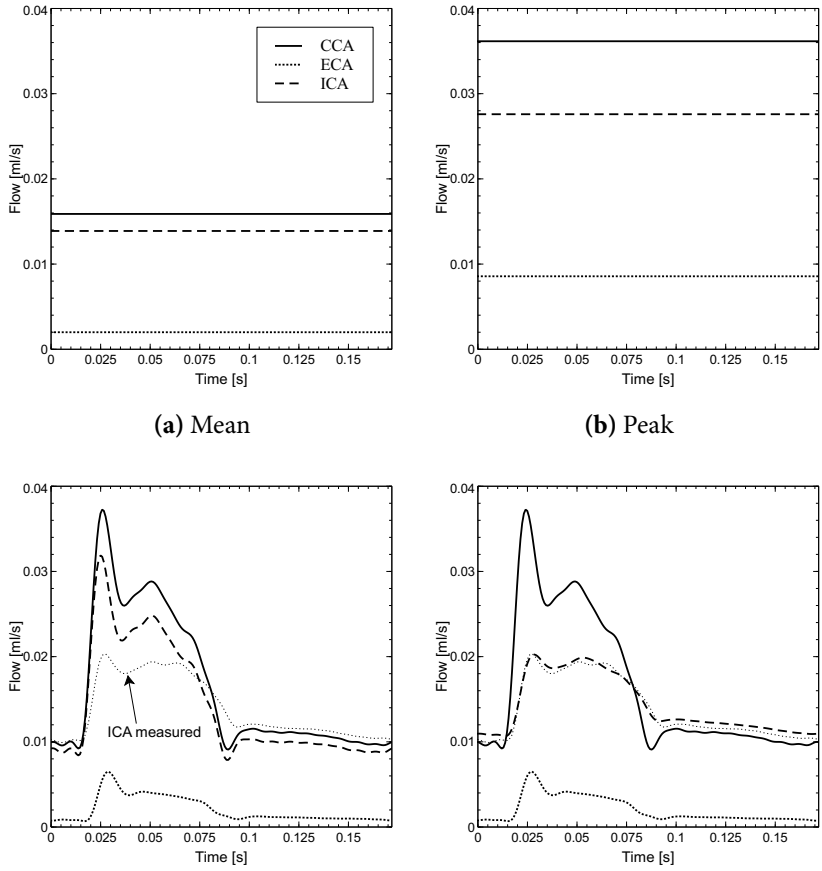

(a) Mean **(b)** Peak

(c) Transient **(d)** FSI

Figure 9.1: Overview of the flow across the boundaries for the different simulation types. (a) constant flow based on the mean velocity measured. (b) constant flow based on the peak velocity measured. (c) measured flow at the CCA and ECA and free outlet at the ICA. (d) measured flow at the CCA and ECA and windkessel at the ICA. For subfigures (c) and (d) the measured ICA flow is plotted as a reference

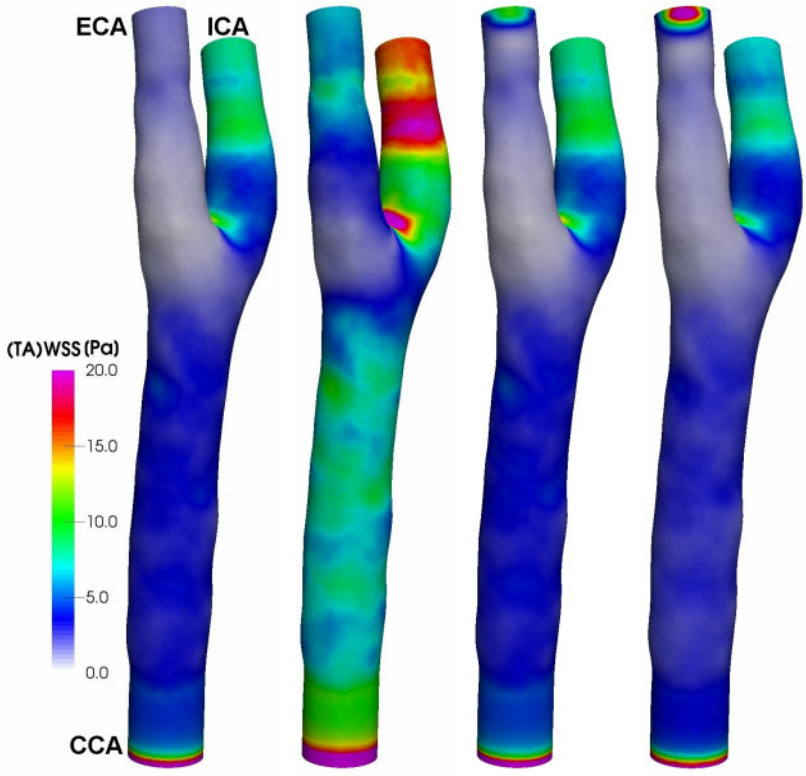

(a) Mean **(b)** Peak **(c)** Trans **(d)** FSI

Figure 9.2: The WSS (steady state simulations) or TAWSS (transient CFD and FSI) pattern for the different types of simulation: (a): steady state CFD with mean mass flow (b): steady state CFD with peak mass flow (c): transient CFD (d):transient FSI.

the TAWSS increases. Therefore, an increase in WSS is visible from left to right in figure 9.5 (with only *Rest2* having a slightly higher value compared to *Active1*).

In figure 9.6, the normalised TAWSS is plotted on the diastolic geometry for the FSI simulations of the 5 different physical conditions of the mouse . The TAWSS was normalised by dividing it by the average value of the subsequent case. For *Anaesthesia*, *Rest1*, *Rest2*, *Active1* and *Active2* the average TAWSS was respectively: 2.85, 3.08, 5.12, 4.77 and 8.11 Pa. Because the pressure was increased to simulate the high locomotor activity states (*Active1* and *Active2*), the diameter has increased for those cases (see figure 9.11). The normalised TAWSS distribution is, however, very similar for the different cases. The most apparent difference is the relatively higher TAWSS at the inner bend of the bifurcation.

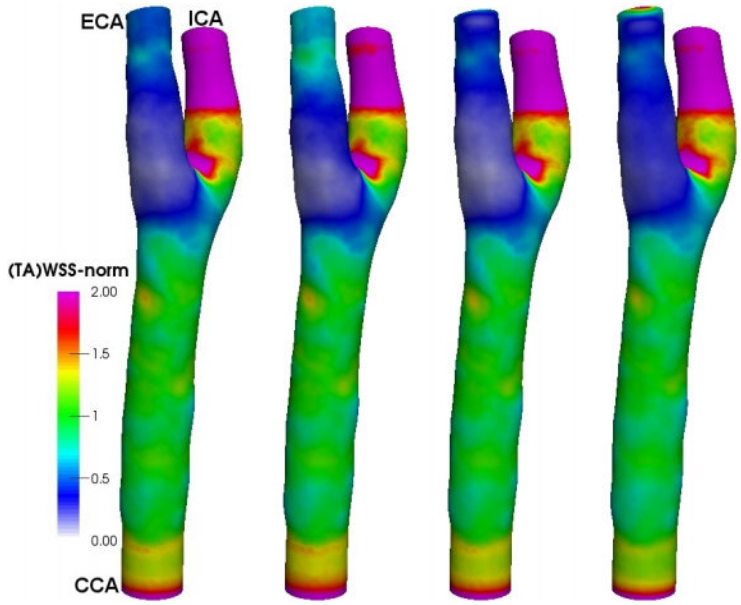

(a) Mean **(b)** Peak **(c)** Trans **(d)** FSI

Figure 9.3: The normalised WSS (steady state simulations) or TAWSS (transient CFD and FSI) pattern for the different types of simulation. The values were normalised by dividing them by the respective average values of 3.25, 7.54, 3.42 and 2.85Pa. (a): steady state CFD with mean mass flow (b): steady state CFD with peak mass flow (c): transient CFD (d):transient FSI.

9.3.2.2 OSI

The dimensionless FSI OSI was not normalised like the TAWSS. For the cases describing a different condition for mouse 3L the OSI is plotted in figure 9.7. In both the CCA and ICA branch, no differences are discernible between the different conditions. For the ECA, globally the same region has an elevated value in all 5 cases. A similar pattern is visible for the *Anaesthesia* case and the rest cases (*Rest1* and *Rest2*), but the maximum is not the same for all those cases. In case *Active2*, the maximal value is clearly increased and the zone with an elevated OSI spreads out further.

9.3.2.3 FSI Recirculations

In the *Anaesthesia* condition, no flow recirculations were visible in this bifurcation (or any of the other bifurcations of chapter 8). When adapting the BCs for the different physical states of the mouse, flow recirculations became most apparent in the early deceleration phase in the cases with high locomotor activity (*Active1* and *Active2*). To visualise the presence of recirculation structures, the line integral convolution (LIC) of the normalised FSI WSS was

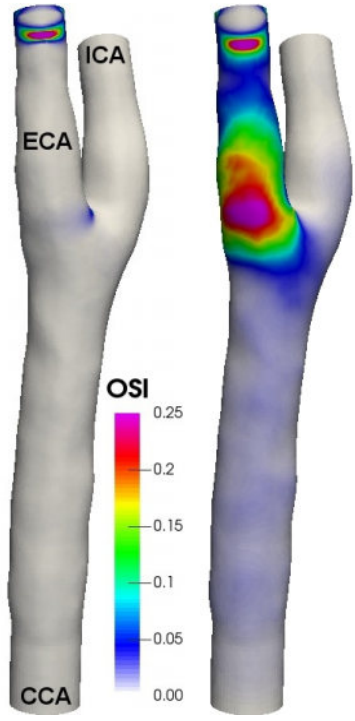

(a) CFD **(b)** FSI

Figure 9.4: The OSI pattern for transient CFD and FSI simulations: (a): virtually no oscillations present in the flow pattern for a CFD simulation (b): more oscillations present in the ECA for a FSI simulation.

plotted in the early deceleration phase for the 5 physical condition cases for mouse 3L in figure 9.8. The LIC is the mathematical equivalent on a surface of putting drops of ink in flow/vector field. Figure 9.8e shows that a substantial zone with reversed WSS is present for case *Active2* in the outer bend (frontal side) of the ECA. This zone overlaps with the zone where the OSI is elevated in figure 9.7e. for both cases *Rest2* and *Active1* (figures 9.8c and 9.8d), smaller zones with reversed WSS are present. Although the reversed WSS is clearly present, the magnitude of the vectors in this reversed zone is low.

For FSI *Active2*, the most extreme case with high locomotor activity and the highest anaesthesia influence estimate, the velocity is plotted in figure 9.9. The velocity plots (figures 9.9b to 9.9e), show the LIC for the velocity vector field in the mid plane of the ECA. This velocity field is plotted for 4 time points that are indicated on the CCA boundary flow curve in figure 9.9a.These results show a clear flow recirculation zone in the deceleration phase (figures 9.9c and 9.9d). The velocity in these flow recirculation zones is very low.

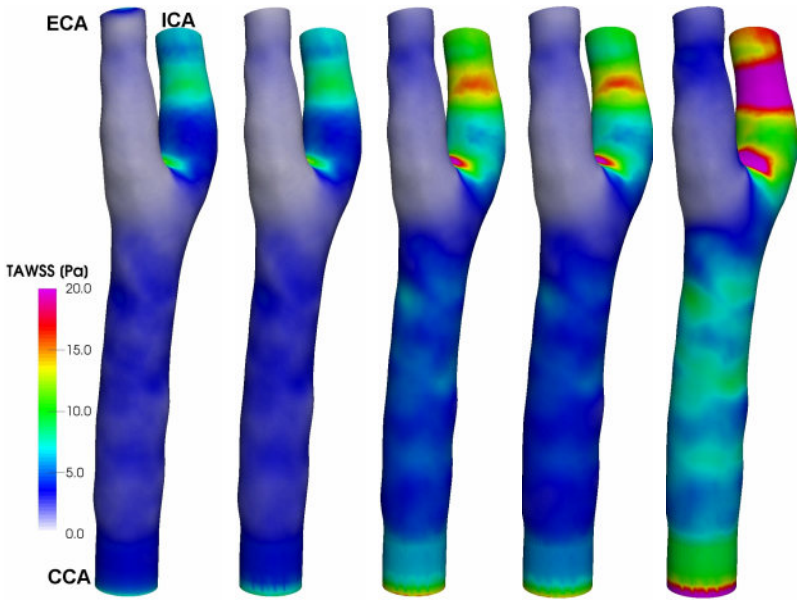

(a) *Anaesthesia* **(b)** *Rest1* **(c)** *Rest2* **(d)** *Active1* **(e)** *Active2*

Figure 9.5: The TAWSS for mouse 3L under different circumstances: anaesthesia (a: *Anaesthesia*), conscious-rest lower bound (b: *Rest1*), conscious-rest higher bound (c: *Rest2*), high locomotor activity lower bound (d: *Active1*) and high locomotor activity higher bound (e: *Active2*). These circumstances were simulated by changing the boundary conditions according to [27].

9.3.3 Zones with WSS reversal

For the different simulation types the zones with reversed WSS were identified. For the transient simulations this was done in the early deceleration phase (point c in figure 9.9a). Reversed WSS was defined according to the scalar product with the normal of the CCA boundary. If the scalar product with the WSS was negative (component in the direction of the CCA according to the normal), the zone was indicated to have a reversed WSS. The area [mm^2] with reversed wall shear stress is plotted in figure 9.10 for the different simulation types and the different BCs. At the stagnation point, the WSS vector is perpendicular to the CCA-inlet normal and therefore the current definition of reversed WSS is not applicable in this zone. This zone (coloured in blue in the close up on figure 9.9a) accounts for the small false positive values in all cases. Physical flow and WSS reversal at the outer bend of the ECA sinus are only present for cases *Rest2*, *Active1* and *Active2*. For the FSI simulations the largest area is exposed to WSS reversal. Reversed WSS is present for the same cases for transient CFD simulations, but the exposed area is a bit smaller. For the peak velocity steady state CFD simulations a considerably smaller area is exposed to reversed WSS.

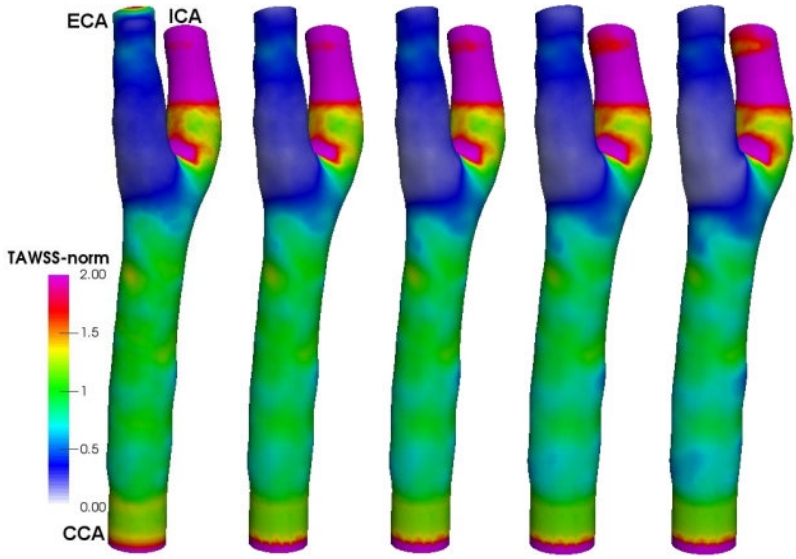

(a) *Anaesthesia* **(b)** *Rest1* **(c)** *Rest2* **(d)** *Active1* **(e)** *Active2*

Figure 9.6: The normalised TAWSS (divided by the mean value of respectively 2.85, 3.08, 5.12, 4.77 and 8.11 Pa) for mouse 3L under different circumstances: anaesthesia (a: *Anaesthesia*), conscious-rest lower bound (b: *Rest1*), conscious-rest higher bound (c: *Rest2*), high locomotor activity lower bound (d: *Active1*) and high locomotor activity higher bound (e: *Active2*). These circumstances were simulated by changing the boundary conditions according to [27].

9.4 Discussion

9.4.1 Steady CFD vs. Transient CFD vs. Transient FSI

In this chapter, different possible modelling strategies to simulate the murine carotid haemodynamics were compared. The focus of the comparison is on the WSS and HWPs reflecting oscillatory motion of flow. A second part of this chapter dealt with the influence of the activity state of the mouse on these simulations. The influence of anaesthesia and locomotor activity were modelled.

From figure 9.3d it is clear that the (normalised) WSS pattern is the same for all the modelling strategies, despite the clearly different BCs that were applied. Even the inclusion of the pulsatile nature of the blood flow (in transient CFD and FSI) and/or the inclusion of the buffering capacity of the carotid artery (CA) (FSI) had little effect.

Although the normalised WSS patterns are similar, the absolute values for the different simulations differ because the total flow through the specific geometry differ between the different simulations. Moreover, the FSI

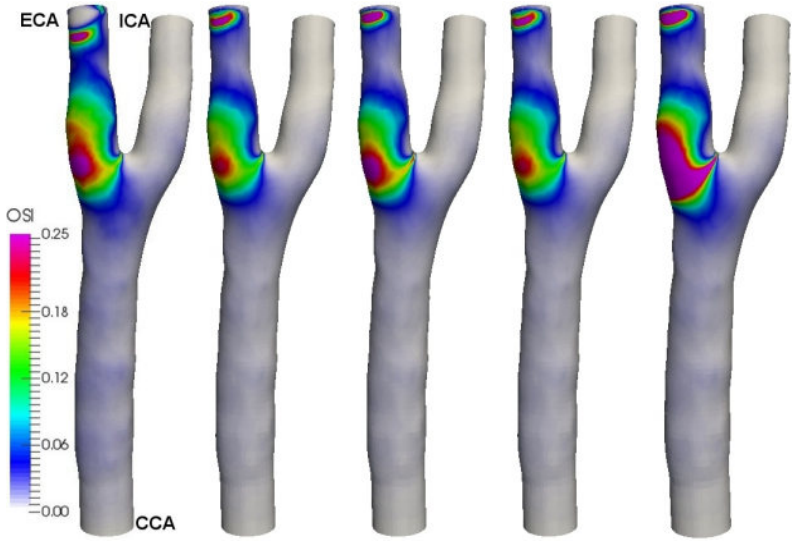

(a) *Anaesthesia* **(b)** *Rest1* **(c)** *Rest2* **(d)** *Active1* **(e)** *Active2*

Figure 9.7: The OSI for mouse 3L under different circumstances: anaesthesia (a: *Anaesthesia*), conscious-rest lower bound (b: *Rest1*), conscious-rest higher bound (c: *Rest2*), high locomotor activity lower bound (d: *Active1*) and high locomotor activity higher bound (e: *Active2*). These circumstances were simulated by changing the boundary conditions according to [27].

geometry gets inflated during the simulations (figure 9.11: CFD-FSIcase0), resulting in the globally lower WSS for the FSI simulation compared to the transient CFD simulation.

The larger impact is found for parameters reflecting the oscillatory behaviour of the WSS. Obviously, the steady state simulations cannot assess the oscillatory behaviour of the WSS. In figure 9.4 on page 185, the OSI is compared for transient CFD and FSI simulations. The clearly higher oscillatory character of the ECA flow for the FSI simulations is due to the buffering of the CA. This results in a net instantaneous flow imbalance and thus a net in/outflow difference in the model. Therefore, the FSI boundary condition is a less restrictive condition for small oscillations to occur compared to the CFD simulations. For the CFD simulations there is always an instantaneous balance of mass.

9.4.2 Influence of anaesthesia and activity

Mohri *et al.* showed that lower flow measurements due to anaesthesia can have a big influence on the simulation results[8]. Similar to their results, we also observed the presence of flow recirculation (in the ECA) when the influence of anaesthesia and locomotor activity are taken into account. These

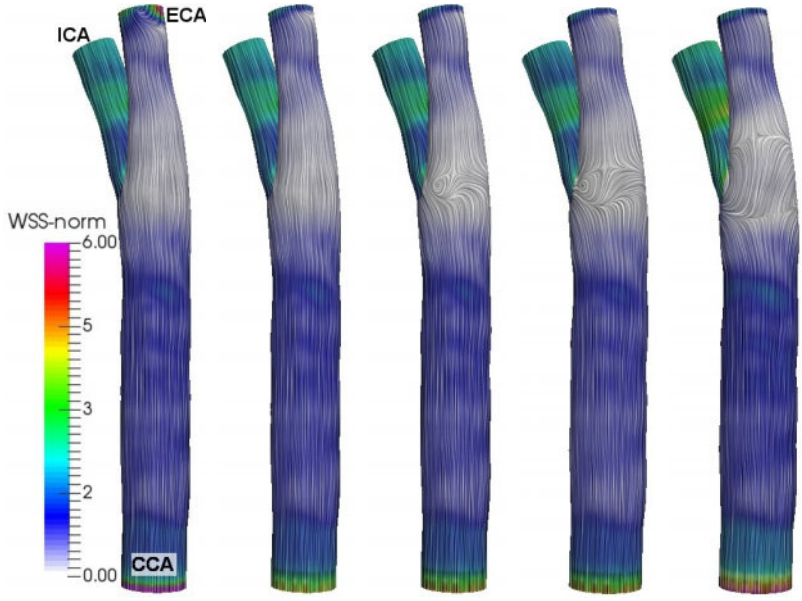

(a) *Anaesthesia* **(b)** *Rest1* **(c)** *Rest2* **(d)** *Active1* **(e)** *Active2*

Figure 9.8: The WSS in the conscious and active state at the early deceleration phase for mouse 3L. The LIC is used to visualise recirculation zones in the WSS at the anterior side of the ECA. The different calculated circumstances are: anaesthesia (a: *Anaesthesia*), conscious-rest lower bound (b: *Rest1*), conscious-rest higher bound (c: *Rest2*), high locomotor activity lower bound (d: *Active1*) and high locomotor activity higher bound (e: *Active2*). These circumstances were simulated by changing the boundary conditions according to [27].

flow recirculations were present at the outer sinus of the ECA for both the steady state and transient simulations. For the transient simulations they were mainly present during the deceleration phase. As a result of the changed BC (see table 9.1 on page 180) the peak systolic Reynolds number for the CCA changes from 13.38 to 39.57 for the anaesthesia to the high locomotor activity case. For the same cases the Womersley number increases from 0.44 to 0.70, indicating the possibility of changes in flow behaviour. Due to this changed flow behaviour, the results of the simulations assuming anaesthesia conditions should be interpreted with caution.

Nonetheless, the normalised TAWSS patterns for all these different and heavily adapted conditions did not show clear differences. Therefore we can conclude that the normalised TAWSS patterns are rather robust with regard to different activity levels of a mouse. Therefore, it makes sense to identify zones with high/low TAWSS compared to the remainder of the bifurcation/vasculature, because the location of these zones is robust with regard to changing physical activity levels. Reporting and comparing absolute

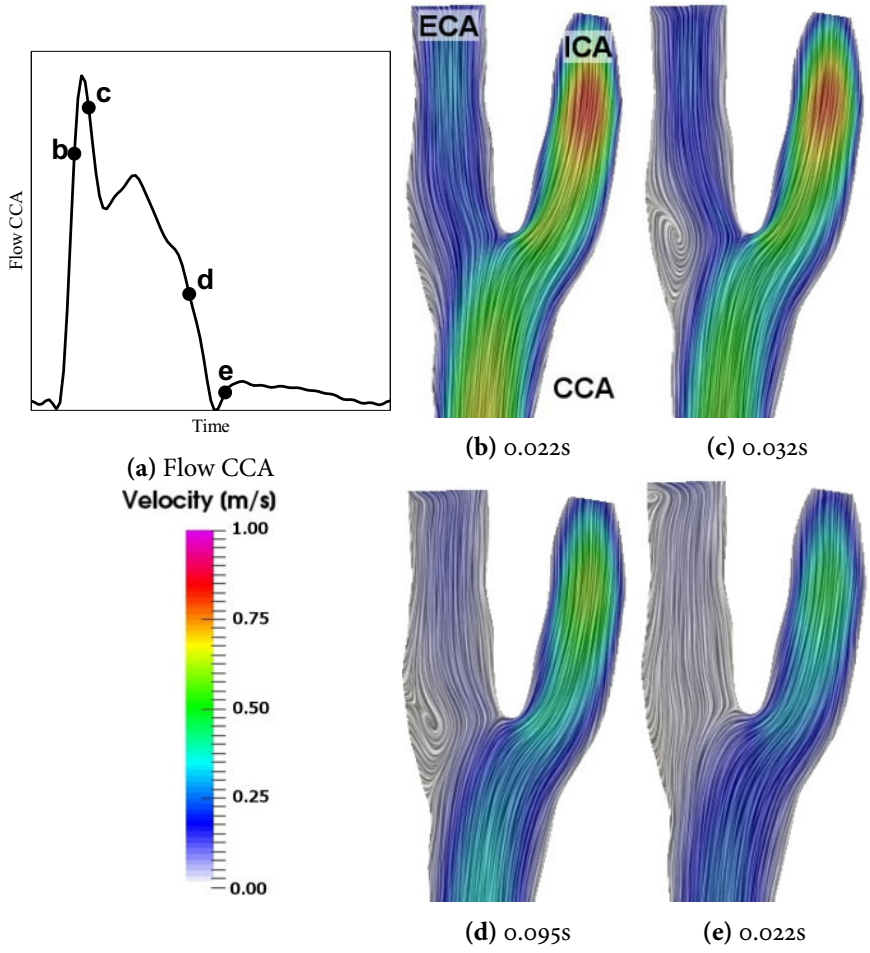

(a) Flow CCA

(b) 0.022s **(c)** 0.032s

(d) 0.095s **(e)** 0.022s

Figure 9.9: Flow recirculation in the ECA when in high locomotor activity (*Active2*) for mouse 3L. The LIC is used to visualise recirculation zones in the mid plane of the ECA. a) The different time points at which the velocity field is shown in subfigures b, c,d and e

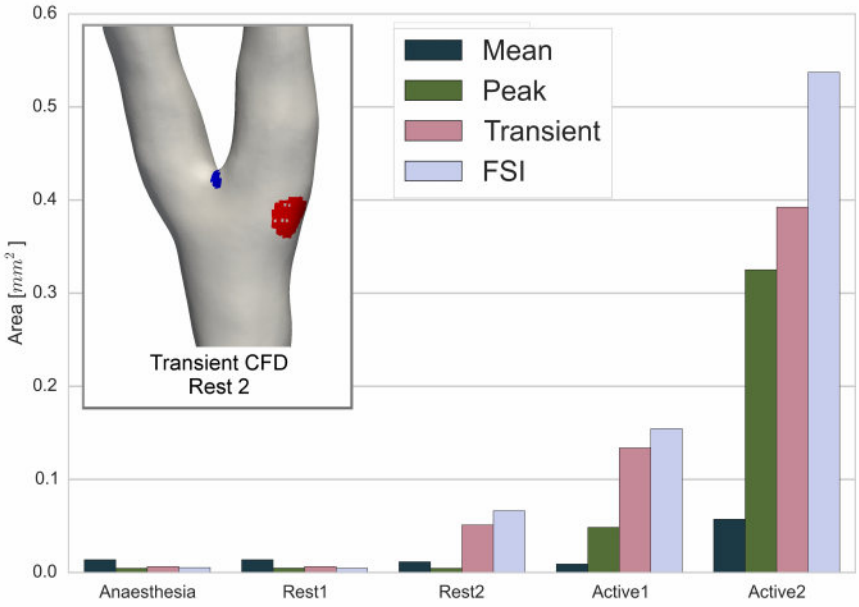

Figure 9.10: Reversed WSS area[mm²] for the different simulation types with different sets of BC mimicking anaesthetic, conscious and active conditions. Close up of the transient CFD case 4 condition with the 2 different zones with reversed WSS present: stagnation point (blue) and the outer sinus of the ECA (red)

values of the WSS/TAWSS on the other hand is much more subject to the precise boundary conditions and level of physical activity that were applied

On the other hand, OSI shows a different distribution in the different simulations (figure 9.7 on page 188). The location of the region with elevated OSI is the same for those simulations, but the shape and size of this location differs. Caution should be taken when comparing the actual values. The largest differences were seen in when simulating extensive locomotor activity (cases *Active1* and *Active2*).

It should be noted, however that the increase in blood flow through the CCA at locomotor activity is probably overestimated in these simulations and thus results in an worst case scenario. The flow rescaling fractions were based on an increase of cardiac output measured by Janssen *et al.* [27] (similar to what Mohri *et al.* did [8]). At high locomotor activity, the cardiac output increases but this is mainly because of an increase in blood flow towards the skeletal muscles [33]. The main perfusion area of the CA is the brain. In humans, the rise in cerebral blood flow only peaks at the onset of physical activity and decreases during constant physical activity, while the cardiac output is still at an elevated level [34]. Hiura *et al.* quantified the initial increase due to physical exercise (steady-state cycling) for healthy humans to

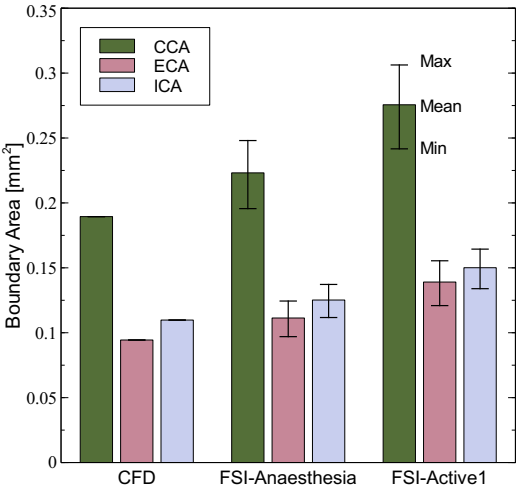

Figure 9.11: Cross-sectional area at the boundaries for the different simulation types. The CFD simulations have a constant cross-sectional area. The FSI simulations inflate the artery, resulting in the same minimal area but higher mean and maximum areas at higher distensions. For cases *Anaesthesia*, *Rest1* and *Rest2* the windkessel pressure does not change, resulting in the same (not plotted) areas (within a 1% margin). For cases *Active1* and *Active2* the pressure is increased, resulting in an even further inflation of the artery.

be 27.9±28.6% and the increase during prolonged exercise to be 2.6±13.5%. Both of these changes are smaller than the increase in cardiac output with respectively 92% and 118% [35]. Therefore, it is likely that in mice the change in blood flow through the CA is smaller than the change in cardiac output during exercise. If the blood flow to the brain is assumed to be constant during this (prolonged) locomotor activity, cases *Active1* and *Active2* should be ignored and *Rest2* is the most extreme case. *Rest2* is right at the border of the initiation of recirculation in this geometry. Therefore, under the constant blood flow assumption it is difficult to say if recirculation will be present or not (*Rest2* is an upper bound for the influence of anaesthesia).

9.4.3 Conclusion

Simple steady state CFD simulations can be used to assess the WSS pattern in the murine carotid bifurcation. However, the average WSS value differs between different simulation strategies. To be able to assess the oscillatory behaviour (OSI) of the WSS, the buffering effect of the elastic CA should be taken into account and FSI simulations are indispensable. The effect of anaesthesia and locomotor activity on the WSS patterns is minimal, but absolute levels are likely different. Our simulations show that it is possible

that flow recirculation and WSS reversal could occur when the mice are in a high locomotor activity state.

Bibliography Chapter 9

[1] V. Peiffer, S. J. Sherwin and P. D. Weinberg, 'Does low and oscillatory wall shear stress correlate spatially with early atherosclerosis? A systematic review', *Cardiovascular Research*, vol. 99, no. 2, pp. 242–250, 2013.

[2] D. N. Ku, D. P. Giddens, C. K. Zarins and S. Glagov, 'Pulsatile flow and atherosclerosis in the human carotid bifurcation. Positive correlation between plaque location and low oscillating shear stress.' *Arteriosclerosis*, vol. 5, no. 3, pp. 293–302, 1985.

[3] Y. S. Chatzizisis, A. U. Coskun, M. Jonas, E. R. Edelman, C. L. Feldman and P. H. Stone, 'Role of endothelial shear stress in the natural history of coronary atherosclerosis and vascular remodeling: molecular, cellular, and vascular behavior.' *Journal of the American College of Cardiology*, vol. 49, no. 25, pp. 2379–93, 2007.

[4] T. Asakura and T. Karino, 'Flow patterns and spatial distribution of atherosclerotic lesions in human coronary arteries', *Circulation Research*, vol. 66, no. 4, pp. 1045–1066, 1990.

[5] A. Gnasso, C. Irace, C. Carallo, M. S. De Franceschi, C. Motti, P. L. Mattioli and A. Pujia, 'In Vivo Association Between Low Wall Shear Stress and Plaque in Subjects With Asymmetrical Carotid Atherosclerosis', *Stroke*, vol. 28, no. 5, pp. 993–998, 1997.

[6] Y. Nakashima, A. S. Plump, E. W. Raines, J. L. Breslow and R. Ross, 'ApoE-deficient mice develop lesions of all phases of atherosclerosis throughout the arterial tree', *Arteriosclerosis, Thrombosis, and Vascular Biology*, vol. 14, no. 1, pp. 133–140, 1994.

[7] G. S. van Bochove, R. Straathof, R. Krams, K. Nicolay and G. J. Strijkers, 'MRI-determined carotid artery flow velocities and wall shear stress in a mouse model of vulnerable and stable atherosclerotic plaque.' *Magnetic Resonance Materials in Physics, Biology and Medicine*, vol. 23, no. 2, pp. 77–84, 2010.

[8] Z. Mohri, E. M. Rowland, L. A. Clarke, A. De Luca, V. Peiffer, R. Krams, S. J. Sherwin and P. D. Weinberg, 'Elevated Uptake of Plasma Macromolecules by Regions of Arterial Wall Predisposed to Plaque Instability in a Mouse Model', *PLoS ONE*, vol. 9, no. 12, e115728, 2014.

[9] C. Cheng, R. de Crom, R. van Haperen, F. Helderman, B. Mousavi Gourabi, L. C. a. van Damme, S. W. Kirschbaum, C. J. Slager, A. F. W. van der Steen and R. Krams, 'The role of shear stress in atherosclerosis: action through gene expression and inflammation?', *Cell biochemistry and biophysics*, vol. 41, no. 2, pp. 279–294, 2004.

[10] A. Feintuch, P. Ruengsakulrach, A. Lin, J. Zhang, Y.-Q. Zhou, J. Bishop, L. Davidson, D. Courtman, F. S. Foster, D. A. Steinman, R. M. Henkelman and C. R. Ethier, 'Hemodynamics in the mouse aortic arch as assessed by MRI, ultrasound, and numerical modeling.' *American journal of physiology. Heart and circulatory physiology*, vol. 292, no. 2, H884–H892, 2007.

[11] P. Ruengsakulrach, A. K. Joshi, S. Fremes, S. Foster, J. BUTANY, B. Wiwatanapataphee and Y. Lenbury, 'Wall shear stress and atherosclerosis: numerical blood flow simulations in the mouse aortic arch', *Wseas Transactions on Fluid Mechanics*, vol. 3, no. 2, pp. 90–100, 2008.

[12] H. Zhu, J. Zhang, J. Shih, F. Lopez-Bertoni, J. R. Hagaman, N. Maeda and M. H. Friedman, 'Differences in aortic arch geometry, hemodynamics, and plaque patterns between C57BL/6 and 129/SvEv mice.' *Journal of biomechanical engineering*, vol. 131, no. 12, p. 121 005, 2009.

[13] B. Trachet, A. Swillens, D. Van Loo, C. Casteleyn, A. De Paepe, B. Loeys and P. Segers, 'The influence of aortic dimensions on calculated wall shear stress in the mouse aortic arch.' *Computer methods in biomechanics and biomedical engineering*, vol. 12, no. 5, pp. 491–499, 2009.

[14] B. Trachet, A. Swillens, D. Loo, C. Casteleyn, A. De Paepe, B. Loeys and P. Segers, 'Wall shear stress in the mouse aortic arch: does size matter?', in *4th European Conference of the International Federation for Medical and Biological Engineering*, Springer, 2009, pp. 1994–1998.

[15] P. Assemat, J. A. Armitage, K. K. Siu, K. G. Contreras, A. M. Dart, J. P. Chin-Dusting and K. Hourigan, 'Three-dimensional numerical simulation of blood flow in mouse aortic arch around atherosclerotic plaques', *Applied Mathematical Modelling*, vol. 38, no. 17-18, pp. 4175–4185, 2014.

[16] P. Assemat, K. K. Siu, J. Armitage, S. N. Hokke, A. Dart, J. Chin-Dusting and K. Hourigan, 'Haemodynamical stress in mouse aortic arch with atherosclerotic plaques: Preliminary study of plaque progression', *Computational and Structural Biotechnology Journal*, vol. 10, no. 17, pp. 98–106, 2014.

[17] J. Suo, D. E. Ferrara, D. Sorescu, R. E. Guldberg, W. R. Taylor and D. P. Giddens, 'Hemodynamic shear stresses in mouse aortas: implications for atherogenesis.' *Arteriosclerosis, thrombosis, and vascular biology*, vol. 27, no. 2, pp. 346–51, 2007.

[18] J. M. Greve, A. S. Les, B. T. Tang, M. T. Draney Blomme, N. M. Wilson, R. L. Dalman, N. J. Pelc and C. a. Taylor, 'Allometric scaling of wall shear stress from mice to humans: quantification using cine phase-contrast MRI and computational fluid dynamics.' *American journal of physiology. Heart and circulatory physiology*, vol. 291, no. 4, H1700–8, 2006.

[19] B. Trachet, M. Renard, G. De Santis, S. Staelens, J. De Backer, L. Antiga, B. Loeys and P. Segers, 'An Integrated Framework to Quantitatively Link Mouse-Specific Hemodynamics to Aneurysm Formation in Angiotensin II-infused ApoE -/- mice.' *Annals of biomedical engineering*, vol. 39, no. 9, pp. 2430–2444, 2011.

[20] M. D. Ford, A. T. Black, R. Y. Cao, C. D. Funk and U. Piomelli, 'Hemodynamics of the mouse abdominal aortic aneurysm.' *Journal of biomechanical engineering*, vol. 133, no. 12, p. 121 008, 2011.

[21] Y. Huo, X. Guo and G. S. Kassab, 'The flow field along the entire length of mouse aorta and primary branches.' *Annals of biomedical engineering*, vol. 36, no. 5, pp. 685–699, 2008.

[22] B. Trachet, J. Bols, G. De Santis, S. Vandenberghe, B. Loeys and P. Segers, 'The Impact of Simplified Boundary Conditions and Aortic Arch Inclusion on CFD Simulations in the Mouse Aorta: A Comparison With Mouse-specific Reference Data', *Journal of Biomechanical Engineering*, vol. 133, no. 12, p. 121 006, 2011.

[23] M. Van Doormaal, Y.-Q. Zhou, X. Zhang, D. a. Steinman and R. Mark Henkelman, 'Inputs for Subject-Specific Computational Fluid Dynamics Simulation of Blood Flow in the Mouse Aorta', *Journal of Biomechanical Engineering*, vol. 136, no. 10, p. 101 008, 2014.

[24] Y. Hoi, Y.-Q. Zhou, X. Zhang, R. M. Henkelman and D. A. Steinman, 'Correlation between local hemodynamics and lesion distribution in a novel aortic regurgitation murine model of atherosclerosis.' *Annals of biomedical engineering*, vol. 39, no. 5, pp. 1414–22, 2011.

[25] D. De Wilde, B. Trachet, N. Debusschere, F. Iannaccone, A. Swillens, J. Degroote, J. Vierendeels, G. R. De Meyer and P. Segers, 'Assessment of shear stress related parameters in the carotid bifurcation using mouse-specific FSI simulations', *Journal of Biomechanics*, In press, 2015.

[26] B. Trachet, J. Bols, J. Degroote, B. Verhegghe, N. Stergiopulos, J. Vierendeels and P. Segers, 'An Animal-Specific FSI Model of the Abdominal Aorta in Anesthetized Mice', *Annals of Biomedical Engineering*, vol. 43, no. 6, pp. 1298–1309, 2015.

[27] B. J. a. Janssen, T. De Celle, J. J. M. Debets, A. E. Brouns, M. F. Callahan and T. L. Smith, 'Effects of anesthetics on systemic hemodynamics in mice.' *American journal of physiology. Heart and circulatory physiology*, vol. 287, no. 4, H1618–H1624, 2004.

[28] V. Komarek, 'Normative Biology, Husbandry, and Models - Mouse Physiology', in *The Mouse in Biomedical Research*, II, vol. III, Elsevier, 2007, ch. 2, pp. 23–90.

[29] D. De Wilde, B. Trachet, C. Van der Donckt, B. Vandeghinste, B. Descamps, C. Vanhove, G. R. Y. De Meyer and P. Segers, 'Vulnerable plaque detection and quantification with gold particle-enhanced computed tomography in atherosclerotic mouse models.' *Molecular imaging*, vol. 14, pp. 9–19, 2015.

[30] J. Bols, L. Taelman, G. De Santis, J. Degroote, B. Verhegghe, P. Segers and J. Vierendeels, 'Unstructured hexahedral mesh generation of complex vascular trees using a multi-block grid-based approach', *Computer Methods in Biomechanics and Biomedical Engineering*, pp. 1–10, 2015.

[31] P. Moireau, N. Xiao, M. Astorino, C. A. Figueroa, D. Chapelle, C. A. Taylor and J.-F. Gerbeau, 'External tissue support and fluid-structure simulation in blood flows.' *Biomechanics and modeling in mechanobiology*, vol. 11, no. 1-2, pp. 1–18, 2012.

[32] J. L. Van Herck, G. R. De Meyer, W. Martinet, C. E. Van Hove, K. Foubert, M. H. Theunis, S. Apers, H. Bult, C. J. Vrints and A. G. Herman, 'Impaired Fibrillin-1 Function Promotes Features of Plaque Instability in Apolipoprotein E-Deficient Mice', *Circulation*, vol. 120, no. 24, pp. 2478–2487, 2009.

[33] E. N. Marieb and K. Hoehn, 'Anatomy & Physiology', Pearson In. Pearson Benjamin Cummings, 2008.

[34] J. S. Querido and a. W. Sheel, 'Regulation of cerebral blood flow during exercise.' *Sports medicine (Auckland, N.Z.)*, vol. 37, no. 9, pp. 765–82, 2007.

[35] M. Hiura, T. Nariai, K. Ishii, M. Sakata, K. Oda, J. Toyohara and K. Ishiwata, 'Changes in cerebral blood flow during steady-state cycling exercise: a study using oxygen-15-labeled water with PET', *Journal of Cerebral Blood Flow & Metabolism*, vol. 34, no. 3, pp. 389–396, 2014.

Chapter 10

Correlation between atherosclerosis and shear stress metrics in the carotid arteries of mice developing atherosclerosis *

10.1 Introduction

Atherosclerosis is a slowly progressing chronic inflammatory disease of the medium-sized and large arteries characterised by the development of atherosclerotic plaques. These atherosclerotic plaques consist of lipids accumulating in the arterial wall and inflammatory cells (including macrophages) [1]–[4]. Haemodynamics is generally assumed to play a crucial role in the initialisation and development of atherosclerosis. This is mediated by the shear forces that the blood flow exerts on the endothelial cells, with zones experiencing low and oscillatory shear stresses being more prone to the development of atherosclerosis [5], [6]. CFD allow researchers to obtain precise local shear stress distributions. However, it is not straightforward to link shear stress

*This chapter is based on the work: D. De Wilde, B. Trachet, G. R. Y. De Meyer and P. Segers, 'Shear stress metrics and their relation to atherosclerosis: an in vivo follow-up study in atherosclerotic mice', *Annals of Biomedical Engineering*, In press, 2016

patterns calculated by CFD to atherosclerosis development, as described in detail by Peiffer *et al.* in their systematic review [7].

A first important problem is that atherosclerosis develops slowly with the disease altering arterial geometry, hereby changing the shear stress distributions that occur. Therefore two conflicting types of data are needed for within-subject association studies of shear stress patterns and plaque initiation. First, measurements in a non-diseased condition (i.e. vascular geometry and flow information for the boundary conditions) are indispensable to set up an accurate CFD model of the reference state. Second, the plaque distribution in the arteries needs to be quantified after plaque initiation and progression. Due to the slow progression of atherosclerosis in humans, it is almost impossible to assess the pre- and post-disease state in the same subject. A second limitation of the current scientific evidence with regard to the association between atherosclerosis and (low and oscillatory) wall shear stress, is that it is not straightforward to quantitatively link the shear stress distribution with the plaque initiation metric. Regression analysis is most commonly used to study their association [8], [9]. However, this analysis presumes a linear relationship between both variables, which is not valid a priori. Moreover, a linear regression analysis implicitly assumes that the different observations are mutually independent. Peiffer *et al.* showed that neither of these assumptions can be justified and proposed a novel method for quantifying spatial correlations between shear stress distributions and patterns of atherosclerosis: the surrogate sample data analysis [10]. With this technique none of the assumptions that are required for the regression analysis, have to be made. Rowland *et al.* showed that using this technique the correlation coefficient, including its confidence interval (CI), can be calculated [11].

Another challenge is to quantify the impact of the flow field and to select the appropriate HWP. Over the past decades, several metrics have been introduced, ranging from simple time-averaged wall shear stress values to more complex parameters accounting for the directionality of the shear stress. To the best of our knowledge, there is no consensus on which HWP provides the strongest association with the location of atherosclerosis. Most studies focusing on the correlation between HWPs and atherosclerosis development are limited to the classical magnitude-based HWPs (TAWSS, OSI and RRT), but even for these parameters no consensus is reached [7].

Chapter 7 describes a novel methodology to quantify macrophage infiltration *in vivo* in atherosclerotic plaques in the carotid bifurcation of ApoE$^{-/-}$ and ApoE$^{-/-}$ Fbn1$^{C1039G+/-}$ mice [4]. When fed a Western type diet, ApoE$^{-/-}$ mice develop stable atherosclerotic plaques, which are morphologically similar to human plaques [12]–[14]. Our experimental protocol consisted of

repeated gold-nanoparticle-enhanced μCT scans and we demonstrated that the contrast agent accumulates in the macrophage rich regions of the plaque over time [15]. In chapter 8 we performed FSI simulations in the carotid bifurcation of ApoE$^{-/-}$ mice. We calculated detailed and realistic shear stress metrics based on subject-specific *in vivo* measurements that were acquired before any atherosclerosis was present [16]. The baseline data used for the computational analysis were obtained in the same animals in which macrophage infiltration and plaque formation were studied for the experimental analysis.

In the present chapter, we link the results of the computational chapter (i.e. FSI calculated shear stress patterns prior to plaque formation) to the results of our experimental chapter (i.e. distribution of macrophage infiltration as a marker for plaque formation). At the individual bifurcation level we applied the surrogate sample data analysis technique suggested by Peiffer *et al.* [10], to test for a spatial correlation between the shear stress patterns occurring before plaque development and the macrophage distribution within the plaque afterwards. At the population level, a one sample t-test was applied at the paired shear stress and lesion patterns to assess the correlation at the population level as suggested by Rowland *et al.* [11]. We also compared some of the most commonly used shear stress metrics with more recently defined metrics such as transWSS [17] and harmonic-based indices [18], [19].

10.2 Materials and Methods

10.2.1 Mice

This study was performed on a subset (4 female ApoE$^{-/-}$ mice) of data that was available from previous studies [15], [16], and we refer to these studies for details regarding the experimental methods. All experiments were conducted according to the EC guidelines and were approved by the animal ethics committee of Ghent University (ECD 12/26). Animals were fed a Western type diet (TD88137, Harlan Teklad, Madison, Wis, USA) from the age of 6 to 26 weeks. At weeks 10, 15 and 20 after the start of the diet (mice aged 16, 21 and 26 weeks), the animals underwent an imaging protocol consisting of μCT and US. HWPs were obtained from FSI simulations at week 10 in all 4 animals, and for both the left and right carotid territory. As for the contrast accumulation data, data from 2 out of 4 animals at week 15 had to be excluded due to motion artefacts during the μCT measurements. At week 20, one of the 4 animals had developed a severe stenosis preventing a correct segmentation of the right carotid bifurcation (ECA).

10.2.2 In vivo measurements and FSI simulations

At the three time points, the μCT protocol consisted of a measurement before and after the injection of 100 μl/25g body weight Aurovist (Nanoprobes, Yaphank, NY, USA), which accumulated over time in the macrophages of the atherosclerotic plaques located near the carotid bifurcation. As such, μCT measurements performed at weeks 15 and 20 enabled the visualisation of contrast accumulation, and thus macrophage infiltration, in the arterial wall. To quantify contrast accumulation, the proportional length of the normal (total length of 0.3 mm) was calculated with respect to the luminal surface with contrast, as shown in figure 10.1 1G. Further details are provided in [15].

Mouse-specific FSI simulations in the left and right carotid bifurcation were performed based on measurements at week 10. At this time, no signs of inward remodelling could be detected, and we considered the blood flow and haemodynamic wall parameters to be equivalent to the situation prior to the onset of atherosclerosis. The segmented μCT geometry was used for the vascular model, PW Doppler US provided velocity waveforms and M-mode US measurements provided diameter curves that served as boundary conditions. Further methodological details are provided in [16].

10.2.3 Derived haemodynamic wall parameters

We considered two groups of HWPs, proposed over the past decades in literature as quantitative markers capable of identifying "disturbed" blood flow: the magnitude-based and the harmonic-based. Magnitude-based parameters are TAWSS, OSI [20], RRT [21] and the transWSS [17]. In the group of the harmonic-based parameters, the DH [18] and the HI [19] were calculated.

$$\text{transWSS} = \frac{1}{T}\int_0^T \left| \vec{\tau} \cdot \left(\vec{n} \times \frac{\vec{\tau}_{mean}}{\|\vec{\tau}_{mean}\|} \right) \right| \mathrm{d}t \quad \text{with} \quad \vec{\tau}_{mean} = \int_0^T \vec{\tau}\,\mathrm{d}t \tag{10.1}$$

$$DH = n \ni \max\left(F\left(n\omega_0\right)\right) \;,\; F \equiv FFT\left(\|\vec{\tau}\|\right) \;,\; \omega_0 = \frac{2\pi}{T} \tag{10.2a}$$

$$HI = \frac{\sum_{n=1}^{\infty} F\left(n\omega_0\right)}{\sum_{n=0}^{\infty} F\left(n\omega_0\right)} \;,\; F \equiv FFT\left(\|\vec{\tau}\|\right) \;,\; \omega_0 = \frac{2\pi}{T} \tag{10.2b}$$

In a previous chapter (chapter 8 on page 149), the TAWSS, the OSI and RRT are already described in more detail for the current datasets and the formulas are shown in equation (8.1). How to calculate the more recently developed metrics is shown in equation (10.1) and equation (10.2). In these

formulas $\vec{\tau}$ is the instantaneous wall shear stress vector, $\vec{\tau}_{mean}$ the cycle-averaged wall shear stress vector and T the period of the cardiac cycle. The movement of the arterial wall in the FSI simulations was taken into account by expressing $\vec{\tau}$ in a local frame of reference attached to the arterial wall. For the fast Fourier transformation (FFT), the parameters are the fundamental frequency ω_o and the harmonic index n so that n ω_o indicates the nth harmonic.

10.2.4 Mapping the carotid bifurcation

A first step to correlate the FSI simulations with macrophage infiltration was to map the bifurcation surface, segmented from measurements at different time points, onto a common mesh. A centreline-based approach using VMTK (`www.vmtk.org`) was followed as proposed by Antiga and Steinman [22]. The bifurcation was split into its 3 main branches (CCA, ECA and ICA). The distance to the bifurcation was chosen as longitudinal coordinate, while the angle around the centreline was taken as circumferential coordinate (ranging from $-\pi$ to $+\pi$ at the medial side of the bifurcation normal, from medial to posterior, lateral, anterior and finally medial; figure 10.1 1). It is important to keep in mind that for the left and right bifurcations, the rotation is opposite (medial-lateral axis is flipped). Then, the longitudinal and angular coordinates were mapped onto a planar rectangular grid (figure 10.1 1D-1H). The grid contained 100 cells in the circumferential direction (resolution 0.0628 rad) and in the longitudinal direction the resolution was 13.5 μm, which resulted in square cells for the average CCA. The flow extensions of the FSI simulations were cut off at the ECA (30 cells) and the CCA (10 cells) to remove transient in/outflow phenomena.

10.2.5 Statistical modelling

At the individual bifurcation level, a single lesion map was compared to a single shear stress map. We applied the surrogate sample data analysis, proposed by Peiffer *et al.* [10], to study correlations between the calculated haemodynamic wall parameters and macrophage infiltration maps. In short, the similarity of the distribution of two different variables (HWP and contrast accumulation) is described by Spearman's rank correlation coefficient ρ_s (adapted from the algorithm described by Rowland *et al.* [11]). The correlation is determined for the original values of the variables and for n_{sur} scrambled distributions of one of the variables (=surrogates).

For the interpretation of the data, a distinction needs to be made between TAWSS, where low values are associated with the susceptibility for atherosclerosis (negative correlation expected), and the other HWP where high values are associated with plaque susceptibility (positive correlation expected). In the case of a negative correlation (TAWSS), one should test

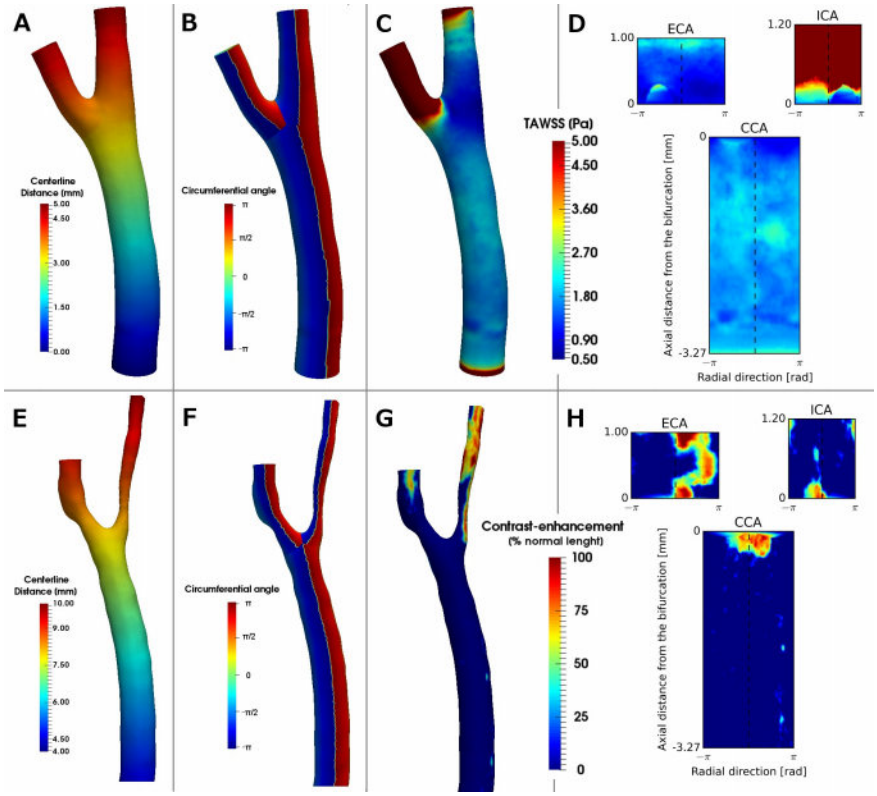

Figure 10.1: Virtually cutting open the 3D geometry of the carotid bifurcation: the FSI (top: A-D) and week 20 μCT dataset contrast-enhancement map (bottom: E-H) of an example mouse. The first coordinate used for the cutting open is the distance along the centreline (A/E). The second coordinate is the circumferential angle ranging from $-\pi...\pi$ (B/F). Both coordinates are mapped to the 2D space for every branch. The cutting line is taken at the medial side and perpendicular to the bifurcation. Next are example parameters for both cases: FSI - TAWSS (C) and week 20 – contrast presence (G). Figure D shows the opened TAWSS map. The horizontal axis loops through consecutively the medial, posterior, lateral, anterior and medial side while ranging from $-\pi$ to π. The lateral side is indicated with a dashed line, splitting the patch in the posterior and anterior side. Figure H shows the cut open representation of the plaque presence map.

whether the correlation coefficient is below the 5% percentile of the random distributions (i.e. the left-hand side of the histogram – left tailed test). For positive correlations, the statistical test ascertains that the original correlation coefficient is higher than the 95% percentile of the random distributions (i.e. the right-hand side of the histogram – right tailed test).

To take into account the spatial autocorrelation of the variables, extra sampling steps (n_{smp}) were performed. The sample size s_{smp} was calculated for every geometry using: $s_{smp} = s_{map}/l_{dec}^2$. In this formula s_{map} was the original number of grid points and l_{dec} the spatial de-correlation length, which was determined with a tailored approach as described in [10] for all the branches separately and all the different HWPs. This resulted in average values for the l_{dec} of 15.42±4.61, 14.90±2.76, 15.35±4.38, 19.05±6.35 and 16.57±5.46 for the TAWSS, OSI, RRT, transWSS and HI respectively. A conservative value of 20 was used for l_{dec} in all the surrogate sample data analysis calculations to assure that all sample points were independent observations and that proper statistical testing was conducted. The final histogram was averaged over n_{smp} histograms (one for each sampling step), with confidence levels as shown in figure 10.2. An error tolerance of 10^{-4} was used for the p-value resulting in averaged values of: n_{sur} = 2600 and n_{smp}=3300. This technique was used to calculate the correlation between the distribution of the HWP (TAWSS, OSI, RRT, transWSS, DH or HI) on the one hand and the macrophage infiltration distribution at weeks 15 or 20 on the other hand. From the correlations found between the different samples, a confidence interval could be calculated as shown by Rowland *et al.* [11]. In the current study the confidence bound (CB) was used instead, which is more appropriate for a single tailed test. The found correlation was deemed significant at $p<0.05$ if the upper confidence bound (UCB)<0 for a left tailed test (expected $\rho_s<0$ - TAWSS) or the lower confidence bound (LCB) >0 for a right tailed test (expected $\rho_s>0$ – other HWP). This was done both on an individual branch level, only considering one branch for every statistical test, and on a bifurcation level, combining the three branches into a single statistical test.

On the bifurcation level a correlation coefficient was found for 7 individual bifurcations (1 dataset was excluded). On the population level, we studied both the Spearman's rank correlation coefficient (ρ_s)(assuming monotonic relationship) and the Pearson's correlations coefficient (r) (assuming linear relationship). First a Fisher r to z transformation was applied because correlation coefficients are not normally distributed [11]. A single tailed one sample t-test was performed to assess if the found correlation was significant.

Next to the previous 'paired' approach, an aggregate approach was performed. Aggregated datasets were obtained by averaging the 7 datasets obtained at week 20. Afterwards, the aggregated lesion map was compared to the aggregated HWP maps using the surrogate sample data analysis method.

Finally, we also tested the relationship between the different haemodynamic wall parameters. A similar t-test method was applied to the HWP maps to check the correlation between the several HWPs. Since the sign of the expected correlations was unknown, a two tailed test was used in this case.

10.3 Results

10.3.1 Contrast (plaque) accumulation

Limited contrast infiltration was present at week 15. On average there was only contrast present (contrast-enhancement over >25% of the normal length) for 0.47±0.58, 2.48±1.30 and 1.19±0.74 %area of the lumen area of the CCA, ECA and ICA, respectively. This resulted in an average of 1.07±0.59%area for the complete bifurcation. With exception of 1 animal and for one bifurcation (4R; 0.39%area), there was a clear increase in contrast accumulation from week 15 to week 20 with values at week 20 of 4.4±1.8, 40.2±12.0, 19.1±10.1 %area for the CCA, ECA and ICA respectively. The extent of contrast accumulation is thus relatively mild in the common carotid artery, and most outspoken in the external carotid artery

10.3.2 Haemodynamics vs. atherosclerosis in individual branches

At week 15 no significant correlations were found for the individual branches for either of the HWPs. The average ρ_s for the RRT was: CCA = 0.020, ECA = -0.145 and ICA= 0.118. The p-values were larger than: 0.12 (TAWSS), 0.12 (OSI), 0.14 (RRT), 0.25 (transWSS), 0.3 (HI) and 0.67 (DH).

At week 20, on an individual branch level, the surrogate data sample analysis revealed a significant positive correlation ($p<0.05$ and LCB>0) between RRT and the amount of plaque accumulation in 4 out of 7 cases in the CCA (table 10.1). No statistically significant results were found for either the ECA or the ICA. In figure 10.4 a visual side by side comparison of (i) the amount of macrophage infiltration at week 20 and (ii) the RRT at week 10 is given for the 7 bifurcations. In the CCA the visual comparison shows that high values of macrophage infiltration and RRT occur close to the bifurcation. In the ECA and the ICA the spatial distribution is visually more different for both metrics as shown by the statistical analysis.

The same statistical trend was observed for OSI (2 times $p<0.05$ and LCB>0 – positive correlation) and TAWSS (4 times $p<0.05$ and UCB<0 –negative correlation) in the CCA. For both of these parameters, no significant correlation was found for the ECA or ICA branch in any of the animals. The transWSS resulted in 2 CCA branches with $p<0.05$ but not LCB>0 and no significant correlation in any of the ECA or ICA branches. For neither DH nor HI a significant correlation was found in any of the branches.

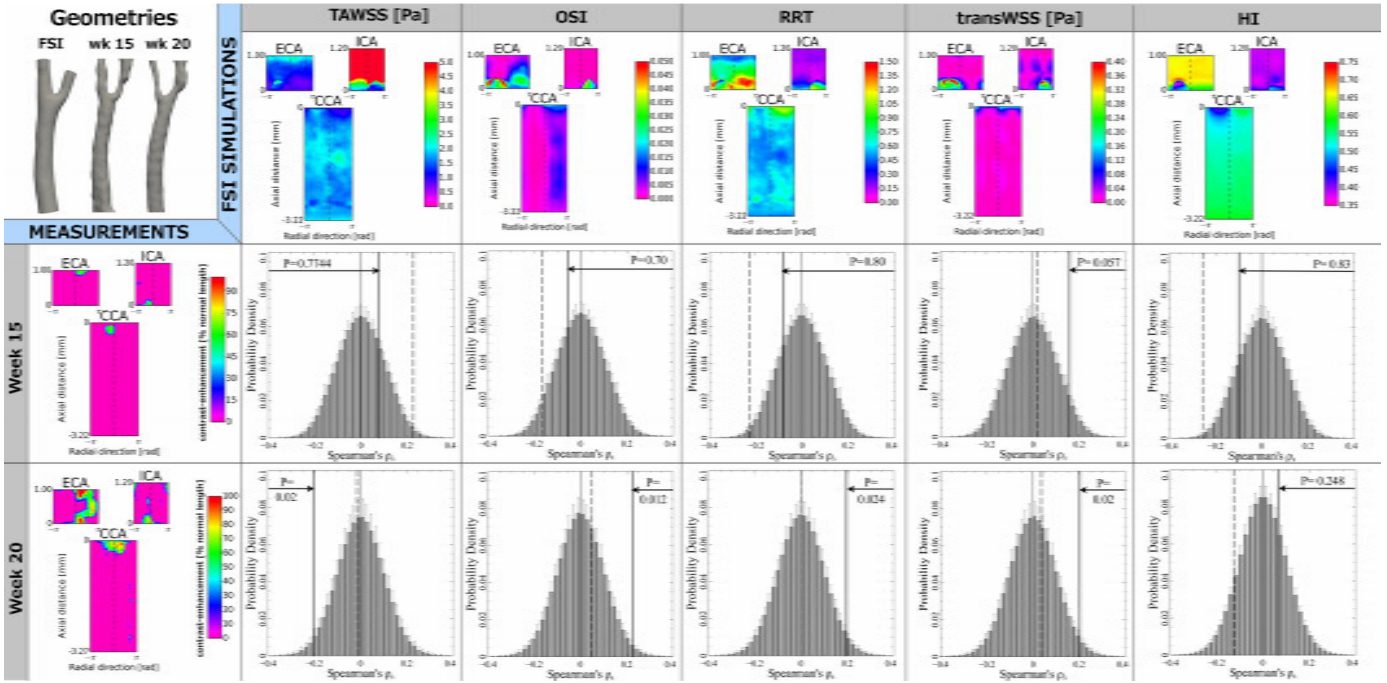

Figure 10.2: An overview of the results of the left carotid bifurcation of mouse 1. The segmented geometries are visible in the upper left corner. The columns are grouped by the 5 FSI calculated HWPs: TAWSS, OSI, RRT, transWSS and HI. The calculated results are visible in the first row for the three branches: CCA, ECA and ICA. The rows are grouped by the contrast-enhanced μCT measurements: week 15 and week 20 after the start of the diet. The first column shows the presence of contrast-enhancement, which is a marker for macrophage infiltration for the three branches. The plotted histograms show the results of the surrogate sample data analysis [10]. The histograms show the mean and standard deviation of the histograms of the Spearman's rank correlation coefficient (ρ_s). The thick line marks the percentile of the discriminating statistic of the original dataset and the dashed lines its upper confidence bound (UCB) (TAWSS) or lower confidence bound (LCB) (OSI, RRT, transWSS and HI). The contrast-enhancement map for week 15 (middle row) is not correlated with either of the HWP maps. However at week 20, the TAWSS has a $p<0.05$ ($p=0.02$) and UCB<0, thus a significant negative correlation (ρ_s=-0.203) was found. The OSI, RRT and transWSS show significant positive correlations with the macrophage infiltration at week 20 of respectively ρ_s=0.224, ρ_s=0.197 and ρ_s=0.203 ($p<0.05$ and LCB>0). Finally, no correlation was found for the HI (p=0. 248).

Table 10.1: Spearman's rank correlation coefficient (ρ_s) between the macrophage infiltration at week 20 and the calculated RRT for the three branches of the left and right carotid bifurcation. Values showing significance in the surrogate data analysis for both conditions (p<0.05 and LCB>0) are indicated by a *. For the right carotid bifurcation of mouse 1 (1R), severe stenosis inhibited the segmentation of the ECA and consequently this bifurcation was removed from the analysis.

Mouse	CCA	ECA	ICA
1L	**0.285***	0.055	0.215
1R	-	-	-
2L	**0.275***	0.046	0.181
2R	**0.331***	0.166	0.26
3L	0.073	-0.554	-0.178
3R	**0.254***	0.107	-0.045
4L	0.134	0.114	-0.354
4R	-0.175	-0.013	0.083

10.3.3 Haemodynamics vs. atherosclerosis in the complete bifurcation

At week 15, our findings did not change when considering the complete bifurcation. None of the classical HWPs correlated significantly with macrophage infiltration after 15 weeks with p-values larger than: 0.39 (TAWSS), 0.23 (OSI), 0.35 (RRT), 0.057 (transWSS), 0.19 (HI) and 0.54 (DH). The DH only differed from the ground harmonic (value = 1) for 0.65±0.67% of the surface, and therefore had a constant value throughout almost the entire bifurcation.

In the second row of figure 10.2, the results at week 15 of the left bifurcation of mouse 1 are shown. The thick black line shows ρ_s between the macrophage infiltration at week 15 and the respective HWPs (TAWSS, OSI, RRT, transWSS and HI). The signs of both ρ_s and its CB (dashed line) are opposite to their theoretically expected values (negative values expected for TAWSS and positive values for OSI, RRT, transWSS and HI) for all HWPs except for the transWSS. Thus, ρ_s=0 is included in the interval confined by the CB. Moreover, p>0.05 in these cases and thus none of the conditions for significance is met. For the transWSS ρ_s=0 is not included in the LCB but still p>0.05, indicating that the correlation is not significant.

However, after 20 weeks a significant negative correlation (p<0.05 and UCB<0) was found in 4 cases (1L, 2L, 2R and 3R) for TAWSS (table 10.2). The RRT yielded similar results but with a significant positive correlation for the same 4 cases. A visual comparison of the macrophage infiltration at week 20 and the RRT for these bifurcations is given in figure 10.4. The OSI only correlated for 2 cases (1L and 3R). The transWSS showed a significant positive

Table 10.2: Spearman's rank correlation coefficient (ρ_s) between the simulated HWPs at week 10 and the macrophage infiltration at week 20 on the individual bifurcation level. Values showing significance (p<0.05 and UCB<0 for ρ_s<0 or LCB>0 for ρ_s>0) are indicated by a *. It should be noted that in the bifurcation 4R almost no atherosclerosis was present.

	TAWSS	OSI	RRT	transWSS	HI	DH
1L	**-0.203***	**0.224***	**0.197***	**0.203***	0.068	-0.043
1R	-	-	-	-	-	-
2L	**-0.284***	0.157	**0.288***	0.009	0.109	0.058
2R	**-0.244***	0.145	**0.251***	0.119	0.056	0.016
3L	0	-0.108	0.007	0.068	-0.044	0.015
3R	**-0.337***	**0.317***	**0.338***	0.052	**0.276***	0.004
4L	0.018	0.082	0.003	**0.384***	-0.034	0.028
4R	0.046	-0.003	-0.051	0.002	-0.027	0.035

correlation for mice 1L and 4L. Mouse 3R showed a positive correlation for HI. No significant correlation could be found for DH.

For mouse 1L the last row of figure 10.2 shows a significant negative correlation for TAWSS (p<0.05 and both ρ_s and its UCB are negative), as evidenced by a 1-tailed test. For the OSI and the RRT on the other hand, a significant positive correlation was found (p<0.05 and both ρ_s and its LCB are positive).

10.3.4 Haemodynamics vs. atherosclerosis on a population level

In table 10.3 the Spearman's rank correlation coefficient (ρ_s) and the Pearson's correlation coefficient (r) are listed for the population (N=7) at week 20. The correlation coefficient is low (ρ_s < 0.15) for all wall shear stress metrics. On average the TAWSS shows a negative correlation (-0.144) and the other metrics show on average a positive correlation. For the TAWSS, OSI, RRT and transWSS this correlation is significant (p<0.05). The Pearson's correlation coefficient (r) shows the same trends as ρ_s. In this case, a significant positive population correlation was found for OSI (0.160), RRT (0.232) and HI (0.129). The statistical test on the aggregated datasets showed that the correlation was higher, but still the same HWPs showed a significant correlation (TAWSS, OSI, RRT and transWSS).

10.3.5 Comparison of the HWPs

10.3.5.1 Visual comparison for a single bifurcation

A graphical overview of the interdependence of the HWPs for the carotid bifurcation of mouse 3L is shown in figure 10.3. This figure is a slightly

Table 10.3: Overview of the population average correlation between several HWPs at week 10 and the macrophage infiltration at week 20. Both ρ_s and r are listed. Significant results (p<0.05) are annotated by *. Between brackets the p-value resulting from a one sample single tailed t-test is shown. The last two row shows the results for the surrogate sample data analysis applied to the aggregate datasets (-agg) for both ρ_s and r. Significant results meeting the two significance conditions are annotated by a *. For the ρ_s RRT, only one significance condition is met (p<0.05 but LCB<0), which is indicated by °.

	TAWSS	**OSI**	**RRT**	**transWSS**	**HI**
ρ_s	**-0.144***	**0.118***	**0.148***	**0.121***	0.057
	(0.027)	**(0.034)**	**(0.024)**	**(0.031)**	(0.118)
r	-0.080	**0.160***	**0.232***	0.039	**0.129***
	(0.183)	**(0.006)**	**(0.013)**	(0.267)	**(0.049)**
ρ_s-agg	**-0.200***	**0.196***	**0.201°**	**0.401***	-0.113
	(0.024)	**(0.028)**	**(0.025)**	**(0.000)**	(0.863)
r-agg	-0.134	**0.489***	**0.575***	0.132	**0.236***
	(0.091)	**(0.000)**	**(0.000)**	(0.108)	**(0.009)**

adapted scatterplot matrix. It contains three kinds of plots in structured way: on the diagonal the histogram of a single HWP is shown, below the diagonal scatterplots show the correlation between HWP-pairs and above the diagonal this correlation between two HWPs is visualised using a hexbin plot.

Every plot on the diagonal shows the distribution of a different HWP by plotting the histogram. The x-axis represents the range of values of the HWP of the subsequent column (x-axes are shared for each column). The CCA, ECA and ICA are shown in red, blue and green respectively as a stacked barchart. As a result the histogram of the whole bifurcation (over all three branches) is represented by the total length of each bar (adding up the different colours/branches) and it is delineated by a small black line. For the TAWSS (upper left corner) two clear peaks are visible in the histogram for the ECA (lowest) and CCA (middle). The ICA does not really show a specific peak but the highest TAWSS values are present in this branch. The x-axis (that depicts TAWSS) is shared with for example the scatter plot comparing TAWSS with OSI (directly below the histogram: second row and first column). Therefore, the points of the ECA (blue +) are located directly under the blue ECA peak in the histogram. For both the OSI and RRT most striking is a right handed tail (high values) for the ECA branch. This indicates that the highest values of the respective HWP is found in the ECA branch. The transWSS shows a right handed tail for the ICA with lower values for both the ECA and CCA. The HI clearly shows a peak for the three different branches with high values of HI present in the ECA.

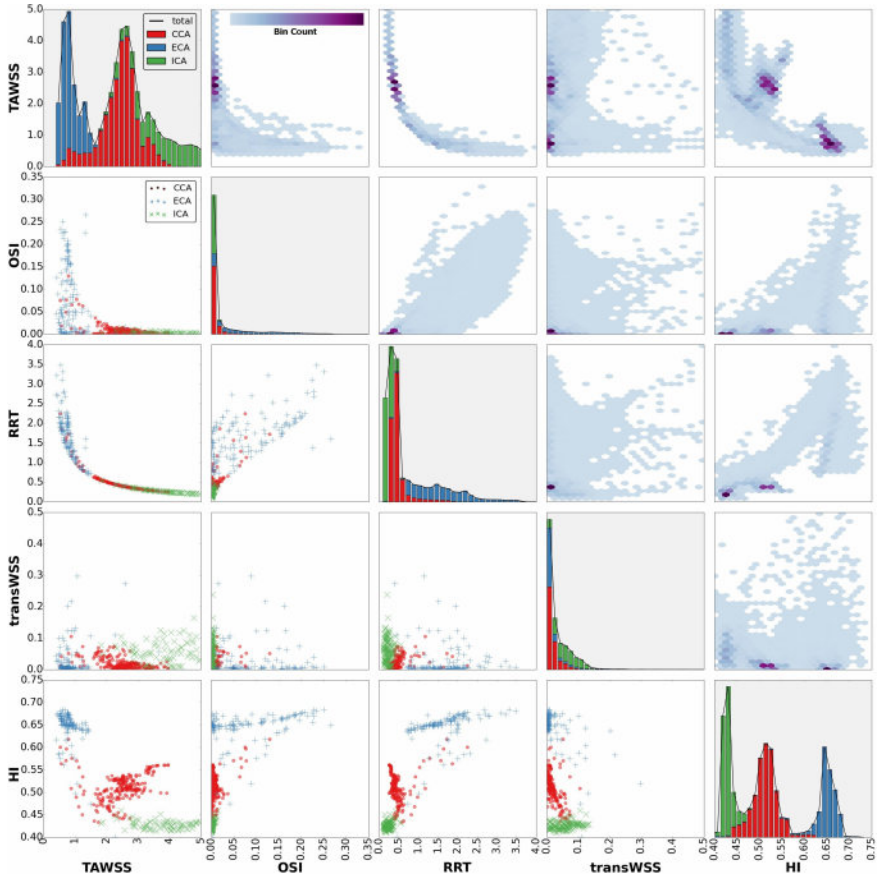

Figure 10.3: Scatterplot matrix of the HWPs in the murine carotid bifurcation (3L): TAWSS[Pa], OSI[-], RRT[-], transWSS[Pa] and HI[-]. On the diagonal of the matrix, the histograms of the different HWPs are plotted for the three branches (CCA-red, ECA-blue and ICA-green). The total histogram is delineated by a black line. Below the diagonal, scatter plots are shown for 500 random points of the surface mesh. On the x-axis, the HWP of the subsequent column is shown and the y-axis shows the HWP according to the subsequent row. These scatter plots can show a clear correlation (example: scatter plot at row 3-RRT and column 1-TAWSS) or can show the absence of a correlation (example: scatter plot at row 4-transWSS and column 2-OSI). Not all the points can be plotted in a scatter plot, the large amount would render the scatter plot unreadable. Therefore, above the diagonal 2D-histograms (hexbin-plots) of all the points in the surface mesh are shown. The 2D-space is divided in hexagons to form a honeycomb structure. The amount of points in every hexagon is indicated by the colour scale. The regions with a higher point density are shown in a darker colour. In the 2D-histograms, no distinction between the three branches is made. The x-axis and y-axis are ordered in the same manner as for the scatter plots.

The plots below the diagonal are scatter plots in which 500 random points of the surface mesh are shown. In each of this scatter plots two different HWPs are plotted against each other, according to the position of the scatter plot in the matrix. The x-axes and the y-axes are the same within each column and row respectively. In the scatter plots different markers differentiate between the three branches: red o - CCA, blue + - ECA and green x - ICA. These plots give a clear first indication whether the two HWPs included in the plot are linked or not. The most clearly (inversely) linked are the TAWSS and the RRT, as evidenced by the clear hyperbolic shape. Also the TAWSS and the OSI appear to be inversely dependent shown by a less obvious hyperbolic shape of the plot. Between the OSI and RRT, this relation appears to be more or less linear, although there is a lot of scatter. For the correlations between the transWSS and the other HWPs, it is difficult to see a clear relationship in these plots. The HI appears to be negatively correlated to the TAWSS and positively with the OSI and RRT. For the HI, there is a lot of scatter present so this relations are not very clear.

The plots above the diagonal show 2D-histograms (hexbin plots) of the same HWP-pairs. In these plots, the differentiation between the three branches is lost, but in contrast to the scatter plots (below the diagonal) all the points of the surface mesh were included. This kind of plot is a natural extension of the normal 1D-histogram (see diagonal plots) to 2D. The domain is divided in hexagonal bins and every bin is coloured according to the number of points present in that bin. Therefore, a different point density is more obvious in this representation. The same relations between the different HWPs were found.

10.3.5.2 Comparison of the HWPs on a population level

The correlations between the different HWPs on a population level are listed in table 10.4. As can be anticipated, there were strong correlations between RRT and TAWSS and OSI. HI correlated reasonably well (correlation coefficient magnitude from 0.45 to 0.68) with the TAWSS, RRT, OSI and transWSS. Lowest correlations were between transWSS and TAWSS, OSI and RRT (all below 0.25).

10.4 Discussion

We present the first study that assesses the spatial correlation between commonly used haemodynamic wall parameters and the location of contrast accumulation in macrophages (~atherosclerosis development), in paired as well as aggregated data of the carotid arteries in ApoE$^{-/-}$ mice.

Table 10.4: Heatmap of the different HWPs and the Spearman's rank correlation coefficient between them for all bifurcations (N=7). For every correlation the 95% confidence interval is given in sub- and superscript. The cells are coloured according to the mean value of the correlation coefficient.

TAWSS	OSI	RRT	transWSS	HI	
-	$-0.66^{-0.59}_{-0.73}$	$-0.97^{-0.95}_{-0.98}$	$0.25^{0.37}_{0.14}$	$-0.65^{-0.57}_{-0.73}$	**TAWSS**
	-	$0.71^{0.78}_{0.64}$	$-0.07^{0.05}_{-0.19}$	$0.56^{0.66}_{0.46}$	**OSI**
		-	$-0.22^{-0.10}_{-0.33}$	$0.68^{0.77}_{0.59}$	**RRT**
			-	$-0.45^{-0.37}_{-0.54}$	**transWSS**
				-	**HI**

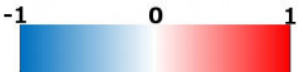

10.4.1 Week 15

No correlation was found between any of the studied HWPs and the macrophage infiltration at week 15, neither on the single branch level nor on the bifurcation level. The main reason is that almost no contrast accumulation had occurred in the carotid bifurcation at this specific time point. Note that the contrast accumulation measured at week 15 results from contrast injected at week 10. Therefore it is plausible that we missed the exact time point where contrast accumulation significantly speeds up. The radiation experienced by the animals during the μCT measurements puts ethical constraints that prevented us from performing more frequent (e.g. weekly) measurement of macrophage infiltration.

10.4.2 Week 20: individual branch level

When studying the association between haemodynamics and atherosclerosis on the individual branch level, no correlation was found between the HWPs and the macrophage infiltration in both ECA and ICA. The HWPs display rather smooth patterns while the macrophage infiltration distribution is more irregular (see e.g. figure 10.4 and extra figures in Appendix C on page 251). For the CCA, the HWPs and macrophage infiltration overlap in the region closest to the bifurcation. This results in a positive correlation in 6 out of 7 cases (significant for 4 cases) for the RRT. For both the OSI and TAWSS, the same trends are visible.

10.4.3 Week 20: individual bifurcation level

On the individual bifurcation level, a clear correlation with the macrophage infiltration map was found for both RRT and TAWSS (4 out of 7 cases significant) and a moderate correlation was found for both OSI and transWSS

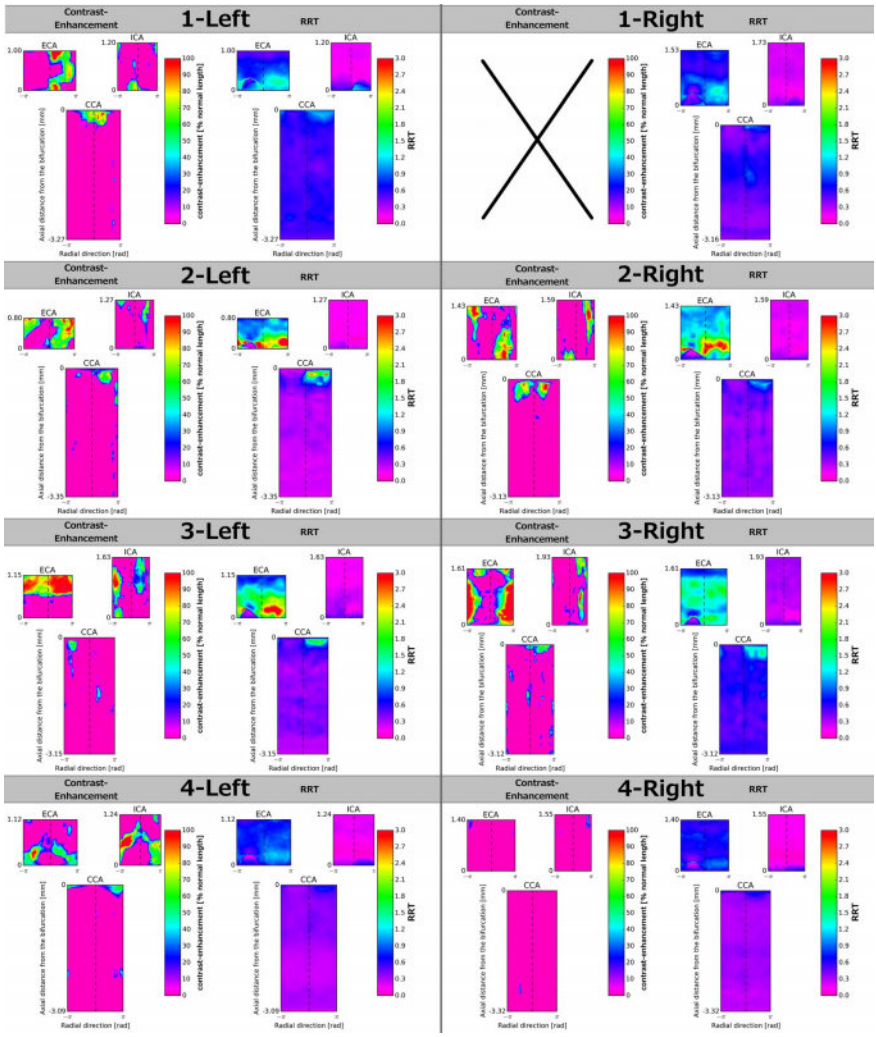

Figure 10.4: A side by side comparison between the contrast-enhancement related to macrophage infiltration at week 20 and the calculated RRT. The cut open branches of the left and right carotid bifurcations for the 4 mice are shown. The contrast-enhancement measurement of the right carotid bifurcation of mouse 1 failed.

(2 out of 7 cases significant) (table 10.1). The limited correlation magnitude (around 0.2 – 0.3) shows that processes other than the haemodynamics are involved in the complex process of atherosclerotic plaque initiation. This also shows when comparing the left with the right bifurcation for a single mouse. The HWP distributions are similar for both sides in most mice but the macrophage infiltration often differs between both sides (figure 10.4). In this study, the haemodynamics cannot explain the difference in plaque location between the left and the right bifurcation and other processes are likely involved. Important to note is the consistent negative correlation for TAWSS and the positive correlation for RRT. This provides important evidence for the low and oscillatory shear stress hypothesis, as we are (to the best of our knowledge) the first to compare pre-disease HWPs with a quantitative metric for plaque development on a within-subject basis.

10.4.4 Week20: population level

For the whole population, a significant Spearman's rank correlation was found for the TAWSS, OSI, RRT and transWSS (table 10.3 and figure 10.5). These data confirm the results found on an individual bifurcation level and further support the low and oscillatory shear stress hypothesis. The magnitude-based HWPs prove to have predictive value with regard to atherosclerotic plaque development. The harmonic-based parameters (HI and DH), do not seem to add extra relevant information in this study given their low correlation coefficients. When assuming linearity and thus calculating the Pearson's r, the correlation for TAWSS and transWSS drops, indicating that those are not linearly correlated with macrophage infiltration. Aggregating the data (last row in Table 3) leads to an overestimation of the correlation, confirming data reported by Ku *et al.* [23] and Rowland *et al.* [11]. Especially for the more irregular patterns of transWSS, aggregating leads to smoothing and an overestimation of the correlation. This indicates the importance of taking the individual correlations into account and suggests that the results of aggregated data should be interpreted with caution.

10.4.5 Comparing comparisons: which HWP to choose?

It is not a trivial task to assess which of the proposed HWPs best captures the relation between haemodynamics and atherosclerosis. The classical magnitude-based HWPs (TAWSS, OSI and RRT) are highly correlated to each other (table 10.4). This has been reported previously in the human carotid bifurcation by Lee *et al.* [24].

In addition to the "traditional" parameters we calculated the recently introduced transWSS metric, which was developed by Peiffer *et al.* to better discriminate between uniaxial and multidirectional flow [17]. In the carotid bifurcation of the ApoE$^{-/-}$ mice in this study, the correlation found for

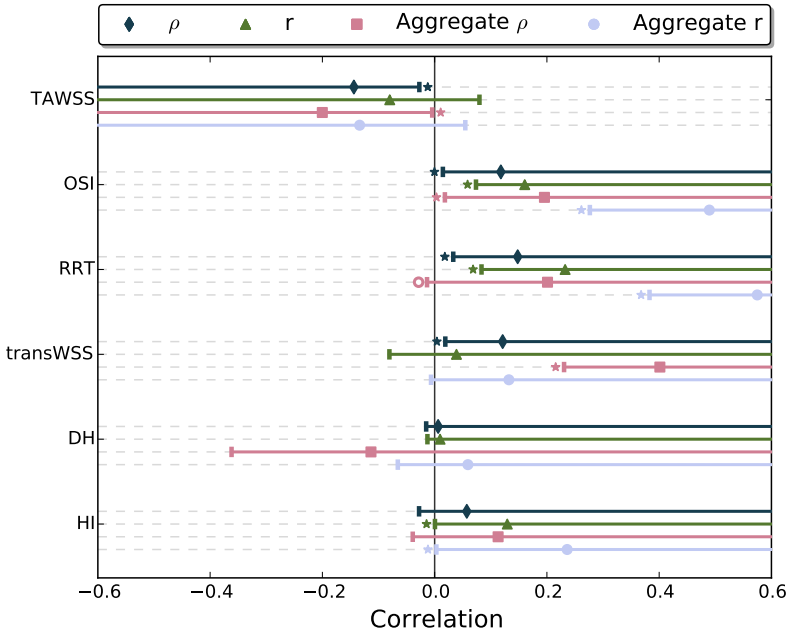

Figure 10.5: A graphical representation of the data in table 10.3. For the different HWPs, ρ_s and r are plotted together with their CB. Significant results (both the p-value and the CB conditions) are indicated by a star. For the aggregate ρ_s RRT, only one significance condition is met ($p<0.05$ but $LCB<0$), which is indicated by °.

transWSS was lower compared to TAWSS and RRT. A possible explanation for this low correlation might be the specific haemodynamic conditions in the mouse carotid, where flow is highly organised due to the low Reynolds numbers (peak Re is in the order of 12). The correlation with the classical HWPs is low, indicating that the transWSS indeed describes a different aspect of blood flow induced shear forces on the arterial wall. We did not calculate gradient-based haemodynamic wall parameters because of the reported high correlation with magnitude-based HWPs [24].

We also calculated two harmonics-based indices: the dominant harmonic (DH) introduced by Himburg *et al.* [18] and the harmonic index (HI) introduced by Gelfand *et al.* [19]. Both metrics describe the frequency-dependent response of the vascular endothelial cells with regard to atherosclerosis initiation [25]. In the present study, DH did not provide any additional information, because it only differed from the first harmonic at a very small zone in between the ECA and ICA branch; the stagnation point of the blood flow. HI on the other hand showed a pattern similar to (the inverse of) the TAWSS. Globally, HI is elevated in the ECA while its value is reduced in the CCA. Compared to TAWSS, this pattern shows an even smoother distribution

at the locations distant from the bifurcation. In the immediate vicinity of the bifurcation HI is not particularly elevated, while TAWSS shows a more outspoken drop. Overall, this results in a lower spatial correlation between HI and contrast accumulation.

10.4.6 Statistical methodology

The surrogate sample data analysis test, which is extensively used in the current work, is inherently a single tailed testing approach. For all the HWPs it is known a priori if the correlation would be positive (OSI, RRT, transWSS, HI and DH) or negative (TAWSS) and thus a single tailed approach can be applied. For consistency, a single tail t-test was also applied at the population level. A two tailed approach would result in p-values twice as large and would thus yield values around (and just above) the 0.05 confidence level.

The l_{dec} is an important parameter for the surrogate sample data analysis. We followed the same tailored approach as described by Peiffer *et al.* [10], calculating the dissimilarity of the neighbouring pixels at different length scales. The l_{dec}, is the length for which this dissimilarity reaches a maximum plateau value and the pixels become uncorrelated. In the CCA, where some of the HWPs (OSI and HI) have a more or less constant value, no such plateau value could be found in 11 (out of 14) cases. For the other branches and the other parameters, a clear plateau value was found. Because an overestimation of l_{dec} reduces the specificity but has no implication for the statistical correctness, the l_{dec} was taken to be 20 in all cases. With this value, the ratio of l_{dec} to the number of circumferential pixels (20/100=1/5) is more or less equal to the ratio proposed by Peiffer *et al.* (in their case l_{dec} ranged from $2\sqrt{2}$ to $3\sqrt{2}$ for ~20 circumferential pixels).

Rowland *et al.* defined a second condition for the surrogate data analysis test: if the value ρ_s=0 is included in the confidence interval for ρ_s, the result is not significant [11]. This leads to an inconsistency: the first condition of the approach deals with an inherently single tailed p-value while the second condition deals with a double tailed confidence interval. In the current work we have chosen to use the confidence bounds for the second condition, which is the single tailed equivalent of the confidence interval.

When comparing different statistical methods for assessing spatial correlations, Rowland *et al.* [11] described other possible statistical methods that could replace the surrogate sample data analysis applied in the current work. However, both the restricted randomisation and the bootstrap approach, which were proposed as alternative methods, are computationally more demanding than the surrogate sample data analysis. The bootstrapped approach was not used in this work due to the low amount of datasets (n=7). The Fourier-based restricted randomisation approach cannot be applied to the whole

bifurcation due to the irregular shape of the bifurcation (not rectangular because 3 branches are present). For the discrete wavelets-based restricted randomisation, the computational cost and complexity are even higher and rotations should be added to overcome poor directional selectivity, which was judged too complex for the added benefit.

10.4.7 Limitations

One of the main limitations in the current study was that we did not have baseline measurements before the mice were put on a diet. For ethical reasons the amount of (high radiation) μCT measurements was restricted. At week 10 after the start of the diet no narrowing of the carotid arteries was visible and we assumed a pre-disease state. Nevertheless (small) plaques may have been present that may have influenced the local haemodynamics. Moreover, even if the animals were 16 weeks old at this stage and thus fully grown, we still measured at a single point in time and could not account for changes in vascular functioning that may have occurred during the study.

There are some technical considerations to be kept in mind when interpreting our data. A major potential source of inaccuracy is the mapping of the 3D bifurcation geometry onto the 2D grid. This mapping should result in the same 2D decomposition for the bifurcation geometry measured at 3 different time points: week 10 (used for the FSI simulations and the assessment of haemodynamic wall parameters), week 15 (macrophage infiltration 1) and week 20 (macrophage infiltration 2) after the start of the diet. To assess the impact of potential angle misalignment, the macrophage infiltration was shifted in the circumferential direction with 5 pixels (angular shift of 18°) in both directions with respect to the HWPs data. The influence on the results was minimal with a difference in significance level in 4 out of 35 calculated values at week 20 (cases 2L/R: change for OSI from not significant to significant with still LCB<0; case1L : for TAWSS and RRT still p<0.05 but respectively UCB>0 and LCB<0). On average the difference induced by the angle shift for the correlation coefficient was 3.73% with the highest values for the OSI (on average 0.076: 7.65%). Therefore, we can conclude that the method is rather robust to small mapping misalignments.

After the mapping, both the HWP and the macrophage infiltration datasets have been resampled to a common rectangular grid, and therefore our results might depend on the chosen grid size parameters. The statistical testing of the current methodology was recalculated with a rectangular grid that had 50 circumferential cells instead of 100 (axial size of 27.0 μm) and thus an l_{dec} of 10 instead of 20 to validate the grid size dependency. Virtually no difference was found with the original results. The sampling-based on l_{dec} thus provides a good solution to acquire grid size independent results.

We used mouse-specific FSI simulations to assess the spatial distribution of haemodynamic wall parameters. This is a complex and time consuming procedure. Given the low Reynolds numbers and highly organised flow in the mouse carotid, we verified whether a simple estimation of the TAWSS for every branch based on Poiseuille flow assumptions, omitting the need for FSI simulations, would not suffice to come to the same conclusion. Although the same negative trends were visible compared to the FSI results, the correlation was lower for ρ_s and comparable for r. This indicates that the Poiseuille flow assumption can give a first estimate, but that knowing the correct TAWSS distribution using the FSI simulations has added value.

Finally, the correlations that were found were statistically significant (on a population level) but still remained low. Atherosclerosis is a complex process involving different mechanisms and our results indicate that haemodynamics provides only a partial explanation for its localized nature. For example, the regions with high macrophage infiltration (figure 10.4) differ much more between different mice than the regions with high RRT. The rate of plaque progression can also differ between animals and might be different from one location to another. In combination with only 2 measured time points this may partially explain the differences found between animals and possibly even between the left and the right bifurcation of a single mouse.

10.4.8 Conclusion

We investigated the spatial correlation between several pre-disease FSI calculated shear stress parameters and the macrophage infiltration after atherosclerotic plaque development. Overall, our study indicates that:

(i) The association between haemodynamics and atherosclerosis is most apparent when assessed at the level of the entire carotid bifurcation; the association is much weaker when assessed at the individual branch level

(ii) The association is stronger for the data measured at week 20 than week 15

(iii) The association is stronger for the population compared to individual carotid bifurcations

(iv) Of all parameters tested, the strongest spatial correlation between haemodynamics and atherosclerosis development was observed for RRT and TAWSS

(v) Aggregating the data led to an overestimation of the correlation.

Bibliography Chapter 10

[1] B. Ludewig, R. M. Zinkernagel and H. Hengartner, 'Arterial Inflammation and Atherosclerosis', *Trends in Cardiovascular Medicine*, vol. 12, no. 4, pp. 154–159, 2002.

[2] W. Insull, 'The Pathology of Atherosclerosis: Plaque Development and Plaque Responses to Medical Treatment', *The American Journal of Medicine*, vol. 122, no. 1, S3–S14, 2009.

[3] P. Libby, 'Inflammation in atherosclerosis.' *Nature*, vol. 420, no. 6917, pp. 868–74, 2002.

[4] C. Van der Donckt, J. L. Van Herck, D. M. Schrijvers, G. Vanhoutte, M. Verhoye, I. Blockx, A. Van Der Linden, D. Bauters, H. R. Lijnen, J. C. Sluimer, L. Roth, C. E. Van Hove, P. Fransen, M. W. Knaapen, A.-S. A.-S. Hervent, G. W. De Keulenaer, H. Bult, W. Martinet, A. G. Herman and G. R. Y. De Meyer, 'Elastin fragmentation in atherosclerotic mice leads to intraplaque neovascularization, plaque rupture, myocardial infarction, stroke, and sudden death.' *European heart journal*, vol. 36, no. 17, pp. 1049–1058, 2014.

[5] S. Glagov, C. Zarins, D. P. Giddens and D. N. Ku, *Hemodynamics and atherosclerosis. Insights and perspectives gained from studies of human arteries*, 1988.

[6] A. M. Malek, S. L. Alper and S. Izumo, 'Hemodynamic shear stress and its role in atherosclerosis.' *JAMA : the journal of the American Medical Association*, vol. 282, no. 21, pp. 2035–2042, 1999.

[7] V. Peiffer, S. J. Sherwin and P. D. Weinberg, 'Does low and oscillatory wall shear stress correlate spatially with early atherosclerosis? A systematic review', *Cardiovascular Research*, vol. 99, no. 2, pp. 242–250, 2013.

[8] F. J. H. Gijsen, J. J. Wentzel, A. Thury, B. Lamers, J. C. H. Schuurbiers, P. W. Serruys and A. F. van der Steen, 'A new imaging technique to study 3-D plaque and shear stress distribution in human coronary artery bifurcations in vivo', *Journal of Biomechanics*, vol. 40, no. 11, pp. 2349–2357, 2007.

[9] A. K. Joshi, R. L. Leask, J. G. Myers, M. Ojha, J. Butany and C. R. Ethier, 'Intimal thickness is not associated with wall shear stress patterns in the human right coronary artery', *Arteriosclerosis, Thrombosis, and Vascular Biology*, vol. 24, no. 12, pp. 2408–2413, 2004.

[10] V. Peiffer, A. A. Bharath, S. J. Sherwin and P. D. Weinberg, 'A novel method for quantifying spatial correlations between patterns of atherosclerosis and hemodynamic factors.' *Journal of biomechanical engineering*, vol. 135, no. 2, p. 021 023, 2013.

[11] E. M. Rowland, Y. Mohamied, K. Yean Chooi, E. L. Bailey and P. D. Weinberg, 'Comparison of Statistical Methods for Assessing Spatial Correlations Between Maps of Different Arterial Properties', *Journal of Biomechanical Engineering*, vol. 137, no. 10, p. 101 003, 2015.

[12] J. Jawien, R. Nastalek, R. Korbut, J. Jawień, P. Nastałek and R. Korbut, 'Mouse models of experimental atherosclerosis', *journal of physiology and pharmacology*, vol. 55, no. 3, pp. 503–517, 2004.

[13] A. A. Pendse, J. M. Arbones-Mainar, L. A. Johnson, M. K. Altenburg and N. Maeda, 'Apolipoprotein E knock-out and knock-in mice: atherosclerosis, metabolic syndrome, and beyond.' *Journal of lipid research*, vol. 50 Suppl, no. December 2008, S178–S182, 2009.

[14] S. C. Whitman, 'A practical approach to using mice in atherosclerosis research.' *The Clinical biochemist. Reviews*, vol. 25, no. 1, pp. 81–93, 2004.

[15] D. De Wilde, B. Trachet, C. Van der Donckt, B. Vandeghinste, B. Descamps, C. Vanhove, G. R. Y. De Meyer and P. Segers, 'Vulnerable plaque detection and quantification with gold particle-enhanced computed tomography in atherosclerotic mouse models.' *Molecular imaging*, vol. 14, pp. 9–19, 2015.

[16] D. De Wilde, B. Trachet, N. Debusschere, F. Iannaccone, A. Swillens, J. Degroote, J. Vierendeels, G. R. De Meyer and P. Segers, 'Assessment of shear stress related parameters in the carotid bifurcation using mouse-specific FSI simulations', *Journal of Biomechanics*, In press, 2015.

[17] V. Peiffer, S. J. Sherwin and P. D. Weinberg, 'Computation in the rabbit aorta of a new metric - the transverse wall shear stress - to quantify the multidirectional character of disturbed blood flow.' *Journal of biomechanics*, vol. 46, no. 15, pp. 2651–2658, 2013.

[18] H. A. Himburg and M. H. Friedman, 'Correspondence of low mean shear and high harmonic content in the porcine iliac arteries.' *Journal of biomechanical engineering*, vol. 128, no. 6, pp. 852–856, 2006.

[19] B. D. Gelfand, F. H. Epstein and B. R. Blackman, 'Spatial and spectral heterogeneity of time-varying shear stress profiles in the carotid bifurcation by phase-contrast MRI', *Journal of Magnetic Resonance Imaging*, vol. 24, no. 6, pp. 1386–1392, 2006.

[20] X. He, 'Pulsatile Flow in the Human Left Coronary Artery Bifurcation: Average Conditions', *Journal of Biomechanical Engineering*, vol. 118, no. 1, pp. 74–82, 1996.

[21] H. A. Himburg, D. M. Grzybowski, A. L. Hazel, J. A. LaMack, X.-M. Li and M. H. Friedman, 'Spatial comparison between wall shear stress measures and porcine arterial endothelial permeability.' *American journal of physiology. Heart and circulatory physiology*, vol. 286, no. 5, H1916–H1922, 2004.

[22] L. Antiga and D. A. Steinman, 'Robust and Objective Decomposition and Mapping of Bifurcating Vessels', *IEEE Transactions on Medical Imaging*, vol. 23, no. 6, pp. 704–713, 2004.

[23] D. N. Ku, D. P. Giddens, C. K. Zarins and S. Glagov, 'Pulsatile Flow and Atherosclerosis in the Human Carotid Bifurcation', *Arteriosclerosis*, vol. 5, no. 3, pp. 293–302, 1985.

[24] S.-W. Lee, L. Antiga and D. A. Steinman, 'Correlations among indicators of disturbed flow at the normal carotid bifurcation.' *Journal of biomechanical engineering*, vol. 131, no. 6, p. 061 013, 2009.

[25] H. A. Himburg, S. E. Dowd and M. H. Friedman, 'Frequency-dependent response of the vascular endothelium to pulsatile shear stress.' *American journal of physiology. Heart and circulatory physiology*, vol. 293, no. 1, H645–H653, 2007.

V

Conclusions

Chapter 11

Conclusions and future perspectives

In the current work the link between WSS and atherosclerosis development was explored, integrating *in vivo* research in a mouse model of atherosclerosis with imaging and compuatational techniques. The overall research question we put forward was: "Is there an individual and quantitative link between baseline wall shear stress and subsequent plaque development in mouse models of atherosclerosis?"

11.1 Research Goals

Three different intermediate goals were stated that should lead to answering the research question.

Goal 1. *Development of an in vivo measurement technique to localise the atherosclerotic plaques*

It is indispensable to be able to *in vivo* identify atherosclerotic plaques in mice during plaque progression. In chapter 7, a novel application of the gold nanoparticle contrast agent Aurovist 15nm for μCT was described. Using this contrast agent, we were able to *in vivo* visualise macrophage infiltration in atherosclerotic plaques using an μCT technique based on a pre- and a post-contrast injection scan. Although MRI based methods were already described in literature, the current μCT based technique enabled us to perform measurements at a superior resolution, which is required for murine

applications. Moreover, macrophages are a very important marker for plaque vulnerability that are difficult to image.

The importance of this imaging methodology should not be underestimated. The *in vivo* aspect made it possible to follow up plaque progression at 2 time points.

Goal 2. *Setup of a measurements-based computational model to calculate the WSS without sacrificing the mouse.*

A computational FSI model of the blood flow in the murine carotid arteries has been described in chapter 8. To the best of our knowledge, this is the first computational model describing the haemodynamics inside the murine carotid arteries and bifurcation.

Stricto sensu, no significant modifications or additions were made to the different existing models and methods that already have been described and applied in literature, mainly oriented toward studies in humans. In the current work several state-of-the-art existing models were combined and integrated for the first time by our group: external tissue support (using springs), axial prestress (using the BI method) and diastolic inflate prestress (using a second run of the BI method). All these methods were necessary to obtain a stable FSI model in the challenging environment of the murine carotid bifurcation. The innovative methodological aspect of this work is in the aggregation of the different methodologies into one coherent model.

Goal 3. *Applying a statistical model to quantify the link between the haemodynamic metrics and the plaque locations.*

Finally, in chapter 10 a statistical model was applied to relate the shear stress metric maps with the macrophage infiltration on a within-subject basis. Following this methodology we demonstrated that a correlation exists between WSS patterns and the plaque formation. This relation was stronger on the population level compared to the individual bifurcation level. On the individual branch level, only a weak correlation was found for the CCA branch, while the correlation was absent for the ECA and the ICA branches.

Is there an individual and quantitative link between baseline wall shear stress and subsequent plaque development in mouse models of atherosclerosis?

Answering the research question

The simple answer to the central research question is *"Yes"*. However, in reality the answer is not as simple as that.

We did find significant correlations for our population (n=7 bifurcations) between several HWPs (TAWSS, OSI, RRT and transWSS) and the macrophage infiltration at a later stage, when this correlation was determined over the whole carotid bifurcation. This is a most promising result, given that the correlation is significant (with $p<0.05$) for such a small sample size. However, we do have to keep in mind that the statistical testing was a 1-tailed approach. This is a valid approach due to the theoretical description of the HWPs that already defines whether we are interested in a negative (TAWSS) or a positive (other HWPs) correlation.

Although the found (bifurcation) correlations were deemed significant, one still has to remain critical. The absolute values of the correlation coefficients ranged from 0.118 to 0.148, which is still rather low. It is thus save to state that these HWPs only describe a small part of the process leading to atherosclerosis. Moreover, in recent years newer HWPs have been proposed that have been claimed to provide stronger mechanistic links with atherosclerosis development. In the current thesis, we tested the harmonic based HWPs, but they did not provide a stronger association with atherosclerosis in the murine carotid bifurcation. Moreover, most of the tested HWPs demonstrated high degrees of collinearity.

Haemodynamics are only one factor contributing to the atherogenic process and thus the magnitude of the correlation between both will likely never be very high. Nonetheless, there are still other factors that (partially) explain the relatively low correlations between haemodynamics and atherosclerosis that were found in the current work. Some of these factors are inherent to the methodology of imaging, modelling and statistics. To calculate the correlation between the baseline state and the diseased state at a later time point, we needed to map both geometries on a single grid. Especially when severe stenosis occurs, this mapping will never be perfect, even with the best mapping algorithms, due to the high geometrical differences between both geometries. Moreover, macrophage infiltration only highlights one part of atherosclerosis formation. Next to this, we start from images with limited resolution and artefacts. Furthermore, the pipeline to get to the correlation between the HWPs and the macrophage infiltration is long, possibly including extra artefacts. Although several physical processes are included in the modelling part, model assumptions have to be made. In the current thesis the most stringing ones are: the assumption of Newtonian behaviour of the blood and isotropy of the arterial wall. Therefore, reality is only approximated, possibly further clouding the relation between WSS and atherosclerosis development.

Other, statistical reasons for the relatively low correlation were introduced on purpose. The Spearman's rank correlation coefficient generally results in a lower correlation coefficient compared to the Pearson's correlation coefficient but it is theoretically the better choice because the different HWPs are not linearly correlated to macrophage infiltration. Moreover, we showed that aggregating of the data, which is commonly done in literature, overestimates the correlation.

Another limitation of the current work are the "baseline" simulations. The simulations were based on measurements done at 10 weeks after the start of the diet. Because there is not sign of plaque development (= no narrowing of the arteries) visible yet, we assume that this is a valid model for the baseline state. However, the absence of visible narrowing does not does not assure that there is no influence of (minor) plaque formation present yet. Therefore, our baseline measurements could be biased by initial plaque formation.

What about humans?

The current work was restricted to mouse models. Of course the final goal is still to better understand atherosclerosis in humans. We are, in my opinion, still a long way from that final goal. As explained in chapter 2, the atherosclerotic plaques in the recently developed genetically modified mouse models are morphologically similar to human plaques. However, there are still differences and the induced genetic defects may also affect the plaque formation and the general health of the mouse in different ways, which are not all well understood yet. The measurements described in this dissertation show that in the $ApoE^{-/-}$ and $ApoE^{-/-}$ $Fbn1^{C1039G+/-}$ mouse models, the atherosclerosis develops preferentially at the ECA compared to the ICA. On the other hand in humans, clinical complications are commonly found because of atherosclerotic plaques that developed in the ICA[1], [2].

More specifically with regard to haemodynamics, there are still some major differences between mice and humans, the most prominent ones being the higher heart rate and the smaller dimensions. This leads to much lower Reynolds (~25 times lower [3]) and Womersley (~9 times lower [3]) numbers in mice compared to humans and thus towards more laminar flow patterns. In the carotid bifurcation this leads to the absence of flow recirculation zones at the outer side of the sinus in the base model described in chapter 8, while this phenomenon has been reported in numerously publications in humans. Adaptation of the BCs to active, non-anaesthetised conditions was necessary for limited recirculation to occur. These very different temporal WSS patterns between mice and humans make it more difficult to directly compare or translate the results. The different HWPs that were calculated

in the current thesis were, most of the time, defined in the human context and they were defined in an attempt to describe the atheroprone effect of the WSS. The fact that the murine haemodynamic environment is substantially different from the human haemodynamic environment may hamper their applicability for the setting of the mouse carotid artery. At the same time, however, our findings also questions the generalizability of the use of some of these metrics.

Still, one has to keep in mind the main reason why in this work we chose to set up these studies in a mouse model of atherosclerosis. The long time span for atherosclerosis to develop in humans makes it almost impossible to conduct a similar study in the human setting. Once the atherosclerotic plaque has formed and stenosis is present, the haemodynamic environment changes dramatically. The haemodynamic environment still has an important influence on the plaque development and possibly even on the vulnerability or plaque rupture. However, the change in the haemodynamic environment hampers studies aiming for a spatial correlation and/or a causal link between baseline haemodynamics and plaque initiation. Some groups have tried to virtually remove the atherosclerotic plaque to obtain a baseline setting, but this is very challenging. Mice are already a step closer to the human case, in comparison with the numerous *in vitro* studies linking WSS with different molecular pathways towards atherosclerosis. Therefore, future research could be directed to animal models that mimic the human even more closely such as pigs or non-human primates.

11.2 What about rupture?

After reading chapter 8, one might find it somewhat disappointing that we limited our focus on the haemodynamics. After all, this chapter distinguishes itself from work done by other research groups by including the external tissue and prestress, which allows for a more realistic simulation of the wall mechanics. A logic next step for the current research is to include the mechanical behaviour of the arterial wall and the atherosclerotic plaque. A first step can be to model the atherosclerotic plaque together with a more realistic arterial wall model, without the presence of blood flow in a purely computational solid mechanics model (because the shear stresses exerted by the blood are much lower compared to the mechanical stresses in the arterial wall). A second step is to include this mechanical plaque and arterial wall models in the FSI methodology described in the current thesis.

Both of these steps are not minor, mainly because even more challenging imaging is required. For the current work, one of the main limitations was that the thickness of the arterial wall was unknown and estimated to be 10%

of the arterial diameter. To be able to build realistic CSM or FSI models, this assumption should be avoided and preferentially the layered structure of the arterial wall (intima, media and adventitia) should be included in the model. To be able to build such models, the 3D-geometry of the arterial wall needs to be known with high accuracy. To include the atherosclerotic plaque, the requirements are even more demanding because of for example the small thickness of the cap of the plaque. Next to this, the soft tissue contrast that is needed to image the plaque and the layered structure of the wall also places a restriction on viable imaging techniques. Recent advances such as synchrotron-based X-ray tomographic microscopy [4] and 3D cryo-imaging [5] can provide sufficient soft tissue contrast at superior resolutions which makes it feasible to construct a highly accurate 3D model of the atherosclerotic plaque and wall. The main disadvantage is that these techniques are *ex vivo*. In future projects, the baseline haemodynamics could be assessed using the methodological framework presented in the current thesis with at the end stage a full FSI model including the plaque and more realistic wall mechanics based on highly accurate *ex vivo* imaging.

11.3 Where to go from here?

As mentioned above there are 2 main new directions that the current research can take: (i) proceeding towards animal models such as pigs that are more closely related to humans and (ii) extending the current framework to also include more realistic models for the arterial wall and plaque to expand the research field towards plaque rupture.

The current thesis fused advancement made in different research fields including: preclinical imaging, image processing, development of animal models, statistics and computational modelling. Indispensable for the current research were: (i) development of a murine vascular μCT contrast agent (ii) better image reconstruction algorithms for CT (iii) development of robust coupling code for FSI simulations (iv) development of advanced statistical models to study spatial correlations. Therefore, future opportunities will present themselves when significant advances are made in any of those research fields. The inclusion of the atherosclerotic plaque in the computational solid mechanics model has already become feasible due to recent advances in (*ex vivo*) imaging.

Next to this, one should aim to render the proposed methodology more efficient, reducing the manual labour needed. The two most labour intensive steps were the high quality segmentation (needed for the FSI model) and a high quality (fluid and structural) mesh. Both are subject to a lot of scientific interest and development. Large industrial companies, such as Materialise,

Ansys or Simulia, provide newer and better performing algorithms every year. In the coming years this will probably significantly reduce the manual labour, providing the opportunity to include more animals in similar studies, needed to obtain statistically more robust results.

11.4 Take home message

In this work, we have shown that gold nanoparticle- enhanced μCT can be applied to visualise macrophage infiltration *in vivo* in the atherosclerotic plaque of mice. Moreover, a methodology was presented to calculate the haemodynamics in the carotid bifurcation of those mice. Most importantly, we showed that the haemodynamic wall shear stress at the baseline stage is linked to macrophage infiltration in the atherosclerotic plaques at a later stage on an individual mouse level.

Bibliography Chapter 11

[1] J. a. Deweese, a. G. May and E. O. Lipchik, 'Anatomic and Hemodynamic Correlations in Carotid Artery Stenosis', *Stroke*, vol. 1, no. 3, pp. 149–157, 1970.

[2] T. G. Phan, R. J. Beare, D. Jolley, G. Das, M. Ren, K. Wong, W. Chong, M. D. Sinnott, J. E. Hilton and V. Srikanth, 'Carotid Artery Anatomy and Geometry as Risk Factors for Carotid Atherosclerotic Disease', *Stroke*, vol. 43, no. 6, pp. 1596–1601, 2012.

[3] J. Suo, D. E. Ferrara, D. Sorescu, R. E. Guldberg, W. R. Taylor and D. P. Giddens, 'Hemodynamic shear stresses in mouse aortas: implications for atherogenesis.' *Arteriosclerosis, thrombosis, and vascular biology*, vol. 27, no. 2, pp. 346–51, 2007.

[4] B. Trachet, R. A. Fraga-Silva, A. Piersigilli, A. Tedgui, J. Sordet-Dessimoz, A. Astolfo, C. Van der Donckt, P. Modregger, M. F. M. Stampanoni, P. Segers and N. Stergiopulos, 'Dissecting abdominal aortic aneurysm in Ang II-infused mice: suprarenal branch ruptures and apparent luminal dilatation', *Cardiovascular Research*, vol. 105, no. 2, pp. 213–222, 2015.

[5] D. Roy, G. J. Steyer, M. Gargesha, M. E. Stone and D. L. Wilson, '3D Cryo-Imaging: A Very High-Resolution View of the Whole Mouse', *The Anatomical Record: Advances in Integrative Anatomy and Evolutionary Biology*, vol. 292, no. 3, pp. 342–351, 2009.

VI

Appendices

Appendix A

Linear mixed models

A.1 Introduction

Linear mixed models were used in chapter 6 (analysis of ultrasound data) and chapter 7 (analysis of macrophage infiltration data). All these datasets are similarly structured and the same statistical methodology was followed. Because this statistical model is not generally known, a short introduction is described in this appendix.

A.2 Description of the numerical data

For all these datasets we want to study how a single numerical variable or parameter, for example the velocity at peak systole, differs between groups of animals, taking into account grouping variables such as the time on the diet, measuring location or measuring side. The different subjects are grouped in several ways. First, species ($ApoE^{-/-}$ or $ApoE^{-/-}$ $Fbn1^{C1039G+/-}$), is taken as a between-subjects grouping factor, because this is a factor that differentiates between the different mice (subjects). Side (left or right), location (CCA, ECA or ICA) and time (weeks 0, 5, 10, 15 or 20) are within-subject grouping factors. These within-subject factors, differentiate between several measurements done in the same subject (mouse). Statistically the latter are different from the between-subject measurements because they are repeated measurements on the same mouse. Therefore, they are in some degree correlated to each other. Thus, they can not be included in the statistical model as independent measurements. An overview of the different grouping factors, their nature and possible values is given in table A.1.

Table A.1: Grouping variables used in the linear mixed model analysis. Some of the analyses take only 2 time points (weeks 15 and 20) into account while for others all 5 time points (weeks 0, 5, 10, 15 and 20) are taken into account.

factor	nature	possible values
species	between-subjects	$ApoE^{-/-}$ — $ApoE^{-/-}$ $Fbn1^{C1039G+/-}$
time	within-subject	weeks 0 – 5 – 10 – 15 – 20
side	within-subject	left — right
location	within-subject	CCA – ECA – ICA

A.3 GLM: repeated measures ANOVA

The repeated measures analysis of variance (ANOVA) (a general linear model (GLM)), is the more traditional approach used in the scientific world to compare group means of dependent variables across repeated measurements over time. Using an ANOVA procedure, the group means of more than 2 groups can be compared. Therefore, this can be seen as a generalization of the t-test. For analyzing a repeated measurements experiments, there are some severe limitations related to the ANOVA analysis that are difficult to meet [1], [2]:

- The datasets have to be complete (meaning subjects with at least one missing data point have to be excluded)
- A common set of time periods is needed (time between measurements exactly the same for all subjects)

A.4 Linear Mixed Model (LMM)

A.4.1 Why LMM in the current PhD thesis?

In comparison with the GLM, the LMM has two main strengths for (bio)medical data: (i) accommodate for missing data points (often present in longitudinal datasets) (ii) model individual, nonlinear characteristics [1]. Especially the ability of the test to deal with missing data is essential with respect to the current research.

Missing data points are present in for some of the mice in all our datasets. For the US data, this is mainly because the high amount of measurements done on an individual mouse. For both the PW Doppler US and the M-mode US measurements, the measurements include: 5 time points, 3 locations and 2 sides. This results in 30 measurements for both the PW Doppler US and the M-mode US measurements. Next to this, the presence of atherosclerosis made these measurements challenging and technically difficult to perform.

Next to this, the limited time frame (duration of the anaesthesia was limited to one hour) and irregular response to the anaesthesia of the sick animals further complicated the measurements. For the μCT measurements, less measurements are done although 4 measurements are needed for the macrophage-infiltration visualization results in chapter 7 on page 117 (2 time points but pre- and post-contrast injection). However, these measurements are much more challenging with motion artifacts, difficult registration and segmentation compromising accurate results. This leads to only a small amount of measurements that are complete and that thus can be included in an GLM analysis.

A.4.2 LMM: basic principles

This section gives a short overview of the principles behind the LMM, based on three major literature sources[*,†,‡].

A linear model describes the responses of the model (y) in function of fixed effects and an error term (ε). The fixed effects are effects that affect the population mean. They can be repeated and an example in the current PhD thesis is the between-subject factor measuring location (CCA, ECA or ICA). This effect is repeatable, in a next study it is possible to measure the same locations again, and it could be possible that the location has an influence on the average value measured. More specifically for this study the fixed effects are always considered to be factors (categorical, qualitative data). No fixed covariates (quantitative data) were studied in the current thesis.

A general linear model can be described by:

$$y = \underbrace{X\beta}_{fixed} + \underbrace{\varepsilon}_{residual} \tag{A.1}$$

In this equation the vector y (n x 1 with n the number of responses) represents the responses(=measurements) of the model and the term $X\beta$ denotes the fixed effects. β (p x 1 with p the number of factors) is a vector representing the unknown fixed effects and X (n x p) the associated independent, grouping variables (X is called the design matrix). ε (n x 1) represents a vector with the errors.

In contrast to the general linear model, the LMM can deal with responses that are described by both fixed and random effects. The random effects

[*] SPSS, 'Linear mixed-effects modeling in SPSS: An introduction to the MIXED procedure', *Technical Report*, LMEMWP–1002, 2002.

[†] C. Kincaid, 'Guidelines for Selecting the Covariance Structure in Mixed Model Analysis', in *Proceedings of the Thirtieth Annual SAS Users Group International Conference*, SAS Institute Inc, Cary, NC: SAS Institute Inc, 2005.

[‡] W. A. Jensen, 'Profile Monitoring for Mixed Model Data', PhD, 2006.

have no effect on the population mean but it they affect the mean of a single subject (=mouse). As an example we will consider the PW Doppler US measured blood velocity in section 6.2 on page 102. The LMM is able to take into account both the fixed effect of measurement location and the random differences between different mice into account. If the measured velocities in a specific mouse are higher for all measurement locations, the random effects include this in the model.

The fitted LMM can be described as:

$$y_i = \underbrace{X_i\beta}_{fixed} + \underbrace{Z_i\gamma_i}_{random} + \underbrace{\varepsilon_i}_{residual} \tag{A.2}$$

The subscript i denotes different subjects (=mice). In this formula Y_i is a vector(n_i x 1 with n_i the number of measurements on mouse i) that gives the responses of the model (=the measurements). The term $X_i\beta$ describes the fixed effects. In this term β denotes the different unknown fixed effects (p x 1 with p the number of factors) and X_i is the fixed effects design matrix (n_i x p). The design matrix X represents the independent variables in the model (=grouping variables). In other words, for every measurement it describes to which groups, according to the grouping variables, the measurement belongs. It can be seen that the influence of the fixed effects β do not differ between mice (no subscript i for β), the influence of the fixed effects is the same for all subjects. The random effects are incorporated in the term $Z_i\gamma_i$. γ_i (q x 1 with q the number of random effects) denotes the unknown random effects and Z_i is the design matrix (n_i x q) of the random effects. Another interpretation of the random effects, is that they represent the subject-specific regression coefficients that characterize the natural heterogeneity in the population [4]. More specifically in the current research, the (average) difference between different mice is modelled as a random effect and thus included in the random term $Z_i\gamma_i$. Finally, ε_i (n_i x 1)denotes the residual errors.

The described LMM was fitted to the measurements using SPSS Statistics 22 (IBM, Armonk, NY, US). The specific parameters are described in the subsequent chapters when the analysis is performed. For more details on the procedure the reader is referred to the manual of SPSS.

Bibliography Appendix A

[1] C. Krueger and L. Tian, 'A comparison of the general linear mixed model and repeated measures ANOVA using a dataset with multiple missing data points.' *Biological research for nursing*, vol. 6, no. 2, pp. 151–157, 2004.

[2] C. S. Davis, 'Statistical Methods for the Analysis of Repeated Measurements'. 2002, p. 415.

[3] SPSS, 'Linear mixed-effects modeling in SPSS: An introduction to the MIXED procedure', *Technical Report*, LMEMWP–1002, 2002.

[4] C. Kincaid, 'Guidelines for Selecting the Covariance Structure in Mixed Model Analysis', in *Proceedings of the Thirtieth Annual SAS Users Group International Conference*, SAS Institute Inc, Cary, NC: SAS Institute Inc, 2005.

[5] W. A. Jensen, 'Profile Monitoring for Mixed Model Data', PhD, 2006.

Appendix B

Surrogate sample data analysis

B.1 Introduction

This appendix gives an overview of the surrogate sample data analysis (SSDA), as this method is an important tool used in this thesis (in 10). The SSDA was first described by Peiffer *et al.*[*] and later further refined by Rowland *et al.*[†]. This section is thus mainly an overview of their work with only minor adaptations.

The SSDA was developed to quantify the correlation between (an aggregated) atherosclerotic plaque distribution (=lesion map) and (an aggregated) haemodynamic wall parameter distribution (= haemodynamic map). As a criterion to conclude that correlation is present, most early publications used a linear regression analysis [3], [4]. However, there are two main prerequisites needed to do a linear regression analysis that are very strict and that are not always valid in these kind of datasets:

1. a linear relationship between the variables
2. the data points are independent of each other

[*] V. Peiffer, A. A. Bharath, S. J. Sherwin *et al.*, 'A novel method for quantifying spatial correlations between patterns of atherosclerosis and hemodynamic factors.' *Journal of biomechanical engineering*, vol. 135, no. 2, p. 021 023, 2013.

[†] E. M. Rowland, Y. Mohamied, K. Yean Chooi *et al.*, 'Comparison of Statistical Methods for Assessing Spatial Correlations Between Maps of Different Arterial Properties', *Journal of Biomechanical Engineering*, vol. 137, no. 10, p. 101 003, 2015.

The process that leads from disturbed blood flow to atherosclerosis development, is complicated and includes a lot of interfering factors. Therefore the relationship between a lesion map and a haemodynamic map will most likely not be linear. The HWPs are calculated in the grid points of the numeric mesh. If all the grid points are included in the linear regression test, this results in a problematic testing approach. Indeed, using a finer calculation mesh will result in a higher number of data points and thus in a higher power of the statistical test. The outcome of the test is thus mesh-size dependent, although the mesh size is a pure numerical property.

Peiffer *et al.* [1] solved this dual problem with a dual solution. Both of them are described below.

1. linear relationship →surrogate analysis
2. independence →sample analysis

When applying the SSDA to study the correlation between atherosclerosis and haemodynamic maps, both distributions need to be known in the same grid. This 2D-grid has to be spaced equally in both directions. Therefore, the luminal surface has to be mapped onto a 2D-grid. Several methods have already been developed to do this; in the current work a VMTK (`http://www.vmtk.org`) based approach has been followed. More information about the mapping can be found in chapter 10 on page 199 or in the publication of Antiga and Steinman [5].

B.2 Surrogate analysis

The surrogate analysis is applied to overcome the limitation of the linear relationship. First a quantitative measure describing the similarity between two different maps is needed (a HWP map and a lesion map), which is called the discriminating statistic. This enables the algorithm to order different (HWP) maps according to the similarity to a base map (lesion map). For this discriminating statistic, Peiffer *et al.* proposed the sum of the absolute differences after normalization (for example by division with the L2-norm) of the maps (equation (B.1a) with x and y the values of both maps). Another possibility is to use the correlation coefficient as the discriminating statistic as proposed by Rowland *et al.* [2]. Pearson's correlation coefficient r (equation (B.1b))can be used, but this assumes that the relation between the lesion map and the haemodynamic map is linear. Spearman's correlation coefficient ρ_s (equation (B.1c))on the other hand only assumes a monotonic relation between the two variables. For the ρ_s, the pointwise values of both maps (x

and y) are replaced by their ranks (r and s). When using either the absolute differences or ρ_s, the assumption of a linear relationship can be circumvented.

$$Discriminating\ Statistic = \sum_{i=1}^{n} |x_i - y_i| \tag{B.1a}$$

$$r = \frac{\sum_{i=1}^{n} (x_i - \bar{x})(y_i - \bar{y})}{\sqrt{\sum_{i=1}^{n} (x_i - \bar{x})^2} \sqrt{\sum_{i=1}^{n} (y_i - \bar{y})^2}} \tag{B.1b}$$

$$\rho_s = \frac{\sum_{i=1}^{n} (r_i - \bar{r})(s_i - \bar{s})}{\sqrt{\sum_{i=1}^{n} (r_i - \bar{r})^2} \sqrt{\sum_{i=1}^{n} (s_i - \bar{s})^2}} \tag{B.1c}$$

In the current work and the remainder of this appendix, ρ_s is used by default unless it is mentioned explicitly that r was calculated.

A flowchart of the surrogate analysis is given in figure B.1. The first step is to calculate ρ_s between the lesion map and the haemodynamic map, which is called the original ρ_s. Afterwards, the haemodynamic map is randomly shuffled generating a surrogate haemodynamic map. For this surrogate haemodynamic map a surrogate ρ_s is calculated, describing the similarity between the original lesion map and the randomly shuffled haemodynamic map. In the current work, this step was repeated for 250 times to generate 250 surrogate ρ_s values. Afterwards, a histogram is determined of the 250 (or more) surrogate ρ_s values and the percentile of the original ρ_s value (for the original maps) is determined. An extra 250 surrogate ρ_s values are calculated as long as the resulting percentile is not below the convergence criterion of 10^{-4}.

A simplified graphical illustration of this procedure is given in figure B.2. In this illustration 3 surrogate pairs (right) are generated from the original maps (left). The percentile of the original ρ_s is indicated on top of the histogram of the surrogate values.

It is also clear from figure B.2 that the surrogate sample analysis is a single tailed approach. For the example in the figure, the ρ_s value of the original maps is smaller than most of the randomly shuffled surrogate datasets, meaning that the negative correlation is more outspoken than in most of the random shuffled distributions. If the original ρ_s is smaller than 95% of the surrogates, we can conclude that the negative correlation is significant according to this test. Thus for the left tailed test, looking for a negative

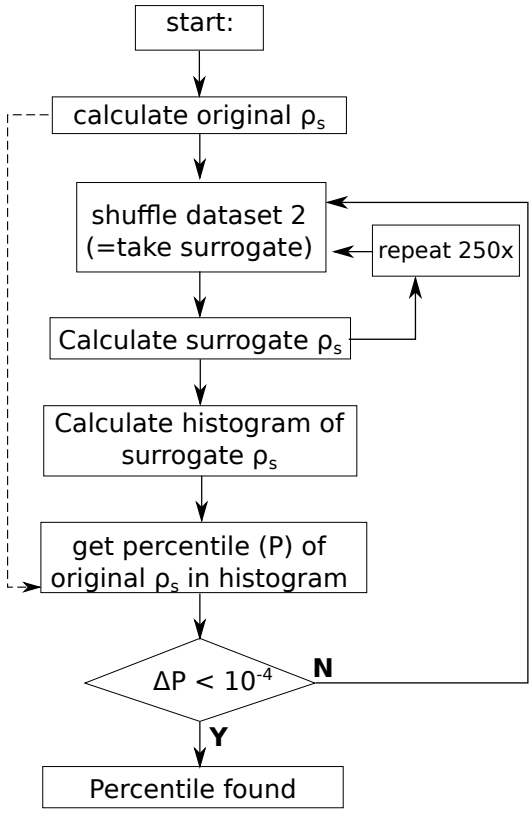

Figure B.1: Schematic drawing of the surrogate analysis. In the diagram n_{sur} is the number of surrogates taken (number of iterations) and i_{sur} the iterator (adapted from [1]).

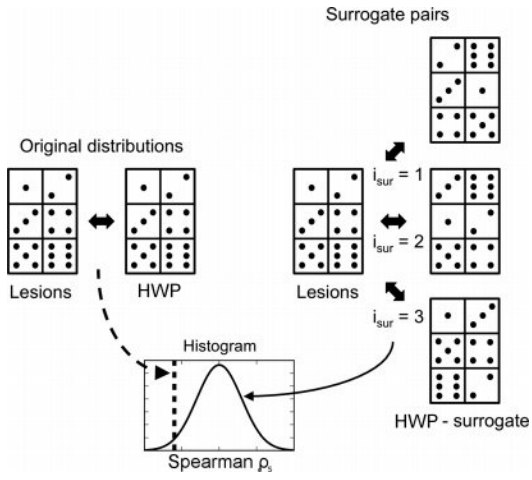

Figure B.2: Illustration of the surrogate data analysis (adapted from [1])

correlation, the original ρ_s values has to be below the 5% percentile. The p-value of the test is equal to the percentile of the original ρ_s in the surrogate histogram. When looking for a positive correlation (right tailed test), the original ρ_s has to be larger than 95% of the surrogate ρ_s values. This means that the p-value of the right-tailed test equals the 1-percentile.

B.3 Sample analysis

Although the surrogate analysis eliminates the need for a linear relation between both maps, the independence of the data points is still not guaranteed. Therefore, Peiffer *et al.* introduced a second step of randomizations by taking random samples of the original maps[1], see flowchart figure B.3. The surrogate data analysis is applied for 250 random samples of the original maps. This results in 250 percentile values for the original samples compared to the surrogates of these samples. The resulting p-value for the SSDA, is the median value of the individual surrogate data analysis. Extra surrogate analyses are performed as long as the resulting median percentile differs more than the convergence criterion of 10^{-4}.

The sample and surrogate steps are illustrated in figure B.4 for 2 sample steps (i_{smp}) and 2 surrogate steps (i_{sur}). For both sample steps, a different random sample of the original datasets was taken (coloured in black).

To ensure that the subsampling overcomes the spatial autocorrelation, the number of points that is included in each subsample is critical. The decorrelation length l_{dec}, is the spatial distance for which two samples are not correlated any more. For a given l_{dec}, a given sample size (s_{smp}) of $s_{smp} = s_{map}/l_{dec}$ with s_{map} the size of the map, ensures that on average one pixel is selected from each l_{dec}^2 square subregion. To determine the length scale l_{dec} at which the autocorrelation diminishes, the same tailored approach as described by Peiffer *et al.* was followed[1]. Rowland *et al.* [2]warn that more than one l_{dec} can be present in a dataset. Underestimating the l_{dec} implies that not all the spatial autocorrelation is removed and that the data points are not mutually independent. Overestimating the l_{dec} implies that the smaller spatial scales are not included in the testing procedure and this results in a lower specificity of the test. When applying the SSDA in chapter 10, we have ensured to not underestimate the l_{dec} in order to assure correct testing.

B.4 Confidence bound adaptation

Rowland *et al.* [2] made some further refinements to the method of Peiffer *et al.* [1]. A first adaptation was the use of ρ_s instead of the sum of the absolute differences for the discriminating statistic, as described above. They also included the confidence interval into the analysis.

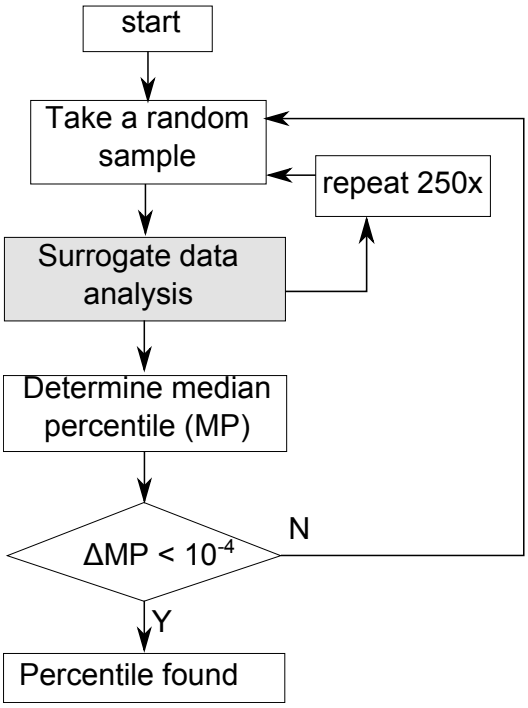

Figure B.3: Schematic drawing of the surrogate sample data analysis. A schematic of the surrogate analysis is given in figure B.1. In the current diagram, the sample iterations are shown. N_{smp} is the number of samples taken and i_{smp} the iterator (adapted from [1]).

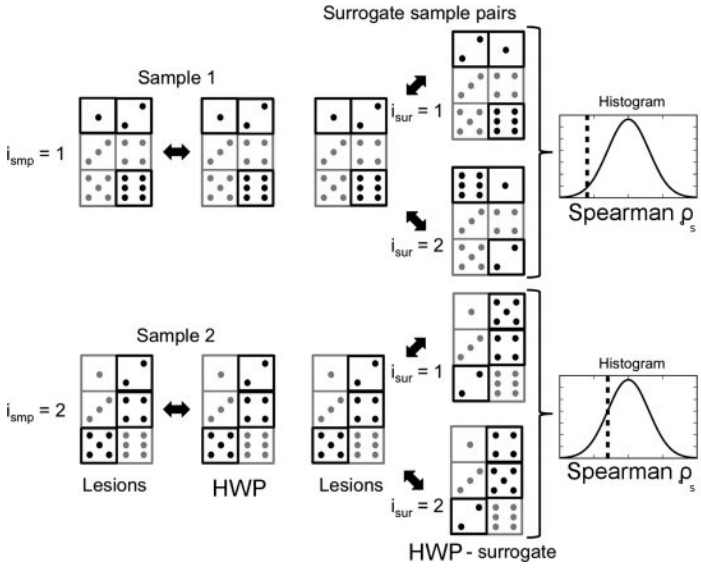

Figure B.4: Illustration of the surrogate sample data analysis (adapted from [1])

The SSDA described in the previous section results in a single tailed p-value for the statistical test. The first condition for significance is: p-value<0.05. This condition is graphically represented in figure B.5a for a positive correlation.

As Rowland *et al.* mentioned, a part of the testing procedure is to obtain the distribution of the ρ_s for several subsamples. From this distribution one can then calculate the two tailed confidence interval or the one tailed confidence bound (CB). In the current work, the upper confidence bound (UCB) was used for the left tailed tests (negative correlation) and the lower confidence bound (LCB) for the right tailed tests (positive correlation). This ensures that both conditions, i.e. the condition for the p-value and the condition for the CB, are one tailed and thus consistent.

For a negative correlation, this second condition stipulates that for 95% of the subsamples that are analyzed, the found value for ρ_s has to be negative. In a formula this becomes: UCBρ_s<0. For the positive correlation case the test has to make sure that the found ρ_s is positive for at least 95% of the subsamples: LCBρ_s>0. This second condition is plotted for an example case in figure B.5b.

B.5 Other methods to account for spatial autocorrelation

When comparing different statistical methods for assessing spatial correlations, Rowland *et al.* [2] described other possible statistical methods that could replace the SSDA applied in the current work. However, both the restricted randomization and the bootstrap approach, which were proposed as alternative methods, are computationally more demanding than the SSDA. In contrast to the previous authors [1], [2], the surrogate sample data analysis was applied to individual spatial maps (branch and bifurcation level) instead of on aggregated spatial maps or groups of spatial maps. Therefore, the bootstrapped approach [6] could not be used, because we compare individual maps. At the population level, we could apply a paired t-test in the current work, rendering the bootstrapped approach unnecessary. The Fourier based restricted randomization approach [2] cannot be applied to the current datasets due to their irregular shape. For the discrete wavelets based restricted randomization [7], [8], the computational cost and complexity are even higher and rotations should be added to overcome poor directional selectivity, which was judged too complex for the added benefit.

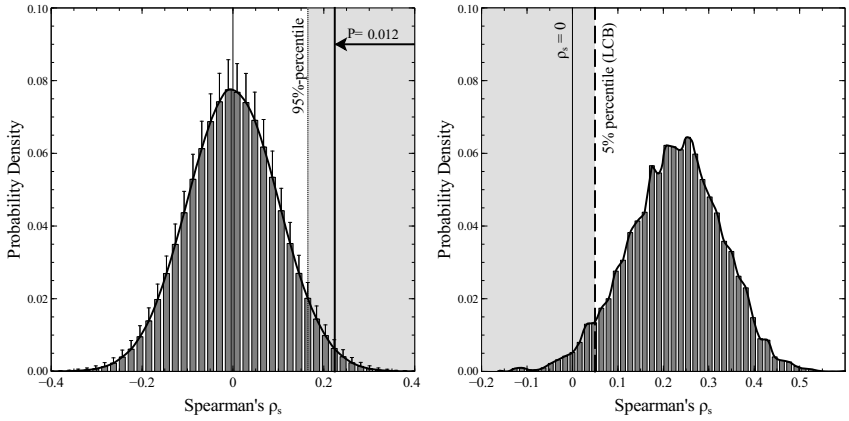

(a) condition 1: p-value SSDA **(b)** condition 2: CB surrogates

Figure B.5: Graphical representation of the conditions for significance for the SSDA. In this example a one-tailed test for a positive correlation is illustrated, which relates the OSI with the macrophage infiltration at week 20 for mouse 1L (see chapter 10 on page 199). (a) the original condition for the SSDA proposed by Peiffer *et al.* [1].For every sample, the p-value is equal to 1- the percentile of the original sample compared to the surrogates. For significance, the median p-value for all samples (p=0.012, thick black line), has to be lower than 0.05 and thus has to be located in the grey area. (b) for the second condition the histogram of the correlation coefficients of the original samples has to be calculated. The condition for significance stipulates that the LCB has to be higher than 0 (ρ has to be in the grey area) .

Bibliography Appendix B

[1] V. Peiffer, A. A. Bharath, S. J. Sherwin and P. D. Weinberg, 'A novel method for quantifying spatial correlations between patterns of atherosclerosis and hemodynamic factors.' *Journal of biomechanical engineering*, vol. 135, no. 2, p. 021 023, 2013.

[2] E. M. Rowland, Y. Mohamied, K. Yean Chooi, E. L. Bailey and P. D. Weinberg, 'Comparison of Statistical Methods for Assessing Spatial Correlations Between Maps of Different Arterial Properties', *Journal of Biomechanical Engineering*, vol. 137, no. 10, p. 101 003, 2015.

[3] F. J. H. Gijsen, J. J. Wentzel, A. Thury, B. Lamers, J. C. H. Schuurbiers, P. W. Serruys and A. F. van der Steen, 'A new imaging technique to study 3-D plaque and shear stress distribution in human coronary artery bifurcations in vivo', *Journal of Biomechanics*, vol. 40, no. 11, pp. 2349–2357, 2007.

[4] J. J. Wentzel, F. J. Gijsen, J. C. Schuurbiers, R. Krams, P. W. Serruys, P. J. De Feyter and C. J. Slager, 'Geometry guided data averaging enables the interpretation of shear stress related plaque development in human coronary arteries', *Journal of Biomechanics*, vol. 38, no. 7, pp. 1551–1555, 2005.

[5] L. Antiga and D. A. Steinman, 'Robust and Objective Decomposition and Mapping of Bifurcating Vessels', *IEEE Transactions on Medical Imaging*, vol. 23, no. 6, pp. 704–713, 2004.

[6] M. Wood, 'Bootstrapped Confidence Intervals as an Approach to Statistical Inference', *Organizational Research Methods*, vol. 8, no. 4, pp. 454–470, 2005.

[7] V. Deblauwe, P. Kennel and P. Couteron, 'Testing pairwise association between spatially autocorrelated variables: a new approach using surrogate lattice data.' *PloS one*, vol. 7, no. 11, e48766, 2012.

[8] N. G. Kingsbury, 'The dual-tree complex wavelet transform: a new technique for shift invariance and directional filters', *Proc 8th IEEE DSP Workshop Utah*, paper 86, 1998.

Appendix C

Comparison between macrophage infiltration and different HWPs

List of Figures in Appendix C

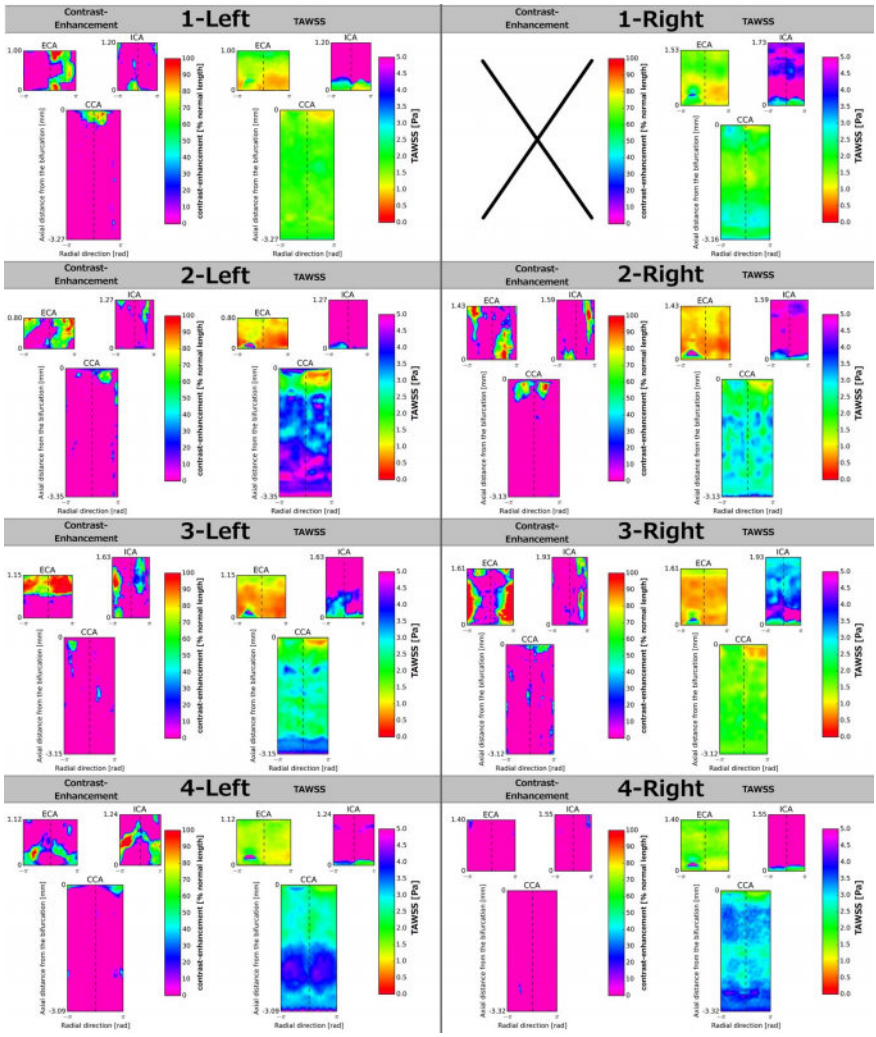

Figure C.1: Overview of the three branches (CCA, ECA, ECA) of the 8 carotid bifurcations (left and right) of the 4 ApoE$^{-/-}$ mice. For every bifurcation locations with macrophage infiltration at week 20 and the TAWSS pattern are placed side by side.

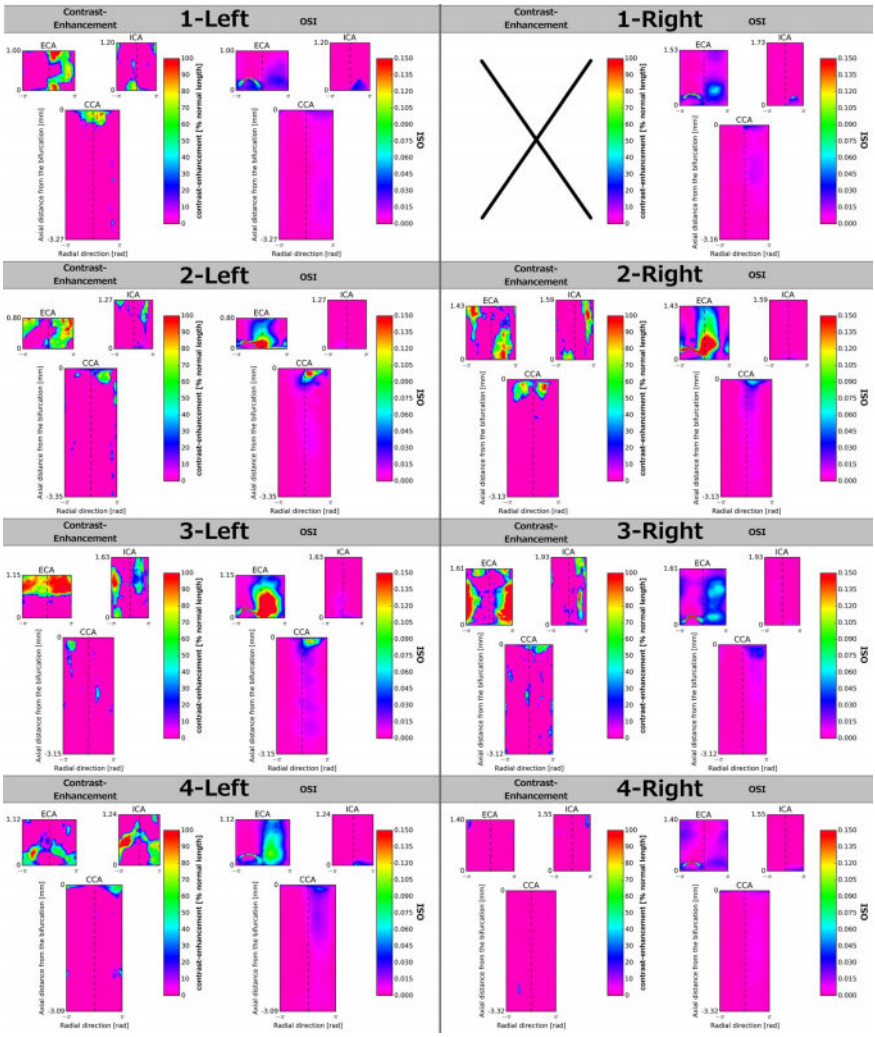

Figure C.2: Overview of the three branches (CCA, ECA, ECA) of the 8 carotid bifurcations (left and right) of the 4 ApoE$^{-/-}$ mice. For every bifurcation locations with macrophage infiltration at week 20 and the OSI pattern are placed side by side.

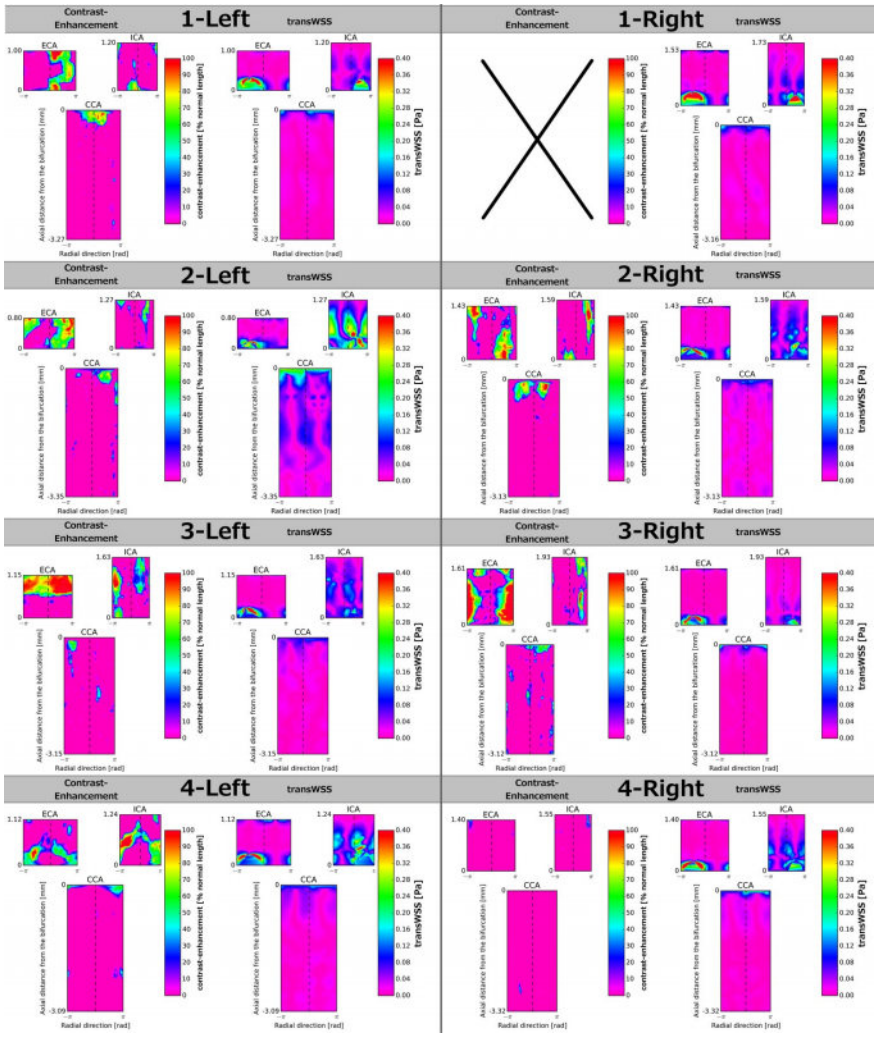

Figure C.3: Overview of the three branches (CCA, ECA, ECA) of the 8 carotid bifurcations (left and right) of the 4 ApoE$^{-/-}$ mice. For every bifurcation locations with macrophage infiltration at week 20 and the transWSS pattern are placed side by side.

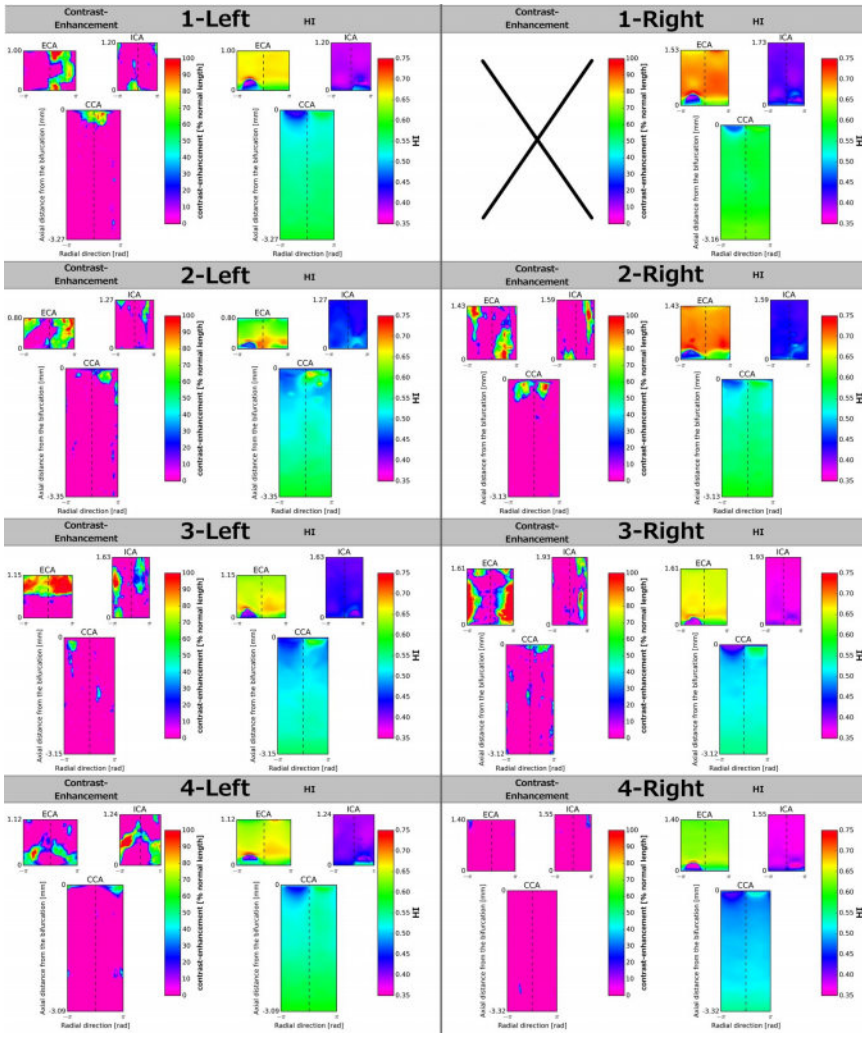

Figure C.4: Overview of the three branches (CCA, ECA, ECA) of the 8 carotid bifurcations (left and right) of the 4 ApoE$^{-/-}$ mice. For every bifurcation locations with macrophage infiltration at week 20 and the HI pattern are placed side by side.

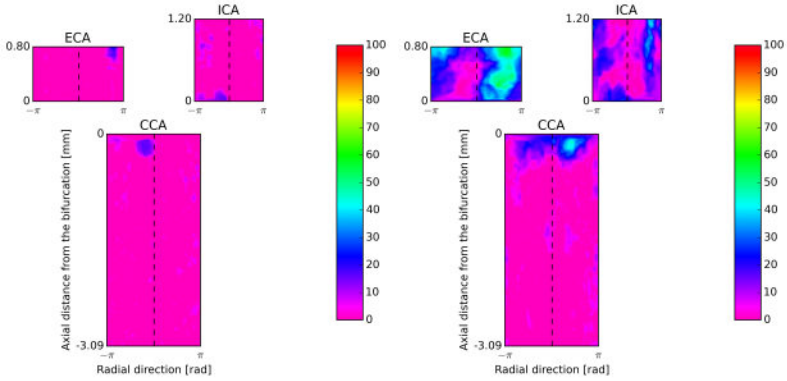

(a) week 15 **(b)** week 20

Figure C.5: The aggregated macrophage infiltration datasets for (a) week 15 and (b) week 20.

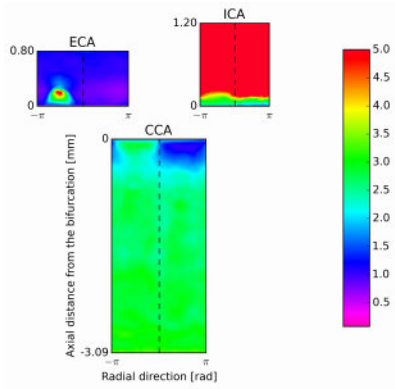

(a) TAWSS (Pa)

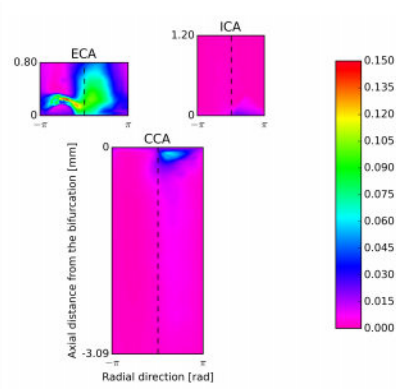

(b) OSI

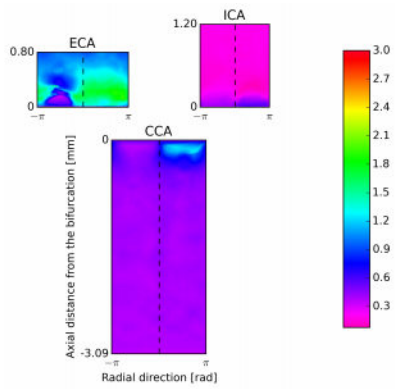

(c) RRT

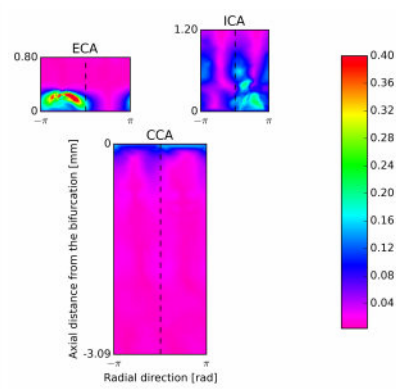

(d) transWSS (Pa)

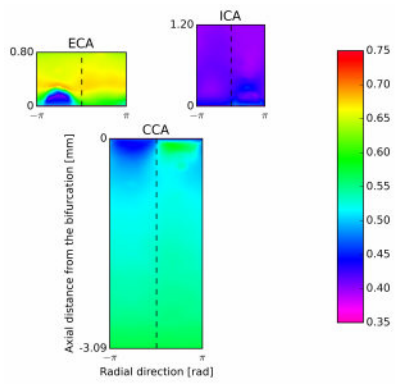

(e) HI

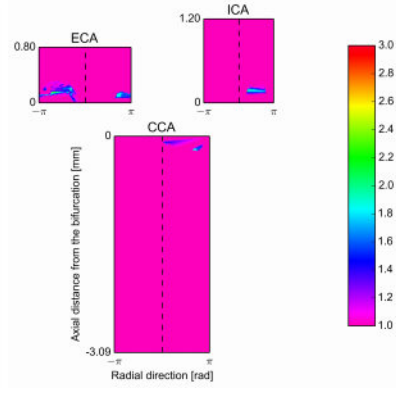

(f) DH

Figure C.6: Aggregated FSI caculated WSS metric datasets: (a) TAWSS, (b) OSI, (c) RRT,(d) transWSS, (e) HI and (f) DH

List of Figures

List of Tables